

University of Nottingham
UK | CHINA | MALAYSIA

Rock-Fluid Interactions in Geothermal Reservoir Systems and the Implications for Carbon Sequestration

Grace Belshaw

School of Chemistry

Thesis Submitted to the University of Nottingham for the degree of Doctor of Philosophy

July 2021

i. Abstract

This thesis aims to examine whether andesitic rock samples are likely to be good targets for permanent carbon sequestration via mineral trapping, as an alternative to basaltic-type reservoirs which have been proven to be successful. The CarbFix project in Iceland and the Wallula Basalt Pilot Scale project both reported results from field scale studies that suggested carbonation reactions had occurred within just two years in basaltic-type reservoirs, which is a significant improvement on the thousands of years needed for other geological carbon storage methods to be considered permanent. Carbon dioxide was successfully sequestered in these systems, after mineral dissolution reactions with the injected acidic fluids, which released divalent cations able to combine with the dissolved CO_2 and precipitate carbonate minerals. However, there is a significant lack of research examining whether alternative volcanic rocks such as andesite may also be suitable. If alternative volcanic rocks can also be utilised as targets for permanent carbon sequestration in short timescales, this would expand the accessibility of the CarbFix project to more global locations and help mitigate the impacts of rising CO_2 concentrations in the atmosphere.

Rock samples from the region of Rantau Dedap on the Island of Sumatra, Indonesia, were first characterised in detail to examine their mineralogical and chemical compositions, with results indicating they were of andesitic composition. Batch reactor experiments were conducted under elevated temperatures of 100^{o}C and pH values close to 3 using crushed andesite type rock samples, to simulate carbon sequestration conditions close to the site of injection. The release of silicon into the experimental fluids was used to calculate a bulk rock dissolution rate of the order 10^{-11} mol/m^2/s for the andesite type rocks, which is roughly 1-2 orders of magnitude slower than reported basaltic dissolution rates. Mineral dissolution in basaltic systems is considered to be the rate limiting step in the permanent carbon sequestration via mineral trapping process, and so these results indicate that permanent sequestration of CO_2 in andesitic systems may take slightly longer than the basaltic systems

which saw sequestration in just two years. However, significant divalent cation release was observed as a result of mineral dissolution, which suggests andesitic samples may still have a good carbon sequestration potential.

To expand on these findings, batch experiments were conducted using resin embedded andesite rocks, at temperatures of 100^{o}C and increased concentrations of CO_2 and calcium, to simulate conditions further from the site of injection. Some mineral dissolution was observed as well as divalent cation release. Evidence from electron microscope and energy dispersive x-ray techniques indicated two of the samples which had a feldspar composition with a higher anorthite content had an increased amount of calcite minerals present at the end of the 3-day experiments. These results give a positive indication that andesite samples are likely to support relatively rapid carbon sequestration via mineral trapping under conditions relevant to CO_2 injection. The two samples also had a higher content of alteration minerals present compared to the third sample which indicates that the presence of calcic-plagioclase and/or alteration minerals increase the potential for permanent carbon sequestration in andesitic-type reservoir systems.

Batch experiments were conducted to examine the impact of using fluids with increase NaCl concentrations up to 2.1 M, instead of freshwater, on the dissolution of feldspar minerals. If saline type fluids can be used as well as freshwater to dissolve CO2 for subsurface injection in volcanic rock systems, the feasibility of using this technique for carbon sequestration will be made more accessible in new locations worldwide. Silicon and aluminium release into the fluids in all experiments of a similar magnitude with varying NaCl concentrations indicates that using saline fluids is unlikely to have a negative impact on the carbon sequestration potential of a volcanic rock reservoir. Comparison between two feldspar mineral compositions indicates that a sample with a higher anorthite content may be more effective at buffering the acidity of acidic saline fluids, which is essential for initiating carbonation reactions, and so targeting such mineralogy’s is likely to be most effective.

The water adsorption isotherms of samples before and after use in rock-fluid experiments were collected for andesitic rock samples, to determine whether a change in mineralogy as a result of acidic fluid dissolution has an impact on the water adsorption capacity of the rocks. The results indicate the andesitic samples have a water adsorption capacity of roughly 5.0 – 9.2 mg/g, which is comparable to previous studies using rock samples from other geothermal reservoir systems. The collected isotherms indicate that the water adsorption capacity of the samples increases after reaction with representative geothermal fluids, particularly if acidic fluids are used. The authors interpret this is a result of increased reactive surface areas after reaction and gives some indication that the water adsorption capacity of a reservoir is unlikely to be negatively impacted as a result of changing mineralogy during injection of acidic fluids.

Overall, the results from this whole project indicate that andesitic rock samples should be further examined as potential targets for permanent carbon sequestration and that utilising seawater instead of freshwater for CO_2 injection is likely to be a viable alternative and make the technique more globally accessible. However, significant research is still needed in these areas, to examine more long-term impacts of such suggestions and in particular, the impact of inducing such precipitation reaction will have on the overall permeability of a volcanic rock reservoir system. The impact of alterations minerals on the carbon sequestration potential in terms of possible cation release on dissolution, and permeability reducing properties on precipitation should be examined particularly closely.

ii. Publications

Papers

Vandeginste, V., Siska, A., Belshaw, G., Kilpatrick, A. 2021. Effect of salinity on the kinetics of pyrite dissolution in oxygenated fluids at 60˚C and implications for hydraulic fracturing. *J. Nat. Gas Sci. Eng.*

Ji, Y., Walkinshaw, C., Belshaw, G., Vandeginste, V. 2021. Effect of polyacrylamide friction reducer on calcite dissolution rate at 25˚C and implication for hydraulic fracturing. *J. Nat. Gas Sci. Eng.*

Vandeginste, V., Belshaw, G., Player, I. (2017). WSF Bursary Report: Mobilisation of elements during shale-water contact. The Newsletter of the Royal Society of Chemistry Water Science Forum, 18 (2).

Conference Abstracts

Belshaw, G., Azis, H., Sapiie, B., Muljadi, B., Vandeginste, V. 2020. Cation Release from Geothermal Reservoir Rocks. Goldschmidt Abstracts, 2020, 162.

Belshaw, G., Gonciaruk, A., Steer, E., Alfiady, A., Azis, H., Muljadi, B., Vandeginste, V. 2019. Rock-Fluid Interactions in Geothermal Reservoir Systems. Goldschmidt Abstracts, 2019, 246.

Vandeginste, V., Siska, A., Belshaw, G. 2019. Pyrite Dissolution Rate in Saline Fluids and Implications for Fracking. Goldschmidt Abstracts, 2019, 3457.

Prizes

2019 Best Poster Prize at the School of Chemistry Postgraduate Symposium, University of Nottingham.

2020 Best Poster Prize at the Women in Chemistry Conference, University of Nottingham.

iii. Acknowledgments

Firstly, a huge thank you to my supervisor, Prof. Veerle Vandeginste, for sharing your expertise and wisdom with me, and providing constant support throughout my whole PhD and preceding MSci project. I have learned so much under your guidance, both in terms of scientific knowledge and, more generally, personal development skills that have helped me gain confidence and trust in my own abilities. Thank you also to my co-supervisors for your guidance and expert contributions, Dr Bagus Muljadi and Dr Matthew Hall. I also extend a big thank you to those researchers who contributed to some of the work for this project, Mr Harry James Potter (MSci) and Dr Hossein Fazeli. I have a huge appreciation for the various members of staff who patiently provided their valued time and extensive knowledge including; Mr Mark Guyler for his technical assistance setting up high-pressure equipment, Dr Elisabeth Steer for her seemly unlimited geological knowledge and electron microscope expertise at the Nanoscale and Microscale Research Centre, Dr Aleksandra Gonciaruk for assistance and training with water adsorption equipment, Dr William Lewis and Dr Stephen Argent for their assistance and training with PXRD instrumentation. To the various members of the Vandeginste Geochemistry group thank you for your support, with a special thanks to Carla Martín-Clavé for so much more than your geological knowledge, for being an amazing friend, moltes gràcies. To my fellow postgraduate demonstrators, Joshua Baptiste and David Kemp, thank you for making all those hours not feel like work at all. To so many other lunch time pals and sports companions, thank you for being essential distractions from work.

I sincerely thank and acknowledge the University of Nottingham School of Chemistry for providing the funding and resources that supported my PhD project and to Supreme Energy and the Bandung Institute of Technology who provided all the rock sample used throughout this project as well as extensive geothermal energy expertise. Thank you to the various organisations that awarded me with travel grants (the Royal Society of Chemistry, the Geological Society and the University of Nottingham Graduate School), which enabled me to attend and present at Goldschmidt Conference 2019, Barcelona and Goldschmidt Conference 2020, Hawai'i, (no thanks extended to the Covid-19 pandemic that prevented physical attendance and travel to Hawai'i).

To my wonderful family, Mum, Dad and George, forever there through all my highs and lows, thank you for being such a constant source of support and love. A big shout out to Uncle Rob, for the countless times you've asked, 'can I call you Dr Belshaw yet?', your insistence on me getting this far was motivation in itself! To some very important and incredible women in science I'm so grateful to have had in my life for the past 8 years and who I know will be there always; Chloe Peach - thank you for always being my personal cheerleader and outrageously funny, Shaw Building lockdown dance routines made everything brighter, Ellen Guest – thank you for being right next to me every step of the way, from the beginning of our undergraduate, all through our postgraduate and now onwards to the south of England, the concept of doing things separately is increasingly unlikely and I hope it stays that way, Lizzie Killalea – thank you for coming with me to freshers fair all those years ago, I can't wait to admire our fully grown avocado trees in 20 years' time and remember starting them together in our jungle home. Finally, to an amazing group of friends, thank you all for being such genuinely wonderful and hilarious people, Emma Barton, Franki Phillips, Hannah Glover, Jen Roberts, Joshua Mallins, Kate McGonigle and Rhian Morris I needed every single one of you to get this far. Thank you so much, love you all.

iv. Abbreviations

AF	alkali feldspar
BET	Brunauer-Emmett-Teller
BSE	back scattered electrons
CCS	carbon capture and storage
EDS	energy dispersive X-ray spectroscopy
EGS	enhanced geothermal systems
EOR	enhanced oil recovery
EPMA	electron probe microanalysis
FHH	Frankel-Hasley-Hill
GSF	Great Sumatran Fault
ICP-OES	Inductively coupled plasma optical emission spectroscopy
IDDP	Iceland Deep Drilling Project
MLA	mineral liberation analysis
MQ	MilliQ
PDF	powder diffraction file
PF	plagioclase feldspar
ppm	parts per million
PXRD	powder X-ray diffraction
RIR	reference intensity ratios
SE	secondary electron
SEM	scanning tunnelling microscopy
SHMP	sodium hexametaphosphate
STP	standard temperature and pressure
WDS	wavelength dispersive X-ray spectroscopy
XRD	X-ray diffraction
XRF	X-ray fluorescence

v. Table of Contents

i. Abstract 1
ii. Publications 4
Papers 4
Conference Abstracts 4
Prizes 4
iii. Acknowledgments 5
iv. Abbreviations 6
v. Table of Contents 7
Chapter 1: Introduction 11
1.1 Climate Change and Global Warming 11
1.2 Geothermal Energy 13
1.2.1 Regions of Geothermal energy 14
1.2.2 Types of Geothermal Energy Plants 16
1.2.3 Advantages of Geothermal Energy 19
1.2.4 Limitations and Challenges of Geothermal Energy 20
1.3 Volcanic Rocks 22
1.3.1 General Mineralogy 22
1.3.2 Feldspar Mineral Classifications 26
1.4 Geological Carbon Sequestration 28
1.4.1 'Traditional' Geological Storage of Carbon Dioxide 28
1.4.2 Mineralisation of Carbon Dioxide 30
1.4.3 Targeting Basaltic Reservoir Formations – Laboratory Scale Experiments 32
1.4.4 Field scale basaltic carbon sequestration projects 36
1.4.5 Laboratory scale studies using alternative rock types. 41
1.4.6 Utilising seawater for carbon sequestration 44
1.5 Water Adsorption 48
1.6 Research Objectives. 51
1.7 References 53
Chapter 2: Experimental Methodology 63
2.1 Materials 63
2.1.1 Geological Setting of Rock Samples 63
2.1.2 Rock Sample Preparation 64

2.2 Microscopy of Rock Samples 66
2.2.1 Petrography with optical Microscopy 66
2.2.2 Scanning Electron Microscopy 70
2.3 Mineralogical Analysis of Rock Samples 72
2.3.1 Powder X-ray Diffraction Analysis 72
2.4 Geochemical Analysis of Rock Samples 75
2.4.1 X-ray Fluorescence Analysis 75
2.4.2 Microprobe Analysis 76
2.5 Experimental Set-up 78
2.5.1 Batch Reactor Experiments 78
2.5.2 High Pressure CO_2 Experiments 79
2.6 Fluid Analysis 83
2.6.1 pH measurements 83
2.6.2 Inductively Coupled Plasma – Optical Emission Spectroscopy 83
2.7 Gas Adsorption Techniques 86
2.7.1 BET Analysis 86
2.7.2 Water Adsorption Isotherms 87
2.8 References 89
Chapter 3: Interaction of andesitic geothermal reservoir rocks with neutral and acidic fluids at 100°C to assess cation release extent. 91
3.1 Introduction 91
3.2 Materials and Methods 94
3.2.1 Materials 94
3.2.2 Preparation and Characterization 94
3.2.3 High Temperature Batch Reactor Experiments 96
3.2.4 Post Experimental Analysis 97
3.2.5 Geochemical Modelling 97
3.3 Results 99
3.3.1 Rock Characterization 99
3.3.2 Fluid Data 104
3.3.3 Post Experiment Solid Analysis 106
3.3.4 Geochemical calculations 107
3.4 Discussion 109
3.4.1 Mineral Dissolution Rates 109
3.4.2 pH Neutralisation 112

3.4.3 Secondary Mineral Formation 113
3.4.4 Implications for Carbon Storage in Andesitic Reservoirs 114
3.5 Conclusions 118
3.6 References 120
Chapter 4: Experimental CO_2 Storage in Andesitic Geothermal Reservoir Rocks – examining the possibility of carbonate mineral precipitation. 125
4.1 Introduction 125
4.2 Methodology 127
4.2.1 Materials 127
4.2.2 Sample preparation and characterisation 127
4.2.3 High Temperature Batch Experiments 130
4.2.4 Fluid Analysis 130
4.3 Results 132
4.3.1 MLA 132
4.3.2 EPMA 135
4.3.3 SEM 135
4.3.3 Fluid Composition 139
4.4 Discussion 142
4.4.1 Mineral dissolution 142
4.4.2 Mineral precipitation 144
4.4.3 Implications for carbon sequestration 146
4.5 Conclusions 150
4.6 References 153
Chapter 5: Impact of increasing sodium chloride concentrations on the dissolution of feldspar minerals – implications for using seawater instead of freshwater for carbon sequestration in volcanic rock reservoirs. 158
5.1 Introduction 158
5.2 Experimental Methodology 161
5.2.1 Solid and Solution Preparation 161
5.2.2 Batch Reactor Set-up 162
5.2.3 Solid Mineral Analysis 162
5.2.4 Fluid analysis 163
5.3 Results 168
5.3.1 Characterisation of mineral samples 168
5.3.2 Experimental fluid analysis 170

5.4 Discussion 173
5.4.1 The variation of pH in saline solutions 173
5.4.2 Mineral dissolution in acidic solutions 174
5.4.3 Impacts of salinity of mineral dissolution 175
5.4.4 Implications for CO_2 sequestration in volcanic rocks using seawater. 177
5.5 Conclusions 178
5.6 References 180
Chapter 6: The impact of mineralogy on the water adsorption capacity of andesitic geothermal reservoir rocks. 184
6.1 Introduction 184
6.2 Theoretical Background 188
6.3 Methods 191
6.3.1 Experimental samples 191
6.3.2 Water Adsorption Experiments 191
6.3.3 Nitrogen BET analysis 194
6.4 Results 196
6.4.1 Nitrogen BET experiments 196
6.4.2 Water adsorption isotherms 196
6.5 Discussion 199
6.5.1 Impact of rock-fluid interactions on surface areas 199
6.5.2 Impact of rock-fluid interactions on water adsorption capacity 199
6.5.3 Isotherm hysteresis loops 202
6.5.4 Impact of other alteration minerals 203
6.6 Conclusions 205
6.7 References 207
Chapter 7: Concluding Remarks 210
7.1 Rock sample characterisation 210
7.2 Mineral dissolution and release of divalent cations from andesitic rock samples 211
7.3 Potential for carbonate mineral formation in andesitic rock systems 214
7.4 The impact of elevated NaCl concentrations on the magnitude of feldspar dissolution 216
7.5 The impact of rock sample mineralogy on the water adsorption capacity of andesitic geothermal reservoir rocks 218
7.6 References 220
Appendix 222

Chapter 1: Introduction

1.1 Climate Change and Global Warming

In the past 200 years concentrations of carbon dioxide (CO_2) in the atmosphere have drastically risen, from around 270 parts per million (ppm) to over 400 ppm in 2018 (Figure 1.1) (Grotzinger and Jordan, 2014a; IPCC, 2018). There is a multitude of scientific evidence (such as oxygen and carbon stable isotope analysis (Retallack, 2002)) that links this increase with the onset of the industrial revolution and the use of fossil fuels (Department of Energy and Climate Change, 2016; Edenhofer *et al*., 2014; McCarthy *et al*., 2001). The rate of increase in CO_2 per year over the last decade has been observed to be close to 2.3 ppm per year, a rate which is approximately one hundred times faster than natural changes can account for (Snæbjörnsdóttir *et al*., 2020). The burning of fossil fuels releases gases such as CO_2, nitrous and sulphurous oxides (NO_x, SO_x), and methane (CH_4) into the atmosphere (McCarthy *et al*., 2001). These gases contribute to the enhanced greenhouse effect, trapping heat within the atmosphere and causing the measured rise in global average temperatures.

This temperature rise has already had a notable effect on climatic, ecological and societal systems across the world, such as a decrease in air quality in populated areas, species extinctions and rising sea temperatures (Grotzinger and Jordan, 2014b; McCarthy *et al*., 2001). Increased awareness of these negative impacts has led to a wide acceptance that across the world, we need to switch our reliance on fossil fuels to more renewable energy sources and also find ways to capture and store the excess CO_2 released, with the aim of preventing global temperatures rising above 1.5^{o}C compared to pre-industrial levels (IPCC, 2018). Earth's geology can be harnessed to help find solutions to these problems. Geothermal energy is a highly promising and arguably underutilised renewable energy resource, capable of providing a stable baseload of power to a multisource renewable energy grid (Mock *et al*., 1997). We can also utilise certain reservoirs as potential sites for permanent carbon

sequestration, with the CarbFix project in Iceland and the Wallula Basalt Pilot Project in the US demonstrating this at the field scale (Matter *et al*., 2016; McGrail *et al*., 2017b).

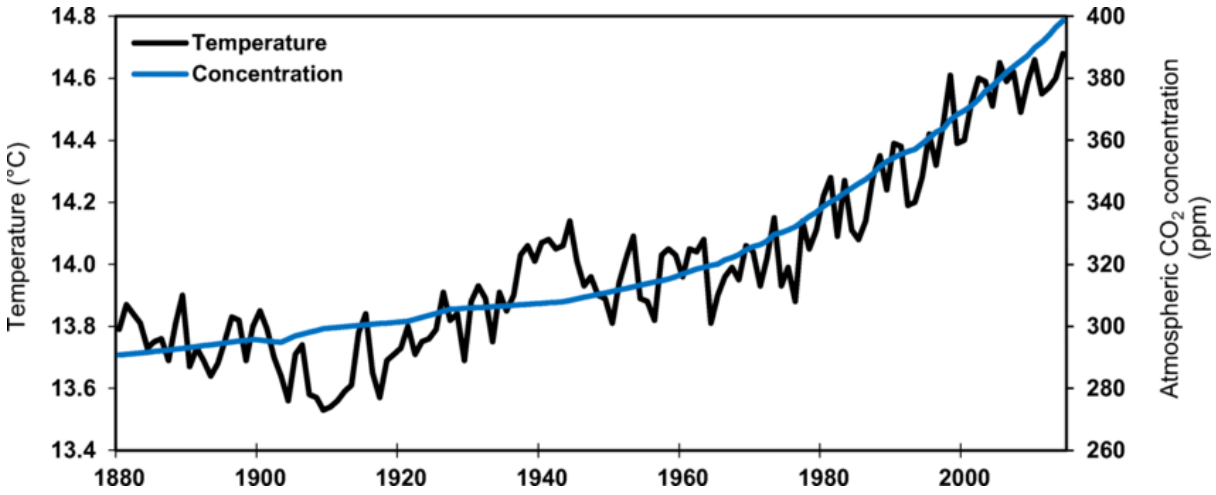


Figure 1.1: Correlation between global average temperature rise and an increase in atmospheric CO_2 concentrations. Figure reproduced from El-Montasser and Ben-Salha, 2019 with permission of Springer.

1.2 Geothermal Energy

Geothermal energy is harnessed from the heat found below the Earth's surface. Gravitational energy released during the violent origin of the Earth and its core formation heated the deep interior and the decay of radioactive isotopes at depth continues to generate a constant source of heat (Grotzinger and Jordan, 2014c). Convection currents in the molten mantle of the Earth transfer this heat up towards the Earth's crust, which is generally split into six main plates. These six plates are either moving towards each other and colliding, or moving away from each other (depending on location) at a rate of 2 to 20 cm per year (Mock *et al*., 1997). The relative motion of these plates is one of the factors that leads to different thicknesses of crust and creates areas where the internal heat of the Earth easily reaches the surface, often identifiable due to an abundance of volcanic activity (Holmukhe, 2009). The geothermal gradient within any part of the crust is defined as the increasing rate of temperature with depth. This rate varies, with the accepted average around a 25-30^{o}C increase per km depth, but in areas where the crust has been thinned and stretched this rate may be much higher, closer to 50^{o}C per km depth (Grotzinger and Jordan, 2014c; Holmukhe, 2009).

The heat being emitted from within the Earth can be harnessed as geothermal energy, usually in the form of hot water or steam, to use either directly as a heat source or to drive turbines to produce electricity. The presence of this heat energy exists across the entire extent of the Earth's surface, but the changing geothermal gradient means that harnessing it as geothermal energy varies in its ease and cost of extraction (Holmukhe, 2009; Sawin *et al*., 2017). The amount of energy that can be generated from thermal energy primarily depends on the temperature, with higher temperatures having a higher energy-producing potential (both in the form of heat and electricity producing potential) (National Renewable Energy Laboratory, 2012). A good geothermal energy resource also needs a source of water, which is heated by the hot rocks of the crust and can be extracted via wells from below the surface at a geothermal power plant. Water has a high heat capacity and latent heat of vaporisation and is therefore

the most important carrier of the energy in geothermal wells. There are places where the water from within a rock system continuously makes its way to the surface naturally and so geothermal energy can be extracted with relative ease, whereas in other places deep boreholes are needed and/or water may need to actively be injected into the system (Holmukhe, 2009).

The concept of geothermal energy has been around for thousands of years, with historians around the world giving evidence of communities using natural hot springs for cooking, cleaning and bathing (Mock *et al*., 1997). However, the first reported instance of drilling to investigate deeper resources occurred at Larderello in Italy, in 1856. The first real development of power generation at this Italian site commenced in 1913, when a 12.5 MW electric power plant started continuous operation, with the heat energy captured via steam evolving from the site. The US is the current leader in terms of the amount of energy generated from geothermal reservoirs, where electricity production at The Geysers in California started in the 1960's and remains the largest electricity producing plant in the world (Duque, 2013).

1.2.1 Regions of Geothermal energy

As discussed, there are areas where the geothermal gradient is higher, usually coinciding with crustal plate boundaries. Hence, there are areas and countries of the world that are more suitably placed to extract geothermal energy with greater ease and lower costs (with current technologies), examples of which are parts of Asia, New Zealand, Eastern Europe, Western US, Mexico and Central America (Holmukhe, 2009). The top producers of geothermal energy (as of the end of 2020) are shown in Figure 1.2 (Richter, 2021).

There are other areas of the world that have huge potential for geothermal energy extraction due to the relatively low thickness of the crust but are very difficult to access with current technologies, namely tectonic plate boundaries located deep below sea level such as the Mid-Atlantic Ridge fault line. Despite it not being the largest producer, arguably one of the most

well-known producers of geothermal energy is Iceland, which is one of the few areas that is located on this particular fault above sea level. Its location and its relatively small population mean that the country has the highest installed geothermal heat capacity per capita (Sawin *et al*., 2017), with roughly 68% of its energy coming directly from geothermal sources (Ragnarsson, 2015).

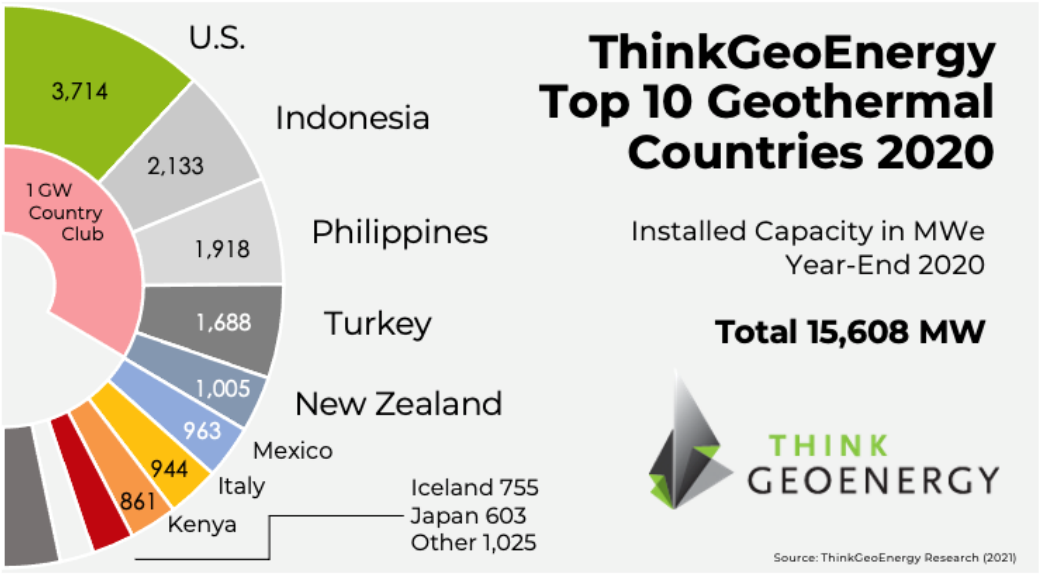


Figure 1.2: Schematic showing the Top 10 Geothermal Energy producing countries in the world in terms of installed power generation capacity in MW (Richter, 2021).

The US is currently the world's largest producer of geothermal energy in terms of total GW produced, mainly due to the large Geothermal Power Plant located at The Geysers in California (Sanyal and Enedy, 2011). California is located on the west coast of America, on a tectonic plate boundary which means it has a few specific locations with a higher-than-average geothermal gradient, perfectly suited for geothermal energy extraction. The second largest producer is Indonesia (Figure 1.2). Indonesia is located in an area sometimes known as 'The Ring of Fire', which is a particularly geologically active area, with tectonic plate boundaries giving rise to a large amount of volcanic activity and a high geothermal gradient. Some theoretical estimates predict that Indonesia may harbour up to 40% of the entire worlds

geothermal potential, but despite having over 250 geothermal sites across the country, it may only be utilising 6% of its potential extractable sources (Suharmanto *et al*., 2015), meaning it has huge potential for expansion of this power and heat source. The significance of this region in developing geothermal energy makes it a highly interesting area of research, hence the rock samples used for the experiments in this study are samples taken from an active geothermal well in Indonesia.

1.2.2 Types of Geothermal Energy Plants

There are several types of geothermal energy plant, generally classified based on the geothermal fluid used and the thermodynamic cycle adopted. Initially, plants can be split into two main types – vapour dominated, or liquid (both vapour and water) dominated. The water may either be already present naturally within the fractures and porosity of the rock system, or the site may be a hot-dry rock system, where water is artificially introduced via injection to be heated and then extracted in a cycle. The basic principle of all sites is that water is heated by hot rocks below the earth's surface and the resulting reservoirs can then be accessed by drilling to bring the hot water to the surface (Figure 1.3). Steam/vapour is then produced to turn a turbine to generate electricity. The heat may also be used directly and transported as heat, for example, as building or bathing waters.

Vapour-dominated plants tend to be located very close to areas of recent volcanism and plate boundaries where the geothermal gradient is steep, and boreholes drilled into the rock systems release vapour/steam. The temperature of geothermal fluid evolved from the production wells tends to be higher than 180^{o}C. Vapour dominated plants were the first to achieve commercial viability due to the relative ease of utilising the evolved steam to turn a turbine directly to produce electricity, as well as the high energy density arising from high temperatures (Holmukhe, 2009). Both the site at Larderello, the first commercially viable power plant, and The Geysers in California, the world's largest field by production, are vapour dominated resources. Both these sites make use of the waters naturally present in the system,

but it has become apparent that operation can be improved by reinjecting fluids into the reservoir to maintain fluid volumes and pressures (Duque, 2013).

Liquid dominated plants have production wells that produce fluids at a temperature lower than 180^{o}C. The geothermal fluid may be evolved as a mixture of vapour and liquid, or just as hot liquid. There are several types of plant set up that make use of these resources. Flashed steam plants are operated, where the hot geothermal fluid is suddenly introduced to a region of lower pressure, meaning the fluid is flashed to produce steam which can then turn a turbine. Binary fluid plants are also an option, where the hot geothermal fluid cycle evolving from the rock system is used to heat a working fluid cycle with a lower boiling temperature, which therefore is heated to produce a vapour to turn the turbines. Both flashed steam and binary cycle plants may also use the hot geothermal fluid as a direct heat source as well as to produce electricity (Duque, 2013; Holmukhe, 2009).

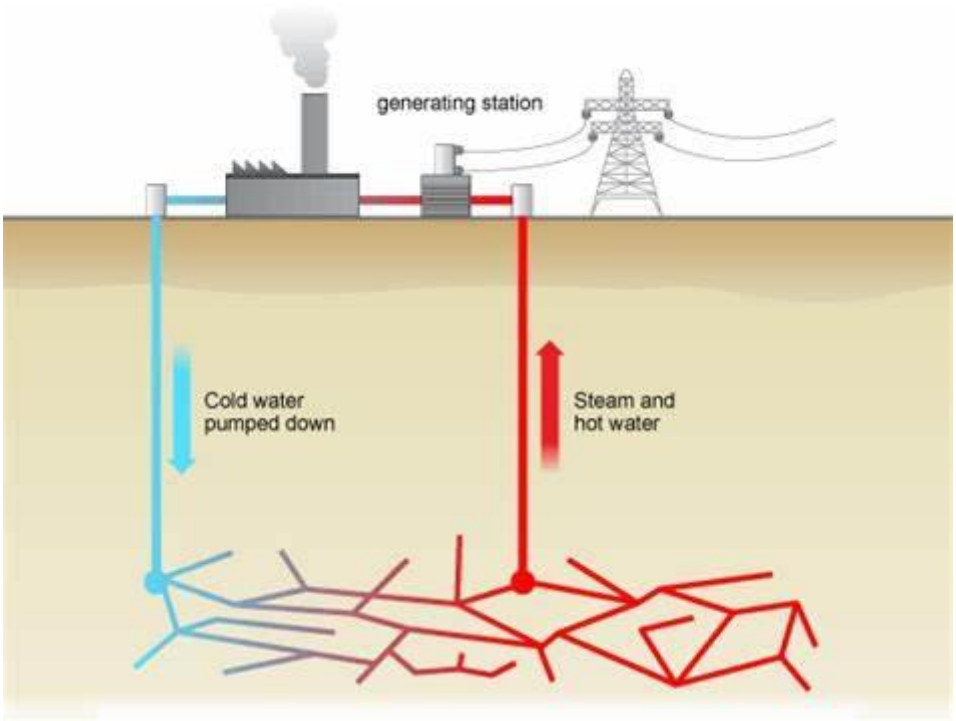


Figure 1.3: Schematic illustrating the basic principal of a geothermal energy power plant, cold water injected into the subsurface, being heated by the naturally occurring heat of the

subsurface and then being extracted for power generation or as a heat source (Design Engine, 2015).

Enhanced Geothermal Systems (EGS) have gained more attention in recent years. These systems make use of resources with high thermal energy but lack any or sufficient in situ water and/or permeability for the geothermal fluid to be transported through. The technology makes use of techniques already well established in the Oil and Gas industry, by artificially fracturing the subsurface rock to create permeability. The fluid is then circulated through the system via an injection well to inject cooler fluids into the rock system, which is heated as it travels through the fractures and emerges as the hot geothermal fluid at the production well. Unlike hydraulic fracturing operations in the Oil and Gas industry, special chemicals and proppants are not required and the fracturing is not needed continuously after initial fracture system has been created (Edenhofer *et al*., 2014; National Renewable Energy Laboratory, 2012; Sawin *et al*., 2017).

There is an even newer type of plant which is being investigated for use in Iceland. In 2017, the Iceland Deep Drilling Project (IDDP) completed drilling of a borehole that is over 4.5 km in depth. They hit a magmatic intrusion at a much shallower depth than they originally expected. The IDDP was able to produce fluids from this well at a temperature of 427^{o}C, which is high enough for the water to be in its supercritical state. Modelling suggests that these supercritical geothermal fluids could provide ten times the power output of a conventional geothermal well (Sawin *et al*., 2017).

Ground source heat pumps are a form of geothermal energy that have a much lower energy potential but are used widely for smaller uses due to the ease of installation. They use the relatively constant temperature of the Earth's near surface as a heat source for heating when the air temperature is cooler, and a heat sink for cooling when the air temperature is hotter. These tend to be used for commercial and residential buildings and can be used almost anywhere (National Renewable Energy Laboratory, 2012). They are currently in use all over

the world, but inconsistencies in the reporting of their installation means statistics on their abundance are not reliable.

1.2.3 Advantages of Geothermal Energy

Geothermal energy can be used as a constant base load source of power within an electricity grid that utilises multiple renewable energy sources. Compared to the natural fluctuations in wind and solar energy production it does not suffer from large power fluctuations as the temperature of the Earth's subsurface is relatively constant. Subsurface thermal energy is present across the globe, and some estimates predict it has a higher energy potential than all fossil fuels and in fact, more energy than the Earth's population currently uses (Mock *et al*., 1997). There is significant capacity for expanding energy production in several locations. According to one Icelandic estimate as much as 40 quads (1.17×10^{13} kWh) of electricity could be generated each year from accessible geothermal sources but currently only about 0.3 quads per year is actually being generated, which still supplies over 68% of the country's electricity needs (Grotzinger and Jordan, 2014d). Indonesia is currently the second largest producer of geothermal energy in the world but it's estimated that existing capacity is still less than 6% of the country's total geothermal power potential (Sawin *et al*., 2017). Geothermal energy is a much cleaner energy source than fossil fuels with the CO_2 emissions from a single geothermal energy plant only about 5-6% equivalent of that released from a coal power plant with a similar capacity (Aradóttir *et al*., 2015). There is clearly a significant opportunity to expand geothermal energy production, particularly in areas where the technology is well established, and the geology lends itself well to providing more easily extractable thermal energy.

During market fluctuations lower costs of fossil fuels can reduce demand for drilling rigs in the fossil sector, which can benefit geothermal energy development as drilling is one of the largest costs associated with establishing a successful energy plant (Sawin *et al*., 2017). Many of the technologies and skills gained from the fossil sector are directly applicable to the geothermal

energy sector. Experts from the oil and gas drilling sector can be consulted and the drilling knowledge is well established and familiar, so workers can simply be transferred to the geothermal sector, rather than training a whole workforce from scratch. An example of this knowledge transfer taking place occurred in the early months of 2020, when the price of oil plummeted due to the Covid-19 pandemic. The rapid drop in demand for oil led to uncertainty in the drilling job market, which sparked a collaboration in Canada between the oil service sectors to redeploy workers into the geothermal energy sector. As well as securing jobs to help protect the economy during the pandemic, this strategy may also contribute towards Canada's targets to reduce emissions and expand its goals for net-zero baseload power (Bergenson, 2020; CAODC, 2020; Richter, 2020).

1.2.4 Limitations and Challenges of Geothermal Energy

Constructing geothermal energy plants has some disadvantages that are commonly associated with all large-scale drilling projects. Despite the cumulative knowledge from the oil and gas industry as well as the geothermal sector, only 60% of wells are deemed as successful in the exploration stage of reservoir production (IFC, 2013). Since drilling costs can add up to half the cost of geothermal energy production, this results in a significantly high financial risk for prospective energy companies which can make geothermal an unattractive proposition (Angelone and Labini, 2014).

Once a geothermal energy reservoir is in production, there are other physical challenges and environmental problems associated with the energy plant construction and production. These include noise pollution, physical disturbance of the site and unfavourable aesthetics. However these problems are minimal when compared to other types of energy resource production like oil extraction, as far fewer wells are needed to set up a comparable site (Holmukhe, 2009). The biggest physical concern is the possibility of induced seismicity and ground subsidence caused by various processes of the energy extraction timeline. The slow sinking of the land surface, known as subsidence, may occur at geothermal developments as the subsurface

fluids under hydrostatic pressure may be supporting the overburden of the rock formation. As the fluid is withdrawn for energy production, this overburden is no longer supported as it was and can result in surface sinking above the site of fluid withdrawal (DiPippo, 2008). This can be countered by reinjecting fluids into the subsurface to replace those withdrawn, as is done to maintain reservoir pressures for efficient production anyway, but this needs to be carefully planned and the site assessed in detail to minimise risks. Minor seismic events have also been reported in areas located near geothermal energy production plants, although since most developed geothermal resources are located in tectonically active areas it can be difficult to separate naturally occurring events from development-related events (National Renewable Energy Laboratory, 2012). This can be a particularly significant issue with EGS, which may make use of hydraulic fracturing to create permeability within a site. In July 2013, an EGS site in Switzerland produced a seismic event of magnitude 3.5, as a result of an unexpected encounter with a pocket of gas at 4450 m depth, which significantly reduced public confidence in EGS geothermal plant development (Angelone and Labini, 2014). Again, these risks need to be carefully considered and managed to ensure geothermal reservoirs are safely exploited.

Since geothermal energy producing reservoirs are often located in volcanically and tectonically active regions, naturally occurring volcanic gases such as CO_2 and H_2S may be released alongside the fluids being extracted from the systems (Fridriksson *et al*., 2016). The CO_2 released from a geothermal energy plant is usually (at maximum) only about 5-6% of that released from an equivalent sized coal burning energy plant (Aradóttir *et al*., 2015). However, all emissions need to be mitigated to ensure geothermal energy can be utilised as a completely renewable and clean energy source.

1.3 Volcanic Rocks

1.3.1 General Mineralogy

Geothermal energy sites are, by nature, often located in what are known as igneous or more specifically volcanic (if the rocks have solidified from lava during volcanic activity) rock types. Volcanic rock samples are classified according to both their texture and mineralogical composition. Texture refers mainly to the size and shape of the mineral crystals. Coarse-grained rocks have crystals large enough to be seen with the naked eye, fine-grained rocks have crystals too small to be seen macroscopically. Texture gives an indication of the conditions under which the rocks formed from the hot magma or lava. Large crystals indicate slow cooling to allow enough time for growth, suggesting deep burial associated with high temperatures. Fine-grained crystals indicate a faster rate of cooling with no time for large crystal growth, suggesting either shallower burial with lower temperatures, or even that the magma erupted as lava above the surface and cooled quickly in air. Under very fast rates of cooling, glassy textures may form, where no crystals had any opportunity to grow. An igneous rock may have a mixed texture, referred to as a porphyry, in which large phenocrysts (crystals) 'float' in a fine-grained crystal matrix. Phenocrysts form in the magma body when it is still deep below the earth's surface, then before it completely crystallises a change occurs (e.g. a volcanic eruption) bringing the magma closer to the surface, resulting in cooler temperatures, and the formation of a fine-grained matrix surrounding the previously formed phenocrysts (Grotzinger and Jordan, 2014e).

Igneous rocks are also classified according to their mineralogical composition, based on relative proportions of silicate minerals. These minerals include quartz, feldspars, muscovite and biotite micas, amphiboles, pyroxenes and olivine, which form a systematic series. This classification series combined with texture is represented in Figure 1.4. Felsic minerals are

highest in silica and feldspar minerals, mafic minerals at the other end of the scale are lowest in silica and have higher concentrations of magnesium (Mg) and iron (Fe). These adjectives are applied to both minerals and rocks containing high proportions of those minerals (Grotzinger and Jordan, 2014e).

The chemical composition of the common minerals of igneous rocks are displayed in Table 1.1. Mafic minerals crystallise at higher temperatures than felsic minerals, meaning they crystallise earlier during the cooling of a magma. Felsic rocks are high in feldspar content, one of the most abundant rock forming minerals on Earth. Plagioclase feldspars form a solid solution with varying ratios of calcium (Ca) and sodium (Na) and as Figure 1.4 shows, they are richer in Na at the felsic end and richer in Ca at the mafic end of the scale. Following the observed trends for mafic vs. felsic minerals, Ca-rich plagioclases crystallise at higher temperatures than Na-rich crystals, creating an order of crystallisation commonly known as Bowen's Series (Bowen, 1928). It is important to recognise feldspar minerals form a series, including the alkali feldspar types (such as orthoclase) and plagioclase feldspars. Also, the chemical formulae given in Table 1.1 are idealised formulae of the end members of the series. In reality, minerals are likely to have varying ratios of the different cations appearing in the formulas, with one cation sometimes being dominant. Understanding the mineralogy of the samples in this project is essential, as it provides information on which cations are available within the rock formation being studied. The cations available after dissolution reactions will influence the precipitation reactions that can subsequently take place to sequester CO_2 (Section 1.4). Links can then be made to other geological formations around the world to predict optimum sights for this acidic gas sequestration. Plagioclase is an abundant mineral found across the Earth's surface in various rock types, estimated to make up about 35% of the continental crust (Wolff-Boenisch *et al*., 2004).

Basaltic rocks are commonly occurring volcanic rocks, which make up around 10% of the continental surface and most of the ocean floor (Matter *et al*., 2016). This rock type is rich in

minerals such as olivine, pyroxene and plagioclase feldspars, which contain varying amounts of calcium, magnesium and/or iron within their chemical structures (Table1.1). On average, basalt contains 7-10 wt% Ca, 5-6 wt% Mg, and 7-13 wt% Fe (Matter *et al*., 2009). Andesite rock types are also relatively common volcanic rock systems, which also contain high levels of plagioclase feldspars, but a lower composition of olivine and pyroxene and an increased amount of quartz compared to basaltic rocks (Figure 1.4). This implies andesite type rocks will commonly have appreciable levels of calcium, but less magnesium and iron contained within the minerals.

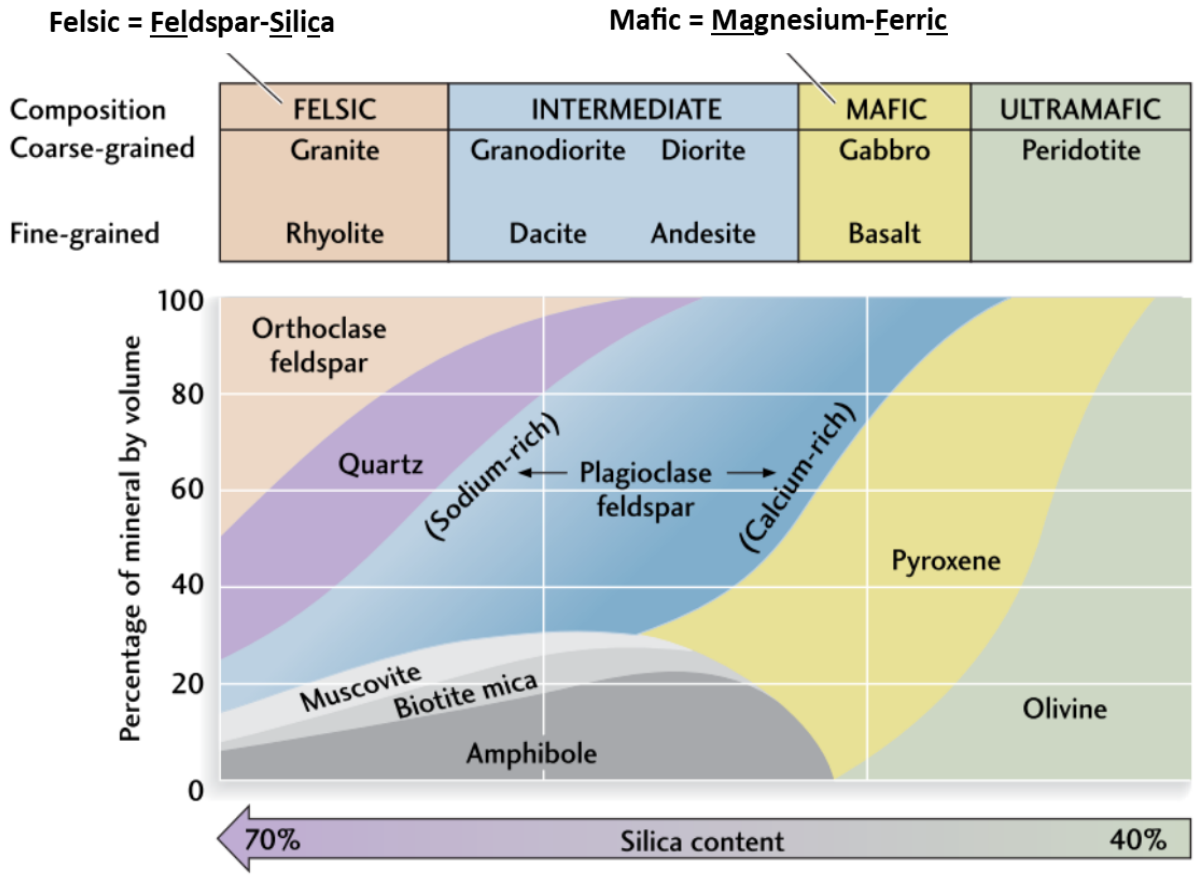


Figure 1.4: Classification model for igneous rocks. The y axis shows the mineral content as a percentage of the total rock volume. The x axis shows the silica content as a percentage of a rocks weight (Grotzinger and Jordan, 2014e).

Based on existing literature for the mineralogy of other geothermal reservoirs in Indonesia, it is expected that the samples studied in this present report will be of intermediate composition.

Studies completed on the island of Java have commonly found rocks to be of mainly andesitic composition (Purnomo and Pichler, 2014). A system in Awibengkok has andesitic-to-rhyodacitic rocks, with identified minerals including alkali and plagioclase feldspars, quartz, pyroxene, biotite and hornblende (Stimac *et al*., 2008). The Kamojang geothermal reservoir located in West Java has primary mineral occurrences of feldspar, pyroxenes and olivine, with high levels of hydrothermal alteration producing silica, feldspars, zeolites, carbonates, iron oxides, iron sulphides, sulphates and clay groups (Utami, 2000). This assemblage has been classified as andesitic to basaltic-andesitic in composition, which is an intermediate type of rock, based on the model shown in Figure 1.4.

Table 1.1: Chemical compositions of common minerals of igneous rocks, separated according to mafic or felsic classifications (Grotzinger and Jordan, 2014e).

Felsic Minerals		Mafic Minerals	
Mineral	Chemical Composition	Mineral	Chemical Composition
Quartz	SiO_2	Biotite (Mica)	$(K,Mg,Fe,Al)Si_3O_{10}(OH)_2$
Orthoclase-feldspar	$KAlSi_3O_8$	Amphibole group	$(Mg,Fe,Ca,Na)Si_8O_{22}(OH)_2$
Plagioclase-feldspar	$NaAlSi_3O_8$-$CaAl_2Si_2O_8$	Pyroxene group	$(Mg,Fe,Ca,Al)SiO_3$
Muscovite (mica)	$KAl_3Si_3O_{10}(OH)_2$	Olivine	$(Mg,Fe)_2SiO_4$

This composition found for geothermal systems in Indonesia can be compared to other systems around the world. The Hellisheidi site in Iceland is the location of the CarbFix project and literature reports this as having basaltic rock composition, which is at the mafic end of the scale (Alfredsson *et al*., 2013). This composition suggests there will be different ratios of cations available at the Iceland injection site compared to potential sites in Indonesia. Basaltic compositions will have higher levels of olivine and pyroxenes providing more Fe and Mg cations. Basalt is one of the most common rock types in the Earth's crust, making up the majority of the sea floor(Streck *et al*., 2005).

1.3.2 Feldspar Mineral Classifications

As has been briefly described and illustrated in Figure 1.4 and Table 1.1, 'feldspar' is a general name given to a group of minerals that form a solid solution series. They contain varying amounts of sodium, potassium, and calcium in their structures, contained within a 3D aluminosilicate framework (Figure 1.5). The framework of SiO_4^{4-} and AlO_4^{5-} tetrahedra hosts the K^+, Na^+ and/or Ca^{2+} ions within the voids acting as the charge compensating cations. This mineral group is estimated to make up roughly 60% of the Earth's continental and oceanic crust (Skorina and Allanore, 2015) and is common in many volcanic rock types, so it is important to understand the general chemistries.

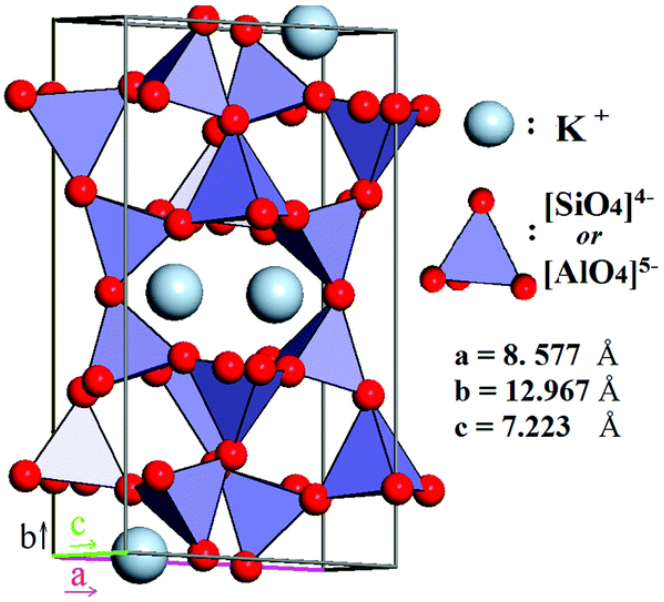


Figure 1.5: Idealised crystal structure of a feldspar aluminosilicate mineral group, specifically indicating the potassium end member, though Na^+ (represented by a blue sphere) or Ca^{2+} could also be substituted in its place. Red spheres represent oxygen atoms, and the silicon or aluminium units are represented by purple tetrahedra. Figure reproduced from (Skorina and Allanore, 2015) *with permission from the Royal Society of Chemistry.*

Feldspar minerals that contain sodium and potassium cations are known as alkali feldspars, and minerals that contain sodium and calcium cations are known as plagioclase feldspars. The composition of a feldspar mineral is often expressed in terms of its three endmembers, orthoclase ($KAlSi_3O_8$), albite ($NaAlSi_3O_8$) and anorthite ($CaAl_2Si_2O_8$), where the term endmember describes a mineral of extreme purity within a solid solution series. The three endmembers can be displayed on a ternary diagram, with various sub-mineral names defined based on the percent composition of each cation within the structures (Figure 1.6).

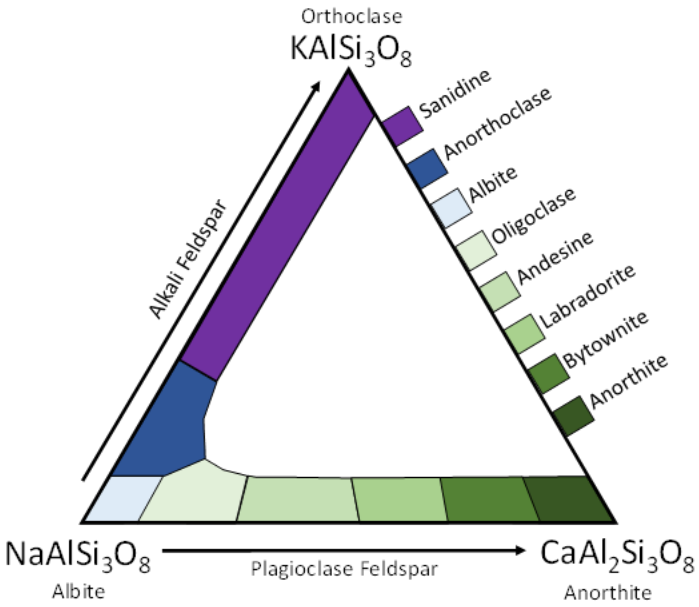


Figure 1.6: Ternary phase diagram illustrating the names of various feldspar minerals, including the chemical formulae of the endmember minerals, the general characterisation of alkali or plagioclase feldspar, and various names assigned to minerals with various percent compositions of the endmember species.

1.4 Geological Carbon Sequestration

1.4.1 'Traditional' Geological Storage of Carbon Dioxide

It is widely accepted that Carbon Capture and Storage (CCS) need to be drastically upscaled if we want to achieve the aims of the Paris agreement to keep global average temperature increase below 1.5^{o}C (compared to pre-industrial levels) (IPCC, 2018). However, sufficiently large scale CCS deployment is yet to be achieved, with around 40 Mt CO_2 being captured annually by 2016, with estimates of in excess of 190 Gt needed as a minimum (UNFCCC, 2016). Utilising geological sites for the capture and storage of CO_2 is not a new concept. Porous (often sedimentary) formations have been particularly well studied because they are widely available and also usually have a high level of permeability, meaning they have a large storage capacity in terms of physical space to store CO_2 (Bachu, 2003; IPCC, 2005). There is also extensive experience in these systems drawn from the oil and gas industry which has exploited these formations for decades (IPCC, 2005), and formations such as depleted oil and gas reservoirs and deep un-mineable coal seams have been targeted for storage (Brennan and Burruss, 2006). The sector often uses CO_2 injection for Enhanced Oil Recovery (EOR), a process whereby CO_2 is injected into fossil fuel reservoirs which have experienced reduced production capacity with the combined aim of storing CO_2 and recovering financially valuable resources. In 2018, 14 of the 18 large-scale CCS projects that were operational were based on EOR (Global CCS Institute, 2018). However, this situation is not ideal for the long term, as fossil fuels are produced from this process which offsets many of the CCS benefits.

Another disadvantage of CCS in porous sedimentary formations is the need for an overlying impermeable caprock layer to prevent CO_2 leakage over time (Kampman *et al*., 2016). The CO_2 injected into geologic formations is commonly in either the gaseous or supercritical state.

At pressures above around 74 bar and 31°C, CO_2 will be in its supercritical state, which is likely in CCS target formations owing to the increasing temperature and pressure with depth in the subsurface (Schaef *et al*., 2010). Both gaseous and supercritical CO_2 will be more buoyant than the target formation waters, which leads to a significant risk of leakage back into the atmosphere via the permeable layers that are targeted for CCS, hence the need for an impermeable caprock overlying the target storage formation (Gislason *et al*., 2014). The process of long-term storage of CO_2 in porous formations relies first on structural trapping – physically containing the CO_2 in the target formation, such as with the impermeable caprock. Then dissolution of the CO_2 into the formation waters can occur and migration of this further into the subsurface leads to solubility trapping, and residual trapping in the pore space (Gunter *et al*., 1993). Finally, the dissolved CO_2 in the form of bicarbonate anions can combine with divalent cations, and under suitable pH conditions carbonate minerals may precipitate, permanently sequestering the CO_2. However, this process of reaching permanent storage can take thousands of years to complete (Snæbjörnsdóttir *et al*., 2020) and so formations would need long-term monitoring, which has significant cost implications.

There is also concern that injecting CO_2 and/or fluids containing increased concentrations of it into the subsurface could lead to some groundwater contamination. The presence of CO_2 can cause the acidification of fluids, which may lead to some mineral dissolution and consequent mobilisation of trace elements such as arsenic and lead into the groundwater system. Modelling experiments (Zheng *et al*., 2009) conducted in sandstone type saline aquifers yielded results indicating that concentrations of arsenic and lead in nearby groundwater sources may increase as a result of CO_2 injection into a deep saline aquifer. However, the maximum permitted level of arsenic was exceeded in only a few cases and that for lead was never exceeded, suggesting the impact may easily be mitigated. The risks associated from element mobilisation in sedimentary type reservoirs highlight the importance of site selection and identifying areas with a Suitable caprock layer to prevent leakage of various species from the target injection site.

1.4.2 Mineralisation of Carbon Dioxide

The limitations of these CCS techniques in porous sedimentary/sandstone type formations naturally led to various research groups and other interested parties to consider how the risks could be mitigated. The final stage of permanent sequestration has clear benefits, with a huge reduction in the risks from leakage and an end to the need for expensive monitoring projects. Efforts turned to investigating how the overall process could be accelerated, to reach the stage of permanent sequestration in a shorter timescale.

As CO_2 dissolves in water it forms carbonic acid, as shown in the first step of Equation 1.1, which ultimately leads to an increase in the acidity of the fluids, as dissociation leads to an increase in proton concentrations in the fluids (Baines and Worden, 2004).

$$CO_{2\,(g)} + H_2O_{\,(aq)} \leftrightarrow H_2CO_{3\,(aq)} \leftrightarrow H^+_{\,(aq)} + HCO_3^-{}_{(aq)} \leftrightarrow 2H^+_{(aq)} + CO_3^{2-}{}_{(aq)} \quad (1.1)$$

If divalent cations, such as Ca^{2+}, Mg^{2+} and/or Fe^{2+} are present in the solutions they may combine with the carbonate anion to form carbonate minerals (Equation 1.2) which then precipitate out of solution, thereby permanently sequestering the CO_2 as solid products (Alfredsson *et al*., 2013).

$$(Ca,Mg,Fe)^{2+} + CO_3^{2-} \leftrightarrow (Ca,Mg,Fe)CO_3 \quad (1.2)$$

These Equations demonstrate that the process of permanently sequestering CO_2 in the form of carbonate minerals relies on there being divalent cations available in the solution (Baines and Worden, 2004). It is also evident that the H^+ ions produced in Equation 1.1 need to be consumed to drive the reaction forward (Gislason *et al*., 2010). Carbonate minerals tend to precipitate only if the pH of the solution is near neutral values, as they rapidly dissolve under acidic conditions (Pokrovsky and Schott, 2002).

Gunter *et al.* (1993) compared several scenarios of injecting CO_2 into sedimentary aquifers: the injection of CO_2 into a formation fluid in the absence of any mineralogical considerations,

the possible reactions if injected into a carbonate type aquifer and the possible reactions if injected into a siliciclastic type of aquifer. They concluded that divalent cation-bearing siliciclastic reservoirs had the highest carbon sequestration potential compared to other reservoir types and they attributed this finding to the increased availability of divalent calcium and magnesium cations contained within aluminosilicate minerals, with the dissolution of these minerals also acting to neutralise the acidic fluids to allow carbonate formation (Gunter *et al*., 1993). Bachu, 2000 also highlighted the importance of evaluating the geological nature of the target reservoirs for their suitability as sequestration targets, alongside other considerations such as economic, political, and societal criteria. Other studies also highlight the benefits of injecting CO_2 into porous carbonate-sandstone type formations, as carbonate minerals dissolve quickly and act to buffer the acidity created by injecting the CO_2, which ultimately leads to conditions more suited to sequestration of the CO_2 by carbonate mineral formation (Bertier *et al*., 2006). However, there are clear limitations to this idea as dissolving carbonate minerals actually releases additional carbonate anions into the solution, with net carbonate mineral formation potentially close to zero (Baines and Worden, 2004).

Rosenbauer *et al*., 2005 conducted experiments examining reactions between limestones and plagioclase-rich arkosic sandstones, and CO_2-saturated brine solution to investigate implications for CO_2 sequestration in saline aquifers. They highlighted that ordinarily the storage of CO_2 in limestone aquifers is normally limited to only solubility type trapping mechanisms. However, they reported that supercritical CO_2 reacted with brine and arkose resulted in the formation of carbonate mineral phases and therefore sequestration of CO_2. Wigand *et al*., 2008 also examined potential interactions between sandstones and formation fluids in saline aquifers and observed the dissolution of dolomite cement, k-feldspars and albite, which did aid in buffering the solution pH. However, they also performed geochemical modelling experiments on longer timescales and reported that mineral trapping via carbonate formation is a process that requires increased timescales, up to thousands of years. The research by these various groups was an important step in highlighting the need to carefully

consider which reservoir formations might be targeted to reduce the timescales needed to result in permanent CO_2 sequestration.

1.4.3 Targeting Basaltic Reservoir Formations – Laboratory Scale Experiments

Although finding ways to accelerate the process to reach a state of permanent CO_2 sequestration in porous sandstone-type reservoirs was significant, it is still evident that a reduction in the timescale from thousands to possibly hundreds of years does not make this form of CCS any more economically attractive for large scale applications. Sedimentary basins simply have insufficient amounts of divalent cations contained in their minerals to support sufficient mineral trapping (Sass *et al*., 2002). The understanding gained from the highlighted literature on which minerals and reactions appeared to be most beneficial directed research towards targeting alternative rock types that do have significantly higher quantities of divalent cation containing minerals.

Large igneous provinces such as flood basalts occur across the Earth and often are near power-producing and population centres. They are already recognised as playing an important role in the global carbon cycles (Brady and Gíslason, 1997; Retallack, 2002; Tajika, 1998; Varekamp *et al*., 1992). These formations tend to have some localised porous areas within them with reasonable permeability, commonly serving as regional aquifers (McGrail *et al*., 2003). Initially, the interest in these formations was largely focussed on their iron-rich nature and research was conducted investigating the potential for carbonation reactions that might occur between dissolved CO_2, and divalent iron cations released from dissolution of the rock forming minerals, with calcium and magnesium reactions also of some interest. To liberate these divalent cations, the minerals in the rocks need to be dissolved. This can happen in acidic solutions, for example pyroxene dissolution can increase concentrations of all three cations in solution (Equation 1.3) (Zhang *et al*., 2015):

$$Ca(Mg,Fe)Si_2O_{6\,(S)} + 2H_2O + 4H^+ \leftrightarrow Ca^{2+} + Mg^{2+}(Fe^{2+}) + 2H_4SiO_4 \qquad (1.3)$$

Several factors influence the rate of dissolution of minerals, thereby influencing the number of these divalent cations that might be made available in solutions. Pyroxene and olivine dissolution rates both increase with increasing temperature and decrease with increasing pH, although pyroxene dissolution rates tend to be slower than olivine (Luhmann *et al*., 2017). Dissolution of feldspars increases in high and low pH solutions, with the slowest rate of dissolution at close to neutral pH values, which creates a U-shaped dissolution curve as a function of pH (Luhmann *et al*., 2017).

McGrail *et al.* (2003) monitored the change in CO_2 pressure as a function of time within a batch reactor system, using basaltic rock samples and reaction fluids at 90^{o}C and 1500 psi (10 GPa) of pressure. They highlighted that a typical basalt aquifer will likely have a pH range between 8 and 9.5 and that the injection of pressurised CO_2 will lower this to around pH 3.5 in the local area of injection. They hypothesised that as iron-rich phases such as pyroxenes, olivines, spinel and glassy mesostasis are unstable at such pH values they would dissolve, which would have the combined effect of first releasing Fe^{2+} into the fluids and buffering the acidity to allow iron carbonate minerals to form. They observed a rapid pressure drop within the first 200 hours of experiment and provided evidence that this was not due to any leakage from the reactor, leading them to conclude some carbonation reactions must have taken place to sequester the CO_2. The authors conducted further studies, with (McGrail *et al*., 2006) expanding the experiments and providing electron microscope evidence of calcite formation on samples exposed to CO_2-saturated water for 32 weeks. No siderite ($FeCO_3$) formation was observed, contrary to their initial hypothesis. Basalts tend to contain up to 25% combined molar concentration of Ca, Mg and Fe, and although Fe tends to be a major component, siderite precipitation kinetics are slow compared to calcite which helped explain the observations in that particular study as lab experiments are unlikely to be conducted over sufficient timescales to observe siderite formation (McGrail *et al*., 2006).

Another group of authors examined the dissolution rates of a selection of volcanic glasses as a function of their composition ranging from basaltic to rhyolitic in nature, at pH values of 4 and 10.6 and temperatures of 25 to 74^{o}C (Wolff-Boenisch *et al*., 2004). The aim was to compare the far-from-equilibrium dissolution rates of these samples. As well as the true dissolution rate the overall rate a rock sample will dissolve at is dependent on a number of factors, such as aqueous transport of dissolved species away from the rocks surface (Murphy *et al*., 1989) and the effect of the reverse reaction at near-equilibrium conditions (Oelkers *et al*., 1994). Wolff-Boenisch *et al.* (2004) used mixed flow reactors in an attempt to minimise these factors which may have obscured the true far-from-equilibrium dissolution rates. The results of this study indicated that the dissolution rates (normalised to measured geometric surface area of the samples) at 25 degrees varied exponentially with silica content of the glasses. The lifetime of a 1 mm basaltic glass sphere at pH 4 was calculated to be 500 years, whereas a rhyolitic glass sphere in equivalent conditions was calculated to have a lifetime of 1500 years.

The finding that basaltic glasses dissolve at a faster rate compared to rhyolitic glasses can be explained by examining their chemical compositions. Studies have examined the dissolution rate of aluminosilicate minerals as a function of pH and relative Si/Al ratios. As albite dissolves, the Si/Al ratio of 3 means that removal of Al leaves partially linked silica tetrahedra, whereas anorthite with an Si/Al ratio of 1 leaves completely detached silica tetrahedra (Oelkers and Schott, 1995). This means that continued dissolution of albite would require further Si-O bonds (which are chemically relatively strong) to break, but the removal of Si from anorthite does not (Oelkers *et al*., 1994; Oelkers and Schott, 1995). These authors went on to conduct further work which concluded that the dissolution rates of natural silicates are related to the number of Si-O bonds present and the degree to which they are bridged together to form a polymerised Si-O network (Oelkers and Gislason, 2001). Figure 1.4 and Table 1.1 describe the mineralogy of volcanic rocks and demonstrate that basaltic-type samples have a higher proportion of minerals such as olivine, pyroxene and calcic plagioclases, while rhyolitic rocks tend to be

composed of quartz and alkali feldspars. Of this selection of minerals, olivine and pyroxene have the fastest dissolution rates and calcic plagioclases tend to have faster dissolution rates than alkali feldspars. Quartz has a highly polymerised Si-O structure and hence has a very slow dissolution rate. Therefore, it is evident that rhyolitic samples would have a slower dissolution rates than basaltic samples, as an extension of their component mineral dissolution rates.

Wolff-Boenisch *et al*., 2006 expanded on their work by examining the effect of crystallinity on the dissolution rates and CO_2 consumption capacity of silicates. They reported that an increasing Si:O ratio increases the difference between crystalline mineral and equivalent glass dissolution rates. Results suggest that Si-rich rhyolitic glasses dissolve more than 1.6 orders of magnitude faster than the compositionally corresponding minerals, whereas ultra-mafic glasses and their corresponding minerals have similar dissolution rates. The authors wanted to examine the implications these varying dissolution rates might have for carbon sequestration and so they used the summarised dissolution rates to determine calcium release rates from the natural rock samples, which can then be used to give an estimate for those rocks CO_2 consumption capacity. They concluded that the calcium release rates of samples with the lower Si:O ratios (i.e. basaltic samples) is around 2 orders of magnitude faster than samples with higher Si:O ratios (i.e. rhyolitic samples), which has significant implications for the long-term CO_2 consumption capacity of these samples (Wolff-Boenisch *et al*., 2006).

Various other studies have been conducted investigating the dissolution rates of basaltic samples as divalent cation sources for carbon sequestration. Schaef and McGrail, 2009 investigated the dissolution of Columbia River basaltic samples which contain minerals such as plagioclases, augite, non-crystalline glassy mesostasis, magnetite and ilmenite. They reported the sample dissolution rates decrease with increasing pH (pH 3 to 7) and they observed conversion of CO_2 into stable carbonate minerals within days. The authors continued to extend their investigations, with experiments running for 3 years also indicating significant

carbonate mineral formation within CO_2-saturated systems with basaltic samples (Schaef *et al*., 2010). They also conducted experiments to expand the examined conditions in an attempt to further simulate deep injection conditions and reported finding that surface coating of carbonate minerals on the original basaltic samples increased with increasing pressure (Schaef *et al*., 2011). Studies have also been conducted focussing on the dissolution rates of individual minerals, such as olivine (Chen and Brantley, 2000; Pokrovsky and Schott, 2000; Rosso and Rimstidt, 2000), plagioclase feldspars (Chen and Brantley, 1997; Hamilton *et al*., 2000; Oelkers and Schott, 1995; Stillings and Brantley, 1995) and basaltic glass (Daux *et al*., 1997; Gislason and Oelkers, 2003; Oelkers and Gislason, 2001; Techer *et al*., 2001). In summary, these studies indicate olivine has the fastest dissolution rate (relatively), followed by calcic plagioclases and then alkali feldspars.

1.4.4 Field scale basaltic carbon sequestration projects

Many of the laboratory scale and geochemical modelling experiments investigating interactions between basalt and CO_2 charged waters discussed in the previous section were conducted by two main groups of researchers, both of which developed their ideas through further field scale pilot projects. The first of these is called the CarbFix project. It was initiated by a collaboration between individuals at Reykjavik Energy (a geothermal energy company in Iceland), Columbia University (US), CNRS Toulouse (France) and the University of Iceland (Gislason *et al*., 2010; Matter *et al*., 2009). The initial concept and goal of the project was established in 2006, to create a “demonstration project designed to show the world that CO_2 can be economically removed from the atmosphere and stored in basalt”, and the project was officially launched in 2007 (Gíslason *et al*., 2018). After conducting a range of modelling and laboratory studies, an injection site just 3 km south of the Hellisheidi geothermal power plant in SW Iceland was identified (Gislason *et al*., 2010). Having a sequestration site in close proximity to a CO_2 source has several economic benefits, as less extensive piping and transport infrastructure is needed.

The project involves a pilot gas separation plant to collect CO_2 and H_2S from the steam evolving from the geothermal energy power station (Matter *et al*., 2009). The separated gases are dissolved in spent geothermal water which is then injected into the basaltic subsurface of the target site. The economic cost of separating gases makes up the majority of the total project cost, so investigating whether a mixture of gases could be injected has the potential to make the technique more economically viable. The composition of the rocks at the target site are mafic to ultramafic (~45 – 40% SiO_2), with both glassy and crystalline components (Alfredsson *et al*., 2008).

To monitor any CO_2 sequestration within the reservoir, the project created a monitoring and verification system specifically suited for the method of in situ mineral carbonation, described in detail by Matter *et al*., 2011. In summary, Trifluormethylsulpher pentafluoride (SF_5CF_5) and acid red dye (amidorhodamine G) are non-reactive tracers, which were mixed into the water stream, so the physical transport process of the injected fluid could be monitored. Radiocarbon (^{14}C) was added to the water stream to tag the injected CO_2 as a reactive tracer, so the changing concentrations of ^{14}C in the water stream and the presence of it in carbonate minerals would indicate recent carbonate precipitation.

The CarbFix project can be considered to have made positive achievements on several points. Initial reports from the project confirmed their injection method was successful in preventing the buoyancy of CO_2 usually associated with injecting it into the subsurface. By dissolving the CO_2 in water for injection, solubility trapping was demonstrated in less than 5 minutes (Gislason *et al*., 2014; Sigfússon *et al*., 2015). This helps minimise some the of risk associated with supercritical or gaseous state CO_2, which would likely be prone to leakage without an impermeable caprock layer. A disadvantage of this method is the volumes of water needed, with only about 5% of the injected mass attributed to CO_2 (Gislason *et al*., 2014), but the readily available and continuous flow of water evolving from the associated geothermal power plant means this is not a major problem for the CarbFix site. Injection tests in 2011 and 2012

involved injecting 175 tons of dissolved CO_2. In 2012, a further injection test of 60 tons of a CO_2-H_2S-H_2 gas mixture was also performed (Gislason *et al*., 2014). Reactive transport modelling of the site suggested 80% of the injected CO_2 would be mineralised within just 5 years, a significantly shorter timescale than predicted for mineral trapping in other geological systems (Aradóttir *et al*., 2012).

The findings of the project were reported by Matter *et al*., 2016, who demonstrated via mass balance calculations using the ^{14}C differences that >95% of the injected CO_2 was mineralised in just 2 years by water-CO_2-basalt interactions. This is significantly faster than previous reported timescales for mineralisation in sedimentary formations (Figure 1.7). The formation of calcite was confirmed by examining secondary mineral precipitates collected from monitoring wells at the site, with electron microscopy and energy dispersive spectroscopy techniques confirming the identity as calcite, and radiocarbon isotope analysis of the precipitates leading them to conclude the injected CO_2 was the source. The authors predict the finding of such a fast conversion rate is a result of several factors, including the rapid solubility trapping achieved by dissolving the CO_2 in water, the release of divalent cations by relatively rapid dissolution of the basalt, the mixing of the injected water with alkaline formations waters and the dissolution of pre-existing carbonates assisting in neutralising the acidic injection fluid (Matter *et al*., 2016; Snæbjörnsdóttir *et al*., 2017).

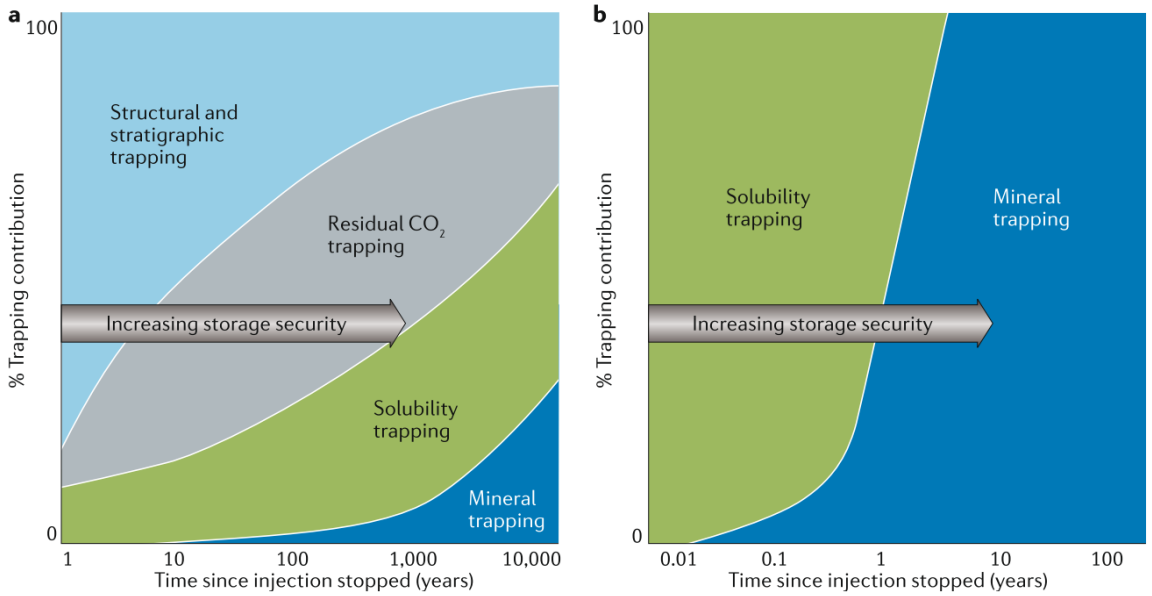


Figure 1.7: Comparison of CO_2 trapping mechanism contribution over time when a) injecting supercritical CO_2 into sedimentary basins and b) injecting water-dissolved CO_2 for mineralisation in basaltic systems. Figure is reproduced from Snæbjörnsdóttir *et al*., 2020 *with permission from Nature Research, Springer.*

One of the concerns associated with mineral carbonation for CO_2 sequestration within geothermal reservoirs, is the possibility that the formation of new minerals within the fractures and pore systems of the reservoir may reduce the permeability, thereby reducing the geothermal energy potential of the system. During the CarbFix pilot project, various temporary pauses in injection of acidic gases were experienced (e.g., due to supply issues associated with the pilot nature of the project etc.). Sporadic and non-continuous injection conditions lead to pH fluctuations, and a significant reduction in the permeability of the injection well (Gíslason *et al*., 2018). Later in the project, a new injection well was utilised with continuous acidic gas injection and the permeability of this well remained steady. The CarbFix project researches concluded this was due to basalt dissolution reactions dominating the flow properties of the injection well, rather than the precipitation of secondary minerals which occurs further away from the well (Gíslason *et al*., 2018).

The success of the original project has led to an upscaling of the technology with CarbFix2, a H2020 funded project. The aims of this project are to upscale the injection of acidic gases into basaltic systems in Iceland and to make the CarbFix geological storage method economically viable and applicable to more regions across Europe (Carbfix, 2021; Gunnarsson *et al*., 2018; Snæbjörnsdóttir *et al*., 2018). Within this, the CarbFix2 project will investigate using seawater as an alternative to fresh water and combining the CarbFix method with Direct Air Capture (DAC) of CO_2.

The second field scale pilot project investigating CO_2 sequestration in basaltic reservoirs was the Wallula Basalt Sequestration Pilot Project, undertaken by the US Department of Energy Big Sky Regional Carbon Sequestration Partnership. The aim was to capture CO_2 from the Boise White Paper Mill, and inject supercritical CO_2 into an area of the Columbia River Flood Basalt (McGrail *et al*., 2010). The basalt was targeted due to its suspected ability to contain and subsequently release sufficient divalent cations to achieve carbonate mineralisation in a relatively short timescale. Site analysis techniques such as seismic surveys and geologic characterisation were carried out to identify a target area, and since the timescale to reach permanent carbon sequestration was not yet known, a region with a low permeability caprock above a Suitable basaltic injection zone was injected to ensure some storage security (McGrail *et al*., 2010). The drilling of a 1253 m deep injection borehole was completed in 2009 (McGrail *et al*., 2011) and over 1000 tonnes of CO_2 was injected in 2013.

The Wallula Basalt Pilot well was decommissioned in 2015, but prior to its closure a suite of geophysical surveys was completed to characterise and assess the presence of CO_2 in the reservoir formation. X-ray diffraction techniques identified ankerite ($Ca(Fe,Mg,Mn)(CO_3)_2$) precipitates, which matched the predictions made from the laboratory scale tests performed by authors in the group (McGrail *et al*., 2017b; Schaef *et al*., 2011). Isotopic characterisation of carbon and oxygen in the precipitates closely matched the isotopic signature of the injected CO_2 (McGrail *et al*., 2017b). These findings confirmed that carbonates had precipitated in the

formation as a result of the supercritical CO_2 injection. Further examination of the precipitates found the carbonates were progressively enriched in Fe and Mn, which must suggest some dissolution of the basaltic minerals in the reservoir which would have released these cations to be available for inclusion in the carbonate precipitates (McGrail *et al*., 2017a). This finding matched the results of the laboratory scale experiments made over several years with the Columbia Basalt (Schaef *et al*., 2010, 2009). Taken together, these findings confirmed that carbonate minerals had formed within 2 years of injection into the Columbia River Flood Basalt system.

Hydrological testing was also conducted post-injection into the Wallula site, to assess small- to intermediate-scale permeability changes to the reservoir system that may be attributed to CO_2 injections, with results compared to pre-injection characterisation of the site. The results suggest no discernible changes in the hydrological properties in the near- to intermediate-scale interflow zone (McGrail *et al*., 2017b). This is a reassuring finding, that the precipitation of secondary minerals as a result of CO_2 injection into a basaltic reservoir does not negatively impact the near-well permeability.

1.4.5 Laboratory scale studies using alternative rock types.

A more limited amount of research has been conducted to investigate whether a similar method to the CarbFix/Wallula projects could be utilised in alternative volcanic rock types. There is a particular lack of work examining crystalline, rather than glassy samples. Ultramafic and mafic basaltic type rocks targeted in field studies so far do tend to contain a high molar percentage of the identified essential cations (Ca, Mg and Fe) and dissolve at appreciable rates, and the proven success of the projects in permanently sequestering CO_2 on such short timescales is due to these factors. However, andesite-type samples also contain significant amounts of plagioclase-type minerals, which have been identified as important cation sources for CO_2 sequestration. If this rock type were also proven to be Suitable for rapid carbon

sequestration via mineralisation, there would be increased potential to expand this technique to further locations worldwide.

Takaya *et al*., 2015 used batch type experiments to examine the interactions between CO_2-charged fluids and crystalline rocks of andesite to rhyolite compositions, for between 1 and 56 days. Their results indicate that the concentration of silica in the fluids increased throughout the experimental durations, particularly for the samples most basaltic in nature, which reflects the results found in previous studies (Wolff-Boenisch *et al*., 2006). Previously, studies have highlighted the importance of a rapid rock dissolution rate for carbonate mineralisation applications, as the dissolution of silicate minerals helps neutralise the acidity induced by adding CO_2 to the systems (McGrail *et al*., 2006; Wolff-Boenisch *et al*., 2006). The results from Takaya *et al*. (2015) indicate that the acid neutralisation potential of the examined samples depends largely on the mineralogy of the samples, rather than the bulk-rock chemical composition. This observation should be examined further, as it may have implications for selecting essential characteristics for a carbon sequestration target reservoir.

Takaya *et al*. (2015) also found that in the tuffaceous andesite and rhyolite samples, the bulk of the cation concentrations which were released from the samples entered the fluids on the first day of experiment which likely reflects rapid ion exchange reactions with clays and zeolites. Ion-exchange reactions commonly occur between minerals and cations in solution, where an ion held by a negative charge to a surface is exchanged for another. A simplified equation to describe this is presented by (Carroll, 1959) (Equation 1.4). The release of divalent cations by alteration minerals already present within the andesitic samples should be examined further in relation to targeting certain mineralogy's for further carbon sequestration experiments.

$$\text{Na-clay} + H^+ \leftrightarrow \text{H-clay} + Na^+ \quad (1.4)$$

Overall, Takaya *et al*. 2015 conclude that areas of porous andesitic hold promise as CO_2 sequestration sites and suggest more research should be conducted in this area to expand on their findings.

Marieni *et al*., 2018 also conducted experiments using a range of volcanic rock types, from basaltic to rhyolitic, glassy in nature and using flow through column experiments at 250^{o}C and 55 bar, conditions relevant for CO_2 and H_2S sequestration. The results of these experiments suggest that the basaltic and dacite samples were more effective for CO_2 mineralisation, and the rhyolitic sample resulted in more sulphate mineral formation. These findings suggest that more intermediate type volcanic rocks (rather than ultramafic) may also be Suitable for carbon sequestration reservoirs and the authors encourage more work on such samples to be undertaken to expand this knowledge base. Other observations by Marieni *et al*. (2018) include the formation of secondary aluminosilicate minerals, such as albite and epidote. Uptake of divalent cations by such minerals may inhibit carbonate reactions, and this is also an avenue of research that should be expanded to ensure future carbon sequestration projects can achieve maximum success.

Though these studies do provide valuable insights into some alternative volcanic rock types that could be targeted for carbon sequestration, the results are limited compared to the extensive literature available for basaltic samples. In particular, crystalline andesite samples need to be examined as these mineralogies are common in geothermal reservoir systems (BP, 2020; Sugisaki, 1972). For example, large areas of Indonesia, rich in geothermal energy resources (Sawin *et al*., 2017), have reservoir systems of andesitic composition (Boedihardi *et al*., 1993; Purnomo and Pichler, 2014). Basaltic reservoirs were targeted by the CarbFix Project, and the Wallula Basalt Pilot Project as existing literature indicated these rock types would have a high level of available cations and appreciable dissolution rates to enable mineral trapping to occur on reduced timescales (compared to the thousands of years predicted for sedimentary/sandstone type aquifers). The results from these projects indicate

carbon sequestration via mineralisation in basaltic reservoirs to be extremely fast, which opens up the possibility that other rock types may also be suitable, even if they have slightly lower molar volumes of cations and/or slightly slower dissolution rates. The dissolution of andesite samples under conditions relevant to CO_2 injection is an area of research that should be expanded, to examine whether the successes of the field scale carbon sequestration projects in basaltic reservoirs could be replicated in other regions.

1.4.6 Utilising seawater for carbon sequestration

One of the drawbacks of injecting CO_2 into basaltic reservoirs using the CarbFix method is the quantity of water needed. At 25^{o}C the amount of water needed to dissolve 1 kg of CO_2 at atmospheric pressure is 665 kg. This can be reduced to needing just 10 kg of water by increasing the pressure to 64 bars, though this comes at an energy cost. For the Hellisheidi Power plant where CarbFix is based, which emits 21.6 g of CO_2 per kWh of electricity produced, the energy penalty is around 0.2%. A typical coal or gas power plant emits from 385 – 1000 g of CO_2 per kWh with an associated energy penalty ranging from 3 to 10% (Gislason *et al*., 2014). Even if the energy requirement was not a barrier a substantial amount of water is still needed to dissolve and inject the desired amount of CO_2, upwards of hundreds to thousands of tones. This is a clear barrier to expanding the technique to certain locations which may not have excess freshwater available to support this need. Hence, there is a vested interest in investigating whether seawater could be used as an alternative injection fluid, to minimise the strain on freshwater supplies. The solubility of CO_2 decreases in saline fluids and the impact of this in terms of its use as an injection medium for carbon sequestration needs to be considered (Farquhar *et al*., 2015).

Previous research has been conducted looking at injecting CO_2 into sedimentary/sandstone type reservoirs containing saline fluids. Rosenbauer *et al*., 2005 examined CO_2-brine-rock interactions at elevated temperatures and pressures and reported results that suggested samples containing silicate minerals did demonstrate mineral trapping of CO_2 in the form of

carbonate phases. Another study that used moderately saline fluids with 1 M concentrations of NaCl and sandstones reported that K-feldspar, dolomite cement and albite dissolved in the samples, and the fluids remained undersaturated with respect to most minerals including carbonates (Wigand *et al*., 2008), which suggests these particular samples were not suitable for carbon sequestration on appreciable timescales, though few conclusions could be drawn about the direct effect of the salinity in this case.

In considering whether the CarbFix method can be used with seawater instead of freshwater, it is important to examine reactions between volcanic type rocks and saline fluids. Shibuya *et al*., 2013 examined reactions between CO_2 rich seawater at high temperatures and pressures, with an interest in CO_2 sequestration in the modern oceanic crust. The experimental results found that the total carbonic acid concentration in the fluids was reduced, and there was evidence on the basaltic samples of new calcite precipitation. These findings suggest that using the CarbFix method with basaltic samples and saline fluids instead of freshwater may still result in reactions that lead to the permanent sequestration of CO_2 within those systems.

Other research has been conducted to examine the impact of saline fluids on the dissolution of individual minerals that are relevant for subsurface CO_2 injection. Stillings and Brantley, 1995 reported that Na^+ inhibited plagioclase proton-promoted dissolution at 25^{o}C and a pH of 3, due to the competition between Na^+ and H^+ adsorption on surfaces. (Min and Jun, 2016) used up to 4 M concentration of Na^+ in experiments with anorthite, the calcium endmember of plagioclase feldspar. Results reported suggest that these high concentrations of sodium inhibited anorthite dissolution in far-from-equilibrium conditions, with the impact 50% stronger at 35^{o}C compared to 60^{o}C. Potentially, the increased temperatures often associated with volcanic rock reservoirs may reduce any impact Na^+ may have on inhibiting anorthite dissolution in concentrated saline fluids. Since anorthite is a major source of Ca^{2+}, which is necessary for carbon sequestration, this may benefit the implementation of saline fluids as a CO_2 injection medium in basaltic reservoirs. Montserrat *et al*., 2017 used batch experiments

to examine the impact of combining seawater type solution with olivine over periods of days to months. Although they found no direct evidence of carbonate formation, they did report an increase in pH due to mineral dissolution, which means the pH conditions required for carbonate mineral formation (near neutral) could be achieved.

A few laboratory scale studies have investigated carbonate mineral formation when using basaltic samples and fluids with elevated NaCl concentrations. Luhmann *et al*., 2017 conducted core flooding experiments with CO_2-rich NaCl solutions and used calculated liquid saturation states to show siderite ($FeCO_3$) formation was likely to have occurred. Other studies reacted CO_2 charged NaCl solutions with basalt at temperature ranges from 50 – 200^oC (Rosenbauer *et al*., 2012) and 250 – 350^oC (Shibuya *et al*., 2013) and reported evidence of calcite formation within 3-4 months. Other studies have observed induced calcite formation by assuming a situation with increased bicarbonate levels in the starting fluids with elevated NaCl concentrations (i.e., after significant mineral dissolution has already taken place) and combining these solutions with basaltic samples at 90^oC (Wolff-Boenisch and Galeczka, 2018a).

Authors associated with the CarbFix project continue to conduct research with the aim of continually optimising the methods used and deepening the understanding of the processes that make it successful. The continuation of the project has led to CarbFix2, which as discussed is aiming to upscale the process and investigate whether seawater can also be used and an effective injection medium for dissolved CO_2. Marieni *et al*., 2021 used reaction path models to estimate the rate and extent of gas mineralisation reactions during H_2S and/or CO_2-charged freshwater and seawater injection, using basaltic type rocks and temperatures of 260, 170, 100 and 25 degrees. They were able to compare their results to field observations of freshwater injection into the CarbFix2 site (Clark *et al*., 2020), to validate their model. The authors were particularly interested in observing whether any negative impacts of using the seawater arose. Reported issues from previous experiences of other studies include the

injection of seawater in other industrial processes leading to pipe clogging (Bader, 2007; Dai *et al*., 2017), and findings that reactions between basalts and seawater may result in the formation of permeability-destroying clay minerals (Wolff-Boenisch, 2011; Wolff-Boenisch and Galeczka, 2018b). Some of the key findings from Marieni *et al.* (2021) include calculation results that suggest the efficiency of gas-charged seawater for carbon mineralisation is somewhat lower than that of freshwater at temperatures ≥ 170^{o}C but similar ≤ 100^{o}C. Extensive early formation of anhydrite ($CaSO_4$) when using seawater at temperatures > 170^{o}C slows carbon mineralisation, due to the decrease in Ca availability. On the other hand, the authors also discuss the relationship between temperature and reaction rates. The dissolution rate of basaltic glass (based on an activation energy of 25.5. kJ/mol (Gislason and Oelkers, 2003) and the Arrhenius (1889) equation) is estimated to proceed almost two orders of magnitude slower at 25^{o}C compared to at 260^{o}C. This suggests almost two orders of magnitude longer reaction time might be required at the lower temperature to dissolve the same mass of basalt. These findings indicate there is likely to be a medium temperature range that is the ideal compromise between appreciable rates of rock dissolution (required to release divalent cations) at increased temperatures, and conditions for effective carbon mineralisation which seems to favour lower temperatures. Overall, Marieni *et al.* (2021) concluded that seawater is likely to be a good alternative to freshwater in most common basaltic reservoir conditions, which means the CarbFix method could be effectively implemented in other areas outside the Icelandic test site.

The existing literature seems to suggest seawater could be an effective alternative to freshwater. However, there are limited studies compared to the plethora of literature available for freshwater systems and a definite lack of studies exploring the possibility of carbonate formation during CO_2-charged seawater injection into rock reservoirs other than basaltic. Since the implementation of field-scale projects such as CarbFix have high-cost implications, potential financial stakeholders would want and need to be able to draw on a much wider evidence base to be able to make informed decisions to minimise associated risks. Therefore,

there is a clear need to conduct more research in this area, to gain increased understanding of the impacts that might be associated with using seawater to dissolve CO_2 for the process of carbon sequestration via carbonate mineral formation. In particular, laboratory experiments using more saline fluids which can be easily compared to existing experiments using freshwater systems will be vital. The CarbFix project drew on extensive laboratory scale experiments during its design process and the same wide ranging and thorough knowledge base needs to be created to enable equally important projects to be initiated in new regions.

1.5 Water Adsorption

It is important to understand mechanisms of water adsorption in geothermal systems in order for energy companies to determine reserve estimation and lifetime production performance of the reservoir (Roman, 1996). While the heat energy is effectively constant within a geothermal system, production capacity can decrease over a geothermal well's lifetime as water is removed from the system. For example, reservoir pressures have been declining at the Geysers Geothermal Reservoir in California, the largest vapour-dominated geothermal system in the world, since the late 1980's (Gruszkiewicz *et al*., 2001). A report by (Gruszkiewicz *et al*., 2001) states that it is steam that is the pressure-controlling fluid in larger fractures at the Geysers and liquid water is stored in matrix blocks between the fractures, which actually

accounts for the bulk of the reservoir fluid mass. It is believed much of this matrix water is held by adsorption and capillary forces in small fractures and pores. As production of the field is continued, the system is depressurized as steam is extracted. This causes increasing amounts of the matrix water to be flashed to steam, replenishing that being withdrawn through the wells (Gruszkiewicz *et al*., 2001). To combat decreasing pressure, geothermal energy companies reinject fluids into the reservoir system to maximise the energy extraction possible (Hornbrook, 1994).

Geothermal reservoir rocks are relatively low-porosity solids that can retain condensed gas in their structures via physical adsorption. A report from the Stanford Geothermal Programme by (Horne *et al*., 1995) gives an outline of the concepts of adsorption relative to geothermal systems. Physical adsorption is mainly caused by attractive van der Waals forces and may also include electrostatic forces if either the adsorbent or the adsorbate is polar in nature. The physical processes of water adsorption in geothermal reservoir rocks can be described by 3 steps: 1) monolayer adsorption, 2) multilayer adsorption with transition to 3) capillary condensation. In materials with larger pores, multilayers of adsorbed water form as the pressure increases and capillary condensation commences in smaller pores. If the pressure continues to increase, pores with larger radius are progressively filled while multilayer adsorption is taking place. However if the material is microporous, the pores will be completely filled before multilayer adsorption properly develops (Horne *et al*., 1995).

Looking at isotherms produced from water adsorption experiments can give various clues about the mineralogy of a sample. For example, if a sample contains clay, it will be able to adsorb a lot more water than a similar sample without clay. This is because of the mineral structure of so-called swelling clays, which can adsorb water between their structural sheets, due to charged mineral surfaces. This phenomenon can lead to several layers of water being adsorbed between sheets of a clay mineral (Woodruff and Revil, 2011). As an example, the amount of water that can be adsorbed on quartz or calcite minerals is around 1 mg/g,

compared to clay minerals which generally are able to adsorb tens to hundreds of mg of water per g of mineral (Keppert *et al*., 2016). The magnitude of water adsorption for a rock sample is relevant when looking at the reserve estimations, and the level of hysteresis seen is relevant when looking at reinjection needed to maintain well productivity. Overall, the capacity of a rock for water adsorption depends on both the mineral composition and the pore fracture system present in the sample (Gruszkiewicz *et al*., 2000). Usually, nitrogen adsorption experiments are also run on the sample. Nitrogen experiments can give information about the surface area and pore size distribution of a sample, most commonly using the BET Equation (Brunauer, 1943).

Gruszkiewicz *et al*., 2001 found that increasing the temperature water adsorption experiments were run at did not noticeably effect the magnitude of water adsorption within the same sample, but they did observe a narrowing of the hysteresis loop (gap between adsorption and desorption isotherms). Another study found that at lower relative pressures monolayer and multilayer adsorption is the dominant process, whereas capillary condensation is more important at higher relative pressures in terms of water retention of the samples (Shang *et al*., 1995). These studies have focussed more on the structure of rocks and influence of fractures and porosity on water adsorption. Although the discussed studies exist on water adsorption for individual minerals, there is little research looking at the influence the overall mineralogy of a sample has on water adsorption capacity. Whilst a clay may be able to adsorb a lot of water as a pure mineral, contained within a sample matrix as a minor component alongside other minerals may limit this capacity and therefore influence the water adsorption capacity of the whole rock sample. Results from nitrogen adsorption experiments giving surface area detail of samples in this present study can be compared to water adsorption experiments to see whether the mineralogy does have a significant influence.

1.6 Research Objectives.

The main research objectives of this present project are:

- To characterise a set of rock samples originating from an active geothermal well in Indonesia, expected to be broadly andesitic in composition. This will involve using a series of analytical techniques to extract mineralogical and geochemical information from the rock samples.

- To investigate the mineral dissolution reactions that take place as a result of rock-fluid interactions in laboratory experiments using andesite-type rock samples, at conditions relevant to CO_2 sequestration and compare these results to dissolution rates in basaltic systems. This will involve using thoroughly characterised rock samples in batch reactor -type experiments at increased temperatures and acidic pH conditions with a range of fluid cation concentrations to examine which rock-fluid interactions take place.

- To investigate whether carbonate mineral formation occurs when using andesitic rock samples in batch reactor experiments at elevated temperature, pressure and CO_2 concentration conditions relevant to CO_2 sequestration in andesite type geothermal reservoirs.

- To examine the impact of elevated NaCl concentration on the magnitude of feldspar mineral dissolution at increased temperatures and under acidic fluid conditions, and discuss the implications for using seawater instead of freshwater for CO_2 dissolution and injection in geological systems for carbon sequestration.

- To examine the impact of mineralogy on the water adsorption capacity of geothermal reservoir rocks. Fluids are often reinjected into geothermal reservoirs to maintain subsurface pressures. The growing interest in co-injecting CO_2 into these reservoirs for carbon sequestration, and the changes in mineralogy this may induce, means there is a need to investigate which impacts an altered mineralogy may have on the water adsorption of the reservoir rocks.

These experiments will contribute to a literature base which is assisting scientists, investors, and policy makers to direct research towards areas which will assist in expanding our ability to effectively capture and store CO_2, a necessity identified by the Paris Climate Agreement if global temperatures are to be prevented from rising 1.5^{o}C above pre-industrial levels.

1.7 References

Alfredsson, H.A., Hardarson, B.S., Franzson, H., Gislason, S.R., 2008. CO 2 sequestration in basaltic rock at the Hellisheidi site in SW Iceland: stratigraphy and chemical composition of the rocks at the injection site. Mineral. Mag. 72, 1–5. https://doi.org/10.1180/minmag.2008.072.1.1

Alfredsson, H.A., Oelkers, E.H., Hardarsson, B.S., Franzson, H., Gunnlaugsson, E., Gislason, S.R., 2013. The geology and water chemistry of the Hellisheidi, SW-Iceland carbon storage site. Int. J. Greenh. Gas Control 12, 399–418. https://doi.org/10.1016/j.ijggc.2012.11.019

Angelone, M., Labini, S.S., 2014. Overcoming Research Challenges for Geothermal Energy. Belgium.

Aradóttir, E.S., Gunnarsson, I., Sigfússon, B., Gunnarsson, G., Júliusson, B.M., Gunnlaugsson, E., Sigurdardóttir, H., Arnarson, M.T., Sonnenthal, E., 2015. Toward

Cleaner Geothermal Energy Utilization: Capturing and Sequestering CO2 and H2S Emissions from Geothermal Power Plants. Transp. Porous Media 108, 61–84. https://doi.org/10.1007/s11242-014-0316-5

Aradóttir, E.S.P., Sonnenthal, E.L., Björnsson, G., Jónsson, H., 2012. Multidimensional reactive transport modeling of CO2 mineral sequestration in basalts at the Hellisheidi geothermal field, Iceland. Int. J. Greenh. Gas Control 9, 24–40. https://doi.org/10.1016/j.ijggc.2012.02.006

Arrhenius, S., 1889. About the heat of dissociation and the influence of temperature on the degree of dissociation of electrolytes. J. Phys. Chem. 4, 96–116.

Bachu, S., 2003. Screening and ranking of sedimentary basins for sequestration of CO2 in geological media in response to climate change. Environ. Geol. 44, 277–289. https://doi.org/10.1007/s00254-003-0762-9

Bachu, S., 2000. Sequestration of CO2 in geological media: Criteria and approach for site selection in response to climate change. Energy Convers. Manag. 41, 953–970. https://doi.org/10.1016/S0196-8904(99)00149-1

Bader, M.S.H., 2007. Sulfate removal technologies for oil fields seawater injection operations. J. Pet. Sci. Eng. 55, 93–110. https://doi.org/10.1016/j.petrol.2006.04.010

Baines, S., Worden, R., 2004. The long-term fate of CO2 in the subsurface: natural analogues for CO2 storage. Geol. Soc. London, Spec. Publ. 233, 59–85. https://doi.org/10.1144/GSL.SP.2004.233.01.06

Bergenson, A., 2020. Growing geothermal industry in Canada supported by Canadian Oil Service Sector [WWW Document]. Hydrog. Fuel News. URL https://www.hydrogenfuelnews.com/growing-geothermal-industry-in-canada-supported-by-canadian-oil-service-sector/8539790/ (accessed 5.4.20).

Bertier, P., Swennen, R., Laenen, B., Lagrou, D., Dreesen, R., 2006. Experimental identification of CO2-water-rock interactions caused by sequestration of CO2 in Westphalian and Buntsandstein sandstones of the Campine Basin (NE-Belgium). J. Geochemical Explor. 89, 10–14. https://doi.org/10.1016/j.gexplo.2005.11.005

Boedihardi, M., Mulyonol, A., Ginting, A., Mosby, M., Radja, V., 1993. Geology, energy potential and development of Indonesia's geothermal prospects, in: Geological Society of Malaysia, Bulletin. pp. 369–385.

Bowen, N.L., 1928. The Evolution of the Igneous Rocks. Princeton Princeton.

BP, 2020. bp Statistical Review of World Energy.

Brady, P. V., Gíslason, S.R., 1997. Seafloor weathering controls on atmospheric CO2 and global climate. Geochim. Cosmochim. Acta 61, 965–973. https://doi.org/10.1016/S0016-7037(96)00385-7

Brennan, S.T., Burruss, R.C., 2006. Specific storage volumes: A useful tool for CO2 storage capacity assessment. Nat. Resour. Res. 15, 165–182. https://doi.org/10.1007/s11053-006-9019-0

Brunauer, S., 1943. The Adsorption of Gases and Vapors Volume 1. Oxford University Press.

CAODC, 2020. CAODC Joins the Geothermal Collaboration Network [WWW Document]. Candian Assoc. Oilw. Drill. Contract. URL https://caodc.ca/content.asp?admin=Y&contentid=341 (accessed 5.4.20).

Carbfix, 2021. carbfix.com/carbfix2 [WWW Document]. URL www.carbfix.com/carbfix2 (accessed 6.16.21).

Carroll, D., 1959. Ion exchange in clays and other minerals. Bull. Geol. Soc. Am. 70, 749–779. https://doi.org/10.1130/0016-7606(1959)70

Chen, Y., Brantley, S.L., 2000. Dissolution of forsteritic olivine at 65C and 2<pH<5. Chem. Geol. 165, 267–281.

Chen, Y., Brantley, S.L., 1997. Temperature- and pH-dependence of albite dissolution rate at acid pH. Chem. Geol. 135, 275–290. https://doi.org/10.1016/S0009-2541(96)00126-X

Clark, D.E., Oelkers, E.H., Gunnarsson, I., Sigfússon, B., Snæbjörnsdóttir, S., Aradóttir, E.S., Gíslason, S.R., 2020. CarbFix2: CO2 and H2S mineralization during 3.5 years of continuous injection into basaltic rocks at more than 250 °C. Geochim. Cosmochim. Acta 279, 45–66. https://doi.org/10.1016/j.gca.2020.03.039

Dai, Z., Kan, A.T., Shi, W., Zhang, N., Zhang, F., Yan, F., Bhandari, N., Zhang, Z., Liu, Y., Ruan, G., Tomson, M.B., 2017. Solubility Measurements and Predictions of Gypsum, Anhydrite, and Calcite Over Wide Ranges of Temperature, Pressure, and Ionic Strength with Mixed Electrolytes. Rock Mech. Rock Eng. 50, 327–339. https://doi.org/10.1007/s00603-016-1123-9

Daux, V., Christophe, G., Advocat, T., Crovisier, J.L., Stille, P., 1997. Kinetic aspects of basaltic glass dissolution at 90°c: Role of aqueous silicon and aluminium. Chem. Geol. 142, 109–126. https://doi.org/10.1016/S0009-2541(97)00079-X

Department of Energy and Climate Change, 2016. UK Energy Statistics, 2015 and Q4 2015. Stat. Press Release 1–16.

Design Engine, 2015. Geothermal Energy: The Overlooked Renewable | Design Engine [WWW Document]. Des. Engine. URL https://design-engine.com/geothermal-energy-the-overlooked-renewable/ (accessed 7.7.21).

DiPippo, R., 2008. Geothermal Power Plants - Principles, Applications, Case Studies and Environmental Impact, 2nd ed. Elsevier.

Duque, M.R., 2013. Geothermal reservoirs: From vapour dominated to conductive systems, in: International Conference on Renewable Energies and Power Quality. Bilbao, Spain. https://doi.org/10.24084/repqj11.286

Edenhofer, O., Pichs-Madruga, R., Sokona, Y., Farahani, E., Kadner, S., Seyboth, K., Adler, A., Baum, I., Brunner, S., Eickemeier, P., Kriemann, B., Savolainen, J., Schlömer, S., Stechow, C. v., Zwickel, T., Minx, J.C., 2014. Climate change 2014: Mitigation of Climate Change. Contribution of Working Group III to the Fifth Assessment Report of the Intergovernmental Panel on Climate Change, IPCC. Cambridge University Press, Cambridge, United Kingdom and New York, NY, USA.

El-Montasser, G., Ben-Salha, O., 2019. A new methodology for assessing the energy use–environmental degradation nexus. Environ. Monit. Assess. 191. https://doi.org/10.1007/s10661-019-7761-0

Farquhar, S.M., Pearce, J.K., Dawson, G.K.W., Golab, A., Sommacal, S., Kirste, D., Biddle, D., Golding, S.D., 2015. A fresh approach to investigating CO2 storage: Experimental CO2–water–rock interactions in a low-salinity reservoir system. Chem. Geol. 399, 98–122. https://doi.org/10.1016/J.CHEMGEO.2014.10.006

Fridriksson, T., Mateos-Merino, A., Audinet, P., Orucu, A.Y., 2016. Greenhouse Gases from Geothermal Power Production, in: Energy Sector Management Assistance Program (ESMAP) Technical Report;009/16. Washington, DC.

Gíslason, S., Sigurdardóttir, H., Aradóttir, E., Oelkers, E.H., 2018. A brief history of CarbFix: Challenges and victories of the project's pilot phase. Energy Procedia 146, 103–114. https://doi.org/10.1016/j.egypro.2018.07.014

Gislason, S.R., Broecker, W.S., Gunnlaugsson, E., Snæbjörnsdóttir, S., Mesfin, K.G., Alfredsson, H.A., Aradottir, E.S., Sigfusson, B., Gunnarsson, I., Stute, M., Matter, J.M., Arnarson, M.T., Galeczka, I.M., Gudbrandsson, S., Stockman, G., Wolff-Boenisch, D., Stefansson, A., Ragnheidardottir, E., Flaathen, T., Gysi, A.P., Olssen, J., Didriksen, K., Stipp, S., Menez, B., Oelkers, E.H., 2014. Rapid solubility and mineral storage of CO2 in basalt, in: Energy Procedia. Elsevier Ltd, pp. 4561–4574. https://doi.org/10.1016/j.egypro.2014.11.489

Gislason, S.R., Oelkers, E.H., 2003. Mechanism, rates, and consequences of basaltic glass dissolution: II. An experimental study of the dissolution rates of basaltic glass as a function of pH and temperature. Geochim. Cosmochim. Acta 67, 3817–3832. https://doi.org/10.1016/S0016-7037(00)00176-5

Gislason, S.R., Wolff-Boenisch, D., Stefansson, A., Oelkers, E.H., Gunnlaugsson, E., Sigurdardóttir, H., Sigfússon, B., Broecker, W.S., Matter, J.M., Stute, M., Axelsson, G., Fridriksson, T., 2010. Mineral sequestration of carbon dioxide in basalt : A pre-injection overview of the CarbFix project. Int. J. Greenh. Gas Control 4, 537–545. https://doi.org/10.1016/j.ijggc.2009.11.013

Global CCS Institute, 2018. The global status of CCS: 2018, The Global Status of CCS.

Grotzinger, J.P., Jordan, T.H., 2014a. The Climate System, in: Understanding Earth. pp. 407–434.

Grotzinger, J.P., Jordan, T.H., 2014b. The Human Impact on Earth's Environment, in: Understanding Earth. pp. 641–672.

Grotzinger, J.P., Jordan, T.H., 2014c. The Earth System, in: Understanding Earth. W. H. Freeman and Company, pp. 3–26.

Grotzinger, J.P., Jordan, T.H., 2014d. Metamorphism: Alteration of Rocks by Temperature and Pressure, in: Understanding Earth. pp. 149–170.

Grotzinger, J.P., Jordan, T.H., 2014e. Igneous Rocks: Solids From Melts, in: Understanding Earth. pp. 91–114.

Gruszkiewicz, M., Horita, J., Simonson, J.M., Mesmer, R.E., 2000. High-temperature adsorption on geothermal reservoir rocks, in: World Geothermal Congress. Tohoku, Japan.

Gruszkiewicz, M.S., Horita, J., Simonson, J.M., Mesmer, R.E., Hulen, J.B., 2001. Water adsorption at high temperature on core samples from The Geysers geothermal field, California, USA. Geothermics 30, 269–302. https://doi.org/10.1016/S0375-6505(00)00049-3

Gunnarsson, I., Aradóttir, E.S., Oelkers, E.H., Clark, D.E., Arnarson, M.Þ., Sigfússon, B., Snæbjörnsdóttir, S., Matter, J.M., Stute, M., Júlíusson, B.M., Gíslason, S.R., 2018. The rapid and cost-effective capture and subsurface mineral storage of carbon and sulfur at the CarbFix2 site. Int. J. Greenh. Gas Control 79, 117–126. https://doi.org/10.1016/j.ijggc.2018.08.014

Gunter, W.D., Perkins, E.H., McCann, T.J., 1993. Aquifer disposal of CO2-rich gases: Reaction design for added capacity. Energy Convers. Manag. 34, 941–948. https://doi.org/10.1016/0196-8904(93)90040-H

Hamilton, J.P., Pantano, C.G., Brantley, S.L., 2000. Dissolution of albite glass and crystal. Geochim. Cosmochim. Acta 64, 2603–2615. https://doi.org/10.1016/S0016-7037(00)00388-4

Holmukhe, R.M., 2009. Geothermal power generation. Pune, India.

Hornbrook, J.W., 1994. The effects of adsorption on injection into and production from vapour dominated geothermal reservoirs. Stanford University.

Horne, R.N., Ramey, H.J., Shang, S., Correa, A., Hornbrook, J., Program, S.G., 1995. The Effects of Adsorption and Desorption on Production and Reinjection in Vapor-Dominated Geothermal Fields, in: Stanford Geothermal Programme. U.S. Department of Energy, Stanford University, pp. 1973–1977.

IFC, 2013. Success of geothermal wells: A global study, International Finance Corporation.

IPCC, 2018. Summary for Policymakers, in: Masson-Delmotte, V., Zhai, P., Portner, H.-O., Roberts, D., Skea, J., Shukla, P.R., Pirani, A., Moufouma-Okia, W., Pean, C., Pidcock, R., Connors, S., Matthews, J.B.R., Chen, Y., Zhou, X., Gomis, M.I., Lonnoy, E., Maycock, T., Tignor, M., Waterfield, T. (Eds.), Global Warming of 1.5oC. An IPCC Special Report on the Impacts of Global Warming of 1.5oC above Pre-Industrial Levels and Related Global Greenhouse Gas Emission Pathways, in the Context of Strengthening the Global Response to the Threat of Climate Change,. Geneva.

IPCC, 2005. Carbon dioxide capture, IPCC Special Report on Carbon DIoxide Capture and Storage. Prepared by Working Group III of the Intergovernmental Panel on Climate Change. Cambridge University Press. https://doi.org/10.1002/9783527818488.ch15

Kampman, N., Busch, A., Bertier, P., Snippe, J., Hangx, S., Pipich, V., Di, Z., Rother, G., Harrington, J.F., Evans, J.P., Maskell, A., Chapman, H.J., Bickle, M.J., 2016. Observational evidence confirms modelling of the long-term integrity of CO2-reservoir caprocks. Nat. Commun. 7. https://doi.org/10.1038/ncomms12268

Keppert, M., Žumár, J., Čáchová, M., Koňáková, D., Svora, P., Pavlík, Z., Vejmelková, E., Černý, R., 2016. Water Vapor Diffusion and Adsorption of Sandstones: Influence of Rock Texture and Composition. Adv. Mater. Sci. Eng. 2016, 1–7. https://doi.org/10.1155/2016/8039748

Luhmann, A.J., Tutolo, B.M., Tan, C., Moskowitz, B.M., Saar, M.O., Seyfried, W.E., 2017. Whole rock basalt alteration from CO2-rich brine during flow-through experiments at 150 °C and 150 bar. Chem. Geol. 453, 92–110. https://doi.org/10.1016/j.chemgeo.2017.02.002

Marieni, C., Přikryl, J., Aradóttir, E.S., Gunnarsson, I., Stefánsson, A., 2018. Towards 'green' geothermal energy: Co-mineralization of carbon and sulfur in geothermal reservoirs. Int. J. Greenh. Gas Control 77, 96–105. https://doi.org/10.1016/j.ijggc.2018.07.011

Marieni, C., Voigt, M., Clark, D.E., Gíslason, S.R., Oelkers, E.H., 2021. Mineralization potential of water-dissolved CO2 and H2S injected into basalts as function of temperature: Freshwater versus Seawater. Int. J. Greenh. Gas Control 109. https://doi.org/10.1016/j.ijggc.2021.103357

Matter, J.M., Broecker, W.S., Gislason, S.R., Gunnlaugsson, E., Oelkers, E.H., Stute, M., Sigurdardóttir, H., Stefansson, A., Alfreõsson, H.A., Aradóttir, E.S., Axelssone, G.,

Sigfússon, B., Wolff-Boenisch, D., 2011. The CarbFix Pilot Project - Storing carbon dioxide in basalt. Energy Procedia 4, 5579–5585. https://doi.org/10.1016/j.egypro.2011.02.546

Matter, J.M., Broecker, W.S., Stute, M., Gislason, S.R., Oelkers, E.H., Stefánsson, A., Wolff-Boenisch, D., Gunnlaugsson, E., Axelsson, G., Björnsson, G., 2009. Permanent Carbon Dioxide Storage into Basalt: The CarbFix Pilot Project, Iceland. Energy Procedia 1, 3641–3646. https://doi.org/10.1016/j.egypro.2009.02.160

Matter, J.M., Stute, M., Snæbjörnsdóttir, S.Ó., Oelkers, E.H., Gislason, S.R., Aradóttir, E.S., Sigfússon, B., Gunnarsson, I., Sigurdardóttir, H., Gunnlaugsson, E., Axelsson, G., Alfredsson, H.A., Wolff-Boenisch, D., Mesfin, K.G., Dideriksen, K., Broecker, W.S., 2016. Rapid carbon mineralization for permanent disposal of anthropogenic carbon dioxide emissions. Science (80-.). 352, 1312–1314. https://doi.org/10.1126/science.aad8132

McCarthy, J.J., Canziani, O.F., Leary, N.A., Dokken, D., White, K.S., 2001. Climate Change 2001: Impacts, Adaptation, and Vulnerability. Cambridge University Press, Cambridge, United Kingdom.

McGrail, B.P., Freeman, C.J., Garber, R.D., Beeman, G.H., Tobin, D., Sullivan, E.C., Steffensen, E.J., Wurstner, S.K., Reddy, S., Brown, C.F., Gilmartin, J.P., 2010. Capture and sequestration of CO2 at the Boise White Paper Mill.

McGrail, B.P., Ho, A.M., Reidel, S.P., Schaef, H.T., 2003. Use and Features of Basalt Formations for Geologic Sequestration. Greenh. Gas Control Technol. - 6th Int. Conf. II, 1637–1640. https://doi.org/10.1016/b978-008044276-1/50264-6

McGrail, B.P., Schaef, H.T., Ho, A.M., Chien, Y.-J., Dooley, J.J., Davidson, C.L., 2006. Potential for carbon dioxide sequestration in flood basalts. J. Geophys. Res. Solid Earth 111. https://doi.org/10.1029/2005JB004169

McGrail, B.P., Spane, F.A., Sullivan, E.C., Bacon, D.H., Hund, G., 2011. The Wallula basalt sequestration pilot project. Energy Procedia 4, 5653–5660. https://doi.org/10.1016/j.egypro.2011.02.557

McGrail, P., Schaef, H.T., Spane, F.A., Cliff, J.B., Qafoku, O., Horner, J.A., Thompson, C.J., Owen, A.T., Sullivan, C.E., 2017a. Field validation of supercritical CO2 reactivity with basalts. Environ. Sci. Technol. Lett. 4, 6–10. https://doi.org/10.1021/acs.estlett.6b00387

McGrail, P., Schaef, H.T., Spane, F.A., Horner, J.A., Owen, A.T., Cliff, J.B., Qafoku, O., Thompson, C.J., Sullivan, E.C., 2017b. Wallula Basalt Pilot Demonstration Project : Post-Injection Results and Conclusions. Energy Procedia 114, 5783–5790. https://doi.org/10.1016/j.egypro.2017.03.1716

Min, Y., Jun, Y.S., 2016. Anorthite Dissolution under Conditions Relevant to Subsurface CO2 Injection: Effects of Na+, Ca2+, and Al3+. Environ. Sci. Technol. 50, 11377–11385. https://doi.org/10.1021/acs.est.6b02207

Mock, J.E., Tester, J.W., Wright, P.M., 1997. GEOTHERMAL ENERGY FROM THE EARTH: Its Potential Impact as an Environmentally Sustainable Resource. Annu. Rev. Energy Environ. 22, 305–356. https://doi.org/10.1146/annurev.energy.22.1.305

Montserrat, F., Renforth, P., Hartmann, J., Leermakers, M., Knops, P., Meysman, F.J.R., 2017. Olivine Dissolution in Seawater: Implications for CO2 Sequestration through Enhanced Weathering in Coastal Environments. Environ. Sci. Technol. 51, 3960–3972. https://doi.org/10.1021/acs.est.6b05942

Murphy, W.M., Oelkers, E.H., Lichtner, P.C., 1989. Surface reaction versus diffusion control of mineral dissolution and growth rates in geochemical processes. Chem. Geol. 78, 357–380. https://doi.org/10.1016/0009-2541(89)90069-7

National Renewable Energy Laboratory, 2012. Renewable Electricity Generation and Storage Technologies. Renew. Electr. Futur. Study Renew. Electr. Gener. Storage Technol. Vol. 2 2. https://doi.org/NREL/TP-6A20-52409-2

Oelkers, E.H., Gislason, S.R., 2001. The mechanism, rates and consequences of basaltic glass dissolution: I. An experimental study of the dissolution of basaltic glass as a function of aqueous Al, Si and oxalic acid concentration at 25oC and pH = 3 and 11. Geochim. Cosmochim. Acta 65, 3671–3681.

Oelkers, E.H., Schott, J., 1995. Experimental study of anorthite dissolution and the relative mechanism of feldspar hydrolysis. Geochim. Cosmochim. Acta 59, 5039–5053. https://doi.org/10.1016/0016-7037(95)00326-6

Oelkers, E.H., Schott, J., Devidal, J.L., 1994. The effect of aluminum, pH, and chemical affinity on the rates of aluminosilicate dissolution reactions. Geochim. Cosmochim. Acta 58, 2011–2024. https://doi.org/10.1016/0016-7037(94)90281-X

Pokrovsky, O.S., Schott, J., 2002. Surface chemistry and dissolution kinetics of divalent metal carbonates. Environ. Sci. Technol. 36, 426–432. https://doi.org/10.1021/es010925u

Pokrovsky, O.S., Schott, J., 2000. Kinetics and mechanism of forsterite dissolution at 25 ° C and pH from 1 to 12. Geochim. Cosmochim. Acta 64, 3313–3325.

Purnomo, B.J., Pichler, T., 2014. Geothermal systems on the island of Java, Indonesia. J. Volcanol. Geotherm. Res. 285, 47–59. https://doi.org/10.1016/j.jvolgeores.2014.08.004

Ragnarsson, Á., 2015. Geothermal Development in Iceland 2010-2014, in: Proceedings World Geothermal Congress 2015.

Retallack, G.J., 2002. Carbon dioxide and climate over the past 300 Myr. Philos. Trans. R. Soc. A Math. Phys. Eng. Sci. 360, 659–673. https://doi.org/10.1098/rsta.2001.0960

Richter, A., 2021. ThinkGeoEnergy's Top 10 Geothermal Countries 2020 - installed power generation capcity (MWe) [WWW Document]. ThinkGeoEnergy. URL https://www.thinkgeoenergy.com/thinkgeoenergys-top-10-geothermal-countries-2020-installed-power-generation-capacity-mwe/ (accessed 5.20.21).

Richter, A., 2020. Canadian Oil Service Sector joins forces to support emerging Canadian geothermal industry [WWW Document]. ThinkGeoEnergy. URL https://www.thinkgeoenergy.com/canadian-oil-service-sector-joins-forces-to-support-emerging-canadian-geothermal-industry/ (accessed 5.4.20).

Roman, M.B.S., 1996. Optimization of Injection into Vapour-Dominated Geothermal Reservoirs Considering Adsorption. Stanford University .

Rosenbauer, R.J., Koksalan, T., Palandri, J.L., 2005. Experimental investigation of CO2-brine-rock interactions at elevated temperature and pressure: Implications for CO2 sequestration in deep-saline aquifers. Fuel Process. Technol. 86, 1581–1597. https://doi.org/10.1016/j.fuproc.2005.01.011

Rosenbauer, R.J., Thomas, B., Bischoff, J.L., Palandri, J., 2012. Carbon sequestration via reaction with basaltic rocks: Geochemical modeling and experimental results. Geochim. Cosmochim. Acta 89, 116–133. https://doi.org/10.1016/J.GCA.2012.04.042

Rosso, J.J., Rimstidt, J.D., 2000. A high resolution study of forsterite dissolution rates. Geochim. Cosmochim. Acta 64, 797–811. https://doi.org/10.1016/S0016-7037(99)00354-3

Sanyal, S.K., Enedy, S.L., 2011. Fifty years of power generation at the Geysers geothermal field, California – the lessons learned, in: Thirty-Sixth Workshop on Geothermal Reservoir Engineering. pp. 1–9.

Sass, B.M., Engelhard, M.H., Bergman, P., Byrer, C., 2002. Interaction of Rock Minerals With Carbon Dioxide and Brine : a Hydrothermal Investigation, in: First National Conference on Carbon Sequestration. National Energy and Technology Lab, Washington DC, 14-17 May.

Sawin, J., Seyboth, K., Sverrisson, F., 2017. Renewables 2017 Global Status Report. Paris.

Schaef, H.T., McGrail, B.P., 2009. Dissolution of Columbia River Basalt under mildly acidic conditions as a function of temperature: Experimental results relevant to the geological sequestration of carbon dioxide. Appl. Geochemistry 24, 980–987. https://doi.org/10.1016/j.apgeochem.2009.02.025

Schaef, H.T., McGrail, B.P., Owen, A.T., 2011. Basalt reactivity variability with reservoir depth in supercritical CO 2 and aqueous phases, in: Energy Procedia. Elsevier Ltd, pp. 4977–4984. https://doi.org/10.1016/j.egypro.2011.02.468

Schaef, H.T., McGrail, B.P., Owen, A.T., 2010. Carbonate mineralization of volcanic province basalts. Int. J. Greenh. Gas Control 4, 249–261. https://doi.org/10.1016/j.ijggc.2009.10.009

Schaef, H.T., McGrail, B.P., Owen, A.T., 2009. Basalt- CO2-H2O interactions and variability in carbonate mineralization rates. Energy Procedia 1, 4899–4906. https://doi.org/10.1016/j.egypro.2009.02.320

Shang, S., Horne, N.R., Ramey, H.J.J., 1995. Water vapor adsorption on geothermal reservoir rocks. Geothermics 24, 523–540. https://doi.org/10.1016/0375-6505(95)00008-E

Shibuya, T., Yoshizaki, M., Masaki, Y., Suzuki, K., Takai, K., Russell, M.J., 2013. Reactions between basalt and CO2-rich seawater at 250 and 350°C, 500bars: Implications for the CO2 sequestration into the modern oceanic crust and the composition of hydrothermal vent fluid in the CO2-rich early ocean. Chem. Geol. 359, 1–9. https://doi.org/10.1016/j.chemgeo.2013.08.044

Sigfússon, B., Gislason, S.R., Matter, J.M., Stute, M., Gunnlaugsson, E., Gunnarsson, I., Aradottir, E.S., Sigurdardóttir, H., Mesfin, K.G., Alfredsson, H.A., Wolff-Boenisch, D., Arnarsson, M.T., Oelkers, E.H., 2015. Solving the carbon-dioxide buoyancy challenge: The design and field testing of a dissolved CO2 injection system. Int. J. Greenh. Gas Control 37, 213–219.

Skorina, T., Allanore, A., 2015. Aqueous alteration of potassium-bearing aluminosilicate minerals: From mechanism to processing. Green Chem. 17, 2123–2136. https://doi.org/10.1039/c4gc02084g

Snæbjörnsdóttir, S., Tómasdóttir, S., Sigfússon, B., Aradóttir, E.S., Gunnarsson, G., Niemi, A., Basirat, F., Dessirier, B., Gislason, S.R., Oelkers, E.H., Franzson, H., 2018. The geology and hydrology of the CarbFix2 site, SW-Iceland. Energy Procedia 146, 146–157. https://doi.org/10.1016/j.egypro.2018.07.019

Snæbjörnsdóttir, S.Ó., Oelkers, E.H., Mesfin, K.G., Aradóttir, E.S., Dideriksen, K.,

Gunnarsson, I., Gunnlaugsson, E., Matter, J.M., Stute, M., Gislason, S.R., 2017. The chemistry and saturation states of subsurface fluids during the in situ mineralisation of CO2 and H2S at the CarbFix site in SW-Iceland. Int. J. Greenh. Gas Control 58, 87–102. https://doi.org/10.1016/j.ijggc.2017.01.007

Snæbjörnsdóttir, S.Ó., Sigfússon, B., Marieni, C., Goldberg, D.S., Oelkers, E.H., 2020. Carbon dioxide storage through mineral carbonation. Nat. Rev. Earth Environ. https://doi.org/10.1038/s43017-019-0011-8

Stillings, L.L., Brantley, S.L., 1995. Feldspar dissolution at 25°C and pH 3: Reaction stoichiometry and the effect of cations. Geochim. Cosmochim. Acta 59, 1483–1496. https://doi.org/10.1016/0016-7037(95)00057-7

Stimac, J., Nordquist, G., Suminar, A., Sirad-Azwar, L., 2008. An overview of the Awibengkok geothermal system, Indonesia. Geothermics 37, 300–331. https://doi.org/10.1016/j.geothermics.2008.04.004

Streck, M.J., Dungan, M.A., Bussy, F., Malavassi, E., 2005. Mineral inventory of continuously erupting basaltic andesites at Arenal volcano, Costa Rica: Implications for interpreting monotonous, crystal-rich, mafic arc stratigraphies. J. Volcanol. Geotherm. Res. 140, 133–155. https://doi.org/10.1016/j.jvolgeores.2004.07.018

Sugisaki, R., 1972. Tectonic Aspects of Andesite Line. Nat. Phys. Sci. 240, 109–111. https://doi.org/10.1038/physci240109a0

Suharmanto, P., Fitria, A.N., Ghaliyah, S., 2015. Indonesian Geothermal Energy Potential as Source of Alternative Energy Power Plant, in: Renewable Energy and Energy Conversion Conference and Exhibition. Knowledge E, pp. 119–124. https://doi.org/10.18502/ken.v1i1.325

Tajika, E., 1998. Climate change during the last 150 million years: Reconstruction from a carbon cycle model. Earth Planet. Sci. Lett. 160, 695–707. https://doi.org/10.1016/S0012-821X(98)00121-6

Takaya, Y., Nakamura, K., Kato, Y., 2015. Dissolution of altered tuffaceous rocks under conditions relevant for CO2 storage. Appl. Geochemistry 58, 78–87. https://doi.org/10.1016/j.apgeochem.2015.03.012

Techer, I., Advocat, T., Lancelot, J., Liotard, J.M., 2001. Dissolution kinetics of basaltic glasses: Control by solution chemistry and protective effect of the alteration film. Chem. Geol. 176, 235–263. https://doi.org/10.1016/S0009-2541(00)00400-9

UNFCCC, 2016. Report of the Conference of the Parties on its twenty-first session, held in Paris from 30 Novemeber to 13 December 2015, Framework Convention on Climate Change.

Utami, P., 2000. Characteristics of the Kamojang geothermal reservoir (West Java) as revealed by its hydrothermal alteration mineralogy, in: World Geothermal Congress. Kyushu, Japan.

Varekamp, J.C., Kreulen, R., Poorter, R.P.E., Van Bergen, M.J., 1992. Carbon sources in arc volcanism, with implications for the carbon cycle. Terra Nov. 4, 363–373. https://doi.org/10.1111/j.1365-3121.1992.tb00825.x

Wigand, M., Carey, J.W., Schütt, H., Spangenberg, E., Erzinger, J., 2008. Geochemical effects of CO2 sequestration in sandstones under simulated in situ conditions of deep saline aquifers. Appl. Geochemistry 23, 2735–2745. https://doi.org/10.1016/j.apgeochem.2008.06.006

Wolff-Boenisch, D., 2011. On the buffer capacity of CO2-charged seawater used for carbonation and subsequent mineral sequestration. Energy Procedia 4, 3738–3745. https://doi.org/10.1016/j.egypro.2011.02.307

Wolff-Boenisch, D., Galeczka, I.M., 2018a. Flow-through reactor experiments on basalt-(sea)water-CO2 reactions at 90 °C and neutral pH. What happens to the basalt pore space under post-injection conditions? Int. J. Greenh. Gas Control 68, 176–190. https://doi.org/10.1016/j.ijggc.2017.11.013

Wolff-Boenisch, D., Galeczka, I.M., 2018b. Flow-through reactor experiments on basalt-(sea)water-CO2 reactions at 90 °C and neutral pH. What happens to the basalt pore space under post-injection conditions? Int. J. Greenh. Gas Control 68, 176–190. https://doi.org/10.1016/j.ijggc.2017.11.013

Wolff-Boenisch, D., Gislason, S.R., Oelkers, E.H., 2006. The effect of crystallinity on dissolution rates and CO2 consumption capacity of silicates. Geochim. Cosmochim. Acta 70, 858–870. https://doi.org/10.1016/j.gca.2005.10.016

Wolff-Boenisch, D., Gislason, S.R., Oelkers, E.H., Putnis, C. V., 2004. The dissolution rates of natural glasses as a function of their composition at pH 4 and 10.6, and temperatures from 25 to 74°C. Geochim. Cosmochim. Acta 68, 4843–4858. https://doi.org/10.1016/j.gca.2004.05.027

Woodruff, W.F., Revil, A., 2011. CEC-normalized clay-water sorption isotherm. Water Resour. Res. 47, 1–15. https://doi.org/10.1029/2011WR010919

Zhang, R., Zhang, X., Hu, S., 2015. Basalt-water interactions at high temperatures: 1. Dissolution kinetic experiments of basalt in water and NaCl-H2O at temperatures up to 400°C, 23MPa and implications. J. Asian Earth Sci. 110, 189–200. https://doi.org/10.1016/j.jseaes.2015.03.042

Zheng, L., Apps, J.A., Zhang, Y., Xu, T., Birkholzer, J.T., 2009. On mobilization of lead and arsenic in groundwater in response to CO2 leakage from deep geological storage. Chem. Geol. 268, 281–297. https://doi.org/10.1016/j.chemgeo.2009.09.007

Chapter 2: Experimental Methodology

2.1 Materials

2.1.1 Geological Setting of Rock Samples

The rock core samples used throughout the project were provided by PT Supreme Energy, from a geothermal energy production site, located on the Island of Sumatra in Indonesia in the Rantau Dedap region. Three samples B1, C1 and I1 (Figure 2.1) are from exploration wells taken from approximately 1 to 2 km depth (Supreme-Energy, personal communication, 2018).

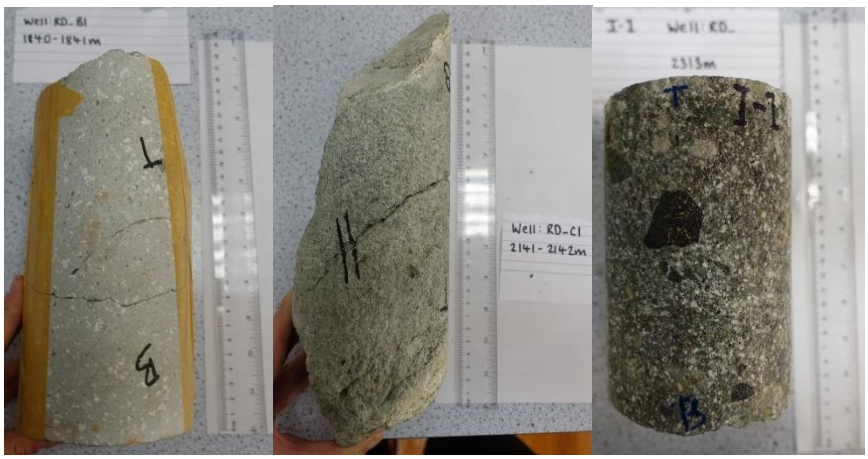


Figure 2.1: Photographic images of the three rock core samples; i) B1, ii) C1 and iii) I1.

The Island of Sumatra formed due to the subduction of the Sundaland Continental Plate with the India-Australia Oceanic Plate. Due to the tectonic stress from the subduction of these two plates, dextral strike slip faults were created which run parallel to the Island of Sumatra, known as the Great Sumatra Fault (GSF) length of 1900 km, consists of 19 segments of dilatational step over, with a length of 60 to 200 km for each segment (Sieh and Natawidjaja 2000). Another result of the subduction of the two plates is a volcanic arc, which causes geological activity such as earthquakes and importantly is the reason for the plethora of geothermal prospects on the Island of Sumatra (Muraoka *et al*. 2010; Santoso *et al*. 1995).

The general mineralogy of the sampling area is of andesitic volcanic composition (Barber, Crow, and Milsom 2005). This is consistent with drilling studies completed by Supreme Energy, with Quaternary-aged andesitic-basaltic volcanic rocks samples from the surface to the top of the reservoir section. Supreme have determined the reservoir itself to consist of Tertiary-aged mixed marine sediment with layers of silicic and andesitic volcanic rocks (Supreme Energy, personal communication, 2018).

2.1.2 Rock Sample Preparation

Due to the natural heterogeneous nature of the core samples, approximately 300 g of each sample was crushed at the beginning of the project, to be used through all the following analysis and experiments, to minimise uncertainties and errors due to sample heterogeneity. It is common knowledge that a crushed rock sample will tend to have a faster dissolution rate compared to samples still in situ in the field, as the process of crushing the sample increases the surface area of the sample. The process of crushing the sample is also likely to have destroyed some of the porosity and related permeability of the samples. However, it is commonly acknowledged that to study rock dissolution on acceptable timescales in the lab, crushing the sample is often necessary and will result in a faster dissolution rate than in the field. The results can be validated by comparison to other lab studies using crushed samples, and related field scale studies measuring changes in situ. Crushing a large portion of the rock samples at the beginning of the project (a larger amount than is predicted necessary) ensures the same batch of crushed sample can be used throughout the project, to at least minimise heterogeneities that would be created through separate crushing sessions. Small pieces of each sample were first separated from the main core using a hammer and mallet. These smaller pieces were then crushed in an agate pestle and mortar and the resulting powder was stored in sealed plastic bags until use.

To determine the composition in terms of weight percent of the clay fraction, the following aqueous dispersion and centrifugation method was used to separate particles ≤ 2 μm, which

is the usual assumed size of any clay minerals present in a sample. A 5 g aliquot was suspended in a 50 mL solution made up of ultra-pure MilliQ (MQ) water, 3% hydrogen peroxide (H_2O_2) and 4 g/L of sodium hexametaphosphate (SHMP) and placed in an ultrasonic bath for 2 hours to remove organics and disperse the clay. A series of centrifugation and washing steps at 4000 rpm for 30 minutes each time was then completed until the fluids remained clear. The solid samples were then suspended again in MQ water and sonicated for 15 minutes to re-disperse the clay. A final shorter centrifugation step for 2 minutes and at 1000 rpm was then completed and the clay suspension (particles ≤ 2 μm in diameter) was decanted to separate it from the rest of the sample.

A mild hydrochloric acid (HCl) treatment on some of the separated clay fraction of each sample was also completed, to further characterise the clay fraction, discussed further in Section 2.3.1. After repeating the steps described above for the clay separation, in a Teflon vial, 0.4 mL of 12.4 M HCl, was added to 4.6 mL of the clay fluid suspension, sealed and boiled at 200^{o}C for 2 hrs on a hot plate. The sample was left to cool before washing with MQ water via centrifugation.

For some of the analyses described in the following sections, 30 μm thickness thin sections of the samples were required. Samples of approximately 2 cm x 2 cm x 4 cm were cut from each of the core rock samples and sent to MiEKiNiA Laboratory (Poland), who returned the thin sections without cover slips and mounted on glass microscope slides for analysis in this project.

2.2 Microscopy of Rock Samples

2.2.1 Petrography with optical Microscopy

Optical microscopy can be used to gain textural information and petrographic detail about the minerals in the rock samples being examined, enabling identification of the rock-type and texture. When observed under a microscope, different minerals have a variety of physical characteristics which can be used to identify them, including shape, cleavage planes and twinning/zoning. When a polarising microscope is used, the observed minerals also display different colours and possible pleochroism, due to the light being refracted which is specific to the crystal structure of each mineral, meaning this can also be used as an identifying characteristic. Since the colour observed will also depend on the thickness of the mineral, thin sections of sample are mounted on glass slides and a standard thickness of 30 μm is acquired, so the observations can be compared across the published literature for characterisation of the samples (MacKenzie and Adams 1994).

A polarising microscope is equipped with a rotating sample stage, two polarising filters above and below the stage and both a transmission and sometimes a reflection light source. The polarising filters are set perpendicular to each other, so when the transmission light source below is passed through them, they create what is known as crossed-polarised light. The polariser above the sample, commonly referred to as the analyser, can be removed from the light path to observe the sample in plane-polarised light. The thin sections may also be examined under reflected light, with no polarisation to gain certain additional pieces of information, usually used in the case of opaque minerals (MacKenzie and Adams 1994).

Due to the structure of minerals, the atomic bonding within a plane of the crystal is likely to be strong compared to the bonding between the planes of that mineral. This means minerals that contain such planes cleave more easily along these directions and the presence (or absence) of such planes and the angles between them can be used as an identifying characteristic. For

example, micas have perfect cleavage along one plane, so can easily be split into thin sheets. Angles between cleavage planes can help distinguish between two types of minerals which might otherwise look very similar. For example, the pyroxene group has two cleavages at 90^{o} angles which can be seen in Figure 2.2 i), whereas the amphiboles intersect at an angle of 120^{o} which can be seen in Figure 2.2 ii). So these two minerals can be distinguished based on their different cleavage planes (MacKenzie and Adams 1994).

Several minerals occur in what are known as twins. They are crystals of the same mineral in which the orientations of two (or more) parts have a simple relationship to each other, such as rotation about 180^{o} around a crystallographic axis. Certain twinning patterns are characteristic of different minerals within the feldspar group, such as plagioclase feldspars which show polysynthetic twinning, which occurs where the twin operation is repeated a number of times (MacKenzie and Adams 1994).

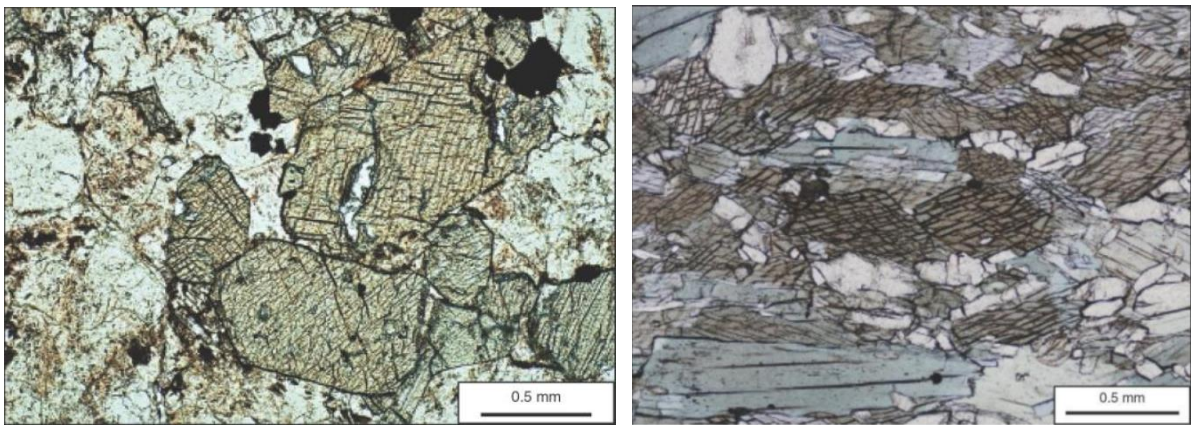


Figure 2.2: i) Clinopyroxene crystals observed in plane polarised light, showing two cleavages at approximately 90^{o} (MacKenzie and Adams 1994), ii) Amphibole crystals (light brown) showing two cleavages at approximately 120^{o} observed in plane polarised light (MacKenzie and Adams 1994).

A few minerals in thin section can be recognised by their colour in plane-polarised light, called the absorption colour, as in Figure 2.2 (i) with grey coloured clinopyroxene minerals. A mineral which shows colour may show different shades as the sample stage is rotated, known as

pleochroism. This happens as crystals in a rock sample are usually arranged randomly, hence cut in different directions within one thin section, and therefore show these different shades depending on each crystal's orientation with respect to the plane of polarisation of the light. Some minerals are opaque in thin section under plane-polarised light as they so not transmit light through them, requiring the use of reflected light to be studied, under which they appear as bright areas. This brightness usually indicates a metal oxide or a sulphide mineral such as pyrite (MacKenzie and Adams 1994).

All minerals (as materials) have an index of refraction, which refers to the ratio of the speed of light in a vacuum, c, to the speed of light in the mineral, c'. The refractive index will always be greater than 1, as c' will always be slower than c. Due to the slight change in its speed on entering a material, a beam of light will change direction ('bend') when it changes from a region of one refractive index to another (Atkins and De Paula 2010b). The symmetry of the mineral crystal structures has an important effect on the index of refraction. Completely amorphous materials and perfectly symmetrical ordered materials have the same structure, or lack of, in all directions. Minerals with these structures therefore only have one index of refraction, light passes through the crystal with the same velocity irrespective of direction, meaning they always appear black/opaque in crossed-polarised light and are known as isotropic minerals (Pichler and Schmitt-Riegraf 1997).

Other minerals have more than one index of refraction, because they have a different structure along at least one axis compared to the others, so the pattern of atoms varies along different directions within the structure. These are known as anisotropic minerals (Pichler and Schmitt-Riegraf 1997). The presence of more than one refractive index means they have a property known as double refraction. This can be measured under crossed-polarised light, known as birefringence, which is defined as the difference between the maximum and minimum refractive indices of a mineral. As plane-polarised light passes through a mineral crystal, it is split into two component light waves, which become out of phase as they travel through the

crystal. On emerging from the crystal they interfere with each other and show interference colours when observed through the analysing polariser (Figure 2.3). The colours are compared to a birefringence chart to assist in identifying the mineral (MacKenzie and Adams 1994).

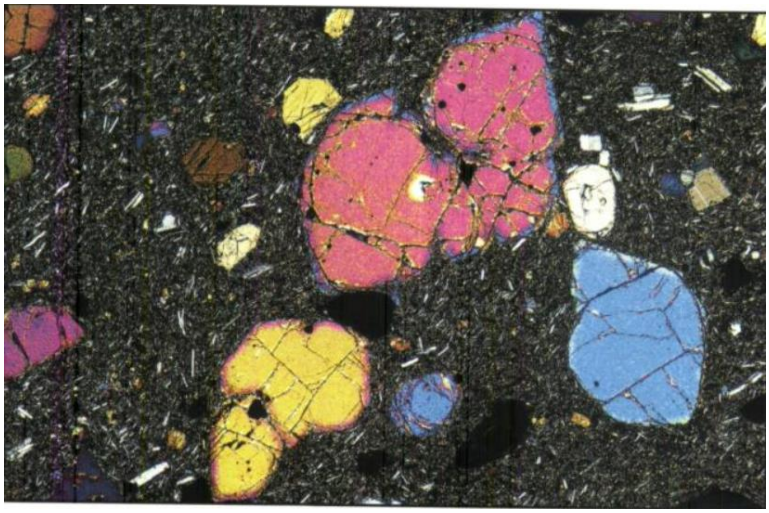


Figure 2.3: An example of phenocrysts of olivine in a volcanic rock, observed in crossed-polarised light. The brightly coloured crystals are the olivine, the dark colour between the crystals is the fine groundmass (MacKenzie and Adams 1994).

As the sample stage of the microscope is rotated, the interference colour of each mineral grain observed through crossed polars changes in intensity. The intensity falls to zero every 90^{o} of rotation, known as the extinction position. If a straight edge of a crystal or cleavage direction is set parallel to a cross hair in the eye piece and the stage is rotated to one of the extinction positions, the angle of rotation between these two positions can be read from the sample stage scale. This is known as the extinction angle and may be of diagnostic value for a mineral (MacKenzie and Adams 1994).

In this project, a Carl Zeiss Axio Scope.A1 optical microscope with reflective and transmitted light modes, polarisers fitted above and below a rotating sample stage was used. Images were obtained using an Axiocam ERc5s camera. Multiple images are taken of an area of interest starting at 2.5x magnification, under reflective light, plane-polarised transmitted light and

rotations under crossed-polarised light. Images at 10x magnification were occasionally acquired to look at areas of interest in more detail.

2.2.2 Scanning Electron Microscopy

In a scanning electron microscope (SEM) a beam of high-energy focussed electrons is generated to target the surface of a sample, with the electron and x-ray signals resulting from the electron-sample interactions revealing various pieces of information about the sample. In some instances, a selected area of the sample is scanned to collect backscattered electron (BSE) data, or secondary electron (SE) data, which can then be processed and viewed as a 2D image to observe spatial variations and phase differences across a sample. The scanned area can range from a cm down to several microns in width using conventional SEM techniques. Additional attachments such as an Energy Dispersive X-ray Spectrometer can also be used to collect semi-quantitative EDS data describing the chemical composition of an area of the sample.

The kinetic energy carried by the focussed electron beam results in a variety of signals produced by the electron-sample interactions as the solid sample causes deceleration of the incident electrons. Secondary electrons (SE) are the result of inelastic scattering with the sample, when the incident electron beam displaces an electron from an inner shell. These SE are lower in energy so only those originating from surface atoms can then be detected, which allows for the creation of detailed topographical images (Reed 2005). Back scattered electrons (BSE) are the result of elastic interactions, where the incident electrons are reflected back after interacting with the sample, which are high in energy so can be detected from regions deeper within the sample than SE. The images resulting from detected BSE are highly sensitive to differences in atomic number, so can give more information on compositional differences within a sample. For example, a mineral containing heavy elements, such as pyrite (FeS_2), will appear as a bright area in a BSE image due to the higher atomic number of Iron, whereas a mineral such as quartz (SiO_2) will appear as a darker area.

As the electrons from the incident SEM beam interact with the sample, they will displace some inner shell electrons in the atoms of the observed sample. Electrons from outer shells will drop down to fill these holes, releasing energy in the form of X-rays in the process (Figure 2.4). These X-ray are characteristic of the energy gap between the electron shells and are therefore characteristic of the atom they originated from. The energy of these X-rays can be collected with an EDS spectrometer and enable semi-quantitative chemical compositional analysis of a targeted area (Atkins *et al*. 2010).

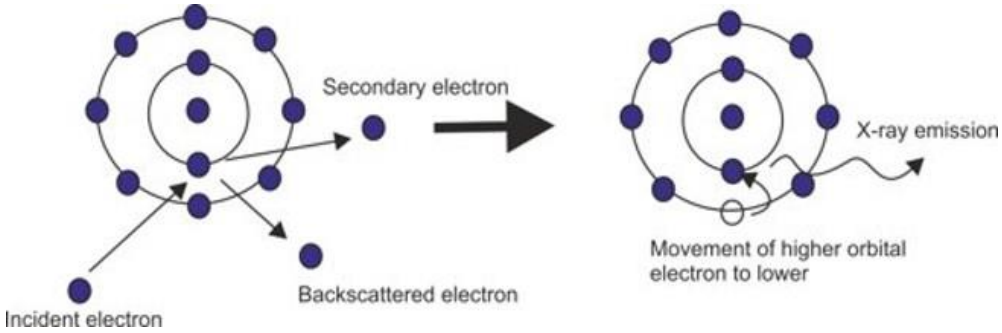


Figure 2.4: Diagram illustrating the process of X-ray emission from an atom during observation with an incident beam of electrons in an SEM or EPMA.

The SEM instrument used throughout this project was a FEI Quanta600 SEM, equipped with SE and BSE detectors and an Oxford Instruments EDX detector. It was also equipped with Mineral Liberation Analyser (MLA) software. Various conditions were used, ranging from an accelerating voltage of 10 – 20 keV, a spot size of 3 -7, with a working distance of 13 mm. Lower beam energies and smaller spot sizes allow for higher resolution imaging, whereas higher beam energies and larger spot sizes are required for EDS and MLA. A working distance of 13 mm is the optimum set-up for EDX detection in this particular instrument. To determine the error associated with the MLA, one of the starting samples (B1_HPnoCa pre) used in Chapter 4 was analysed 3 times under the same set-up conditions. This resulted in an observed 5% error in the resulting area abundance values of the detected minerals.

2.3 Mineralogical Analysis of Rock Samples

2.3.1 Powder X-ray Diffraction Analysis

Powder X-ray Diffraction (PXRD) is a technique used to identify different phases in a crystalline sample, as each phase results in a different diffraction pattern and the relative amounts of each phase present in the sample can be determined (Atkins and De Paula 2010b). Diffraction is a result of interference between waves being scattered by electrons in atoms, which gives a pattern reflecting the separation of those atoms within a crystal. Scattering can be thought of as reflection from two adjacent parallel planes of atoms, separated by a distance d (Figure 2.4), with the angle at which constructive interference occurs between waves of wavelength λ given by Bragg's Equation (2.1):

$$2dsin\theta = n\lambda \qquad (2.1)$$

In the above equation, n is an integer. This means when an X-ray beam is directed at a crystal with an ordered array of atoms, a set of diffraction maxima which combine to be known as a diffraction pattern is produced. Each maximum (reflection) occurs at an angle θ corresponding to a different separation of planes of atoms, d, in that particular crystal. This theory is illustrated in Figure 2.5 (Atkins *et al*. 2010).

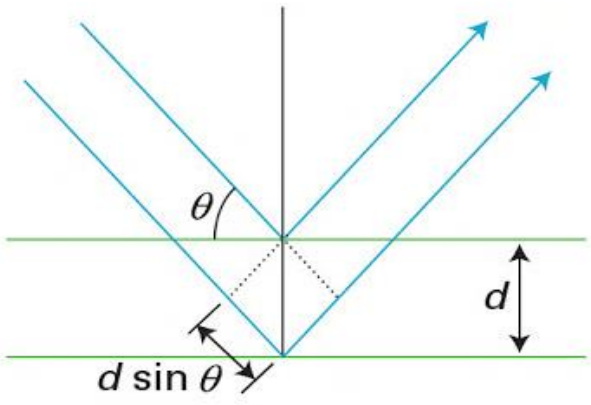


Figure 2.5: Schematic representation of Bragg's equation.

An atom will scatter the X-rays in proportion to the number of electrons it has, and the square of that number is then proportional to the intensities of the diffraction maxima. This means the obtained diffraction pattern is characteristic of the positions and types of atoms present in the crystal and measurement of the X-ray diffraction angles and intensities provides structural information (Atkins *et al*. 2010). Powdered rock samples are polycrystalline and contain large numbers of small crystals orientated at random. In PXRD, the X-ray beam is scattered in all directions by the sample and at some angles constructive interference occurs, given by Bragg's law (6). The diffractometer measures the angles of the diffracted beams using an electronic detector, which scans around the sample, and the intensity of the detected X-rays is recorded as a function of the detector angle. In the rock samples used in this report, each crystalline phase contributes a unique set of diffraction angles and intensities to the diffraction pattern. This method is typically sensitive enough to detect as low as 5% by mass of a particular crystalline compound in a mixture (Atkins *et al*. 2010).

The PXRD instrument used throughout this project is an X'Pert PRO PANalytical MPD X-ray diffractometer, with normal Bragg-Brentano geometry and CuKα radiation at 40 kV and 40 mA. 20 mm sample size holders were used, and the bulk powder samples were prepared by pressing the appropriate amount of sample into the holder. The samples were scanned over a sampling range of 5 and 70^{o}2θ with a step size of 0.0066 and a scan speed of 0.23^{o} 2θ per second.

For analysis of the clay suspension, 700 µL of the suspension was evenly distributed onto a circular glass disk with a 20 mm diameter that matched the PXRD sample holders and left to dry overnight to leave the solid clay layer behind. Three drops of acetone were dropped onto each disk with the suspension before drying to prevent curling of the sample.

Two clay treatments were performed to distinguish between different mineral patterns. A glycol treatment was used to distinguish between possible illite and smectite peaks (Patarachao *et al*. 1999). Using the samples previously used for clay analysis, 4 drops of glycol solution were dropped evenly onto the samples with a pipette. This was left for a couple of hours to reach partial dryness and then run on the PXRD machine. A second treatment involved using mild HCl to distinguish between chlorite and kaolinite peaks (Biscaye 1964). Chlorite will dissolve in mild HCl but kaolinite will not. The HCl treatment preparation is described in Section 2.1.2. The resulting suspension was then prepared for PXRD analysis the same way as the untreated clay sample.

As well as comparison to published literature for individual minerals, the XRD software DIFFRAC.EVA (Eva) was used to analyse the data, with access to a powder diffraction files reference database (PDF4+) (ICDD 2018) containing diffraction data for hundreds of thousands of materials. The software compares the sample diffraction pattern data to the database and gives a list of suggested phase patterns and the preferred phase assignment can then be selected. Many minerals have polymorphs, meaning they have the same chemical formula but different structures, so careful consideration is needed to match the reference patterns to the sample as accurately as possible. Once assigned, semi-quantitative phase analysis based on reference intensity ratios (RIR) values can be performed (XRD DIFFRAC.EVA: Quick Start Guide 2013). The RIR method scales all diffraction data to an international standard, which by convention is corundum. The scale factor is defined by: Intensity Analyte / Intensity Corundum = I/Ic

The atomic parameters of corundum have been determined, and in the PDF4+ database the I/Ic has been calculated for more than 170,000 materials (Snyder 1992). Natural minerals contain impurities, anion/cation substitutions and other defects, known to influence peak intensities which can slightly change I/Ic values. When extracting I/Ic values and peak areas, Eva assumes all phases have been identified and add up to 100%, meaning errors may occur

if unidentified materials are present. Alongside matrix effects influencing the intensities of different minerals, this means this method is considered a semi-quantitative analysis technique.

2.4 Geochemical Analysis of Rock Samples

2.4.1 X-ray Fluorescence Analysis

X-ray Fluorescence (XRF) can be used to determine the elemental composition of a sample. The process is non-destructive, measuring the secondary X-rays emitted from a sample excited by a primary X-ray source. In this process, a sample is irradiated with high energy X-rays. When these strike an atom in the sample with energy greater than that atom's K or L shell binding energy, an electron from an inner orbital shell of the atom will be ejected. The atom is then unstable, so an electron from a higher energy shell drops down to fill the vacancy. This process releases a fluorescent X-ray, equal to the difference in the energy gap between the outer shell and the inner shell the electron dropped down into. This energy can be measured using XRF spectroscopy and is characteristic of that particular atom. The intensity of the peak produced is proportional to the amount of that atom in the sample, so quantitative results are obtained (Atkins and De Paula 2010a).

For this project, the elemental composition of the powder samples was examined by XRF analysis, using an Epsilon 3 XL High Performance benchtop Energy Dispersive X-ray Fluorescence Spectrometer System, operated by a colleague, Dr. Teresa Needham, in the School of Geography. A range of elements were analysed, including those expected in volcanic rock types such as calcium, potassium, silicon, aluminium, sulphur and several other commonly occurring metal elements.

2.4.2 Microprobe Analysis

Electron Microprobe analysis (EPMA) is primarily the same as SEM and can be used to obtain qualitative and quantitative elemental detail of a solid sample. A focussed electron beam is targeted on the area of interest, to yield X-rays from a sample, with small 'spot' sized down to a few microns in diameter making precise analysis of targeted minerals in a sample accessible. A faraday cup also enables close control of a stable beam current. X-rays are generated as a result of inelastic collisions of the incident electrons from the focussed beam, with electrons in the inner shells of the atoms in the sample, which are ejected to leave a vacancy, with X-rays released as a higher-shell electron drops down to fill this vacancy (Figure 2.4). The resulting X-ray spectrum contains lines characteristic of the elements present. EPMA used wavelength dispersive spectroscopy (WDS) techniques, rather than energy dispersive techniques used in EDX analysis. The wavelength of the resulting X-rays are separated by diffraction using analysing crystals with matching d-spacing between the crystal planes. The orientation of the sample, the analysing crystal and the X-ray detector are arranged in a specific way to lie on what is known as 'The Rowland Circle', to ensure only the X-rays of the correct wavelength (depending on which element has been chosen for analysis) are diffracted and therefore collected by the detector (Figure 2.6). By comparing the intensity of the collected X-rays to a known standard, the concentration of the elements can be determined, with an accuracy approaching ±1% and detection limits down to tens of parts per million (by weight). Two dimensional 'maps' can be obtained using a colour scale representing elemental concentrations from the spatial distributions of specific elements (Reed 2005). This technique can be used on polished flat samples, such as thin sections of resin embedded samples, to give geochemical detail on targeted mineral phases.

The chemical composition of the mineral phases of interest in the sample thin sections and resin embedded samples was determined using Microprobe analysis. Standard wavelength dispersive techniques were conducted using a JEOL JXA-8200 electron microprobe, with a

15.0 kV, 20 nA electron beam and a working distance of 11 mm. The samples were carbon coated to a thickness of 15 nm prior to conducting this analysis using an Edwards Evaporation coater.

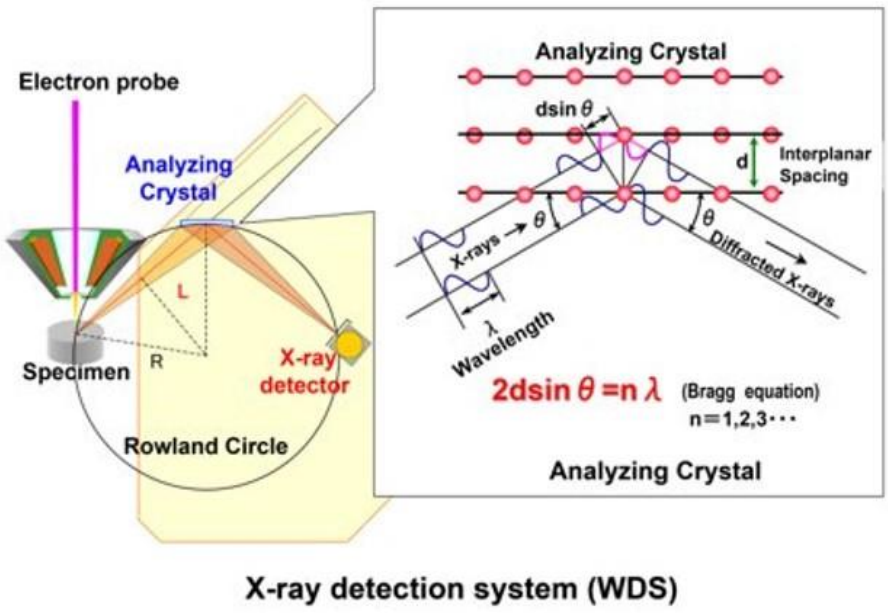


Figure 2.6: Diagram illustrating the orientation of the sample, analysing crystal and X-ray detector used for WDS analysis with EPMA, and a schematic describing the diffraction of selected wavelength X-rays using an analysing crystal (image from: Electronic microprobe JEOL JXA-8230 | ISTerre).

2.5 Experimental Set-up

2.5.1 Batch Reactor Experiments

Batch reactor experiments can be set-up in a number of ways and are usually used for systems with relatively long reaction times (Al Mesfer 2018). The simplest form involves a vessel to hold the reactants and possibly a stirring and heating mechanism, such as a hotplate with magnetic stirring capacity. More sophisticated apparatus may be used to reach higher temperatures or if precise stirring speeds are needed. The vessel may be sealed, if more control is needed over the air space, and be made of chemical resistant materials to avoid contamination or safety risks.

For high temperature batch reactor experiments that do not include increased pressures via gas injection, stainless steel batch reactors that can be sealed in a temperature-controlled oven are used. The reactors have sealed Teflon inserts to prevent contamination from fluid contact with the steel. The total volume of these inserts is 20 mL, however the maximum fluids used it 15 mL, to ensure there is sufficient headspace for gas evolution in experiments with increased temperatures. High fluid to solid ratios are used (relative to real geothermal reservoir systems), mainly 0.15 g of sample with 15 mL of fluid, to ensure reactions take place on a useful timescale for research purposes. Working with higher fluid to solid ratios is commonly known to result in some differences when compared to real reservoir conditions. For example, a higher ratio may increase the time it takes for the reaction to reach equilibrium conditions, whereas a very low ratio would not result in enough reaction products to be effectively measured with the analysis equipment available for this project. A 1:100 rock:fluid ratio was used as a compromise between these scenarios. A series of these experimental set-ups allow variations in temperature, time and fluid composition to be compared.

To examine the progress of a reaction and assess reproducibility, multiple reactors with the same initial set-up and compositions are placed in the controlled oven at the same time, then incrementally removed over the duration of the total experiment time, with sampling of the fluids and solids from one reactor yielding one sample and therefore one data point in each experiment series. All these reactions were duplicate as precisely as possible, enable some error margins to be calculated. The fluids are examined at the beginning of each experiment before contact with the rock sample, as well as throughout the experimental duration, to examine the compositional changes happening within the fluids as a result of rock-fluid interactions. A 'blank' run is always conducted, with no rock sample added, to examine background changes that may occur in the fluids as a result of the experimental conditions. When collecting a sample, the fluids are collected through 0.22 μm PES filters, to ensure no small particulates suspended in the solutions are collected and subsequently dissolve in the fluids before analysis, which would affect the chemical composition results. The solids are collected by washing into tubes and centrifuged at 4500 rpm for 20 minutes, and then dried in a 50^{o}C oven for 3 days before analysis,

In this project, the fluids are designed based on data provided by PT. Supreme Energy on the fluid composition of an active geothermal well (Table 3.1 in Chapter 3). The temperature, pH and salinity are varied to look at different dissolution/precipitation reactions that take place under these variations. Solid samples are analysed before and after reaction using a range of techniques discussed in previous Sections and the fluid samples by Inductively Coupled Plasma Optical Emission Spectroscopy (ICP-OES) and measurement of the pH.

2.5.2 High Pressure CO_2 Experiments

The batch reactor systems described above can be used to investigate a range of experimental conditions, however they are limited in their ability to investigate reactions at increased pressures. Since real geothermal systems are at increased pressures in the subsurface it is important to be able to investigate this variable. Specifically, we are interested

in the interactions taking place when injecting dissolved carbon dioxide, therefore a batch reactor system with the ability to inject CO_2 at increased pressure alongside increased temperatures has been used in this project.

The high-pressure system is a batch reactor method, as there is no aspect of flow in the system. The system comprises a Hastelloy reaction vessel, with all parts in contact with fluids also made of Hastelloy from Parr Instruments, except the sampling tube which was added in house and made from steel tubing and valves from Swagelock, as shown in Figure 2.7. It was found that the steel sampling tube effected the iron content of the fluids, as detected by ICP-OES, so these values cannot be used to obtain accurate findings from the experiments if the fluid has contact with the outlet tubing. The vessel has a total capacity of 450 mL, with the max fluid level of 300 mL before any pressure is added. The experimental fluids used are prepared in the same way as those described in Section 2.5.1. Experiments were run using pieces of rock with an approximate surface area of 0.5 – 1 cm^2, which were embedded in epoxy resin and polished to a 1 µm finish using a Strurers Automated polisher and diamond suspensions. Details of the specific experimental conditions can be found in Chapter 4. To set-up an experiment, the resin embedded sample was added to the reaction vessel, with 300 mL of experimental fluid added before sealing. Mechanical stirring was first started, consistently on setting 1 of the integrated Parr stirring system. Once sealed and connected, the vessel was flushed 3 times with 10 bar CO_2 to minimise oxidative impacts form the air and simulate deep subsurface conditions. To commence and experiment, the vessel was heated externally with the desired temperature set via the control panel, and the system temperature was monitored using a thermocouple from within the vessel interior, mechanical stirring was applied, set at pre-set value of 1 on the integrated Parr Stirring system. As the temperature slowly increased, the pressure was slowly increased incrementally via the inlet valve 2 (V2) (Figure 2.7) of the system the desired final pressure for the experiments was achieved.

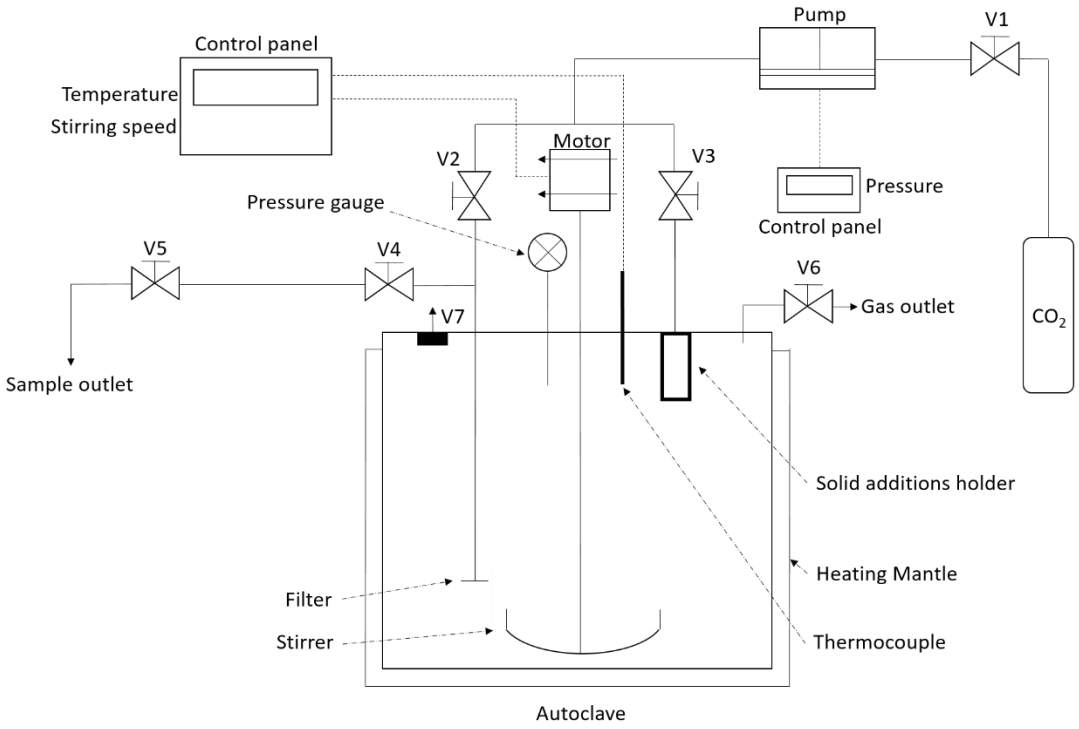


Figure 2.7: Schematic of the high-pressure batch equipment used in this project. V1-V6 are needle valves and V7 is a burst disk exit valve. The system is designed so the pressure flow moves from the CO_2 cylinder towards the autoclave. The sample dip tube ends in a filter, with either pressurised CO_2 moving through this in the autoclave via inlet V2, or experimental fluid moving from the autoclave to the sample outlet system via V4. The pressure is set using the pressure control panel and the pressure inside the autoclave is monitored with the pressure gauge. The stirring speed and temperature are set and monitored via the relevant control panel, which is electronically connected to the heating mantle, thermocouple and motor. The whole autoclave can be removed from the heating mantle, the sample outlet tube can be removed independently via a Swagelock joint of the right hand side of V4, and the whole autoclave 'lid' can be removed from the base vessel to allow experimental fluid to be added prior to set-up and removed when the experiment is terminated.

The fluids are sampled at timed intervals throughout the experimental durations. A sample of fluid is collected before any contact with the vessel and therefore, before any heating or

pressure conditions have been applied. A fluid samples is then also collected through the sampling tube as soon as desired pressure and temperature are achieved. An experiment is sampled several times throughout the experimental duration via the sampling tube. During each sampling process, approximately 1 mL of fluid is first removed and discarded, to minimise the possibility of sampling any residue that may have sat in the sampling tube system rather than the reaction vessel since the previous sampling time. A second amount of fluid of approximately 2 mL in volume is then removed to be used as the experimental fluid sample. After sampling, 2 drops of concentrated HNO_3 is added to to prevent any solid precipitation and the samples are then stored in sealed tubes until measurements are conducted using ICP-OES. At the end of each experiment, a final sample is taken using this same sampling method. Then stirring is stopped and the heating system is switched off. The vessel is left to decrease to a temperature capable of handling, during which time a small pressure decrease was often observed. The pressure in then released in a controlled manner via the release V6. The vessel is dismantled, and the fluids are sampled directly from the vessel through a 0.22 µm PET filter. The rock sample was extracted from the vessel, gently washed with MQ water, and then dried under atmospheric conditions until use for analysis.

2.6 Fluid Analysis

2.6.1 pH measurements

Measuring the pH of the fluids from batch reactor experiments, both before and after, can give an indication that some reaction is taking place within the system. For example, if the starting pH of the fluid is acidic, and the fluid samples extracted throughout the experiment indicate the pH of the fluids has moved closer to neutral values, this would suggest some mineral dissolution has taken place to consume the excess H^+ ions. It is also important to measure the starting pH, if aiming to create an acidic solution to set-up the experimental series by adding small amounts of concentrated acid, to ensure the desired pH is achieved.

For this project an electronic Accumet AE150 benchtop pH meter was used to measure the pH of all the solutions, which requires approximately 1 mL minimum of solution. The pH probe was washed with MQ water between every solution measurement to avoid contamination. Three buffer solutions of fixed pH values 4, 7 and 10 were measured at the start of each use of the pH meter for calibration. For the experiments described in this thesis, the pH could not be measured directly in situ. Instead, the fluid sample was collected, and the pH measured as quickly as possible. The measured fluid sample will therefore have experienced a drop in temperature and pressure conditions compared to the in-situ conditions, which may impact the pH due to CO_2 degassing. This effect is discussed in more detail in Chapter 5.

2.6.2 Inductively Coupled Plasma – Optical Emission Spectroscopy

Inductively coupled Plasma – Optical Emission Spectroscopy (ICP-OES) is an analytical technique used to examine the chemical composition of a sample. The high temperature of the ICP is used to excite the elements in the sample, which emit light at a wavelength characteristic of each element so the composition of the sample can be accurately determined.

An ICP-OES works by flowing argon gas through a narrow quartz tube wrapped in a metal coil. A current is passed through this coil, which induces a strong magnetic field, and a spark then starts the ionization process of the argon gas to form the plasma. The temperature can reach 7000 – 10,000 K, which means even the atomization of stable oxides can take place. Electrons within the atoms of the sample are excited to higher level orbitals, which then release a photon corresponding to the energy gap between the orbitals when the electron drops back down to the original orbital. This gives a characteristic emission wavelength of a particular transition in a particular element, which is detected within the ICP-OES equipment. The intensity of the emission is directly proportional to the amount of that species present, so the concentration of that species in the original solution can be determined. Calibration standard solutions are prepared with known concentrations of each element of interest and measured on the ICP-OES equipment first to create calibration curves. When the samples are then measured, the resulting emission intensities are compared to these calibration curves to determine the concentration of each analyte in the sample solutions (Burrows *et al*. 2013).

As the creation of calibration curves are required to determine the concentrations of the elements in solutions, the measured concentrations are accurate only within the range of these calibration standards and also within the detection limits of the equipment itself. Throughout this project, calibration standards from 0.1 to 30 mg/L are made from a 100 mg/L Fischer Scientific MultiElement Standard chemical mix, for the elements Si, Al, Na, K, Ca, Mg and Fe. It is common for the expected concentrations of some of the elements within the sampled fluids to exceed this 30 mg/L limit by various magnitudes, therefore a series of dilutions of the samples are made to be measured alongside the original undiluted samples. The samples are diluted using 2 % HNO_3 solution, made from ultrapure MQ water and Trace metal grade pure HNO_3 sourced from Sigma Aldrich. Air displacement pipettes are used to create accurate dilutions of the sample solutions, commonly by factors of 1/1000, 1/100 and 1/10. A Perkin Elmer ICP-OES was used to conduct elemental analysis on the experimental fluids throughout

this project. The instrument has a detection limit of 0.1 mg/L and analytical uncertainties within the order of ≤5%. No anion concentrations were analysed in this project, as this requires a series of titration experiments to be conducted, which need several mL of additional experimental fluid to be extracted, which was not feasible with the scales used in this project.

2.7 Gas Adsorption Techniques

2.7.1 BET Analysis

BET (Brunauer-Emmett-Teller) theory allows calculation of the specific surface area of a sample by calculating the amount of an adsorbed gas corresponding to a monolayer on the surface of a sample. The BET adsorption isotherm equation is as follows (Equation 2.2) (Brunauer 1943):

$$\frac{1}{\left[V_a\left(\frac{P_0}{P}-1\right)\right]} = \frac{C-1}{V_m C} \times \frac{P}{P_0} + \frac{1}{V_m C} \tag{2.2}$$

Where P is the partial pressure of adsorbed gas in equilibrium with the surface at 77 K, P_0 is the saturated vapour pressure of adsorbed gas, V_a is the volume of gas adsorbed at standard temperature and pressure (STP), V_m is the volume of gas adsorbed at STP to produce an apparent monolayer on the sample surface and C is a dimensionless constant related to the enthalpy of adsorption of the adsorbate gas on the sample (Brunauer 1943). The BET equation is plotted as an adsorption isotherm, usually at relative pressure (P/P_0) between 0.05 and 0.35, which should give a straight line. The monolayer capacity (nm) is found by (Equation 2.3):

$$nm = \frac{1}{gradient - intercept} \tag{2.3}$$

And the BET constant C is found via (Equation 2.4):

$$C = 1 + \frac{gradient}{intercept} \tag{2.4}$$

The surface area (S_{total}) can be calculated using the molecular cross-sectional area, S (Equation 2.5):

$$S_{total} = \frac{nmNs}{V} \tag{2.5}$$

Where *N* is Avogadro's number and *V* is the molar volume of the adsorbed gas (Brunauer 1943).

Nitrogen adsorption experiments are run on a 3flex surface characterisation analyser from Micromeritics was used to measure the adsorption isotherms. The samples are first degassed overnight under vacuum at 100^{o}C and the dry weight obtained. Analysis is performed at 77 K, achieved by submerging the sample tubes in liquid nitrogen for the duration of the experiment. The sample tubes are dosed with a precise amount of nitrogen gas, equilibrium is achieved, and the changing mass is measured. This process is repeated until a relative pressure (p/p_o) of 0.99 is reached and the adsorption isotherm is collected. The reverse process is then initiated, and the sample tube is incrementally evacuated to obtain the desorption isotherm.

2.7.2 Water Adsorption Isotherms

Conducting water adsorption experiments produces adsorption isotherms which describe the equilibrium relationship between the partial pressure of the adsorbate and the amount adsorbed at a constant temperature. The shapes of the resulting isotherms depend on the chemical composition and physical structure of the adsorbent. Looking at isotherms produced from water adsorption experiments (discussed further in Chapter 6) can therefore give various clues about the mineralogy of a sample. For example, if a sample contains certain types of clay, it will be able to adsorb a lot more water than an otherwise similar sample without clay, as discussed in Chapter 1, Section 1.5.

For the water adsorption experiments, a 3Flex surface characterisation analyser from Micromeritics was used to measure adsorption isotherms using dynamic vapour sorption. This technique measures the changing mass of a sample at a constant temperature as a result of changing humidity. The sample is first degassed overnight under a vacuum at 100^{o}C and the dry weight obtained. The sample tube is then fitted to the 3Flex machine and submerged in a temperature-controlled water bath. The machine doses precise amounts of water vapour into

the tubes, allows equilibrium to be reached and measures the mass. This process is repeated until a relative pressure (p/p_o) of 0.90 is reached. The reverse process is then initiated, and the sample tube is incrementally evacuated to obtain the desorption isotherm. Further details describing the processes needed to optimise this equipment for water adsorption experiments (compared to nitrogen BET analysis) are described in Chapter 6.

2.8 References

Atkins, Peter, Tina Overton, Jonathan Rourke, Mark Weller, and Fraser Armstrong. 2010. "Physical Techniques in Inorganic Chemistry." Pp. 223–54 in *Shriver and Atkins' Inorganic Chemistry*.

Atkins, Peter, and Julio De Paula. 2010a. "Catalysts." Pp. 876–906 in *Atkins' Physical Chemistry*. Oxford University Press.

Atkins, Peter, and Julio De Paula. 2010b. "Materials 2: Solids." Pp. 695–742 in *Atkins' Physical Chemistry*. Oxford University Press.

Barber, A. J., M. J. Crow, and J. S. Milsom. 2005. *Sumatra: Geology, Resources and Tectonic Evolution*. Vol. 31. London: The Geological Society.

Biscaye, Pierre E. 1964. "Distinction between Kaolinite and Chlorite in Recent Sediments by X-Ray Diffraction." *The American Mineralogist* 49:1281–89.

Brunauer, Stephen. 1943. *The Adsorption of Gases and Vapors Volume 1*. Oxford University Press.

Burrows, Andrew, John Holman, Andrew Parsons, Gwen Pilling, and Gareth Price. 2013. "Analytical Chemistry." Pp. 545–47 in *Chemistry*^{3}. Oxford: Oxford University Press.

Gruszkiewicz, Miroslaw, Juske Horita, John M. Simonson, and Robert E. Mesmer. 2000. "High-Temperature Adsorption on Geothermal Reservoir Rocks." in *World Geothermal Congress*. Tohoku, Japan.

ICDD. 2018. *PDF-4*. International Centre for Diffraction Data.

Keppert, Martin, Jaromír Žumár, Monika Čáchová, Dana Koňáková, Petr Svora, Zbyšek Pavlík, Eva Vejmelková, and Robert Černý. 2016. "Water Vapor Diffusion and Adsorption of Sandstones: Influence of Rock Texture and Composition." *Advances in Materials Science and Engineering* 2016:1–7. doi: 10.1155/2016/8039748.

MacKenzie, W. S., and A. E. Adams. 1994. *A Colour Atlas of Rocks and Minerals in Thin Section*. 2nd ed. Manson Publishing Ltd.

Al Mesfer, Mohammed K. 2018. "Experimental Study of Batch Reactor Performance for Ethyl Acetate Saponification." *International Journal of Chemical Reactor Engineering* 16(1).

Muraoka, Hirofumi, Masaaki Takahashi, Herry Sundhoro, Sjafra Dwipa, Yoshio Soeda, Manabu Momita, and Kanichi Shimada. 2010. "Geothermal Systems Constrained by the Sumatran Fault and Its Pull-Apart Basins in Sumatra, Western Indonesia." Pp. 25–29 in *World Geothermal Congress 2010*. Bali, Indonesia.

Patarachao, B., D. D. Tyo, A. Zborowski, K. Davis, J. Kung, S. Ng, and P. H. J. Mercier. 1999. "XRD Analysis of Illite-Smectite Interstratification in Clays from Oil Sands Ores." *Advances in X-Ray Analysis* 62:22–31.

Pichler, H., and C. Schmitt-Riegraf. 1997. *Rock-Forming Minerals in Thin Section*.

Reed, S. J. B. 2005. *Electron Microprobe Analysis and Scanning Electron Microscopy in Geology*. 2nd ed. Cambridge University Press.

Santoso, Djoko, M. Emmy Suparka, Sayogi Sudarman, and Surahman Sauri. 1995. "The Geothermal Fields in Central Part of the Sumatra Fault Zone As Derived From Geophysical Data." Pp. 1363–66 in *World Geothermal Congress, 1995*. Florence, Italy.

Sieh, Kerry, and Danny Natawidjaja. 2000. “Neotectonics of the Sumatran Fault, Indonesia.” *Journal of Geophysical Research* 105(B12):28295–326. doi: 10.1029/2000JB900120.

Snyder, Robert L. 1992. “The Use of Reference Intensity Ratios in X-Ray Quantitative Analysis.” *Powder Diffraction* 7(4):186–93.

Woodruff, W. F., and A. Revil. 2011. “CEC-Normalized Clay-Water Sorption Isotherm.” *Water Resources Research* 47(May):1–15. doi: 10.1029/2011WR010919.

XRD DIFFRAC.EVA: Quick Start Guide. 2013. “XRD DIFFRAC.EVA: Quick Start Guide.”

Chapter 3: Interaction of andesitic geothermal reservoir rocks with neutral and acidic fluids at 100°C to assess cation release extent.

The coded Phreeqc input files used to obtain the geochemical modelling results in this chapter were implemented by a colleague, Dr Hossein Fazeli. The ideas for the design of these codes and all experimental results and combined subsequent analysis and discussions point were conducted by this thesis author.

3.1 Introduction

CO_2 emissions have been increasing over the last century and much of the scientific community agrees this is a direct result of human activities (Department of Energy and Climate Change, 2016; Edenhofer *et al*., 2014; McCarthy *et al*., 2001). Therefore, it is widely accepted that we need to switch our reliance to renewable energy sources, as well as finding ways to capture and store excess CO_2 to prevent global temperatures rising above 1.5^{o}C, compared to pre-industrial levels (IPCC, 2018).

Geothermal energy is a renewable energy source that is successfully being exploited for heat and electricity generation in many areas of the world, however as discussed in Section 1.2.4, there are some challenges associated with CO_2 release from these reservoirs. Several laboratory scale (see Section 1.4.3) and two field scale (see Section 1.4.4) studies have examined the possibility of injecting CO_2 into subsurface basaltic systems. The field scale studies reported successful sequestration within 2 years of injection (Matter *et al*., 2016; McGrail *et al*., 2017b). Sequestration occurs as a result of solid carbonate mineral formation, when the dissolved carbonate anion combines with divalent cations released due to mineral dissolution from the rocks. as illustrated in equation 3.1 (Gislason *et al*., 2010; Hangx and Spiers, 2009; Matter *et al*., 2007; McGrail *et al*., 2006).

$$(Ca,Mg,Fe)^{2+} + CO_2 + H_2O \leftrightarrow (Ca,Mg,Fe)CO_3 + 2H^+ \quad (3.1)$$

The production of solid carbonate minerals also produces acidity in the form of H^+ ions (equation 3.1), which need to be consumed for the reaction to proceed to the right at a desired rate for carbon sequestration. Mafic rocks such as basaltic systems have a high neutralisation capacity, as they provide alkaline earth elements on dissolution, which can then in turn form further carbonate minerals (Matter *et al*., 2007).

However, this basaltic rock type is not available in all regions where geothermal energy is exploited. Volcanic rocks across the world vary in composition, with andesite type a common occurrence (Sugisaki, 1972) which is often associated with areas of high geothermal energy potential (BP, 2020). For example, large areas of Indonesia, rich in geothermal energy resources (Sawin *et al*., 2017), have reservoir systems of andesitic composition (Boedihardi *et al*., 1993; Purnomo and Pichler, 2014).

There is a plethora of studies which have investigated the dissolution of basaltic rocks in relation to carbon sequestration, including but not limited to: Clark *et al*. (2019), Galeczka *et al*. (2014), Gysi and Stefánsson (2011), Matter *et al*. (2007 and 2016), McGrail *et al*. (2017b), Rosenbauer *et al*. (2012), and Shibuya *et al*. (2013). Limited research has been conducted on the possibility of using mineral trapping techniques demonstrated to be successful in basaltic systems, in other rock types. Some laboratory studies have investigated reactions between acidic fluids and a range of volcanic glass samples, such as in Icelandic geological samples (Wolff-Boenisch *et al*., 2006, 2004) and more widespread examples (Marieni *et al*., 2018). Results from these studies indicate glasses with a higher silica content have slower dissolution rates than those with a lower silica content, therefore some predictions can reasonably be made about the behaviour of rocks with a similar chemical composition. However, research needs to be conducted using samples with a higher silicate content and different levels of crystallinity in relation to cation release on mineral dissolution. These studies also focussed on either ambient temperature ranges or much higher (>250^{o}C) temperatures and pH values of 4 or higher. Those studies do give some indication that carbon sequestration in andesite compositions is likely to be feasible but expanding experiments to cover a wider range of

conditions should be conducted to be able to make more accurate predictions about a wider range of naturally occurring conditions. Another study has used samples of andesite and rhyolite composition to investigate the dissolution characteristics of these rocks with CO_2 in solution (Takaya *et al*., 2015). They conclude andesite rocks hold promise as CO_2 sequestration sites and indicate further research with similar samples should be conducted to examine this in more detail. Research needs to be undertaken to overcome this knowledge gap, investigating the dissolution behaviour of andesite samples in relation to cation release for carbon sequestration, particularly at elevated temperatures found in geothermal systems. The objectives of the present study are to (1) investigate the geochemical reactions that occur between rocks of andesite composition and fluids representative of those found in associated geothermal reservoirs, where experimental fluids are made acidic with the addition of HCl, to determine whether cation release from the samples is likely to be significant and (2) discuss the implications these interactions may have, based on cation release by fluid-andesite interactions, on the possibility of implementing techniques in carbon sequestration by mineral formation after reinjection of dissolved CO_2 in geothermal fluids.

3.2 Materials and Methods

3.2.1 Materials

Samples used in this study are taken from a geothermal field located in the Rantau Dedap region of Sumatra, Indonesia. The Sumatra Island formed by the subduction of the Sundaland Continental Plate with the India-Australia Oceanic Plate. Tectonic stress from the subduction has created the dextral strike slip faults that cross parallel to Sumatra Island, known as the Great Sumatra Fault (GSF). Besides the GSF, this subduction has also led to a volcanic arc, causing earthquakes and forming the geothermal prospects in Sumatra Island and the elevated temperature conditions of interest here (Muraoka *et al*., 2010; Santoso *et al*., 1995). According to Sieh and Natawidjaja (2000), the GSF has a length of 1900 km, consists of 19 segments of dilatational step over, with a length of 90 to 120 km for each segment. The mineralogy of the area is generally found to be of andesitic volcanic composition (Barber *et al*., 2005). This is consistent with drilling results, where these Quaternary-aged andesitic-basaltic volcanic rocks are sampled from the surface until the top of the reservoir section. The reservoir section itself consists of Tertiary-aged mixed marine sediment with layer of silicic and andesitic volcanic rocks. Three rock core samples from the geothermal field in Sumatra were provided by PT Supreme Energy for this study. The samples B1, C1 and I1 are from exploration wells taken from approximately 1 to 2 km depth (Supreme Energy personal communication, 2017).

3.2.2 Preparation and Characterization

Multiple pieces of rock were separated from the main cores and crushed to create the powder samples used in this study. The percent composition of the clay fraction (particles ≤ 2µm) of each sample was determined using an aqueous dispersion and centrifugation method and an acid treatment of each sample was conducted to assist in differentiating between chlorite and kaolinite peaks in the Powder X-ray Diffraction (PXRD) patterns (Biscaye, 1964).

Mineralogical phase identification by PXRD was completed on an X'Pert PRO PANalytical MPD X-ray Diffractometer. Normal Bragg-Brentano geometry and CuKα radiation at 40 kV and 40 mA was used with sample holders of 20 mm diameter and samples were scanned over a sampling range of 5 to 70 $^{o}2\theta$ with a step size of 0.0066 and a scan speed of 0.23 $^{o}2\theta$ per second. The bulk powder samples were pressed into 20 mm holders for analysis. For the clay experiments, 700 µL of each clay suspension was pipetted onto 20 mm glass disks with 2 drops of acetone and left to dry overnight, before placing in sample holders for analysis. For phase identification and semi-quantitative analysis, the PDF4 (ICDD, 2018) database was used within the software DIFFRAC.EVA to identify the mineral peak patterns.

The elemental composition of the powder samples was examined using X-ray Fluorescence (XRF) analysis using an Epsilon 3 XL High Performance benchtop Energy Dispersive X-ray Fluorescence Spectrometer System.

Nitrogen BET analysis was completed on a Micromeritics 3flex Surface Characterisation Analyser at 77 K and partial pressures from 0 to 0.99, to calculate the surface area of the samples. Prior to analysis, the powder rock samples were degassed overnight at 100^{o}C. The surface area of B1 was found to be 1.1 ±0.1 m^2/g, that of C1 1.7 ±0.1 m^2/g and that of I1 1.8 ±0.1 m^2/g.

A 30 µm thin section of each sample was observed using a Carl Zeiss Axio Scope A1 optical microscope with both reflective and transmitted light modes and polarising filters situated above and below the sample stage. Images were obtained using a Zeiss Axiocam ERc camera to gain textural and mineralogical information on each of the samples.

The chemical composition of the mineral phases in the thin sections was determined from standard wavelength dispersive techniques using a JEOL JXA-8200 electron microprobe. A 15.0 kV, 20 nA electron beam was used with a working distance of 11 mm. Prior to this analysis, the thin sections were coated with a 15 nm layer of carbon.

3.2.3 High Temperature Batch Reactor Experiments

Stainless steel batch reactors with 25 mL capacity Teflon inserts were filled with 15 mL of fluid and 0.1500 g (weighed accurately on a 4-Figure balance) of powder rock sample (1:100 rock to fluid ratio) then sealed. Fifteen duplicates of this reactor set up were placed in a 100^{o}C oven at the start of each experiment. One reactor was removed to give one individual sample over the course of fifteen days to monitor the progress of the reaction. The fluid pH's were measured at room temperature, which may have resulted in a slight increase in pH compared to that which would be measured in the sealed vessel, as the evolution of some CO_2 from the fluids as the vessel is opened would reduce the acidity. However, this effect is expected to be minimal so it was not seen as an issue for the subsequent data analysis and the pH of the fluids could physically not be measured in the sealed vessel. The fluids were collected through 0.22 µm PES filters and the solids were dried at 50^{o}C for two days. The fluids used in each experiment were designed to simulate geothermal formation waters of the geothermal well. Geochemical data on the composition of these well fluids was provided by PT Supreme Energy, a subset of which is displayed in Table 3.1. The data indicates the fluids are of meteoric origin, with relatively low total dissolved solids and a low salinity.

Table 3.1: Elemental compositions of fluids provided by Supreme Energy PT., alongside the composition of the fluids designed for this study. Field pH measured for Well A is 6.50, field pH measured for well B is 7.07.

Element	Well A (mg/L)	Well B (mg/L)	This study (mg/L)
Na	1020	318	1000
K	188	79.8	150
Ca	29.4	2.93	20
Mg	0.02	<0.01	0
Al	0.326	1.18	0
Cl	1880	521	1716

The experimental fluid compositions were based on examination of the provided data and the composition of Well A was more closely replicated. Solid chloride salts from Fisher Scientific were weighed to the nearest 0.1 mg. NaCl was used to add Na^+, KCl was used to add K^+ and $CaCl_2$ was used to add Ca^{2+}, the composition is shown in Table 3.1. Experiments were run with this pH neutral fluid and acidic fluids adjusted to pH 3 with HCl, to mimic carbon sequestration conditions and compare the contrasting cation release rates (Alfredsson *et al*., 2013). A blank experiment with no added rock samples was also completed to check for background effects from experimental set up, with pH and elemental analysis conducted on the fluids in the same way as the other experiments.

3.2.4 Post Experimental Analysis

A Perkin Elmer Inductively Coupled Plasma Optical Emission Spectrometer (ICP-OES) was used to conduct elemental analysis on the experimental fluids. The instrument has a detection limit of 0.1 mg/L and analytical uncertainties within the order of ≤5%. Calibration standards from 0.1 to 30 mg/L were prepared from 100 mg/L standard solution from Fischer Chemical, for the elements Si, Al, Na, K, Ca, and Mg. For each fluid sample, 1/10 and 1/100 dilutions were made with 2% HNO_3 and measured, along with the full concentration fluids.

The BET surface area of the solids collected after each experiment was also measured, using the same method as that used to find the original pre-experiment values.

3.2.5 Geochemical Modelling

Based on the experimental results, PHREEQC v3 (Parkhurst and Appelo, 1999) was used to perform geochemical modelling calculations, to examine possible primary mineral dissolution and secondary mineral precipitation reactions feasible within the batch experimental systems. The measured pH and cation concentrations of the experimental fluids were used as a basis for these calculations, alongside the mineralogical and geochemical results from solid sample analysis and the calculations were designed to simulate a 360-hour

experimental duration. Ideal balanced thermodynamics equations were used to calculate the anion concentrations, since these were not directly measured in the laboratory experiments. The llnl.dat thermodynamic database (Parkhurst and Appelo, 1999) was used for the majority of the minerals and aqueous speciation, with additional mineral parameters used where necessary from: Carroll and Knauss (2005), Oxburgh *et al*. (1994), Palandri and Kharaka (2004) and Parkhurst and Appelo (2013).

3.3 Results

3.3.1 Rock Characterization

3.1.1.1 Microscopy Results

The hand specimen of core sample B1 has a porphyritic texture, with dark and pale phenocrysts in a grey groundmass (see camera images in Figure 2.1). In thin section (Figure 3.1), the larger crystals are identified as quartz and feldspars, up to 5 mm in length, hosted in a fine grained (< 20 μm) groundmass. Occurrences of green coloration in the groundmass indicates the presence of chlorite, likely as a product of hydrothermal alteration.

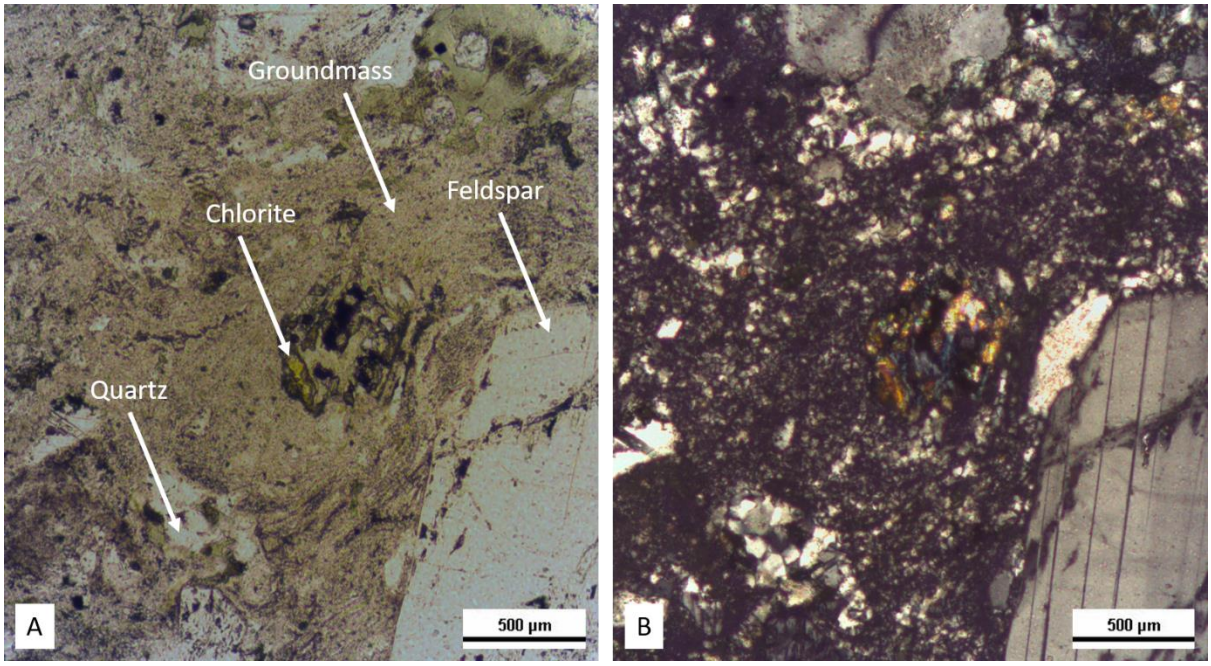


Figure 3.1: Representative optical microscope images of sample B1 under A) plane-polarised and B) crossed-polarised light. Quartz minerals were identified due to bright white colouration under cross-polarised light and pale colour under polarised light. Chlorite was identified due to the green colouration under crossed-polarised and brighter colours under plane-polarised light. Feldspar minerals were identified due to clear cleavage planes, a pale colour under plane-polarised and grey colour in crossed—polarised light. A fine-grained groundmass was observed between the larger crystals, likely composed of quartz and feldspars.

The hand specimen of core sample C1 has an aphanitic and vesicular texture, with visible open and sealed fractures and veins, with significant grey-green coloration. In thin section (Figure 3.2), C1 displayed veins from 2-50 µm in width running through it, filled with a variety of clay minerals and small crystals of calcite. Although the sample appeared aphanitic in texture in hand specimen, there are larger crystals of up to 3 mm in length present, identified as feldspars and quartz, in a fine-grained groundmass. The groundmass contains chlorite characterized by blue-green pleochroism (MacKenzie and Adams, 1994).

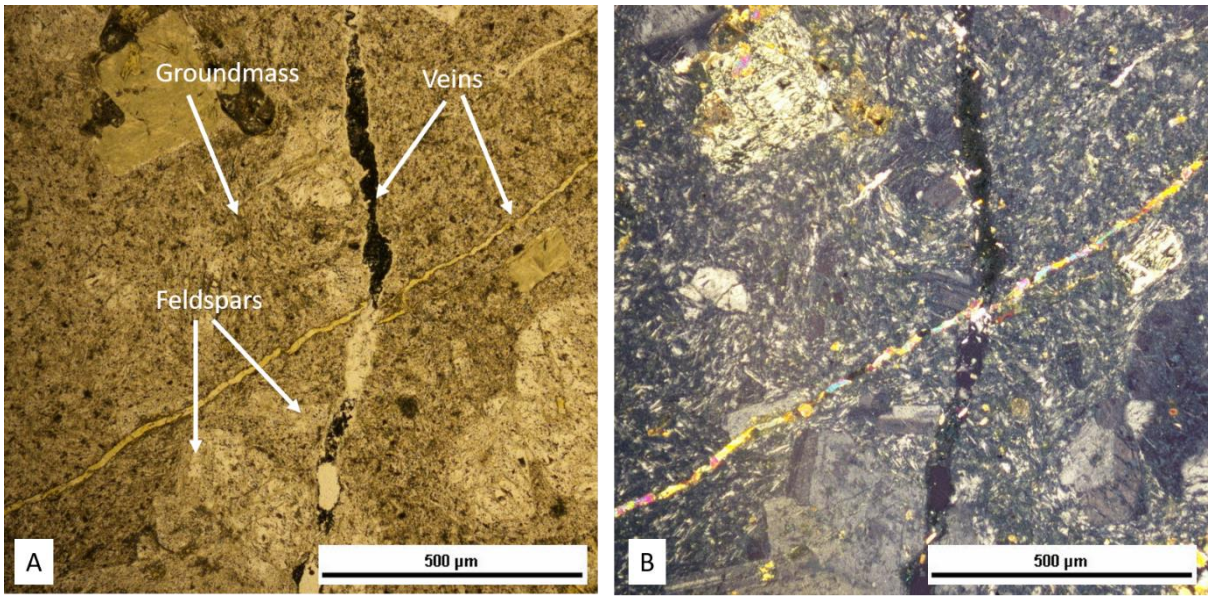


Figure 3.2: Representative optical microscope images of sample C1 under A) plane-polarised and B) crossed-polarised light. Similarly to sample B1, feldspars minerals and a fine grained groundmass was observed. Sample C1 also had many occurrences of veins filled with alteration minerals, likely to be clays and calcite due to bright colours under crossed-polarised light.

The hand specimen of I1 has a phaneritic texture, with dark and pale crystals and some green coloration, again suggesting the presence of chlorite mineral. In thin section (Figure 3.3) this sample has many large feldspar crystals, up to 2 mm in length and also quartz crystals. Similar to the other samples, there is a fine-grained groundmass between the larger crystals.

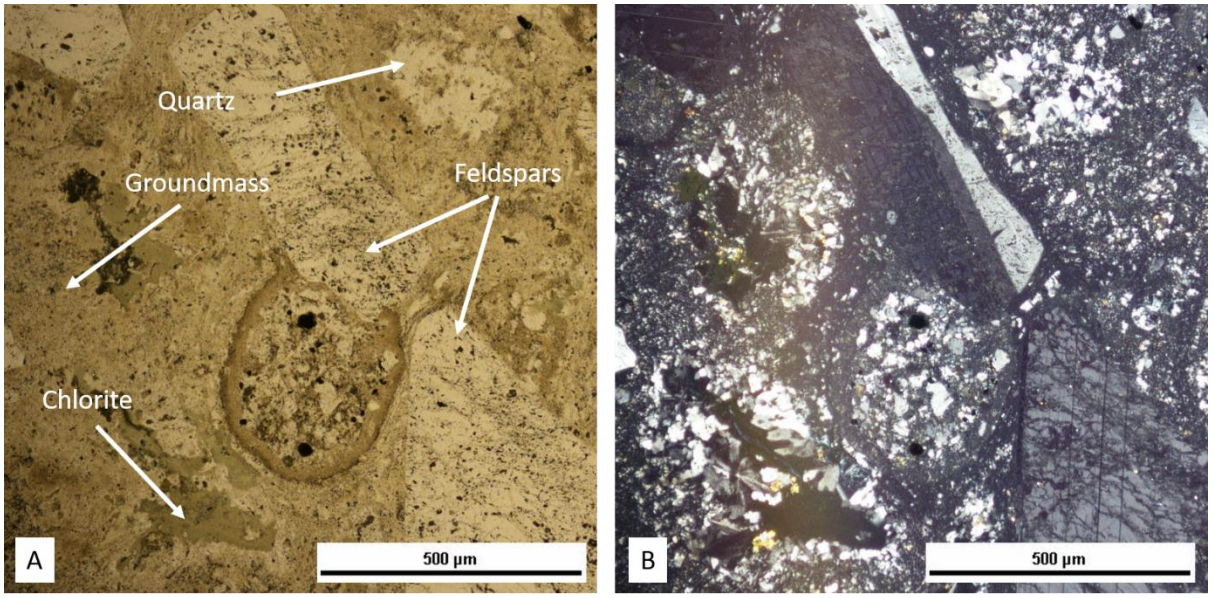


Figure 3.3: Representative optical microscope images of sample I1 under A) plane-polarised and B) crossed-polarised light. Similarly to sample B1 and C1, feldspars minerals, quartz, chlorite and a fine grained groundmass was observed.

3.1.1.2 Mineralogical Characterization

The PXRD patterns for the bulk powder samples (i.e. prior to clay separation) of B1, C1 and I1 are shown in Figure 3.4, alongside the individual patterns for the main phases present. Semi-quantitative PXRD analysis shows that the B1 sample is composed of 76% feldspar, 23% quartz and 1% chlorite; the C1 sample of 69% feldspar, 21% quartz and 10% chlorite; and the I1 sample of 71% feldspar, 25% quartz and 4% chlorite. These analyses are in agreement with the microscopy and geochemical characterization results.

From the clay separation experiments (≤ 2 µm), it was found that B1, C1 and I1 samples contain 5.9%, 13.8% and 8.7% clay, respectively. These separated clay fractions were analysed by PXRD analysis, both before and after an acid treatment, which confirmed the identification of chlorite due to a loss of the chlorite peak.

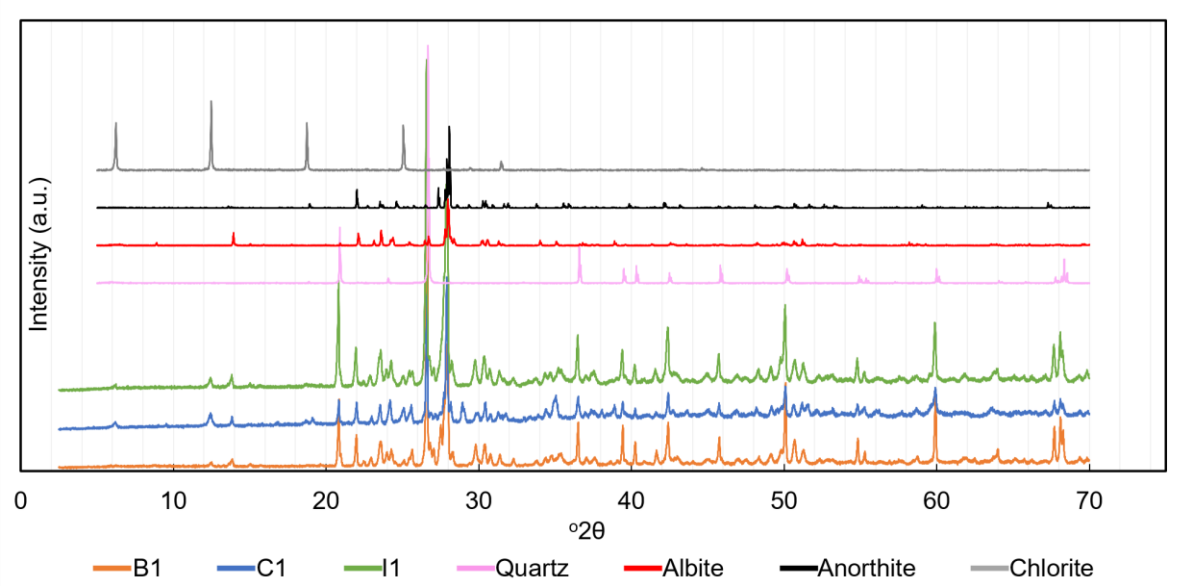


Figure 3.4: PXRD patterns for the three rock samples and reference PXRD patterns for the identified minerals in the sample, for quartz (Levien et al., 1980), albite (Harlow, 1982), anorthite (Wenk et al., 1980) and chlorite (Phillips et al., 1980). The most noticeable differences between the three rock samples are in the region from 5-20 °2θ, with peaks for chlorite that are more defined in the RDC1 sample compared to the other two.

3.1.1.3 Geochemical Characterization

The XRF results (Table 3.2) show the B1 sample consists of 71% SiO_2 and I1 consists of 69% SiO_2, whereas C1 contains only 53% SiO_2. RDB1 has a higher concentration of Na_2O and K_2O, but lower concentrations of CaO, MgO and Fe_2O_3 compared to the RDC1 and RDI1 samples.

Table 3.2: Composition of andesitic samples from a geothermal field in Sumatra, Indonesia. The data were obtained by XRF analysis and reported as weight percentage of oxides.

Sample	SiO_2	Al_2O_3	Na_2O	Fe_2O_3	MgO	CaO	K_2O	Total
B1	71.16	15.59	7.53	1.54	0.48	1.13	2.41	99.84
C1	53.09	18.30	6.57	6.95	4.86	6.75	0.66	97.17
I1	68.55	16.19	7.00	3.06	1.42	2.51	1.23	99.96

Microprobe analysis on the sample thin sections was used to examine the composition of targeted identified feldspar grains to determine normalized chemical formulas of the feldspar crystals (Table 3.3) (Deer *et al*., 2013). Based on 20 analysis points the B1 feldspar crystals are defined as oligoclase-plagioclase composition, with an average formula of $K_{0.04}Na_{0.77}Ca_{0.19}Al_{1.19}Si_{2.81}O_8$. Based on 15 analysis points the feldspar crystals of the C1 sample are defined as labradorite-plagioclase composition, with an average formula of $K_{0.02}Na_{0.34}Ca_{0.64}Al_{1.64}Si_{2.36}O_8$. Based on 25 analysis points the feldspar crystals of the I1 sample are defined as andesine-plagioclase composition, with an average formula of $K_{0.01}Na_{0.68}Ca_{0.31}Al_{1.31}Si_{2.69}O_8$. The microprobe data broadly supports the XRF analysis of each sample.

Table 3.3: Average chemical composition of samples B1, C1 and I1.

Oxide	B1	C1	I1
Na_2O	8.63	3.67	7.27
SiO_2	65.04	51.21	59.65
K_2O	0.64	0.38	0.14
FeO	0.15	1.58	0.29
Al_2O_3	21.54	28.21	26.36
CaO	3.70	12.79	6.06
SrO	n.d.	n.d.	n.d.
SO_3	n.d.	n.d.	n.d.
TiO_2	n.d.	0.52	<0.02
MgO	n.d.	0.61	n.d.
P_2O_5	<0.02	0.09	<0.02
F	0.067	0.08	<0.02
Cl	n.d.	<0.02	<0.02
Total	99.79	99.15	99.83

n.d. *Not detected.*
< *Less than detection limit.*

3.3.2 Fluid Data

The ICP-OES results indicate an increase in Si concentration in the fluids with time in all experiments (Figure 3.5 A). Under acidic conditions either the same (within experimental error) or more Si is released than under the neutral conditions with all samples, with the C1 acidic condition releasing the most and the B1 neutral condition the least by the end of the experiment (15 days reaction time). A linear fit is applied to the initial release of Si in all conditions, based on the first 3 data points (Figure 3.5 B) and used alongside the measured BET surface areas (Table 3.4) to estimate dissolution rates.

Only in the B1 neutral and I1 acidic conditions did the rock samples release a measurable amount of Al into the fluids, with a rapid increase at the start which then remained relatively constant (Figure 3.5 C). The detected Ca in the fluid rises rapidly to 5-10 mg/L in all experiments with the B1 and C1 samples and then stays relatively consistent, except for the C1 acidic experiment, in which the concentration continues to increase to the end of the experiment (Figure 3.5 D). In contrast, the I1 sample releases a larger amount of Ca, approximately 40 ppm, at the start before stabilizing. In general, the Mg concentration in the fluids is higher in the acidic conditions than the neutral conditions with all samples (Figure 3.5 E). The B1 sample in the neutral conditions released no detectable amounts of Mg and the C1 sample released the most Mg in the acidic condition. The I1 sample released the same amounts of Mg in the acidic and neutral conditions. The initial fluids all had 150 mg/L of K added, to simulate geothermal fluid conditions, which subsequently means small changes in its concentration are hard to define due to increased error margins. The I1 sample in both neutral and acidic experiments is the only sample that appears to release any K into the fluids (Figure 3.5 F).

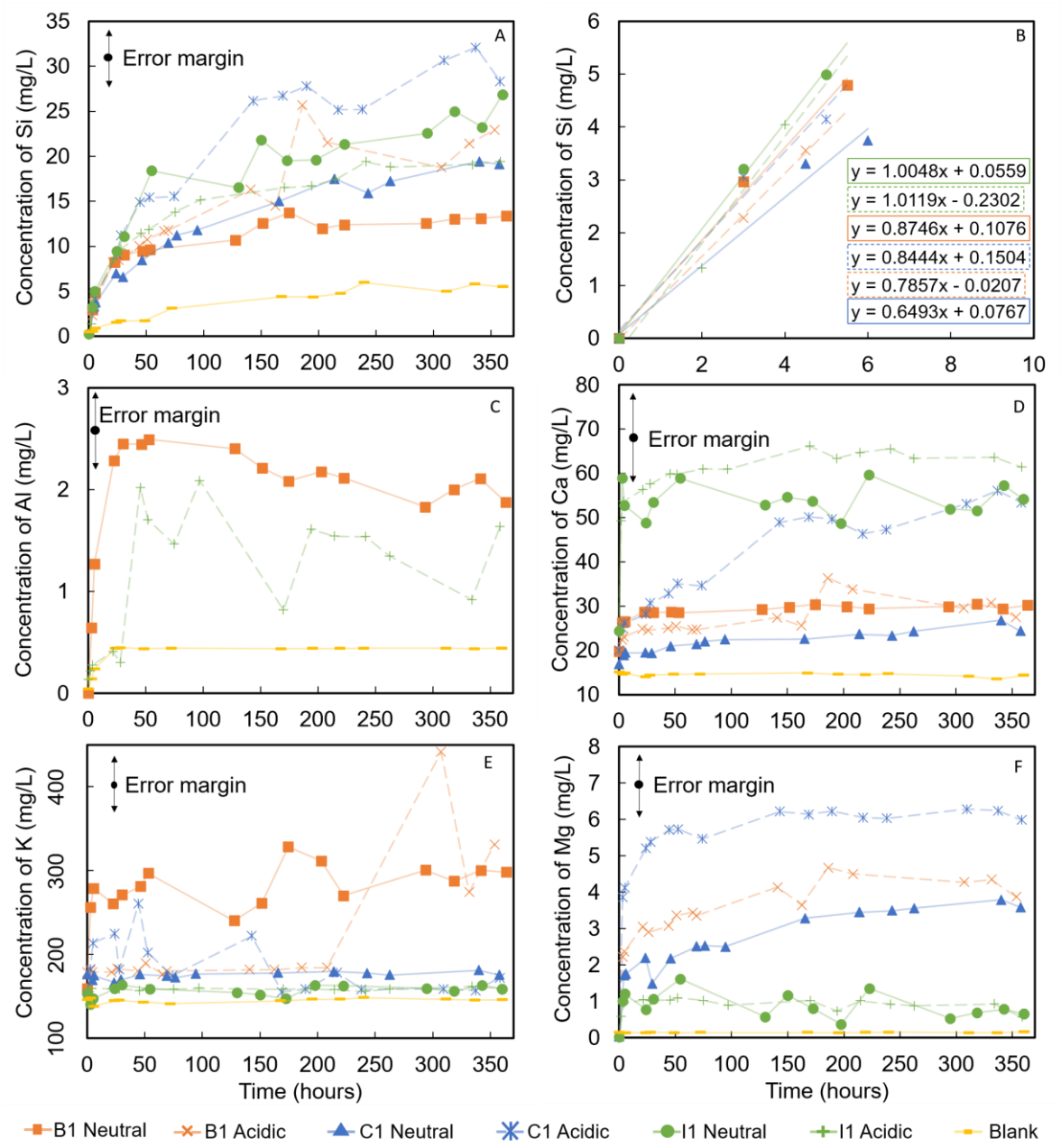


Figure 3.5: ICP-OES data showing the variations in elemental concentrations measured throughout the experimental durations for each sample and condition in mg/L for; (A) silicon release, (B) silicon release within the first 6 hours of the experiments, (C) aluminium release, (D) calcium release, (E) potassium release and (F) magnesium release. Note the different scales of the vertical axes. Error is calculated based on replicate experiments, which resulted in approximately ±15% error. Quantitative date provided in Table A21 of the appendix.

The pH in the acidic experiments with all samples rapidly increases to above the starting value of pH 3 (Figure 3.6), with the B1 sample raising the pH to 6.5, the C1 sample to 5.5 and the I1 sample to close to 7. The highest pH was recorded in the B1 neutral experiment, where the pH increased to alkaline levels at 8.5. The fluid pH in the C1 sample neutral and acidic experiments remained below the neutral value of 7, and the fluid pH in the I1 sample experiments changed little between the acidic and neutral conditions.

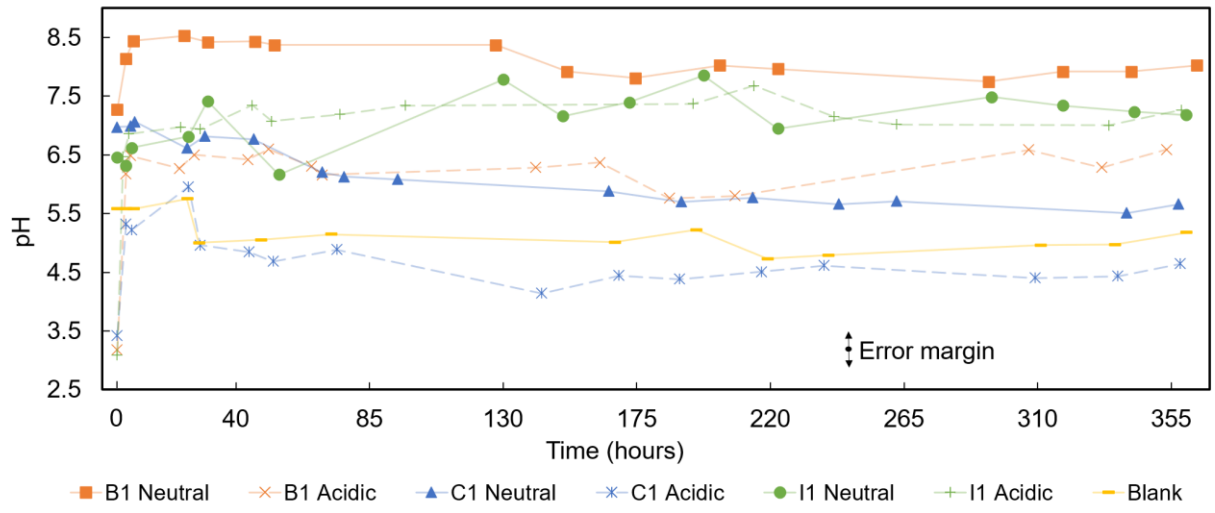


Figure 3.6: Variation in pH measured from the fluids collected throughout the experimental durations for each sample and condition. Error based on pH meter used and replicate data, at ±0.1 pH. Quantitative data provided in table A22 of the Appendix.

3.3.3 Post Experiment Solid Analysis

The PXRD analysis conducted on the dried solid sample after each experiment showed diffraction patterns that were not identical to the original samples. However, the solid samples collected at the end of the experiments were dried and not disaggregated so as to avoid minor contamination, therefore there may be some preferential orientation of the samples on the XRD holders and so these patterns cannot be relied upon for accurate quantification analysis (Kleeberg *et al*., 2008). Generally, they show the same phases as the original sample patterns, but different relative peak heights within each phase when compared to the original unreacted

samples (Figure 3.7). The surface area of the samples was also examined with BET analysis, to indicate whether any surface area changes may have been induced by the rock-fluid interactions taking place (Table 3.4).

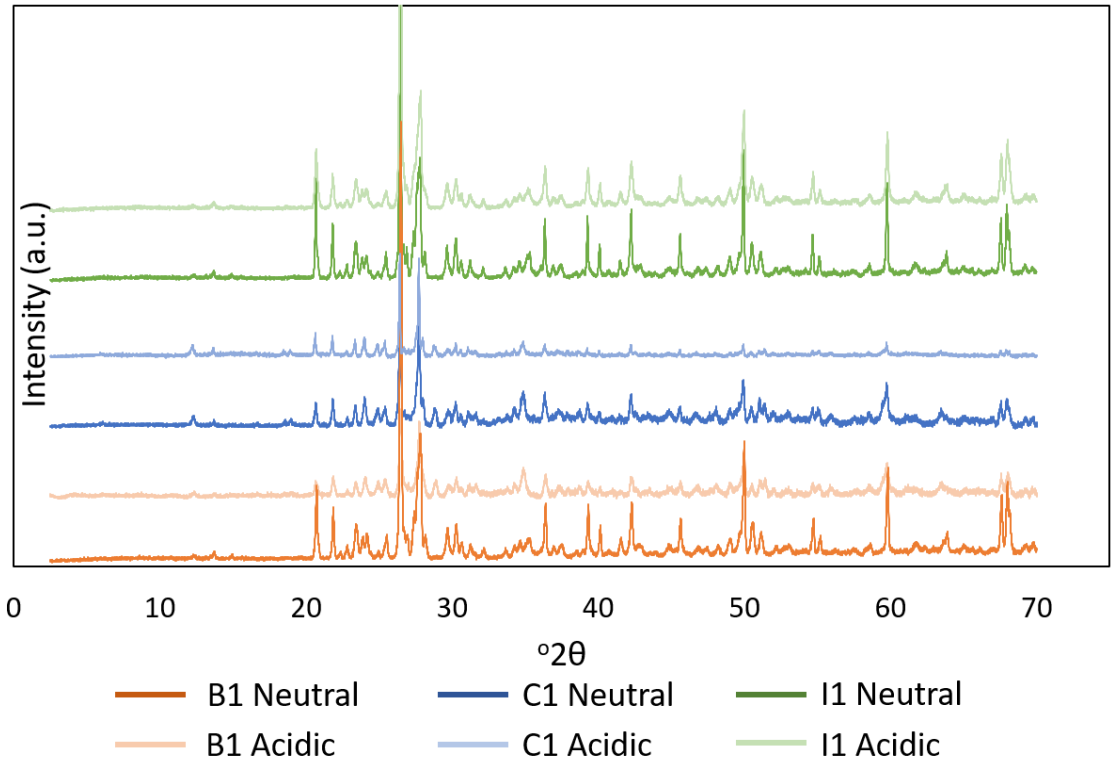


Figure 3.7: PXRD patterns for the bulk samples measured after the experiments using neutral and acidic fluids.

3.3.4 Geochemical calculations

PHREEQC calculations indicate Gibbsite ($Al(OH)_3$) is likely formed as a secondary mineral during the batch experiments. In the experiments with a starting pH close to 3, the calculations indicate gibbsite formation starts after some initial feldspar mineral dissolution and the pH rises to around 5 (see Figure A10 in the appendix). The formation plateaus once a neutral pH is reached in the PHREEQC calculations. The Al concentration in the fluids initially increases, then a sharp decrease coincides with the initiation of Gibbsite formation

(see Figure A10 in the appendix). The Si concentration in the fluids rises continuously throughout all calculated experiments.

3.4 Discussion

3.4.1 Mineral Dissolution Rates

The Na-K-Mg ratios from the fluid data provided from the geothermal well in Indonesia (Table 3.1) were examined using Giggenbach's (1988) classification. This analysis indicates the reservoir fluids are not in full equilibrium, hence further mineral dissolution is expected when using the simulated geothermal fluids and rock samples in this study (Giggenbach, 1988). The experimental results confirm this as Si is released into the fluids for all samples under the experimental conditions tested (Figure 3.5 A). It is important to examine the extent of mineral dissolution under the neutral and acidic pH conditions, as this can give an indication of the magnitude of cation release to be expected when injecting neutral formation waters, or waters with increased acidity due to the presence of dissolved CO_2 for carbon sequestration. It is commonly assumed that the rate limiting step for the sequestration of carbon by mineral formation (equation 3.1) is the release of divalent cations from mineral dissolution (Oelkers *et al*., 2008; Wolff-Boenisch *et al*., 2006), therefore significant cation release rates from target rock formations are essential for successful carbon sequestration. Another important factor in carbon sequestration via this technique is the ability of the rock formation to neutralize the acidic pH conditions created by CO_2 dissolution in the fluids, to enable carbonate mineral formation which requires near neutral pH conditions (Matter *et al*., 2007; Wolff-Boenisch, 2011). Dissolution of minerals such as feldspars are known to neutralize solution pH and may also release additional divalent cations to further enhance carbon sequestration (Shibuya *et al*., 2013). Previous laboratory experimental studies have investigated mainly basaltic type rocks for carbon sequestration via mineral formation (Gislason *et al*., 2010; McGrail *et al*., 2006, 2003; Oelkers *et al*., 2008; Schaef and McGrail, 2009; Wolff-Boenisch *et al*., 2006, 2004), due to the high quantities of minerals such as olivine, pyroxene and plagioclases available for divalent cation release. The success of these studies led to the field scale studies Carbfix in Iceland and the Wallula Basalt Pilot Project in the US, injecting dissolved CO_2 into basaltic reservoirs, which demonstrated that

CO_2 can be mineralized on relatively short time scales in basaltic reservoirs for permanent storage (Kelemen *et al*., 2019; Matter *et al*., 2011, 2016; McGrail *et al*., 2011, 2017b; Snæbjörnsdóttir *et al*., 2020). In contrast, andesitic type rock samples were examined here, to assess whether carbon sequestration is still likely to be possible at appreciable levels and within useful timescales, despite the significantly reduced quantity of olivine and pyroxene minerals for divalent cation release. The mineralogical, geochemical and microscopic characterization confirms the lack of pyroxene and olivine minerals in all samples investigated in this study.

The following mass balance calculation is used to determine the sample dissolution rates, assuming the Si release is a result of feldspar dissolution:

$$R_{dis} \cdot \nu_{i,dis} = \frac{dC_i}{dt} \cdot \frac{V}{A_{dis}} \quad (3.2)$$

Where C_i is the concentration of component *i* in the reactor (mol/L); *t* is time (s); $v_{i,dis}$ is the stoichiometric coefficient of *i* in the dissolution reaction; A_{dis} is the surface area of the mineral (m^2); *V* is the volume of the solution in the reactor (L); and R_{dis} is the dissolution rate ($mol/m^2/s$). As the change in concentration is linear with time during the sampling interval, the reaction rate can be calculated by substituting the average change in concentration with time ($\Delta C_i/\Delta t$) for the time derivative of the concentration in equation 3.2. Only the initial release of Si through time is used to calculate dissolution rates based on the first 3 data points (Figure 3.5 B), to match the far-from-equilibrium conditions that would be present in a hydrothermal system, which would have constant fluid flow through the system. The error associated with this regression (Table A20 of the appendix) indicates the linear fit is appropriate, with only minor error relative to the existing experimental error. The average feldspar composition within each of the samples is determined from examination of the microprobe analysis. The B1 sample has a composition which characterizes it as oligoclase ($K_{0.4}Na_{0.77}Ca_{0.19}Al_{1.19}Si_{2.77}O_8$), hence a stoichiometric coefficient of 2.77 is used. Sample C1 is characterized as labradorite ($K_{0.2}Na_{0.34}Ca_{0.64}Al_{1.64}Si_{2.36}O_8$), hence a stoichiometric

coefficient of 2.36 is used. The I1 sample has a feldspar composition between that of the B1 and C1 samples and is characterized as andesine ($K_{0.1}Na_{0.68}Ca_{0.31}Al_{1.31}Si_{2.68}O_8$), hence a stoichiometric coefficient of 2.68 is used to calculate its dissolution rate. Previous studies have found feldspar dissolution rates across a reasonably large range, from × 10^{-12} mol/m^2/s to ×10^{-8} mol/m^2/s, with similar experimental conditions, between pH 3 and 4 and 100°C (Carroll and Knauss, 2005; Hellmann, 1994; Oelkers and Schott, 1995; Siegel and Pfannkuch, 1984). The rates calculated in this present study fall within this range of values (Table 3.4).

*Table 3.4: Experimental results including initial Si release rate (mg/L/hr) and calculated dissolution rates (*mol/m^2/s*) for each sample.*

Sample, condition	Average formula	Surface Area (m^2/g) of rock powder: Initial (final)	Slope Si (mg/L) vs time (hrs)	Dissolution Rate (mol/m^2/s)
B1, Neutral	$K_{0.04}Na_{0.77}Ca_{0.19}Al_{1.19}Si_{2.81}O_8$	1.1±0.1 (1.0±0.1)	0.8746	4.2×10^{-11}
B1, Acidic	$K_{0.04}Na_{0.77}Ca_{0.19}Al_{1.19}Si_{2.81}O_8$	1.1±0.1 (2.0±0.1)	0.7857	3.8×10^{-11}
C1, Neutral	$K_{0.2}Na_{0.34}Ca_{0.64}Al_{1.64}Si_{2.36}O_8$	1.7±0.1 (3.2±0.1)	0.6493	2.4×10^{-11}
C1, Acidic	$K_{0.2}Na_{0.34}Ca_{0.64}Al_{1.64}Si_{2.36}O_8$	1.7±0.1 (4.7±0.1)	0.8444	3.1×10^{-11}
I1, Neutral	$K_{0.1}Na_{0.68}Ca_{0.31}Al_{1.31}Si_{2.69}O_8$	1.8±0.1 (2.1±0.1)	1.0048	3.1×10^{-11}
I1, Acidic	$K_{0.1}Na_{0.68}Ca_{0.31}Al_{1.31}Si_{2.69}O_8$	1.8±0.1 (2.3±0.1)	1.0119	3.1×10^{-11}

The values calculated for the initial dissolution rates do not reflect the final quantity of Si released into the fluids by the end of the study, likely due to the buffering effects that can take place in batch reactor type experiments. Where the B1 sample under the neutral fluid condition has the fastest dissolution rates (Table 3.4), it releases the least Si overall into the fluids by the end of the experiment (Figure 3.5 A). The slowest initial dissolution rates are for the C1 sample under both pH conditions; however, this sample releases a relatively high amount of Si by the end of the experiment, particularly in the acidic condition which releases the most Si of all experiments. The semi-quantitative results from the PXRD analysis

indicated the B1 sample which has the fastest initial dissolution rate has the highest amount of feldspar present and the C1 sample has the lowest. The microprobe analysis of the samples indicated that the C1 sample has feldspars with a higher calcium content, whereas the B1 sample has those of a higher sodium content. Previous studies have indicated that calcic feldspar types are less stable under acidic conditions compared to alkali feldspars, which gives a possible explanation for why the C1 sample released more Si overall as the feldspar minerals in this sample were more readily dissolved (Blum, 1994; Casey *et al*., 1991; Oelkers and Schott, 1995). These findings combined indicate that the initial dissolution rates are impacted more by the quantity of feldspar mineral available for interactions with the fluids, with a faster rate of Si release for sample B1 with the highest feldspar content, compared to just the type of feldspar present. However, the overall magnitude of mineral dissolution after a 15-day period is impacted more by the type of feldspar mineral present, with C1 releasing more Si by the end of the experimental duration compared to the B1 sample, because it has the less stable calcic-type plagioclase minerals present, rather than sodic-type plagioclase minerals.

3.4.2 pH Neutralisation

Generally, the initial rapid increase of the pH to near neutral values illustrated in Figure 3.6 is most likely explained by the dissolution of feldspar minerals consuming H^+, for example as shown by equation 3.4 for alkali feldspars and equation 3.5 for calcic type feldspars (Matter *et al*., 2011; Shibuya *et al*., 2013; Zhang *et al*., 2015):

$$Na(K)AlSi_3O_8(s) + 2H^+ + H_2O \leftrightarrow Na^+(K^+) + AlSi_3O_5(OH)_4(aq) \quad (3.4)$$

$$CaAl_2Si_2O_8(s) + 2H^+ + H_2O \leftrightarrow Ca^{2+} + Al_2Si_2O_5(OH)_4(aq) \quad (3.5)$$

In the experiments with the B1 and I1 samples, the pH of the solutions increases more than in the experiments with the C1 sample (Figure 3.6). The C1 sample has the lowest amount of feldspar content and therefore it is likely that as less feldspar is available for dissolution, it

is less effective at increasing the acidic pH solutions over the 15 day timescale used in this study. For carbon sequestration, it is important that any H^+ ions present which create acidity are consumed by reactions such as feldspar dissolution, to allow the fluids to reach neutral pH levels suitable for carbonation reactions to take place (Gislason *et al*., 2010; Wolff-Boenisch, 2011). Hence the results of this study suggest that rock systems with a high feldspar content could be good targets for carbon sequestration via carbonate mineral formation, as the pH of the fluids will be increased sufficiently to values that allow carbonate mineral formation.

3.4.3 Secondary Mineral Formation

Despite aluminium being present in all minerals identified in these samples, and silicon release indicating mineral dissolution is taking place, aluminium is only present in detectable amounts in the experiments with B1 neutral and I1 acidic conditions. Since the chemical composition of the feldspar minerals present in these samples lies between that of oligoclase and labradorite, it is expected that aluminium would be released into the fluids, at levels about 2-3 times less than silicon. However, up to 30 ppm of silicon is released in some experiments, with no detected aluminium release. Therefore, either significant non-stoichiometric dissolution must be taking place, or some secondary mineral formation is taking place that removes aluminium from the solution.

The pH variation through the B1 neutral condition experiment reached the highest values, with the pH rising to about 8.5. Previous research under similar experimental conditions has found aluminium hydroxide precipitates at values between pH 5 and 9 (Balintova and Petrilakova, 2011). The mineral gibbsite ($Al(OH)_3$) is concluded to precipitate preferentially in an acidic environment and the bayerite polymorph precipitates rapidly from solution above pH 5.8 (Barnhisel and Rich, 1965; Schoen and Roberson, 1970). In a study conducted on the dissolution kinetics of an aluminosilicate mineral nepheline ($NaAlSiO_4$), at pH 5 the solubility of gibbsite in the experimental solution was low enough that no Al was detected in

the fluids at all (Tole *et al*., 1986). The lack of aluminium release in most experiments therefore is likely due to rapid precipitation of aluminium hydroxide species from the solutions, which have a pH level between 5 and 7. The increased pH values in the RDB1 neutral experiment (particularly within the first few hours) is enough to begin to prevent some aluminium hydroxide precipitation as it is less favourable at alkaline conditions, resulting in the small amount of aluminium released into the fluids (Figure 3.5 C). Though no physical evidence of secondary mineral formation was found (due to the difficulty in measuring small changes in small samples), geochemical modelling calculations performed using PHREEQC supports this idea. As the reactions proceed, the concentration of Si in the fluids is increasing and the pH rises towards neutral values (particularly in the acidic experiments). When the pH values are close to about 5, the calculations indicate Gibbsite becomes saturated and its concentration increases in the system, coinciding with a drop in aluminium concentration in the fluids. No evidence of other secondary mineral formation is seen in the PHREEQC calculations (e.g. kaolinite formation), however, further laboratory experiments on a larger scale would be beneficial here to confirm this finding, as other studies report that kaolinite is a significant aluminium sink (Matter *et al*., 2007).

This is very likely to have implications for the availability of divalent cations for carbonate formation, as any secondary precipitates may capture some of the desired divalent cations (such as Fe^{2+}) within their structures, which would reduce the quantity available for carbonate mineral formation (Gysi and Stefánsson, 2011). Therefore, more research is needed in this area, to assess the impact aluminium hydroxide precipitation may have in field scale studies of carbon sequestration in geothermal reservoirs.

3.4.4 Implications for Carbon Storage in Andesitic Reservoirs

The Carbfix project in Iceland found quantitative evidence to show that up to 95% of the injected CO_2 is mineralized in less than 2 years (Matter *et al*., 2016; Pogge von Strandmann *et al*., 2019). The Wallula Pilot project also reported qualitative evidence indicating the

injected CO_2 was being actively converted to carbonate minerals within 24 months of emplacement (McGrail *et al*., 2017b). This indicates injecting CO_2 into basaltic reservoirs has some huge advantages compared to other forms of geological carbon storage which rely on impermeable cap rocks to seal in CO_2. The dissolution rate of Stapafell crystalline basalt has been reported to be of the order 10^{-10} mol/m^2/s (Gudbrandsson *et al*., 2011), compared to that found in this present study for these andesitic rock samples of 10^{-11} mol/m^2/s. This faster dissolution of basaltic rocks can be attributed to its different mineralogy, as basalt contains minerals such as olivine which have a reported average dissolution rate of 10^{-8} mol/m^2/s (Rimstidt *et al*., 2012). Faster rock dissolution rates will be beneficial as more divalent cations can be released into the fluids in a shorter time scale, meaning faster CO_2 fixation is possible. The dissolution rate of the crystalline andesitic samples in this study is approximately 1-2 orders of magnitude slower compared to reported crystalline basaltic dissolution rates. This also aligns well with previous studies which examined volcanic glasses with a higher silica content under acidic conditions at more ambient temperature conditions (Wolff-Boenisch *et al*., 2006, 2004). Previous literature results have indicated that when a volcanic glass sample with a high silica content has a dissolution rate approximately two orders of magnitude slower than one with a lower silica content, the calcium release rates also follow this trend (Wolff-Boenisch *et al*., 2006). Therefore, it is assumed a similar trend applies to the crystalline rock samples used in this present study.

Although the release rate of calcium is slower in andesite samples compared to basaltic samples, andesitic reservoirs are still likely to be suitable for carbon sequestration, as has also been suggested by Marieni *et al*. (2018). As plagioclase minerals alone release divalent cations at a lower rate than basaltic type rocks, it will take more time for the fluids to reach carbonate mineral saturation state. Although this will generally result in a slower rate of carbonate mineral formation, the carbonate minerals are likely to precipitate further from the injection site in andesitic systems compared to basaltic, which may have benefits in preventing the potential risks of permeability reduction at the injection site due to mineral

precipitation, though this would of course need further investigation with fluid-flow modelling studies as well as examination on the field scale. Other forms of geological carbon storage (such as injection into porous sedimentary-type reservoirs) which rely on solution trapping can take in excess of 1000 years to be considered to have acted as permanent safe storage sites for the CO_2 (Holloway, 1997), whereas the results from field scale studies on mineral trapping in basaltic reservoir rocks have demonstrated permanent storage in two years or less (Matter *et al*., 2016; McGrail *et al*., 2017b; Snæbjörnsdóttir *et al*., 2017). Though andesite-type reservoirs may have slightly slower trapping rates compared to basaltic reservoirs, they should still be examined for their potential to achieve permanent storage of CO_2 at a faster rate than solubility trapping in porous sedimentary-type reservoirs can achieve.

Other divalent species, such as Mg^{2+} and Fe^{2+}, are also important to consider when discussing carbon sequestration via mineral trapping. These species are abundant in basaltic rock types, hence have been an important focus in previous studies examining these rocks and are one of the many reasons basaltic rocks are considered to be the optimal target for rapid mineral trapping of CO_2 (Matter *et al*., 2016; Snæbjörnsdóttir *et al*., 2020). These species are considerably less abundant in andesite type rocks since plagioclase minerals do not contain magnesium or iron as major elements. Minor amounts of magnesium were detected in the fluids in this present study, in particular from experiments using the C1 sample (Figure 3.5 E). This sample had the highest (although still reasonably low) chlorite content. Magnesium is often contained within the chlorite structure, so possibly the magnesium release is from minor dissolution of this mineral. The XRF geochemical analysis of the samples does indicate that sample C1 has a higher MgO compared to the other samples, so this is a reasonable assumption (Table 3.2). This present study has focused on the release of Ca^{2+} from plagioclase minerals within andesitic rocks, but the significance of Mg^{2+} release from alternative samples with higher alteration secondary

minerals present is an avenue of research that should be further investigated, with relevance to divalent cation release for carbon sequestration.

3.5 Conclusions

This study reports andesite rock sample dissolution rates on the order of 10^{-11} mol/m^2/s, in experiments simulating conditions relevant to acidic fluid injection into andesitic type geothermal reservoirs. Other authors have conducted similar studies with basaltic type rocks, and report dissolution rates on the order of 10^{-9} to 10^{-10} mol/m^2/s (Gudbrandsson *et al*., 2011). Basaltic samples have been proven to be highly successful targets for carbon sequestration via carbonate mineral formation (Matter *et al*., 2016; McGrail *et al*., 2017a) and it is commonly assumed that the release of divalent cations via mineral dissolution is the rate limiting step in this process (Oelkers *et al*., 2008; Wolff-Boenisch *et al*., 2006). Therefore, a slower dissolution rate of andesite samples compared to basaltic suggests that mineral carbonation is unlikely to be as rapid. However, appreciable levels of Ca^{2+} were released from the samples, in particular the I1 sample, which is a positive indication that carbonate mineral formation in andesitic rock types is feasible. Various other factors such as reservoir permeability, and the release of alternative divalent cations such as Mg^{2+} and Fe^{2+} from andesite samples with a higher content of alteration minerals may act to assist in the formation of carbonate minerals.

Overall, the author considers this study to report positive results which indicate carbon storage via carbonate mineral formation in andesitic reservoirs should be examined further and considered for larger field scale investigations. The ‘Carbfix method’ proven effective in basaltic reservoirs has the potential to be applied more widely to andesite reservoirs and may be particularly appropriate in geothermal andesite reservoirs where CO_2 emission can be collected and mitigated at the source for economic efficiency. Besides Indonesia, locations such as New Zealand have occurrences of andesitic rocks alongside geothermal energy exploration sites and various other global locations also have andesitic rocks likely to be suitable for carbon sequestration. To start a demonstration pilot project in andesitic reservoirs, more in-depth analysis of other factors should be completed alongside this study, such as assessing the permeability of target reservoirs and ensuring there is sufficient pore

space for carbonate minerals to form in and completing additional laboratory experiments at other temperature conditions relevant to various target formations around the world. Results suggest that the specific mineralogy of the rocks is an important factor in predicting whether an andesitic reservoir will make a good target for carbon sequestration. Rock samples with a high content of calcic-type plagioclase minerals should be focused on to release the highest amount of divalent cations, in the absence of minerals such as olivine and pyroxene found in basaltic rocks. The impact of a higher content of alteration minerals such as chlorite should be examined further, as these minerals may have the potential to release additional divalent cations over the timescales relevant to carbon sequestration in geological systems. These results contribute towards providing much needed information on the feasibility of sequestering carbon dioxide in andesitic rock systems which can help play a part in mitigating global release of greenhouse gases which continues to contribute to rapid global warming and climate change.

3.6 References

Alfredsson, H.A., Oelkers, E.H., Hardarsson, B.S., Franzson, H., Gunnlaugsson, E., Gislason, S.R., 2013. The geology and water chemistry of the Hellisheidi, SW-Iceland carbon storage site. Int. J. Greenh. Gas Control 12, 399–418. https://doi.org/10.1016/j.ijggc.2012.11.019

Aradóttir, E.S., Gunnarsson, I., Sigfússon, B., Gunnarsson, G., Júliusson, B.M., Gunnlaugsson, E., Sigurdardóttir, H., Arnarson, M.T., Sonnenthal, E., 2015. Toward Cleaner Geothermal Energy Utilization: Capturing and Sequestering CO2 and H2S Emissions from Geothermal Power Plants. Transp. Porous Media 108, 61–84. https://doi.org/10.1007/s11242-014-0316-5

Balintova, M., Petrilakova, A., 2011. Study of pH Influence on Selective Precipitation of Heavy Metals from Acid Mine Drainage, in: 14th International Conference on Progress Integration, Modelling and Optimisation for Energy. pp. 5–10.

Barber, A.J., Crow, M.J., Milsom, J.S., 2005. Sumatra: Geology, Resources and Tectonic Evolution, Geological Society, London, Memoirs. The Geological Society, London.

Barnhisel, R.I., Rich, C.I., 1965. Gibbsite, Bayerite, and Nordstrandite Formation as Affected by Anions, pH, and Mineral Surfaces, in: Soil Science Society of America Proceedings. pp. 531–534.

Biscaye, P.E., 1964. Distinction between Kaolinite and Chlorite in Recent Sediments by X-ray Diffraction. Am. Mineral. 49, 1281–1289.

Blum, A.E., 1994. Feldspars in Weathering, in: Parsons, I. (Ed.), Feldspars and Their Reactions. Kluwer Academic Publishers, pp. 595–630. https://doi.org/10.1007/978-94-011-1106-5

Boedihardi, M., Mulyonol, A., Ginting, A., Mosby, M., Radja, V., 1993. Geology, energy potential and development of Indonesia's geothermal prospects, in: Geological Society of Malaysia, Bulletin. pp. 369–385.

BP, 2020. bp Statistical Review of World Energy.

Carroll, S.A., Knauss, K.G., 2005. Dependence of labradorite dissolution kinetics on CO2(aq), Al(aq), and temperature. Chem. Geol. 217, 213–225. https://doi.org/10.1016/j.chemgeo.2004.12.008

Casey, W.H., Westrich, H.R., Holdren, G.R., 1991. Dissolution rates of plagioclase at pH = 2 and 3. Am. Mineral. 76, 211–217.

Clark, D.E., Galeczka, I.M., Dideriksen, K., Voigt, M.J., Wolff-Boenisch, D., Gislason, S.R., 2019. Experimental observations of CO2-water-basaltic glass interaction in a large column reactor experiment at 50 °C. Int. J. Greenh. Gas Control 89, 9–19. https://doi.org/10.1016/j.ijggc.2019.07.007

Department of Energy and Climate Change, 2016. UK Energy Statistics, 2015 and Q4 2015. Stat. Press Release 1–16.

Edenhofer, O., Pichs-Madruga, R., Sokona, Y., Farahani, E., Kadner, S., Seyboth, K., Adler, A., Baum, I., Brunner, S., Eickemeier, P., Kriemann, B., Savolainen, J., Schlömer, S., Stechow, C. v., Zwickel, T., Minx, J.C., 2014. Climate change 2014: Mitigation of Climate Change. Contribution of Working Group III to the Fifth Assessment Report of

the Intergovernmental Panel on Climate Change, IPCC. Cambridge University Press, Cambridge, United Kingdom and New York, NY, USA.

Fridriksson, T., Mateos-Merino, A., Audinet, P., Orucu, A.Y., 2016. Greenhouse Gases from Geothermal Power Production, in: Energy Sector Management Assistance Program (ESMAP) Technical Report;009/16. Washington, DC.

Galeczka, I., Wolff-Boenisch, D., Oelkers, E.H., Gislason, S.R., 2014. An experimental study of basaltic glass–H2O–CO2 interaction at 22 and 50 °C: Implications for subsurface storage of CO2. Geochim. Cosmochim. Acta 126, 123–145. https://doi.org/10.1016/J.GCA.2013.10.044

Giggenbach, W.F., 1988. Geothermal solute equilibria. Derivation of Na-K-Mg-Ca geoindicators. Geochim. Cosmochim. Acta 52, 2749–2765. https://doi.org/10.1016/0016-7037(88)90143-3

Gíslason, S., Sigurdardóttir, H., Aradóttir, E., Oelkers, E.H., 2018. A brief history of CarbFix: Challenges and victories of the project's pilot phase. Energy Procedia 146, 103–114. https://doi.org/10.1016/j.egypro.2018.07.014

Gislason, S.R., Wolff-Boenisch, D., Stefansson, A., Oelkers, E.H., Gunnlaugsson, E., Sigurdardóttir, H., Sigfússon, B., Broecker, W.S., Matter, J.M., Stute, M., Axelsson, G., Fridriksson, T., 2010. Mineral sequestration of carbon dioxide in basalt : A pre-injection overview of the CarbFix project. Int. J. Greenh. Gas Control 4, 537–545. https://doi.org/10.1016/j.ijggc.2009.11.013

Gudbrandsson, S., Wolff-Boenisch, D., Gislason, S.R., Oelkers, E.H., 2011. An experimental study of crystalline basalt dissolution from $2 \leqslant pH \leqslant 11$ and temperatures from 5 to 75 °C. Geochim. Cosmochim. Acta 75, 5496–5509. https://doi.org/10.1016/j.gca.2011.06.035

Gysi, A.P., Stefánsson, A., 2011. CO2–water–basalt interaction. Numerical simulation of low temperature CO2 sequestration into basalts. Geochim. Cosmochim. Acta 75, 4728–4751. https://doi.org/10.1016/j.gca.2011.05.037

Hellmann, R., 1994. The albite-water system: Part I. The kinetics of dissolution as a function of pH at 100, 200, and 300°C. Geochim. Cosmochim. Acta 58, 595–611. https://doi.org/10.1016/0016-7037(94)90491-X

Holloway, S., 1997. An overview of the underground disposal of carbon dioxide. Energy Convers. Manag. 38, 193–198. https://doi.org/10.1016/s0196-8904(96)00268-3

ICDD, 2018. PDF-4. International Centre for Diffraction Data.

IPCC, 2018. Summary for Policymakers, in: Masson-Delmotte, V., Zhai, P., Portner, H.-O., Roberts, D., Skea, J., Shukla, P.R., Pirani, A., Moufouma-Okia, W., Pean, C., Pidcock, R., Connors, S., Matthews, J.B.R., Chen, Y., Zhou, X., Gomis, M.I., Lonnoy, E., Maycock, T., Tignor, M., Waterfield, T. (Eds.), Global Warming of 1.5oC. An IPCC Special Report on the Impacts of Global Warming of 1.5oC above Pre-Industrial Levels and Related Global Greenhouse Gas Emission Pathways, in the Context of Strengthening the Global Response to the Threat of Climate Change,. Geneva.

Kelemen, P., Benson, S.M., Pilorgé, H., Psarras, P., Wilcox, J., 2019. An Overview of the Status and Challenges of CO2 Storage in Minerals and Geological Formations. Front. Clim. 1, 1–20. https://doi.org/10.3389/fclim.2019.00009

Marieni, C., Přikryl, J., Aradóttir, E.S., Gunnarsson, I., Stefánsson, A., 2018. Towards 'green' geothermal energy: Co-mineralization of carbon and sulfur in geothermal reservoirs. Int. J. Greenh. Gas Control 77, 96–105. https://doi.org/10.1016/j.ijggc.2018.07.011

Matter, J.M., Broecker, W.S., Gislason, S.R., Gunnlaugsson, E., Oelkers, E.H., Stute, M., Sigurdardóttir, H., Stefansson, A., Alfreõsson, H.A., Aradóttir, E.S., Axelssone, G., Sigfússon, B., Wolff-Boenisch, D., 2011. The CarbFix Pilot Project - Storing carbon dioxide in basalt. Energy Procedia 4, 5579–5585. https://doi.org/10.1016/j.egypro.2011.02.546

Matter, J.M., Stute, M., Snæbjörnsdóttir, S.Ó., Oelkers, E.H., Gislason, S.R., Aradóttir, E.S., Sigfússon, B., Gunnarsson, I., Sigurdardóttir, H., Gunnlaugsson, E., Axelsson, G., Alfredsson, H.A., Wolff-Boenisch, D., Mesfin, K.G., Dideriksen, K., Broecker, W.S., 2016. Rapid carbon mineralization for permanent disposal of anthropogenic carbon dioxide emissions. Science (80-.). 352, 1312–1314. https://doi.org/10.1126/science.aad8132

Matter, J.M., Takahashi, T., Goldberg, D.S., 2007. Experimental evaluation of in situ CO2 water rock reactions during CO2 injection in basaltic rocks: Implications for geological CO2 sequestration. Geochemistry, Geophys. Geosystems 8. https://doi.org/10.1029/2006GC001427

McCarthy, J.J., Canziani, O.F., Leary, N.A., Dokken, D., White, K.S., 2001. Climate Change 2001: Impacts, Adaptation, and Vulnerability. Cambridge University Press, Cambridge, United Kingdom.

McGrail, B.P., Ho, A.M., Reidel, S.P., Schaef, H.T., 2003. Use and Features of Basalt Formations for Geologic Sequestration. Greenh. Gas Control Technol. - 6th Int. Conf. II, 1637–1640. https://doi.org/10.1016/b978-008044276-1/50264-6

McGrail, B.P., Schaef, H.T., Ho, A.M., Chien, Y.-J., Dooley, J.J., Davidson, C.L., 2006. Potential for carbon dioxide sequestration in flood basalts. J. Geophys. Res. Solid Earth 111. https://doi.org/10.1029/2005JB004169

McGrail, B.P., Spane, F.A., Sullivan, E.C., Bacon, D.H., Hund, G., 2011. The Wallula basalt sequestration pilot project. Energy Procedia 4, 5653–5660. https://doi.org/10.1016/j.egypro.2011.02.557

McGrail, P., Schaef, H.T., Spane, F.A., Cliff, J.B., Qafoku, O., Horner, J.A., Thompson, C.J., Owen, A.T., Sullivan, C.E., 2017a. Field validation of supercritical CO2 reactivity with basalts. Environ. Sci. Technol. Lett. 4, 6–10. https://doi.org/10.1021/acs.estlett.6b00387

McGrail, P., Schaef, H.T., Spane, F.A., Horner, J.A., Owen, A.T., Cliff, J.B., Qafoku, O., Thompson, C.J., Sullivan, E.C., 2017b. Wallula Basalt Pilot Demonstration Project : Post-Injection Results and Conclusions. Energy Procedia 114, 5783–5790. https://doi.org/10.1016/j.egypro.2017.03.1716

Muraoka, H., Takahashi, M., Sundhoro, H., Dwipa, S., Soeda, Y., Momita, M., Shimada, K., 2010. Geothermal Systems Constrained by the Sumatran Fault and Its Pull-Apart Basins in Sumatra, Western Indonesia, in: World Geothermal Congress 2010. Bali, Indonesia, pp. 25–29.

Oelkers, E.H., Gislason, S.R., Matter, J.M., 2008. Mineral Carbonation of CO2. Elements 4, 333–337. https://doi.org/10.2113/gselements.4.5.333

Oelkers, E.H., Schott, J., 1995. Experimental study of anorthite dissolution and the relative

mechanism of feldspar hydrolysis. Geochim. Cosmochim. Acta 59, 5039–5053. https://doi.org/10.1016/0016-7037(95)00326-6

Oxburgh, R., Drever, J.I., Sun, Y.T., 1994. Mechanism of plagioclase dissolution in acid solution at 25°C. Geochim. Cosmochim. Acta 58, 661–669. https://doi.org/10.1016/0016-7037(94)90496-0

Palandri, J.L., Kharaka, Y.K., 2004. A compilation of rate parameters of water-mineral interaction kinetics for application to geochemical modeling, USGS Open File Report. Denver, US. https://doi.org/10.1098/rspb.2004.2754

Parkhurst, D.., Appelo, C.A.J., 1999. User's guide to PHREEQC version 3 - a computer program for speciation, batch-reaction, one-dimensional transport, and inverse geochemical calculations, Water-Resources Investigations Report 99-4259.

Parkhurst, D.L., Appelo, C.A.J., 2013. Description of input and examples for PHREEQC version 3 - A computer program for speciation, batch-reaction, one-dimensional transport, and inverse geochemical calculations, in: U.S Geological Survey Techniques and Methods, Book 6, Available Only at Https://Pubs.Usgs.Gov/Tm/06/A43/. p. 497.

Pogge von Strandmann, P.A.E., Burton, K.W., Snæbjörnsdóttir, S.Ó., Sigfússon, B., Aradóttir, E.S., Gunnarsson, I., Alfredsson, H.A., Mesfin, K.G., Oelkers, E.H., Gislason, S.R., 2019. Rapid CO2 mineralisation into calcite at the CarbFix storage site quantified using calcium isotopes. Nat. Commun. 10, 1–7. https://doi.org/10.1038/s41467-019-10003-8

Purnomo, B.J., Pichler, T., 2014. Geothermal systems on the island of Java, Indonesia. J. Volcanol. Geotherm. Res. 285, 47–59. https://doi.org/10.1016/j.jvolgeores.2014.08.004

Rosenbauer, R.J., Thomas, B., Bischoff, J.L., Palandri, J., 2012. Carbon sequestration via reaction with basaltic rocks: Geochemical modeling and experimental results. Geochim. Cosmochim. Acta 89, 116–133. https://doi.org/10.1016/J.GCA.2012.04.042

Santoso, D., Suparka, M.E., Sudarman, S., Sauri, S., 1995. The Geothermal Fields in Central Part of the Sumatra Fault Zone As Derived From Geophysical Data, in: World Geothermal Congress, 1995. Florence, Italy, pp. 1363–1366.

Sawin, J., Seyboth, K., Sverrisson, F., 2017. Renewables 2017 Global Status Report. Paris.

Schaef, H.T., McGrail, B.P., 2009. Dissolution of Columbia River Basalt under mildly acidic conditions as a function of temperature: Experimental results relevant to the geological sequestration of carbon dioxide. Appl. Geochemistry 24, 980–987. https://doi.org/10.1016/j.apgeochem.2009.02.025

Schoen, R., Roberson, C.E., 1970. Structures of Aluminum Hydroxide and Geochemical Implications. Am. Mineral. 55, 43–77.

Shibuya, T., Yoshizaki, M., Masaki, Y., Suzuki, K., Takai, K., Russell, M.J., 2013. Reactions between basalt and CO2-rich seawater at 250 and 350°C, 500bars: Implications for the CO2 sequestration into the modern oceanic crust and the composition of hydrothermal vent fluid in the CO2-rich early ocean. Chem. Geol. 359, 1–9. https://doi.org/10.1016/j.chemgeo.2013.08.044

Siegel, D.I., Pfannkuch, H.O., 1984. Silicate mineral dissolution at pH 4 and near standard temperature and pressure. Geochim. Cosmochim. Acta 48, 197–201. https://doi.org/10.1016/0016-7037(84)90362-4

Sieh, K., Natawidjaja, D., 2000. Neotectonics of the Sumatran fault, Indonesia. J. Geophys. Res. 105, 28295–28326. https://doi.org/10.1029/2000JB900120

Snæbjörnsdóttir, S.Ó., Oelkers, E.H., Mesfin, K.G., Aradóttir, E.S., Dideriksen, K., Gunnarsson, I., Gunnlaugsson, E., Matter, J.M., Stute, M., Gislason, S.R., 2017. The chemistry and saturation states of subsurface fluids during the in situ mineralisation of CO2 and H2S at the CarbFix site in SW-Iceland. Int. J. Greenh. Gas Control 58, 87–102. https://doi.org/10.1016/j.ijggc.2017.01.007

Snæbjörnsdóttir, S.Ó., Sigfússon, B., Marieni, C., Goldberg, D.S., Oelkers, E.H., 2020. Carbon dioxide storage through mineral carbonation. Nat. Rev. Earth Environ. https://doi.org/10.1038/s43017-019-0011-8

Sugisaki, R., 1972. Tectonic Aspects of Andesite Line. Nat. Phys. Sci. 240, 109–111. https://doi.org/10.1038/physci240109a0

Suharmanto, P., Fitria, A.N., Ghaliyah, S., 2015. Indonesian Geothermal Energy Potential as Source of Alternative Energy Power Plant, in: Renewable Energy and Energy Conversion Conference and Exhibition. Knowledge E, pp. 119–124. https://doi.org/10.18502/ken.v1i1.325

Takaya, Y., Nakamura, K., Kato, Y., 2015. Dissolution of altered tuffaceous rocks under conditions relevant for CO2 storage. Appl. Geochemistry 58, 78–87. https://doi.org/10.1016/j.apgeochem.2015.03.012

Tole, M.P., Lasaga, A.C., Pantano, C., White, W.B., 1986. The kinetics of dissolution of nepheline (NaAlSiO4). Geochim. Cosmochim. Acta 50, 379–392. https://doi.org/10.1016/0016-7037(86)90191-2

Wolff-Boenisch, D., 2011. On the buffer capacity of CO2-charged seawater used for carbonation and subsequent mineral sequestration. Energy Procedia 4, 3738–3745. https://doi.org/10.1016/j.egypro.2011.02.307

Wolff-Boenisch, D., Gislason, S.R., Oelkers, E.H., 2006. The effect of crystallinity on dissolution rates and CO2 consumption capacity of silicates. Geochim. Cosmochim. Acta 70, 858–870. https://doi.org/10.1016/j.gca.2005.10.016

Wolff-Boenisch, D., Gislason, S.R., Oelkers, E.H., Putnis, C. V., 2004. The dissolution rates of natural glasses as a function of their composition at pH 4 and 10.6, and temperatures from 25 to 74°C. Geochim. Cosmochim. Acta 68, 4843–4858. https://doi.org/10.1016/j.gca.2004.05.027

Zhang, R., Zhang, X., Hu, S., 2015. Basalt-water interactions at high temperatures: 1. Dissolution kinetic experiments of basalt in water and NaCl-H2O at temperatures up to 400°C, 23MPa and implications. J. Asian Earth Sci. 110, 189–200. https://doi.org/10.1016/j.jseaes.2015.03.042

Chapter 4: Experimental CO_2 Storage in Andesitic Geothermal Reservoir Rocks – examining the possibility of carbonate mineral precipitation.

4.1 Introduction

As has been discussed in detail in Sections 1.4.3 and 1.4.4, geothermal reservoirs containing basaltic type rocks make excellent targets for carbon sequestration via CO_2 injection. However, basaltic systems are not available worldwide. For example, Indonesian geothermal sites are often associated with andesitic, rather than basaltic rock systems, as are other locations worldwide (Boedihardi *et al*., 1993; BP, 2020; Purnomo and Pichler, 2014; Sawin *et al*., 2017; Sugisaki, 1972). Limited laboratory scale research has been conducted investigating the potential for sequestration of carbon dioxide via carbonation reactions in andesitic locations (Marieni *et al*., 2018; Takaya *et al*., 2015; Wolff-Boenisch *et al*., 2006). Although the high occurrence of divalent cations and rapid dissolution rates of relatively fresh basaltic systems does make them the current most suitable target for permanent carbon sequestration via mineralisation reactions, several studies acknowledge that more research is needed on alternative systems, such as andesitic and those with more alteration minerals, to examine whether the technique can be made available in more locations worldwide (Kelemen *et al*., 2019; Marieni *et al*., 2018; Takaya *et al*., 2015). Previous studies have highlighted the importance of studying bulk rock dissolution, rather than isolated minerals, to evaluate the potential of formations for permanent mineral sequestration of carbon dioxide (Matter *et al*., 2007). It is commonly recognised that the rate limiting step for the sequestration of CO_2 via this mineral sequestration technique is the release of divalent cations from mineral dissolution (Oelkers *et al*., 2008; Wolff-Boenisch *et al*., 2006). Previous studies have investigated cation release from basaltic type rocks in laboratory conditions (Gudbrandsson *et al*., 2011; Wells *et al*., 2017) to determine their suitability for sequestration, and also investigated potential calcite

precipitation with basaltic type systems (Hangx and Spiers, 2009; Schaef *et al*., 2009; Shibuya *et al*., 2013). This present study aims to investigate whether cation release from andesitic rocks is appreciable under CO_2 injection conditions, and to examine whether any calcite precipitation occurs, to assist in evaluating whether conducting larger field scale carbon sequestration projects in andesitic systems may be a viable option.

4.2 Methodology

4.2.1 Materials

Three andesitic core samples (B1, C1 and I1) were provided by Supreme Energy PT, obtained from a geothermal field located in Sumatra Island, Indonesia, from between 1 and 2 km depth. Further description of the sampling location is provided in Section 3.2.1, and an in-depth characterisation of crushed portions of the samples is provided in Section 3.3.1 of this thesis.

4.2.2 Sample preparation and characterisation

The core samples were split open to obtain fresh surfaces and smaller pieces were chipped off from the inside surface of each core. Three pieces were selected from each sample core with sufficient surface area (approx. 1 cm^3) to examine with electron microscopy equipment. The samples were embedded epoxy resin 25 mm diameter blocks and the sample surface polished with a series of abrasive pads and water-based diamond polishes (the finest being 2µm) to expose the desired sample face and achieve a smooth surface for subsequent analysis. All nine samples were then carbon coated to a thickness close to 20 nm using an Edwards evaporation coater. The polished samples were analysed via Mineral Liberation Analysis with a FEI Q600 SEM to obtain mineralogical phase maps of each sample, and Electron Probe Microanalysis (EPMA) with a JEOL JXA8200 Microprobe to gain point analysis chemical composition detail of minerals likely to react such as feldspar minerals. Mineral calibration standards with a known composition similar to that expected from the samples in this study were analysed with the EPMA first, and the probe was operated with an accelerating voltage of 20 keV, probe current of 20 nA and a beam diameter of 2 µm.

After the initial characterisation, the samples were then carefully polished again with the finest grade water suspended diamond polish to just remove the carbon coat. Each sample was individually placed in a batch reactor autoclave system (Figure 1) and reacted under the chosen conditions (Table 1) for each experiment. After experiment, the samples were carbon

coated and analysed using the same SEM MLA and EPMA techniques. The carbon coating is necessary to prevent charge build-up of the non-conductive samples and is the preferred coating for X-ray techniques compared to other metal coatings which can obscure detail in X-ray spectra and would not be compatible with the EPMA standards. Energy Dispersive X-ray Spectroscopy (EDS) techniques (using an EDS detector from Oxford Instruments attached to the SEM) were also used on the samples post experiment to collect compositional maps of areas of interest.

The fluid conditions were chosen to attempt to simulate a variety of geothermal reservoir conditions close to and far from the site of fluid injection. Previous studies indicate significant amounts of calcium are likely to be released into the reservoir fluids due dissolution reactions between silicate minerals and acidic fluids containing dissolved carbon dioxide (Marieni *et al*., 2018; Takaya *et al*., 2015; Wolff-Boenisch *et al*., 2006). The results included in Chapter 3 of this thesis confirm calcium release from these rock samples under acidic fluid conditions. Therefore, 2000 ppm of calcium was included in the fluids at the start of some experiments to simulate conditions where significant mineral dissolution has already taken place. These experiments aim to examine the conditions that might occur if CO_2 injection were to be implemented at this geothermal site in Indonesia. It is assumed significant mineral dissolution would have already take place in this scenario due to the acidic nature of the injected fluids and therefore significant calcium would be available, hence the choice of 2000 ppm of calcium included in some of the starting experimental fluids. In some experimental conditions, a high partial pressure of CO_2 was used (150 bar) to simulate pH values close to 3 which are likely to be experienced close to where carbon dioxide charged fluids are injected into a reservoir and to ensure reactions happened on an appreciable timescale for observation (Matter *et al*., 2007) (Table 4.1). In other experimental conditions, a lower partial pressure of CO_2 was used to simulate conditions which may be experienced at larger distances from the injection site, where the carbon dioxide concentration will have become diluted on mixing with the reservoir fluids and may also have been consumed by mineral dissolution as it passes through the

reservoir rock (Assayag *et al*., 2009; Bickle *et al*., 2017; Matter *et al*., 2007). Experiments are labelled according to the sample used (B1, C1 or I1) and either HP (higher-pressure CO_2) or LP (lower pressure CO_2), and either noCa or Ca indicating if calcium was added to the starting fluids. An experimental duration of 50 hours was chosen, as calcite precipitation reactions are expected to be relatively rapid once saturation state is reached (Lebron and Suarez, 1996; Peng *et al*., 2015; Zhang and Dawe, 1998) and this study is aiming to identify which conditions need to be met in andesitic reservoirs to initiate calcite precipitation.

Fluid data was also provided by Supreme Energy PT obtained from the same geothermal site as the rock samples. This data was used to design the representative geothermal fluids and further information describing its chemistry can be found in Chapter 3, Table 3.1.

Table 4.1: Starting conditions for each experiment, including rock sample used and concentrations of added species.

Experiment identifier	Temperature	CO_2 pressure (bar)	Na (mmol/kg)	K (mmol/kg)	Ca (mmol/kg)	Duration (hours)
B1_HPnoCa	100ºC	150	43.5	7.67	0	50
B1_HPCa	100ºC	150	43.5	7.67	50.0	50
B1_LPCa	100ºC	10	43.5	7.67	50.0	50
C1_HPnoCa	100ºC	150	43.5	7.67	0	50
C1_HPCa	100ºC	150	43.5	7.67	50.0	50
C1_LPCa	100ºC	10	43.5	7.67	50.0	50
I1_HPnoCa	100ºC	150	43.5	7.67	0	50
I1_HPCa	100ºC	150	43.5	7.67	50.0	50
I1_LPCa	100ºC	10	43.5	7.67	50.0	50

4.2.3 High Temperature Batch Experiments

A high-pressure autoclave batch system was used to conduct the rock-fluid experiments in this study (Figure 2.7). At the start of each experiment, a 'blank' fluid sample was collected from the prepared fluids prior to contact with the experimental equipment or sample, the compositions of all starting fluids are found in Table 4.1. Then the resin embedded rock sample was added to the vessel with 300 mL of fluid. The autoclave system was sealed and the system was flushed 3 times with 10 bar CO_2 to simulate anoxic conditions of geothermal fluid injection (Aradóttir *et al*., 2015; Barber *et al*., 2005). The temperature and pressure were incrementally increased to reach desired conditions (Table 4.1). Fluid sample 1 of each experiment was then collected via the sample outlet tube immediately after conditions were reached, and fluid sample numbers 2-5 were taken at incremental time steps throughout each experiment to monitor changing cation concentrations in the fluids. At the end of the 50-hour experimental duration, the heating was stopped, and the pressure slowly vented once the internal temperature dropped to 90^{o}C. The vessel was removed from the heating jacket and left to cool. A final fluid sample 6 was collected directly from the opened vessel and the resin embedded rock sample was collected and gently rinsed with MQ water.

An additional experiment was run using the same conditions and sampling methods as those listed in Table 4.1, but the 'solid sample' used was a round block of resin with no rock sample embedded. This was conducted to confirm the resin material itself was resistant to these experimental conditions and did not influence the fluid compositions of the experiment. Results from ICP-OES analysis confirmed no observed changes in the fluids taken throughout this resin only experiment, which confirmed the use of the resin as a suitable sample containing medium.

4.2.4 Fluid Analysis

A Perkin Elmer Inductively Coupled Plasma Optical Emission Spectrometer (ICP-OES) 2000 DV was used to analyse the fluids collected throughout the experiments. The instrument has

a detection limit of 0.1 mg/L and analytical uncertainties within the order of ≤5%. Calibration standards from 0.1 to 30 mg/L were prepared from 100 mg/L standard solution from Fisher Chemical and ultrapure 2% HNO_3, for the elements Si, Al, Na, K, Ca, and Mg. For each fluid sample, 1/10 and 1/100 dilutions were made with 2% HNO_3 and measured, along with the full concentration fluids.

4.3 Results

4.3.1 MLA

Analysis of the samples pre-experiment with MLA indicates the original samples mineralogy are very heterogeneous in nature, with several alteration minerals present alongside rock-forming minerals. The most abundant minerals in the samples are generally quartz (SiO_2), potassium feldspars ($KAlSi_3O_8$), sodium feldspars ($NaAlSi_3O_8$), plagioclase (Na/Ca feldspars) minerals ($NaAlSi_3O_8$ – $CaAl_2Si_2O_8$), stilbite ($NaCa_4(Si_{27}Al_9)O_{72}$) and chamosite ($(Fe,Mg)_5Al(Si_3Al)O_{10}(OH,O)_8$), with minor amounts of minerals such as titanite ($CaTiSiO_5$), epidote ($Ca_2(Fe,Al)_3(SiO_4)_3(OH)$) and calcite ($CaCO_3$) (full MLA results contained within the appendix, Tables A1-A18 and Figures A1-A9). More specifically, the B1 sample has quartz, albite ($NaAlSi_3O_8$) and potassium feldspars in highest abundance with stilbite also present in significant proportions. The C1 sample contains albite in significantly higher abundance than any other minerals, with quartz, stilbite and chamosite all in similar abundance with smaller amounts of potassium feldspar and plagioclase minerals (the presence of all minerals was confirmed with EPMA). Sample I1 generally has a spread of the most abundant minerals; however, sample S8 showed a particularly high proportion from sodium feldspars compared to the others. Small examples of calcite were observed on some sample surfaces. The B1 samples generally have the highest area abundance of calcite in the pre-experimental samples compared to the other rock samples, whereas the C1 samples have the lowest amount, with the S5 sample showing no measurable areas of calcite in the MLA analysis conducted pre-experiment (Table 4.2). The total composition of the samples (Table 4.2), the mineral formulas of the components (Table 4.2 and Table 4.3) and the % contribution form the cations Ca, Mg, and Fe were used to calculate the molar % of each sample in terms of Ca, Mg, and Fe, which averaged roughly 26% across all the andesitic rock samples used in this study. The amount of these divalent cations is an important consideration, as they are essential for potential carbonate precipitation. This value is similar to values found in previous studies examining basaltic samples (McGrail *et al*., 2006).

To examine any changes in the samples as a result of rock-fluid interactions in each of the experimental conditions, MLA was also conducted on the same samples post experiment, to compare to the pre-experiment analysis. Post experiment, the results for the B1 samples indicate the abundance of the most common minerals remained the same within the 5% error margins across all experimental conditions. All experimental conditions used with the B1 sample resulted in a significant loss of calcite, with only 0.4-2.6% calcite present in the post-experimental analysis compared to pre-experimental measurements (Table 4.2).

The experimental conditions used with the C1 sample resulted in no significant change to the abundance of the most common minerals within the 5% error margins. The MLA results from the C1_HPnoCa experimental condition indicate the abundance of calcite remained the same, though it should be noted that there was only a very small amount of calcite present in the sample before experiment. The C1_HPCa sample initially had no calcite according to the pre-experimental MLA analysis, but post experiment there was an increase, taking the weight % contribution from 0 before experiment to 0.01% after. The C1_LPCa experiment had only 3.3% calcite remaining after the experiment compared to the pre-experiment analysis (Table 4.2).

The post-experimental MLA results for the I1 sample indicate that in the I1_HPnoCa experiment, there was little change in the abundance of the most common minerals. However, in the experimental conditions with added calcium (I1_HPCa and I1_LPCa) there appears to be a slight increase in the area abundance of chamosite and plagioclase minerals above the 5% error margins. The I1_HPnoCa experiment showed a complete loss of calcite, and the I1_LPCa experiment also showed a significant loss of calcite. However, the I1_HPCa experiment had a significant 400% increase in the area abundance of calcite. This trend is similar to the C1 sample in this particular experimental condition (Table 4.2).

Table 4.2: Results from MLA of rock sample surfaces both pre and post experiment, showing the area abundance of minerals in microns squared to the nearest 10 microns. Associated experimental error for each MLA result is 5%, which is the error associated with this measurement technique, as discussed in Section 2.2.2

	Quartz (SiO_2)	Stilbite ($NaCa_4$ ($Al_8Si_{27}O_{72}$))	Chamosite ($(Fe,Mg)_5$ $Al(Si_3Al)$ $O_{10}(OH,O)_8$)	Na/Ca Feldspar ((Na,Ca) $Al_{1.5}Si_{2.5}O_8$)	K Feldspar ($KAlSi_3O_8$)	Na Feldspar ($NaAlSi_3O_8$)	Calcite ($CaCO_3$)
B1_HPnoCa pre	26542050	10482230	3601200	6218580	24875170	38632970	677160
B1_HPnoCa post	26989540	10111940	3561170	6770090	24369700	41755390	16790
B1_HPCa pre	34124420	13069510	3099830	1780110	31417480	35547490	460290
B1_HPCa post	34529560	11942000	2378740	1996490	30944480	36214510	2950
B1_LPCa pre	25919220	10168520	2286420	2239630	23809330	30197930	270440
B1_LPCa post	26492420	9047380	1681670	2643110	23219740	31101690	2140
C1_HPnoCa pre	19178830	15420350	27903370	2172680	8544550	57429550	980
C1_HPnoCa post	19795900	14419730	26906320	1598230	8533060	60550210	980
C1_HPCa pre	10058400	10594850	15620900	1289860	5828510	39783800	0
C1_HPCa post	10349210	9082480	14928160	1037910	5817820	42084260	7290
C1_LPCa pre	17248830	8813380	19982480	1487980	9691590	55348680	9710
C1_LPCa post	17521010	10457930	19480990	1623050	9624200	55096950	280
I1_HPnoCa pre	13147430	9136460	4951410	9678450	26086800	23939580	17360
I1_HPnoCa post	13489160	8294840	5276430	10594210	27031310	26062480	0
I1_HPCa pre	16196740	8028090	3589810	4296450	19483110	38979240	10230
I1_HPCa post	17943670	7478290	5487740	7012400	22669110	42329440	55380
I1_LPCa pre	14813360	6903170	2439770	5920160	19051070	12907520	3100
I1_LPCa post	15479840	6294990	3756440	6987680	19137770	14468790	860

4.3.2 EPMA

Electron probe microanalysis was used to determine the average feldspar chemical composition in each of the rock samples, both before and after they interacted with the experimental fluids. The phase maps created after MLA were used to identify and target feldspar crystals with EPMA. At least 30 separate analysis points were collected and used to find the average composition of the feldspars across the sample (Table 4.3). The full EPMA results data set can be found in the appendix (Table A19).

Table 4.3: Averaged and normalised composition of the feldspars in each rock sample, both before and after experiment, determined by EPMA analysis of at least 30 individual points.

Rock Sample	Average composition before experiment	Average composition after experiment
B1_HPnoCa	$Na_{0.75}K_{0.05}Ca_{0.20}Si_{2.83}Al_{1.17}O_8$	$Na_{0.72}K_{0.05}Ca_{0.23}Si_{2.73}Al_{1.27}O_8$
B1_HPCa	$Na_{0.81}K_{0.08}Ca_{0.11}Si_{2.90}Al_{1.10}O_8$	$Na_{0.87}K_{0.05}Ca_{0.08}Si_{2.86}Al_{1.14}O_8$
B1_LPCa	$Na_{0.84}K_{0.01}Ca_{0.15}Si_{2.83}Al_{1.17}O_8$	$Na_{0.81}K_{0.03}Ca_{0.12}Si_{2.80}Al_{1.20}O_8$
C1_HPnoCa	$Na_{0.90}K_{0.01}Ca_{0.09}Si_{2.96}Al_{1.04}O_8$	$Na_{0.96}K_{0.01}Ca_{0.03}Si_{2.90}Al_{1.10}O_8$
C1_HPCa	$Na_{0.96}K_{0.01}Ca_{0.03}Si_{2.95}Al_{1.05}O_8$	$Na_{0.96}Ca_{0.04}Si_{2.90}Al_{1.10}O_8$
C1_LPCa	$Na_{0.89}Ca_{0.11}Si_{2.90}Al_{1.10}O_8$	$Na_{0.94}K_{0.03}Ca_{0.03}Si_{2.97}Al_{1.03}O_8$
I1_HPnoCa	$Na_{0.63}K_{0.05}Ca_{0.32}Si_{2.72}Al_{1.28}O_8$	$Na_{0.63}K_{0.04}Ca_{0.33}Si_{2.72}Al_{1.28}O_8$
I1_HPCa	$Na_{0.77}K_{0.03}Ca_{0.20}Si_{2.80}Al_{1.20}O_8$	$Na_{0.62}K_{0.11}Ca_{0.27}Si_{2.80}Al_{1.20}O_8$
I1_LPCa	$Na_{0.67}K_{0.01}Ca_{0.32}Si_{2.67}Al_{1.33}O_8$	$Na_{0.69}K_{0.02}Ca_{0.29}Si_{2.74}Al_{1.26}O_8$

4.3.3 SEM

SEM imaging was used to confirm that mineral dissolution had taken place in the rock samples as a result of the experimental conditions they were subjected to. All samples had evidence

of significant dissolution etch pits after experiment, which were not present before experiment on the polished sample surfaces (Figure 4.2).

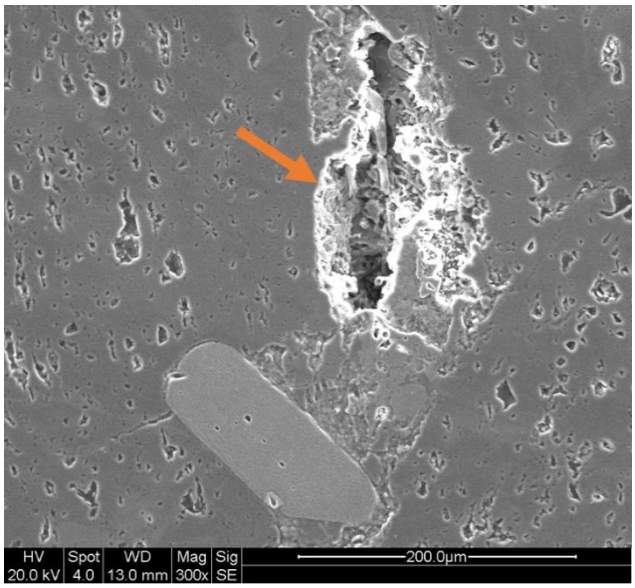


Figure *4.2: Secondary electron SEM image showing significant dissolution pit in the surface of one the B1 samples (B1_HPnoCa), indicated by the arrow. The smaller pits surrounding it were also seen to an extent in the samples pre-experiment, but the abundance and location of these could not be compared pre and post experiment, due to the difficulty in locating exactly the same area in the SEM.*

The MLA phase maps (appendix Figures A1-A9) obtained for the rock samples post experiment were used to identify areas of calcite formation. SEM imaging and EDS analysis was then used to examine these areas more closely. Since the samples were polished perfectly flat prior to experiments, secondary mineral formation can be identified with areas of raised texture on the sample surface. Much of this secondary mineral formation in textural features such as cracks and surface pits was identified as salt (NaCl) using EDS mapping and point analysis (Figure 4.3), with salt formation evidence found in all rock samples after all experiments. The formation of NaCl on the sample surfaces is assumed to be because of precipitation during the process of removing the sample from the equipment. The temperature and pressure are reduced compared to in situ conditions and the sample is then removed from the fluids. Although the sample were gently rinsed with MQ water, this was not done

aggressively to preserve any mineral formation that may have taken place so this can be observed via SEM techniques. Therefore, the salt formation is assumed to be a by-product of this laboratory-based process, which is unlikely to occur in real geothermal reservoir conditions, as the pressure and temperature conditions will remain relatively constant with geothermal fluids always present, which would not allow conditions to promote salt precipitation in the subsurface. The salt precipitation tends to be located along cracks, in dissolution etch pits and along the boundary between the rock sample edge and resin. Some of the secondary mineral formation was identified as calcite using EDS mapping and point analysis (Figure 4.4).

The calcium signals were used to identify areas of increased calcium concentration, which could indicate calcite. The aluminium, silicon, sodium, and chlorine signals were also examined for the same area. If a reduced concentration of these elements was associated with an increased concentration of calcium, it can be assumed the feature of interest is not salt or any of the original rock forming minerals in the sample. The precipitates interpreted as calcite are discrete crystals, of similar morphology to those observed in previous literature studies using basaltic samples (Schaef *et al*., 2013, 2011). The carbon EDS signal is also examined, but the necessity for the samples to be carbon coated prior to SEM analysis means this element cannot reliably used as evidence for calcite formation.

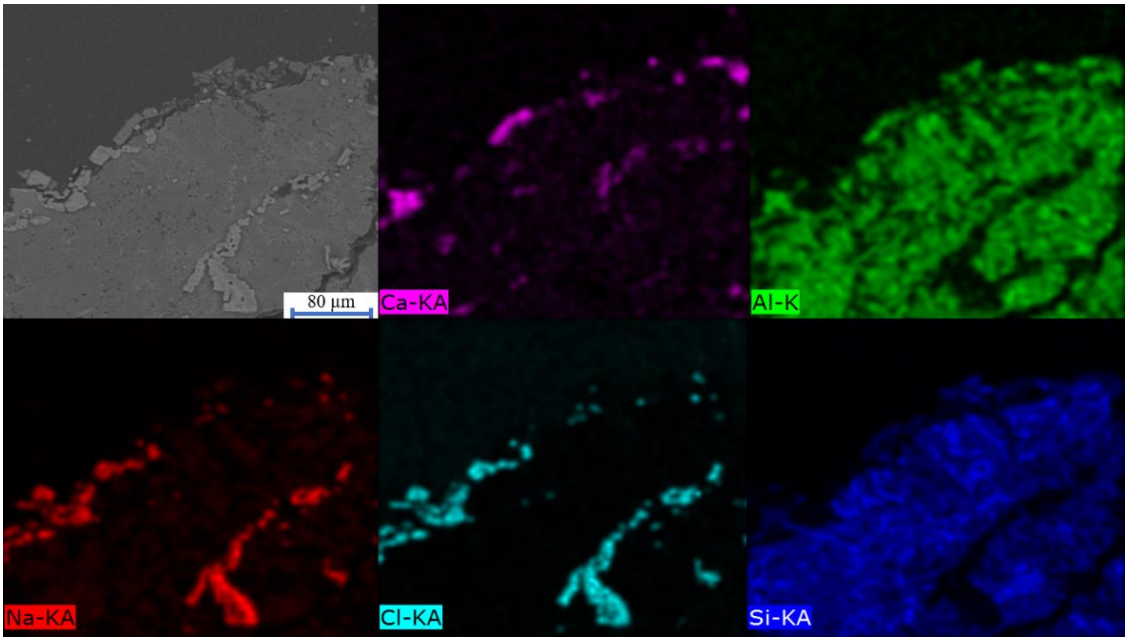


Figure *4.3: EDS mapping of sample C1_HPCa showing an area of salt precipitation, with the sodium and chlorine signals highlighting areas of increased concentration of salt elements. Areas of increased NaCl concentrations coincide with reduced concentrations of aluminium and sodium, which are associated with the rock forming minerals making up the sample's original minerals. The calcium signal is also included since calcite formation was of interest to this study, but areas of increased calcium concentration in this particular area are associated with concentrations of silicon and aluminium, suggesting it incorporated within the original rock formation feldspar minerals, rather than any calcite precipitation. The secondary electron SEM image was taken using an accelerating voltage of 20 keV at a working distance of 13 mm.*

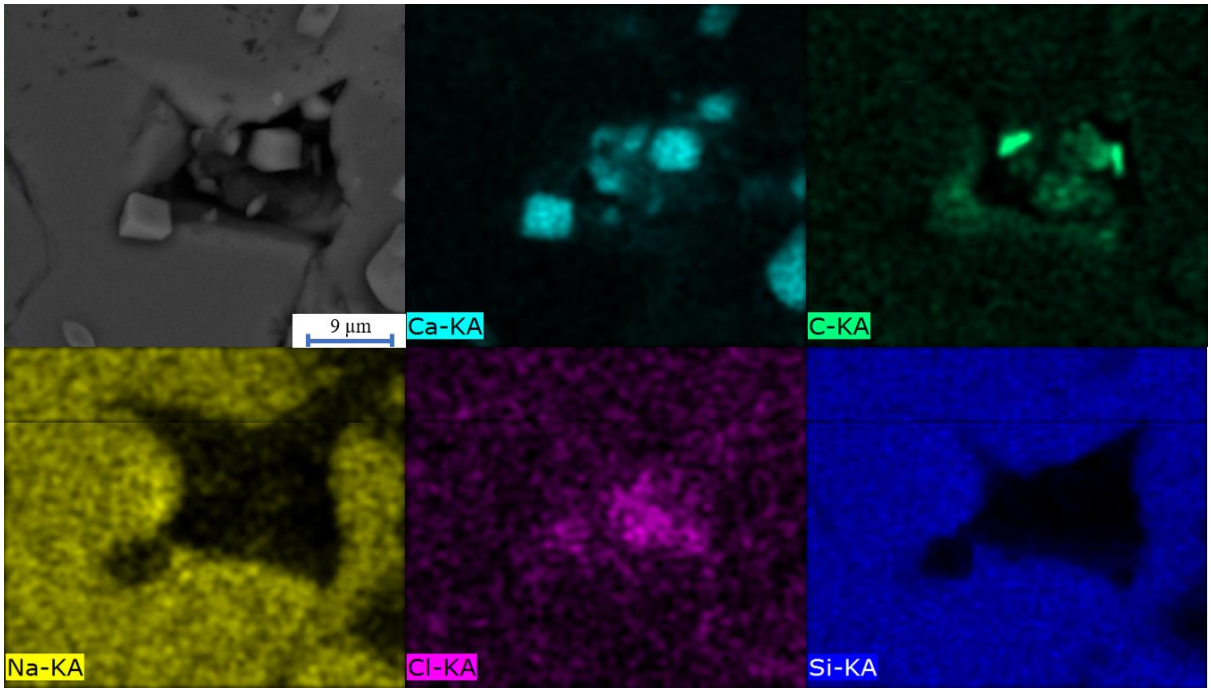


Figure *4.4: EDS mapping of sample I1_HPCa showing an area interpreted as calcite formation, with the calcium signal indicating specific areas of increased calcium concentration. The areas where calcium is particularly concentrated are associated with a lack in concentration of sodium, chlorine, and silicon, indicating the features cannot be identified as salt or any original feldspar rock forming minerals from the sample. The carbon signal shows some increased concentration of this element associated with the calcium concentrations, however, as the whole sample is carbon coated this cannot be used as conclusive evidence for calcite formation. The secondary electron SEM image was taken using an accelerating voltage of 20 keV at a working distance of 13 mm.*

4.3.3 Fluid Composition

The measured silicon release from all rock samples similarly seems to be less pronounced in the conditions with a lower CO_2 concentration compared to those with increased CO_2 concentrations (Figure 4.5A). In all experiments, the silicon increase measured in the fluids is gradual and continuous throughout the experimental duration.

The experimental conditions with a high CO_2 concentration show similar trends in the aluminium release from the different rock samples. The C1 and I1 samples in these high CO_2 conditions show aluminium release up to around 1 ppm at the start, with a slight decline as the experiment continues (Figure 4.5B). The B1 sample shows slightly less aluminium release than the other rock samples but shows a similarly shaped trend of initial increase then gradual decline. The experimental conditions with a lower CO_2 concentration release less aluminium for all rock samples, with the overall release roughly half that for each sample in the equivalent higher CO_2 experimental conditions.

The experiments with no added calcium can be examined for changes in calcium content throughout the experiments in the fluids (it is not possible to examine this in those experiments with added calcium because the error margins become too large to distinguish the small changes that may be attributed to mineral dissolution/precipitation). The B1 and C1 samples do show an increase in calcium concentration, from zero in the initial fluids to between 10-20 ppm by the end of experiment, with the majority of the release occurring rapidly at the start (Figure 4.5C). The I1 sample in this condition shows significantly higher calcium release compared to the other rock samples under the same condition, up to 100 ppm with this release predominantly happening rapidly within the first two samples (2 hours) of the experiment.

In the experimental conditions with no added calcium, for all rock samples there is a small amount of magnesium released into the fluids observed, which occurs rapidly at the start of the experiment and then remains level throughout the remaining experimental duration (Figure 4.5D). In the experiments with added calcium, there is a significantly higher amount of magnesium detected. Small amounts of magnesium chloride ($MgCl_2$) contamination in added calcium chloride ($CaCl_2$) is likely, and so this observation can be mainly attributed to this, rather than as a result of any differing mineral dissolution. This idea is supported as the magnesium concentration in the experiments with added calcium is higher in the fluid samples taken prior to experiment before any initial contact with the rock samples has occurred. In the experimental conditions with added calcium (and therefore added magnesium) this makes the

error margins in the magnesium concentrations larger and therefore it is not possible to distinguish any changes solely due to mineral dissolution or precipitation reactions in the experiments.

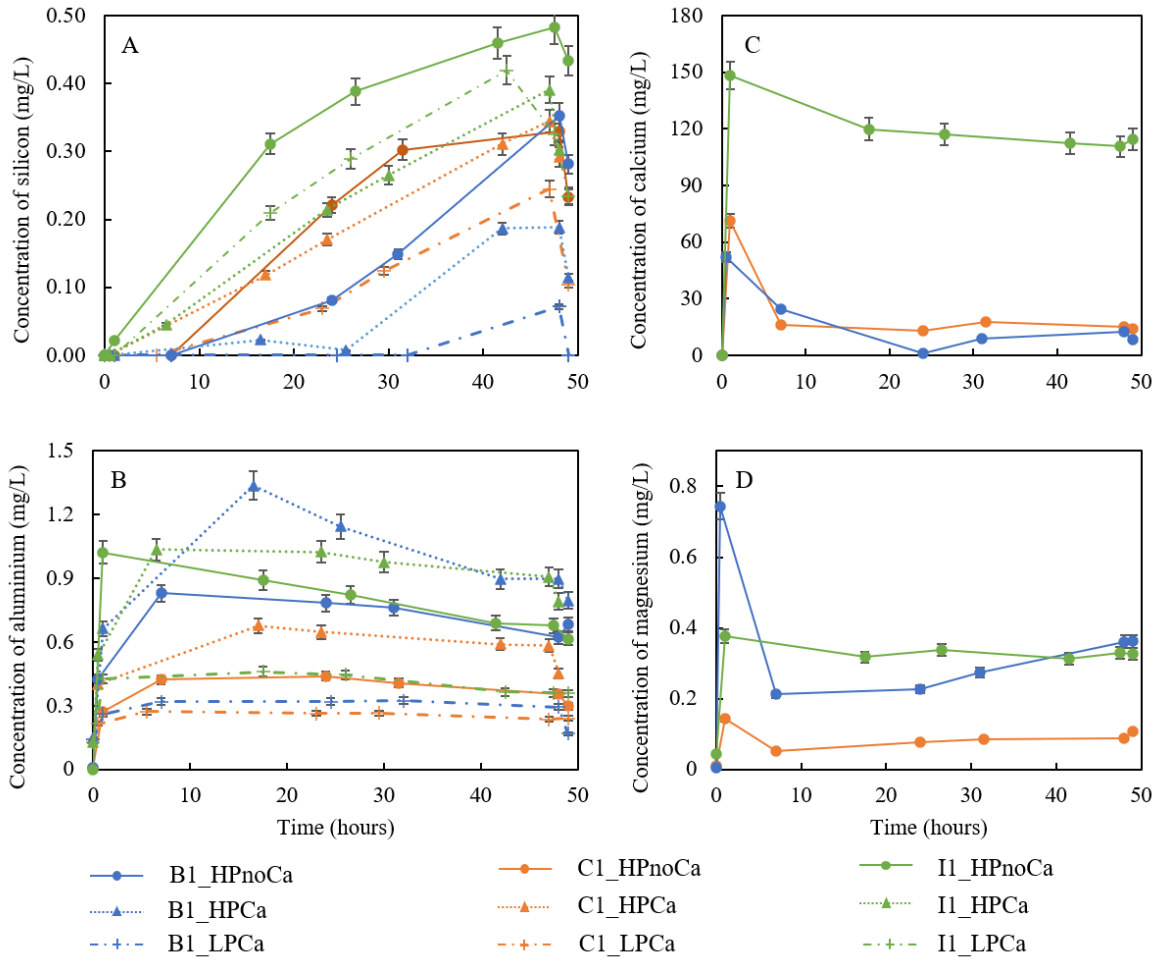


Figure *4.5: Evolution of the concentration of the elements with reaction time for A) silicon, B) aluminium, C) calcium and D) magnesium, in the experimental fluids, measured with ICP-OES. The quantitative data is displayed in table A23 of the appendix.*

4.4 Discussion

4.4.1 Mineral dissolution

The analysis of the fluids indicates some mineral dissolution must be taking place, as the aluminium concentration in all experimental conditions with all samples, increases rapidly to between 0.3 and 1 mg/L above the initial background concentrations measured in the fluids prior to contact with the rock samples (Figure 4.5B). Although this is only a small concentration change, the high fluid to rock ratio used in this study naturally lends itself to small changes in fluid concentrations and so a rise of 1 mg/L is significant and above experimental error in this case. Several of the experiments also show some silicon release into the fluids, most notably the I1 sample across all experimental conditions, and all rock samples in the experimental conditions with a high CO_2 concentration and no added calcium (Figure 4.5A), which is also indicative of mineral dissolution.

No mineral dissolution evidence was observed in the MLA, although the 5% instrumental error margins of this technique may obscure some smaller changes in mineralogy. The most abundant minerals across the samples are quartz, sodium/calcium and potassium feldspars, chamosite and stilbite. Previous literature studies (including but certainly not limited to: Bickle *et al*. (2017), Blum (1994), Carroll and Knauss (2005), Hangx and Spiers (2009), Hartman and Fogler (2007), Luquot *et al*. (2012), Min and Jun (2016), and Takaya *et al*. (2015) investigating the dissolution of all these minerals under acidic conditions, and more specifically in conditions with increased CO_2 concentrations, indicate that the feldspar, chamosite and stilbite minerals in particular are likely to undergo some dissolution in the acidic experimental conditions used in this study. It is likely that each of these minerals experiences some minor dissolution which, in combination, is observed in the cation concentration changes in the fluids (often around 1 mg/L or less) but is not enough for any changes in each individual mineral to be observed in the MLA with its 5% uncertainty error margins.

In the experimental conditions where no calcium was added to the initial fluids, the changing calcium concentration in the fluids can be examined. All rock samples in this condition release some calcium into the fluids very rapidly at the start of the experiments, from 50 mg/L for B1_LPCa to 150 mg/L for I1_LPCa (Figure 4.5C). The I1 sample releases the most calcium into the fluids, with around 100 ppm measured within the first few hours. Some of the detected calcium increase may be attributed to feldspar dissolution. The I1 rock sample in general, and particularly in the I1_HPnoCa experiment, had a feldspar composition with the highest calcium content (Table 4.2) from the EPMA. This sample also released the most silicon into the experimental fluids (Figure 4.5A), suggesting significant mineral dissolution. Plagioclase feldspar mineral dissolution is known to increase with increasing anorthite content (Gudbrandsson *et al*., 2014; Oelkers and Schott, 1995), and the high abundance in general of feldspar minerals in the sample leads to the reasonable assumption that some of the calcium increase detected in the fluids may be attributed to feldspar dissolution. Secondary electron SEM imaging also provides evidence of mineral dissolution. Significant dissolution pits were observed in all samples (Figure 4.2) post experiment, indicating that preferential dissolution of a mineral or minerals with a rapid dissolution rate under these experimental conditions has dissolved or partially dissolved, leaving behind a pit within a surrounding mineral or minerals with a low dissolution rate under these experimental conditions. Similar preferential dissolution features have been seen in experiments using polished basaltic samples (Wells *et al*., 2017).

Some of the calcium detected in the fluids may also be attributed to calcite dissolution. The samples B1 and I1 show a loss of calcite area abundance in the MLA results which supports this idea. The MLA results provide evidence for calcite dissolution across all the experimental conditions for all samples, except C1_HPCa and I1_HPCa. The rapid dissolution of calcite in acidic fluids is a well-known entity, therefore it can reasonably be assumed here that the fluid acidity caused by the increased CO_2 concentrations is sufficient to lead to some calcite dissolution (Peng *et al*., 2015; Regenspurg *et al*., 2015; Rochelle *et al*., 2002). Dissolution of other minor alteration minerals such as anhydrite ($CaSO_4$) may also contribute to the observed

increase in calcium concentrations. All the rock samples had small amounts of anhydrite present according to the MLA before experiment, with no measured anhydrite in the MLA post experiment, suggesting complete dissolution (Kühn *et al*., 2013).

4.4.2 Mineral precipitation

In the experimental condition with a higher CO_2 concentration and calcium added to the initial fluids, the results from the MLA show rock samples C1 and I1 both had an increase in the area abundance of calcite (Table 4.2). Calcium and dissolved carbon dioxide can combine to precipitate solid calcite mineral, as can be seen with equation 4.1 (Gislason *et al*., 2010; Hangx and Spiers, 2009; Matter *et al*., 2007; McGrail *et al*., 2006):

$$(Ca,Mg,Fe)^{2+} + CO_2 + H_2O \leftrightarrow (Ca,Mg,Fe)CO_3 + 2H^+ \quad (4.1)$$

This precipitation process occurs at more appreciable rates, when preceding rock dissolution consumes the generated protons and thereby increases the pH of the fluids to close to neutral values (Wolff-Boenisch, 2011). Future experiments using these samples would benefit from in-situ pH sampling equipment to accurately measure these changes. The results indicate that significant CO_2 concentrations are needed as well as calcium under these experimental conditions, to result in the formation of calcite, as calcite dissolution rather than precipitation was observed in the experimental condition with lower CO_2 concentration and added calcium. However, more experiments with a wider range of conditions need to be conducted to attempt to pinpoint more exactly the ideal concentrations of the two components for calcite formation. It is likely that the higher concentration of CO_2 initially makes the fluids more acidic (Geothermal Communities, 2010; Wolff-Boenisch, 2011), which leads to more mineral dissolution compared to when a lower concentration of CO_2 is used. This increased mineral dissolution will have multiple impacts on the chemistry of the fluids, which may include increased cations available for precipitation reactions as well as mineral dissolution acting to buffer the pH of the solution. If the increased mineral dissolution is able to more effectively buffer the pH of the solution to close to neutral values, then the conditions may become more

suitable for calcite formation (Wolff-Boenisch, 2011), which is why its increase in area abundance was observed in the MLA (Table 4.2).

The MLA phase maps (appendix Figures A1-A9) were used to identify areas where this increase of calcite area abundance occurred, and these areas were then more closely examined with SEM EDS mapping. A few small areas of calcite precipitation were identified by locating areas of texture indicative of secondary mineral formation and then using the EDS to examine the calcium signal, an essential feature of calcite formation (Figure 4.4). If the calcium EDS signal highlighted an area of increased calcium concentration, the aluminium, silicon, sodium and chlorine EDS signals were also examined, as a lack increased signal from these elements in the same feature of interest helps confirm the feature is not a calcium-containing aluminosilicate or salt mineral. Areas of salt precipitation were commonly seen across the sample, particularly along minor fractures and in possible dissolution pits (Figure 4.3).

Experimental studies examining the potential for carbonate mineral formation in basaltic systems found evidence of calcite formation, which led to the initiation of field scale studies. Some of this previous work includes experiments using aqueous solutions with increased temperatures and pressure with increased concentrations of CO_2, which were combined with basaltic rock samples for durations from 95 days to 3.5 years (McGrail *et al*., 2009; Schaef *et al*., 2013, 2011, 2009; Stockmann *et al*., 2011). All these studies observed calcite formation on surfaces, with a variety of crystal morphologies and abundances. Numerical modelling studies conducted prior to this had indicated that basaltic type samples, which contain around 25% combined molar concentration of Ca, Mg and Fe, included in systems with elevated concentrations of CO_2 would initiate carbonate precipitation on the order of around 0.5-1.5 years (Gysi and Stefánsson, 2008; McGrail *et al*., 2006), which was considered to be relatively rapid. The experimental studies clearly provided evidence that this occurred on even shorter timescales, and these encouraging results were used to justify the initiation of field scale projects (Gislason *et al*., 2010; McGrail *et al*., 2010). Calcite formation in these basaltic field

studies was proven with quantitative isotopic and qualitative observations evidence from the injection sites (Matter *et al*., 2016; McGrail *et al*., 2017b, 2017a). The andesitic samples used in this present study have concentrations of divalent cations within their mineralogy's which are comparable to those found in basaltic samples used in experiments investigating carbonate precipitation under similar conditions. The timescales of 3 days used in this present study are far shorter than prior literature examples; however, evidence of calcite precipitation was found with MLA (Table 4.2) and by using SEM imaging and EDS techniques (Figure 4.4).

4.4.3 Implications for carbon sequestration

We can compare the calcium release into the fluids from these andesitic samples to the amounts released in similar studies using basaltic samples. Wells *et al* (2017) conducted experiments using polished pieces of basalt sample at 150˚C and 100 bar of CO_2 pressure and reported approximately 3 mg of calcium was released into 190 mL of experimental fluids within a few days. This would equate to between 10 and 20 mg/L if scaled up to L volumes. Our present study reports similar calcium release at the end of the 50-hour experiment for the B1 and C1 samples in the experimental condition with no calcium added at the start, with the I1 sample releasing even higher amounts, up to 100 mg/L by the end of the experimental duration (Figure 4.5C). Gudbrandsson *et al* (2011) used crushed basaltic samples under acidic pH conditions to examine divalent cation release and reported results after several days indicate calcium to a slightly lesser extent than Wells *et al* (2017) found. The release rate of divalent cations is considered to be one of the most important factors when determining carbonation potential of a reservoir, which will inevitably be linked to the mineralogy of the system. Although basaltic samples are often assumed to have a high carbonation potential due to the presence of minerals such as olivine and pyroxene (with their associated relatively rapid dissolution rates), there are studies that report plagioclase as the most important Ca source for carbonate mineral formation (Marieni and Oelkers, 2018). Since basaltic samples are considered suitable for carbon sequestration due to their appreciable divalent cation release and ability to neutralise acidic fluids (McGrail *et al*., 2006; Wolff-Boenisch *et al*., 2006),

it is reasonable to suggest the andesitic samples used in this study also have high potential for carbon sequestration, since the divalent cation release is also appreciable.

The experimental condition with increased CO_2 and calcium concentrations in combination with the C1 and I1 rock samples does result in some calcite precipitation. This means some of the added CO_2 was sequestered in the form of solid mineral formation in these experimental conditions. The mineralogy of the C1 and I1 samples seems to have facilitated this formation, which indicates that andesitic rock systems may have the potential to be suitable target formation for carbon dioxide sequestration, in the same way as has been proven effective in basaltic systems (Matter *et al*., 2016; McGrail *et al*., 2017b). All rock samples used in this study are described as andesitic in composition, however the results from the MLA indicate the RDC1 and RDI1 samples had a higher area abundance of alteration minerals. This raises the possibility that it is these alteration minerals that influence the fluid compositions in a way that allows calcite precipitation to occur.

Kühn *et al*. (2013) examined the potential for carbonation reaction to occur in basaltic geothermal energy reservoirs as a result of anhydrite dissolution. Results indicated that the presence of anhydrite can assist in the formation of carbonate minerals, due to the release of Ca^{2+} when the anhydrite dissolves in the acidic solutions (acidity induced by CO_2). The process of anhydrite dissolution with reaction of carbonic acid to produce calcite does release additional protons, and so this increased concentration of H^+ ions needs to be consumed for the reaction to proceed, for example by the dissolution of feldspar minerals.

Marieni and Oelkers (2018) reported results indicating that altered mafic reservoirs may be just as efficient as fresh crystalline basaltic reservoirs for carbon sequestration. The presence of alteration minerals such as increased concentrations of albite compared to olivine and pyroxenes has not caused a reduction in Ca release at a magnitude that they considered detrimental to carbonation potential. However, the authors do note this does rely on the precipitation of secondary minerals not altering fluid flow pathways. Further research, such as flow modelling studies, should be conducted to ensure secondary mineral precipitation does

not reduce the injectivity of a target reservoir. Though the mineralogy and divalent cation release of a reservoir is essential when considering its carbon sequestration potential, fluid transport in the subsurface will also have an important influence on the carbonate mineralisation efficiency (Liu *et al*., 2019). A few studies have indicated that reservoirs with slightly slower dissolution kinetics (e.g., altered basaltic reservoirs) may actually be beneficial for the longevity of CO_2 injection into a site. Results suggest more sluggish dissolution would enable the injected CO2 to migrate further from the injection well, and thus the impact of secondary mineral formation is less likely to negatively affect fluid flow near the injection site (Liu *et al*., 2019).

In this present study, the interactions that occurred after just days of reaction with alternative andesitic type rocks was examined, though with increased calcium concentrations in an attempt to reveal any potential for carbonate precipitation further down the timescale of injection. Previous studies have indicated that minerals within andesite samples will release divalent cations into solution (Marieni *et al*., 2018; Takaya *et al*., 2015). Combined with the observation of carbonate mineral formation on the surfaces of the andesitic samples used in this study after just days of reaction, this indicates andesite samples could have high potential for carbon sequestration.

Further longer-term laboratory studies are recommended to examine this potential to expand carbon sequestration via mineralisation across a wider variety of rock systems. The experiments should focus on the amount of detectable calcite after reaction with andesite samples under conditions relevant to carbon dioxide injection and increased calcium concentrations to simulate subsurface conditions further from the site of injection, and examine if surface coatings similar to those found when using basaltic samples for increased timescales can be observed. It is important that future investigations also incorporate modelling studies to examine the long-term fate of any injected CO_2. Previous studies have examined events where CO_2 degassing within volcanic systems has led to increased permeability and transport pathways of gaseous CO_2 up to the surface (Peiffer *et al*., 2018). If we are considering the

injection of acidic gases such as CO_2 into the subsurface, it is essential to ensure negative environmental impacts are avoided, and a greater understanding of the processes which result in CO_2 degassing in such systems will be required (either directly from the volcanic rock systems or from evolution of the gas from that dissolved into the injection fluids).

4.5 Conclusions

Analysis of the sampled fluids indicates that some mineral dissolution is taking place in all experiments, as an increase in the silicon, aluminium, calcium and magnesium concentrations is observed. The I1 sample has an average plagioclase formula with the highest anorthite content and releases the most calcium into the fluids in the condition with the higher pressure of CO_2 and no added calcium. In the experimental condition with a higher CO_2 pressure and calcium added to the initial fluids, the results from the MLA indicate samples C1 and I1 both had an increase in the area abundance of calcite. Areas of interpreted calcite formation were confirmed with EDS mapping. Calcite dissolution rather than precipitation was observed in the experiments with a lower CO_2 pressure and added calcium. This result suggests that significant CO_2 concentrations are required alongside increase calcium concentration to result in the formation of calcite. Further experiments with a wider range of conditions need to be conducted to identify more accurately the ideal concentrations of these two components to promote calcite formation with these andesitic samples.

Previous studies examining the potential for carbon sequestration in basaltic formations conducted laboratory experiments with the aim of observing carbonate precipitation on rock surfaces under conditions relevant for subsurface injection of CO_2 (McGrail *et al*., 2009; Schaef *et al*., 2013, 2011; Schaef and McGrail, 2009; Stockmann *et al*., 2011). The evidence of calcite formation these studies provided led to the initiation of field scale studies examining carbon sequestration potential in basaltic type reservoirs (Gislason *et al*., 2010; McGrail *et al*., 2010). The andesitic samples used in this present study have concentrations of divalent cations comparable to those found in basaltic samples, despite the differences in mineralogy. Although the timescales used here (3 days) are orders of magnitude shorter than those used in the discussed basaltic experiments, a critical finding in this study was the evidence from MLA and EDS techniques which confirmed the formation of minor amounts of calcite minerals have occurred, indicating these andesitic rock samples are likely to be a good target for carbon sequestration. Further longer-term experiments using these andesitic samples should be

conducted to examine if increased timescales promote further calcite formation and ensure experimental results can be more directly compared with previous studies.

The C1 and I1 samples in the experimental condition with increased CO_2 concentration and added calcium resulted in calcite formation observed on the rock sample surfaces. All 3 samples used in this present study are defined as andesitic in composition however, the C1 and I1 samples had an increased area abundance of alteration minerals observed in the MLA. This raises the possibility that these alterations minerals have somehow influenced the fluids in a way that allows calcite formation to occur. However, this conclusion cannot be confirmed without further examination of these particular minerals and their impact on fluid chemistries in conditions relevant to carbon sequestration. Future experiments would benefit hugely from the inclusion of in-situ pH monitoring equipment, which would enable more in-depth analysis of the changing fluid conditions throughout the experimental durations and allow more interpretations on the buffering capacity induced by the samples varying mineralogy's. Future studies should also utilise fluid flow modelling experiments, to examine whether secondary mineral formation may impact the injectivity of a rock system being considered for its carbon sequestration potential.

Overall, the calcium released from the andesitic rock samples used in this study is comparable to that released from basaltic samples under similar experimental conditions (Wells *et al*., 2017) and critically the formation of carbonate minerals was observed in experiments combining high concentrations of calcium with increase CO_2 pressures. Since previous studies used this information to conclude basaltic samples were suitable for carbon sequestration, it is reasonable to suggest that interest in carbon sequestration in andesitic type reservoirs should also be promoted, to expand the potential for permanent mineral trapping of CO_2 to a wider range of volcanic geologies. Andesite type geologies are present across the Earth's surface in various locations (Sugisaki, 1972) and are often associated with areas of high geothermal energy utilisation, such as Indonesia and the Philippines (BP, 2020; Richter, 2021). If permanent carbon sequestration via injection of CO_2 alongside presently injected

geothermal waters can be utilised in andesitic locations as well as basaltic, the CarbFix technique could be utilised more widely and help contribute to reducing global CO_2 emissions.

4.6 References

Aradóttir, E.S., Gunnarsson, I., Sigfússon, B., Gunnarsson, G., Júliusson, B.M., Gunnlaugsson, E., Sigurdardóttir, H., Arnarson, M.T., Sonnenthal, E., 2015. Toward Cleaner Geothermal Energy Utilization: Capturing and Sequestering CO2 and H2S Emissions from Geothermal Power Plants. Transp. Porous Media 108, 61–84. https://doi.org/10.1007/s11242-014-0316-5

Assayag, N., Matter, J.M., Ader, M., Goldberg, D.S., Agrinier, P., 2009. Water–rock interactions during a CO2 injection field-test: Implications on host rock dissolution and alteration effects. Chem. Geol. 265, 227–235. https://doi.org/10.1016/J.CHEMGEO.2009.02.007

Barber, A.J., Crow, M.J., Milsom, J.S., 2005. Sumatra: Geology, Resources and Tectonic Evolution, Geological Society, London, Memoirs. The Geological Society, London.

Bickle, M., Kampman, N., Chapman, H., Ballentine, C., Dubacq, B., Galy, A., Sirikitputtisak, T., Warr, O., Wigley, M., Zhou, Z., 2017. Rapid reactions between CO2, brine and silicate minerals during geological carbon storage: Modelling based on a field CO2 injection experiment. Chem. Geol. 468, 17–31. https://doi.org/10.1016/j.chemgeo.2017.07.031

Blum, A.E., 1994. Feldspars in Weathering, in: Parsons, I. (Ed.), Feldspars and Their Reactions. Kluwer Academic Publishers, pp. 595–630. https://doi.org/10.1007/978-94-011-1106-5

Boedihardi, M., Mulyonol, A., Ginting, A., Mosby, M., Radja, V., 1993. Geology, energy potential and development of Indonesia's geothermal prospects, in: Geological Society of Malaysia, Bulletin. pp. 369–385.

BP, 2020. bp Statistical Review of World Energy.

Carroll, S.A., Knauss, K.G., 2005. Dependence of labradorite dissolution kinetics on CO2(aq), Al(aq), and temperature. Chem. Geol. 217, 213–225. https://doi.org/10.1016/j.chemgeo.2004.12.008

Fridriksson, T., Mateos-Merino, A., Audinet, P., Orucu, A.Y., 2016. Greenhouse Gases from Geothermal Power Production, in: Energy Sector Management Assistance Program (ESMAP) Technical Report;009/16. Washington, DC.

Geothermal Communities, 2010. Chemistry of Thermal Fluids [WWW Document]. Geotherm. Syst. Technol. URL http://www.geothermalcommunities.eu/assets/elearning/3.2.Corrosion&Scalling.pdf (accessed 11.3.17).

Gislason, S.R., Wolff-Boenisch, D., Stefansson, A., Oelkers, E.H., Gunnlaugsson, E., Sigurdardóttir, H., Sigfússon, B., Broecker, W.S., Matter, J.M., Stute, M., Axelsson, G., Fridriksson, T., 2010. Mineral sequestration of carbon dioxide in basalt : A pre-injection overview of the CarbFix project. Int. J. Greenh. Gas Control 4, 537–545. https://doi.org/10.1016/j.ijggc.2009.11.013

Gudbrandsson, S., Wolff-Boenisch, D., Gislason, S.R., Oelkers, E.H., 2014. Experimental determination of plagioclase dissolution rates as a function of its composition and pH at 22°C. Geochim. Cosmochim. Acta 139, 154–172. https://doi.org/10.1016/j.gca.2014.04.028

Gudbrandsson, S., Wolff-Boenisch, D., Gislason, S.R., Oelkers, E.H., 2011. An experimental study of crystalline basalt dissolution from 2 $\leqslant$ pH $\leqslant$ 11 and temperatures from 5 to 75

°C. Geochim. Cosmochim. Acta 75, 5496–5509. https://doi.org/10.1016/j.gca.2011.06.035

Gunter, W.D., Wiwehar, B., Perkins, E.H., 1997. Aquifer disposal of CO2-rich greenhouse gases: Extension of the time scale of experiment for CO2-sequestering reactions by geochemical modelling. Mineral. Petrol. 59, 121–140. https://doi.org/10.1007/BF01163065

Gysi, A.P., Stefánsson, A., 2008. Numerical modelling of CO 2 -water-basalt interaction . Mineral. Mag. 72, 55–59. https://doi.org/10.1180/minmag.2008.072.1.55

Hangx, S.J.T., Spiers, C.J., 2009. Reaction of plagioclase feldspars with CO2 under hydrothermal conditions. Chem. Geol. 265, 88–98. https://doi.org/10.1016/j.chemgeo.2008.12.005

Hartman, R.L., Fogler, H.S., 2007. Understanding the dissolution of zeolites. Langmuir 23, 5477–5484. https://doi.org/10.1021/la063699g

IPCC, 2018. Summary for Policymakers, in: Masson-Delmotte, V., Zhai, P., Portner, H.-O., Roberts, D., Skea, J., Shukla, P.R., Pirani, A., Moufouma-Okia, W., Pean, C., Pidcock, R., Connors, S., Matthews, J.B.R., Chen, Y., Zhou, X., Gomis, M.I., Lonnoy, E., Maycock, T., Tignor, M., Waterfield, T. (Eds.), Global Warming of 1.5oC. An IPCC Special Report on the Impacts of Global Warming of 1.5oC above Pre-Industrial Levels and Related Global Greenhouse Gas Emission Pathways, in the Context of Strengthening the Global Response to the Threat of Climate Change,. Geneva.

Kaszuba, J.P., Janecky, D.R., Snow, M.G., 2005. Experimental evaluation of mixed fluid reactions between supercritical carbon dioxide and NaCl brine: Relevance to the integrity of a geologic carbon repository. Chem. Geol. 217, 277–293. https://doi.org/10.1016/j.chemgeo.2004.12.014

Kelemen, P., Benson, S.M., Pilorgé, H., Psarras, P., Wilcox, J., 2019. An Overview of the Status and Challenges of CO2 Storage in Minerals and Geological Formations. Front. Clim. 1, 1–20. https://doi.org/10.3389/fclim.2019.00009

Kühn, M., Stanjek, H., Peiffer, S., Clauser, C., 2013. Mineral trapping of CO2 in operated geothermal reservoirs – Numerical simulations on various scales. Energy Procedia 40, 454–463. https://doi.org/10.1016/j.egypro.2013.08.052

Lebron, I., Suarez, D.L., 1996. Calcite nucleation and precipitation kinetics as affected by dissolved organic matter at 25°C and pH > 7.5. Geochim. Cosmochim. Acta 60, 2765–2776.

Liu, D., Agarwal, R., Li, Y., Yang, S., 2019. Reactive transport modeling of mineral carbonation in unaltered and altered basalts during CO2 sequestration. Int. J. Greenh. Gas Control 85, 109–120. https://doi.org/10.1016/j.ijggc.2019.04.006

Luquot, L., Andreani, M., Gouze, P., Camps, P., 2012. CO 2 percolation experiment through chlorite/zeolite-rich sandstone (Pretty Hill Formation - Otway Basin-Australia). Chem. Geol. 294–295, 75–88. https://doi.org/10.1016/j.chemgeo.2011.11.018

Marieni, C., Oelkers, E., 2018. Carbon sequestration potential of altered mafic reservoirs. Energy Procedia 146, 68–73. https://doi.org/10.1016/j.egypro.2018.07.010

Marieni, C., Přikryl, J., Aradóttir, E.S., Gunnarsson, I., Stefánsson, A., 2018. Towards 'green' geothermal energy: Co-mineralization of carbon and sulfur in geothermal reservoirs. Int. J. Greenh. Gas Control 77, 96–105. https://doi.org/10.1016/j.ijggc.2018.07.011

Matter, J.M., Broecker, W.S., Stute, M., Gislason, S.R., Oelkers, E.H., Stefánsson, A., Wolff-Boenisch, D., Gunnlaugsson, E., Axelsson, G., Björnsson, G., 2009. Permanent Carbon

Dioxide Storage into Basalt: The CarbFix Pilot Project, Iceland. Energy Procedia 1, 3641–3646. https://doi.org/10.1016/j.egypro.2009.02.160

Matter, J.M., Stute, M., Snæbjörnsdóttir, S.Ó., Oelkers, E.H., Gislason, S.R., Aradóttir, E.S., Sigfússon, B., Gunnarsson, I., Sigurdardóttir, H., Gunnlaugsson, E., Axelsson, G., Alfredsson, H.A., Wolff-Boenisch, D., Mesfin, K.G., Dideriksen, K., Broecker, W.S., 2016. Rapid carbon mineralization for permanent disposal of anthropogenic carbon dioxide emissions. Science (80-.). 352, 1312–1314. https://doi.org/10.1126/science.aad8132

Matter, J.M., Takahashi, T., Goldberg, D.S., 2007. Experimental evaluation of in situ CO2 water rock reactions during CO2 injection in basaltic rocks: Implications for geological CO2 sequestration. Geochemistry, Geophys. Geosystems 8. https://doi.org/10.1029/2006GC001427

McGrail, B.P., Freeman, C.J., Garber, R.D., Beeman, G.H., Tobin, D., Sullivan, E.C., Steffensen, E.J., Wurstner, S.K., Reddy, S., Brown, C.F., Gilmartin, J.P., 2010. Capture and sequestration of CO2 at the Boise White Paper Mill.

McGrail, B.P., Ho, A.M., Reidel, S.P., Schaef, H.T., 2003. Use and Features of Basalt Formations for Geologic Sequestration. Greenh. Gas Control Technol. - 6th Int. Conf. II, 1637–1640. https://doi.org/10.1016/b978-008044276-1/50264-6

McGrail, B.P., Schaef, H.T., Glezakou, V.A., Dang, L.X., Owen, A.T., 2009. Water reactivity in the liquid and supercritical CO2 phase: Has half the story been neglected?, in: Energy Procedia. pp. 3415–3419. https://doi.org/10.1016/j.egypro.2009.02.131

McGrail, B.P., Schaef, H.T., Ho, A.M., Chien, Y.-J., Dooley, J.J., Davidson, C.L., 2006. Potential for carbon dioxide sequestration in flood basalts. J. Geophys. Res. Solid Earth 111. https://doi.org/10.1029/2005JB004169

McGrail, P., Schaef, H.T., Spane, F.A., Cliff, J.B., Qafoku, O., Horner, J.A., Thompson, C.J., Owen, A.T., Sullivan, C.E., 2017a. Field validation of supercritical CO2 reactivity with basalts. Environ. Sci. Technol. Lett. 4, 6–10. https://doi.org/10.1021/acs.estlett.6b00387

McGrail, P., Schaef, H.T., Spane, F.A., Horner, J.A., Owen, A.T., Cliff, J.B., Qafoku, O., Thompson, C.J., Sullivan, E.C., 2017b. Wallula Basalt Pilot Demonstration Project : Post-Injection Results and Conclusions. Energy Procedia 114, 5783–5790. https://doi.org/10.1016/j.egypro.2017.03.1716

Min, Y., Jun, Y.S., 2016. Anorthite Dissolution under Conditions Relevant to Subsurface CO2 Injection: Effects of Na+, Ca2+, and Al3+. Environ. Sci. Technol. 50, 11377–11385. https://doi.org/10.1021/acs.est.6b02207

Oelkers, E.H., Gislason, S.R., Matter, J.M., 2008. Mineral Carbonation of CO2. Elements 4, 333–337. https://doi.org/10.2113/gselements.4.5.333

Oelkers, E.H., Schott, J., 1995. Experimental study of anorthite dissolution and the relative mechanism of feldspar hydrolysis. Geochim. Cosmochim. Acta 59, 5039–5053. https://doi.org/10.1016/0016-7037(95)00326-6

Pearce, J.M., Holloway, S., Wacker, H., Nelis, M.K., Rochelle, C., Bateman, K., 1996. Natural occurrences as analogues for the geological disposal of carbon dioxide. Energy Convers. Manag. 37, 1123–1128. https://doi.org/10.1016/0196-8904(95)00309-6

Peiffer, L., Wanner, C., Lewicki, J.L., 2018. Unraveling the dynamics of magmatic CO2 degassing at Mammoth Mountain, California. Earth Planet. Sci. Lett. 484, 318–328. https://doi.org/10.1016/j.epsl.2017.12.038

Peng, C., Crawshaw, J.P., Maitland, G.C., Trusler, J.P.M., 2015. Kinetics of calcite

dissolution in CO2-saturated water at temperatures between (323 and 373)K and pressures up to 13.8MPa. Chem. Geol. 403, 74–85. https://doi.org/10.1016/j.chemgeo.2015.03.012

Purnomo, B.J., Pichler, T., 2014. Geothermal systems on the island of Java, Indonesia. J. Volcanol. Geotherm. Res. 285, 47–59. https://doi.org/10.1016/j.jvolgeores.2014.08.004

Regenspurg, S., Feldbusch, E., Byrne, J., Deon, F., Driba, D.L., Henninges, J., Kappler, A., Naumann, R., Reinsch, T., Schubert, C., 2015. Mineral precipitation during production of geothermal fluid from a Permian Rotliegend reservoir. Geothermics 54, 122–135. https://doi.org/10.1016/j.geothermics.2015.01.003

Richter, A., 2021. ThinkGeoEnergy's Top 10 Geothermal Countries 2020 - installed power generation capcity (MWe) [WWW Document]. ThinkGeoEnergy. URL https://www.thinkgeoenergy.com/thinkgeoenergys-top-10-geothermal-countries-2020-installed-power-generation-capacity-mwe/ (accessed 5.20.21).

Rochelle, C.A., Bateman, K., Pearce, J.M., 2002. Geochemical interactions between supercritical CO 2 and the Utsira Formation : an experimental study.

Sass, B.M., Engelhard, M.H., Bergman, P., Byrer, C., 2002. Interaction of Rock Minerals With Carbon Dioxide and Brine : a Hydrothermal Investigation, in: First National Conference on Carbon Sequestration. National Energy and Technology Lab, Washington DC, 14-17 May.

Sawin, J., Seyboth, K., Sverrisson, F., 2017. Renewables 2017 Global Status Report. Paris.

Schaef, H.T., McGrail, B.P., 2009. Dissolution of Columbia River Basalt under mildly acidic conditions as a function of temperature: Experimental results relevant to the geological sequestration of carbon dioxide. Appl. Geochemistry 24, 980–987. https://doi.org/10.1016/j.apgeochem.2009.02.025

Schaef, H.T., McGrail, B.P., Owen, A.T., 2011. Basalt reactivity variability with reservoir depth in supercritical CO 2 and aqueous phases, in: Energy Procedia. Elsevier Ltd, pp. 4977–4984. https://doi.org/10.1016/j.egypro.2011.02.468

Schaef, H.T., McGrail, B.P., Owen, A.T., 2010. Carbonate mineralization of volcanic province basalts. Int. J. Greenh. Gas Control 4, 249–261. https://doi.org/10.1016/j.ijggc.2009.10.009

Schaef, H.T., McGrail, B.P., Owen, A.T., 2009. Basalt- CO2-H2O interactions and variability in carbonate mineralization rates. Energy Procedia 1, 4899–4906. https://doi.org/10.1016/j.egypro.2009.02.320

Schaef, H.T., McGrail, B.P., Owen, A.T., Arey, B.W., 2013. Mineralization of basalts in the CO2-H2O-H2S system. Int. J. Greenh. Gas Control 16, 187–196. https://doi.org/10.1016/j.ijggc.2013.03.020

Shibuya, T., Yoshizaki, M., Masaki, Y., Suzuki, K., Takai, K., Russell, M.J., 2013. Reactions between basalt and CO2-rich seawater at 250 and 350°C, 500bars: Implications for the CO2 sequestration into the modern oceanic crust and the composition of hydrothermal vent fluid in the CO2-rich early ocean. Chem. Geol. 359, 1–9. https://doi.org/10.1016/j.chemgeo.2013.08.044

Stockmann, G.J., Wolff-Boenisch, D., Gislason, S.R., Oelkers, E.H., 2011. Do carbonate precipitates affect dissolution kinetics? 1: Basaltic glass. Chem. Geol. 284, 306–316. https://doi.org/10.1016/J.CHEMGEO.2011.03.010

Sugisaki, R., 1972. Tectonic Aspects of Andesite Line. Nat. Phys. Sci. 240, 109–111. https://doi.org/10.1038/physci240109a0

Suharmanto, P., Fitria, A.N., Ghaliyah, S., 2015. Indonesian Geothermal Energy Potential as Source of Alternative Energy Power Plant, in: Renewable Energy and Energy Conversion Conference and Exhibition. Knowledge E, pp. 119–124. https://doi.org/10.18502/ken.v1i1.325

Takahashi, T., Goldberg, D.S., Matter, J.M., 2000. Secure, long-term sequestration of CO2 in deep saline aquifers associated with oceanic and continental basaltic rocks, in: SRI International Symposium, Deep Sea and CO2. The Ship Research Institute, Mitaka.

Takaya, Y., Nakamura, K., Kato, Y., 2015. Dissolution of altered tuffaceous rocks under conditions relevant for CO2 storage. Appl. Geochemistry 58, 78–87. https://doi.org/10.1016/j.apgeochem.2015.03.012

UNFCC, 2015. Adoption of the Paris Agreement. Proposal by the President (Draft Decision), in: Change FCoC (Ed.). United Nations Office, Geneva (Switzerland), pp. 1–32.

Wells, R.K., Xiong, W., Giammar, D., Skemer, P., 2017. Dissolution and surface roughening of Columbia River flood basalt at geologic carbon sequestration conditions. Chem. Geol. 467, 100–109. https://doi.org/10.1016/j.chemgeo.2017.07.028

Wolff-Boenisch, D., 2011. On the buffer capacity of CO2-charged seawater used for carbonation and subsequent mineral sequestration. Energy Procedia 4, 3738–3745. https://doi.org/10.1016/j.egypro.2011.02.307

Wolff-Boenisch, D., Gislason, S.R., Oelkers, E.H., 2006. The effect of crystallinity on dissolution rates and CO2 consumption capacity of silicates. Geochim. Cosmochim. Acta 70, 858–870. https://doi.org/10.1016/j.gca.2005.10.016

Zhang, Y., Dawe, R., 1998. The kinetics of calcite precipitation from a high salinity water, Applied Geochemistry.

Chapter 5: Impact of increasing sodium chloride concentrations on the dissolution of feldspar minerals – implications for using seawater instead of freshwater for carbon sequestration in volcanic rock reservoirs.

Note: The fluid preparation and batch reactor experiments included in this chapter were conducted by Mr. Harry Potter (MSci) under the guidance of this thesis author. The sample characterisation, analysis techniques, data analysis and subsequent discussion points are the work of this thesis author.

5.1 Introduction

The CarbFix method has been proven a successful to rapidly and permanently sequester carbon dioxide however, it is extremely water intensive with approximately 32 tons of freshwater needed to dissolve each ton of CO_2 at 25^{o}C and 25 bar partial pCO_2 (Snæbjörnsdóttir *et al*., 2020). This may create a barrier to the expansion of the CarbFix method to other locations, which may have freshwater conflicts due to lower availability. The most obvious solution is to use a non-freshwater source of water, one which is nearly unlimited in its supply – seawater. The use of seawater as a reinjection medium for dissolved CO_2 into basaltic rocks is very promising as a Carbon Capture and Storage (CCS) solution, as porous basalts near to continental margins have huge storage potential and are adjacent to readily available seawater (Goldberg *et al*., 2008; Snæbjörnsdóttir and Gislason, 2016). Reducing the challenges associated with using such huge amounts of freshwater for carbon sequestration will make the CarbFix method more globally accessible.

However, simply swapping out freshwater for seawater is not a straightforward and predictable solution, as the high amounts of salts and sulphates in seawater can alter reactions pathways and rates of the formation of CO_2 trapping carbonate minerals (Rosenbauer *et al*., 2012). Injecting seawater into subsurface formation in industrial settings has been known to cause

pipe clogging (Bader, 2007; Dai *et al*., 2017). Some studies have also found that basalt-seawater reactions can lead to the formation of clay minerals, which can decrease the permeability of a reservoir and therefore may make it less suitable for fluid injection and/or extraction (Wolff-Boenisch, 2011; Wolff-Boenisch and Galeczka, 2018).

Previous research has found that basalt dissolution may be enhanced in saline fluids (Marieni *et al*., 2020; Wolff-Boenisch, 2011), which potentially means increased release of divalent cations, which are necessary for carbon sequestration. Other studies have reacted basaltic samples with CO_2-charged aqueous NaCl solutions and reported observed evidence of carbonate mineral formation (Luhmann *et al*., 2017; Rosenbauer *et al*., 2012; Shibuya *et al*., 2013). A limited number of studies have been conducted examining the implications of using seawater instead of freshwater for carbon sequestration in volcanic rock systems, with these studies discussed in detail in Section 1.4.6.

Though this plethora of research is great news for injecting CO_2 into basaltic rocks, little research exists examining the potential of other volcanic rock types for this particular carbon sequestration method. Takaya *et al*. (2015) and Marieni *et al*. (2018) examined the potential cation release from volcanic rocks with andesitic compositions and reported that although the release rates are often slower than basaltic rocks, they may still release sufficient amounts for carbon sequestration, particularly if acidic fluids are present. However, seemingly no research has been done on the field scale investigating andesitic rock types or investigating interactions between seawater-type fluids and andesitic-type rock samples.

Plagioclase type minerals are common across basaltic and andesitic type rock samples and are reported as being one of the key sources of Ca^{2+} release for carbon sequestration (Hangx and Spiers, 2009; McGrail *et al*., 2006; Wells *et al*., 2017). Therefore, it is sensible to investigate how these minerals in particular might be impacted by reaction with acidic saline fluids, for the context of carbon sequestration using seawater as the injection medium. A small number of previously conducted studies have investigated some form of these ideas. (Min and

Jun, 2016) recognised the lack of understanding of plagioclase dissolution in high salinity fluids. They conducted batch type experiments with 4 M concentration of Na^+ added to the solutions, with temperatures ranging from 35-90^oC and 100 bars CO_2 pressure. They found evidence suggesting increased Na^+ concentrations inhibited anorthite dissolution and postulated this was due to competition of Na^+ with H^+ at mineral surfaces, leading to less H^+ initiated mineral dissolution.

This present study aims to examine the impact of increasing concentrations of NaCl, a main salt found in seawater, on the dissolution of two feldspar minerals. Feldspars are identified as key minerals which can release divalent cations and buffer acidic solutions to support carbonate mineral formation for permanent carbon sequestration. Feldspar minerals are present in both basaltic and andesite type volcanic rocks; hence it is useful to examine their reactions as the findings may be applied to both types of reservoir rock systems. Batch reactor experiments are used, with the addition of hydrochloric acid (HCl) used to simulate the acidic conditions experienced during CO_2 injection and temperatures of 100^oC are used to make the study applicable to volcanic subsurface reservoirs situated at depths of km scales, which are often subjected to elevated geothermal gradients. The overall aim of this study is to investigate the effect of increased salinity in acidic fluids on the dissolution of feldspar minerals which are commonly found in volcanic rocks, and therefore explore the implications this may have for injecting CO_2-charged fluids for carbon sequestration applications.

5.2 Experimental Methodology

5.2.1 Solid and Solution Preparation

Two different feldspar samples were prepared to compare the impacts of saline fluids on the dissolution and potential cation release from plagioclase minerals with different cation compositions. A mineral sample described as an alkali feldspar (referred to as AF) and another described as plagioclase feldspar (referred to as PF) were crushed with an agate pestle and mortar after to selecting pieces that appeared to be pure mineral, and stainless-steel geological sieves were used to separate the 63 – 125 µm fraction. This fraction was sonicated 5 times in ultrapure MQ water and one time in acetone, and centrifuged in between each wash (1000 rpm, 2 minutes), to remove fine particles such as silt (63 - 2 µm), clay particles (< 2 µm) and organic residues (Eggleston *et al*., 1989). The obtained samples are natural minerals, and therefore these cleaning steps were applied to remove any impurities, since the aim of this study is to examine the impact on feldspar minerals only. After these cleaning steps, the resulting crushed samples was dried and stored in a 50^{o}C oven until use.

Seven solutions with varying sodium chloride (NaCl) concentrations (0, 0.35, 0.70, 1.05, 1.50, 1.75 and 2.10 M) were prepared by dissolving reagent-grade NaCl (≥ 99.5%) in 1 L of MQ water. Due to the low buffering capacity of MQ water, the solution was left to equilibrate with air in a loosely sealed container overnight, in order to obtain stable pH measurements before use. The desired pH for these experiments was 3, to ensure reactions occurred on an appreciable timescale and to simulate the pH conditions expected in the field when CO_2 is dissolved in water for injection. To achieve this, trace metal grade HCl (24-37% w/w, 12 M) was added to each 1L volume of prepared NaCl solution, and the final pH was measured with a benchtop electronic pH meter (± 0.01 pH). In summary, 14 separate seven day experiments were conducted, in duplicate, by testing the two different mineral samples in each of the experimental fluids with the 7 differing NaCl concentrations. These batch experiments do not

include injected CO_2 due to restricted access during this project of equipment available to achieve this. The addition of HCl to achieve acidic pH's is used as an alternative.

5.2.2 Batch Reactor Set-up

Teflon reaction vessels (25 mL total volume) were cleaned first with a soap scrubbing, then a nitric acid (HNO_3, 10%) bath for 24 hours, and finally a MQ water bath for 24 hours and MQ water rinse to minimise contamination. A 15 mg (± 0.05 mg) portion of the prepared feldspar mineral was added to the Teflon reaction vessel, followed by 15 mL of the prepared reaction fluid. The vessel was closed and inserted into the accompanying steel autoclave, which was tightly sealed and placed into a pre-heated oven at a temperature of 150ºC for 7 days (~168 hours). At the end of each experiment, the autoclave was removed from the oven, left for 30 minutes before opening (to ensure the solutions inside were no longer boiling) and a pH measurement of the fluid was immediately taken. The reaction fluid was then collected via syringes with 2 µm PES filters and immediately diluted by a factor of 10 with 2% HNO_3 for ICP analysis. The reaction solids were rinsed into tubes with MQ water, separated via centrifugation and then dried and stored in a 50ºC oven.

5.2.3 Solid Mineral Analysis

The crushed mineral samples were initially characterised with Powder X-ray Diffraction (PXRD) analysis using an X'Pert PRO PANalytical MPD X-ray Diffractometer, using normal Bragg-Brentano geometry, CuKα radiation at 40 kV and 40 mA, over a sampling range of 5 to 70 º2θ with a step size of 0.0066 and a scan speed of 0.23 º2θ per second. For phase identification the PDF4 (ICDD, 2018) database was used within the software DIFFRAC.EVA to identify the mineral phase peak patterns.

Nitrogen BET surface area analysis of the crushed mineral samples was obtained using a Micromeritics 3flex Surface Characterisation Analyzer at 77 K and relative pressure (p/p_0) from 0 to 0.99. Prior to analysis, the crushed samples were degassed overnight under vacuum at

100°C. The surface area of the AF sample was 0.2 (± 0.1) m^2/g and the surface area of the PF sample was 0.1 (± 0.1) m^2/g. Since both surface area values are relatively small and within error of each other, it can be assumed there is little difference between the surface areas of the two sample and it is therefore unlikely any surface area differences will impact the experimental results.

Scanning Electron Microscopy (SEM) was used to obtain high resolution micrographs of the crushed sample surfaces, to examine the morphology of the minerals. A FEI Quanta600 SEM, was used, operating at 10-20 kV and a spot size of 3, with typical beam currents of 0.1 – 10 nA. Prior to analysis, the samples were mounted on aluminium SEM stubs with double sides carbon tape and coated with 15 nm of carbon using an Edwards evaporation coater.

Geochemical compositions of the minerals were determined from standard wavelength dispersive techniques using a JEOL JXA-8200 Electron Microprobe using a 15kV, 20nA electron beam and a working distance of 11 mm. Pieces of uncrushed mineral sample were embedded in epoxy resin and polished with a series of diamond suspensions down to 1 µm, before coating with 15 nm of carbon ready for analysis.

5.2.4 Fluid analysis

5.2.4.1 Experimental fluid preparation

Fluid concentrations of Al and Si were obtained using a Perkin-Elmer Optima 2000 DV ICP-OES. Multi-element calibration standards were prepared using a Fischer Chemical 28 element standard (100 mg/L in a HNO_3 matrix), with concentrations of 0, 0.1, 1, 3, 5, 7 and 10 mg/L. Calibration curves were first created using the prepared standard solutions, with 3 repeats of each measurement and a fluid flow rate of 1.5 mL/min via an autosampler. The elemental compositions of the starting fluids (before contact with solid mineral samples) were measured to obtain the starting background values for each element. These values were subtracted from the final measured values in the reported results, to ensure only the impacts of the rock-fluid interactions are considered. Analysis of Na, K and Ca concentrations are not reported for this

chapter, due to the addition of high concentrations of NaCl (which contains minor impurities) which would have led to a large experimental error as their concentrations would be higher than the concentration limits of the equipment and not allow any meaningful analysis of the changing concentrations of these cations to be conducted.

5.2.4.2 Correcting for matrix effects

In ICP-OES, high salinity solutions can cause non-spectroscopic effects, also known as matrix effects, which may affect the reported elemental concentrations. These matrix effects can be separated into two categories:

1) Matrix induced spectral overlap due to the deposition of solid onto the sampling aperture of the plasma torch. Deposits of dissolved salts can accumulate on the sampling equipment, also known as clogging. A build-up of such solids can reduce the flow of the ions into the plasma, which over time can cause increasing signal drift (Chen, 1995).
2) Matrix induced signal intensity changes (suppression or enhancement) caused by dissolved associated matrix elements, e.g. alkali metals, in the fluid samples (Tan and Horlick, 1987).

Olivares and Houk (1986) tested single matrix elements and reported that matrix interferences, like signal suppression, tend to be greater for elements in the matrix salt with low ionisation energies i.e., Na > Ca > Mg >> Br > Cl. They concluded that when analysing fluids, the combination of several matrix elements may drastically effect signal intensity and thus, the perceived concentration of analyte elements in a fluid sample. As ICP-OES is a sensitive technique, analyte signal will depend on analyte concentration as well as the identity and concentration of the matrix elements. Lighter elements tend to be subject to harsher spectral effects, whereas heavy elements experience more significant suppression (Chen, 1995). Unfortunately, matrix effects are not particularly well understood or quantified for a useful range of conditions. The easiest way to alleviate such issues is to dilute the samples to reduce the salt concentration in the solutions; however, this would not be practical in this study since the expected concentrations of the elements of interest (Al and Si) are expected to be low, hence over-dilution may result in them falling below the detection limits of the equipment.

Another method to attempt to alleviate the effects is to analyse some standard solution containing known concentrations of the matrix elements (Gerotto *et al*., 1995), to create a correction value that can be applied to the measured values of the analyte elements in the experimental solutions.

Since the experimental fluids used in this study have a maximum NaCl concentration of 2.1 M and the solutions were all diluted by a factor of 10 prior to ICP analysis, the highest concentration of NaCl experienced by the ICP equipment would be 0.21 M. Therefore, some correction experiments were first conducted, by making up a series of solutions with 0, 0.01, 0.05, 0.10, 0.15, 0.30 and 0.50 M exact concentration of NaCl, combined with the 0, 0.1, 1, 3, 5, 7 and 10 mg/L concentrations of standard elements as described in the solution preparation in this study. This process was repeated to obtain average values, and the effect on the measured Al and Si concentrations increased with increasing salt concentration (Figure 5.1) was observed.

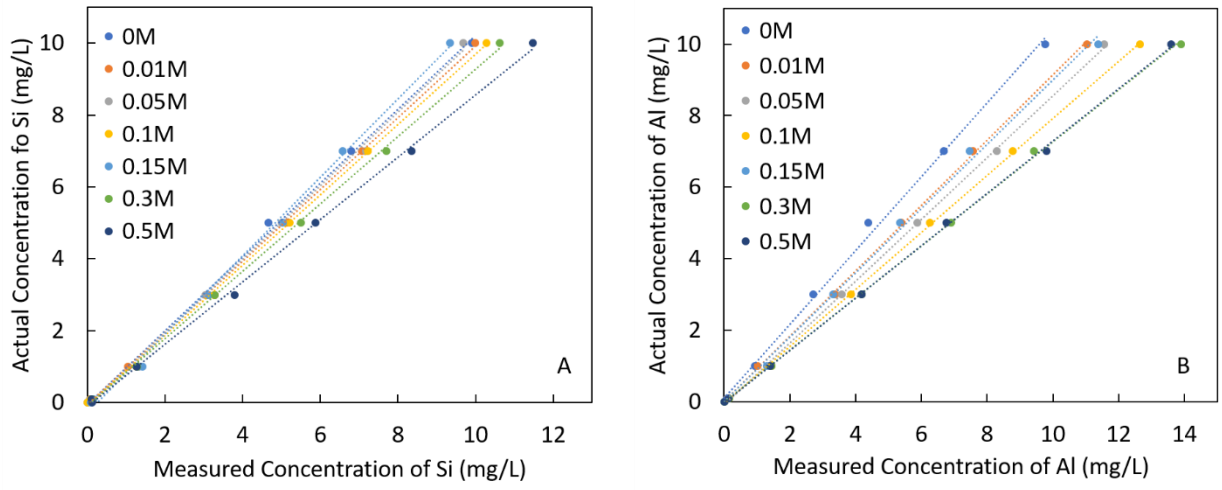


Figure *5.1: Measured concentration of A) Si and B) Al in fluids with known concentration of these elements and increasing concentrations of NaCl in the solutions (quantitative data displayed in Table A24 of the Appendix).*

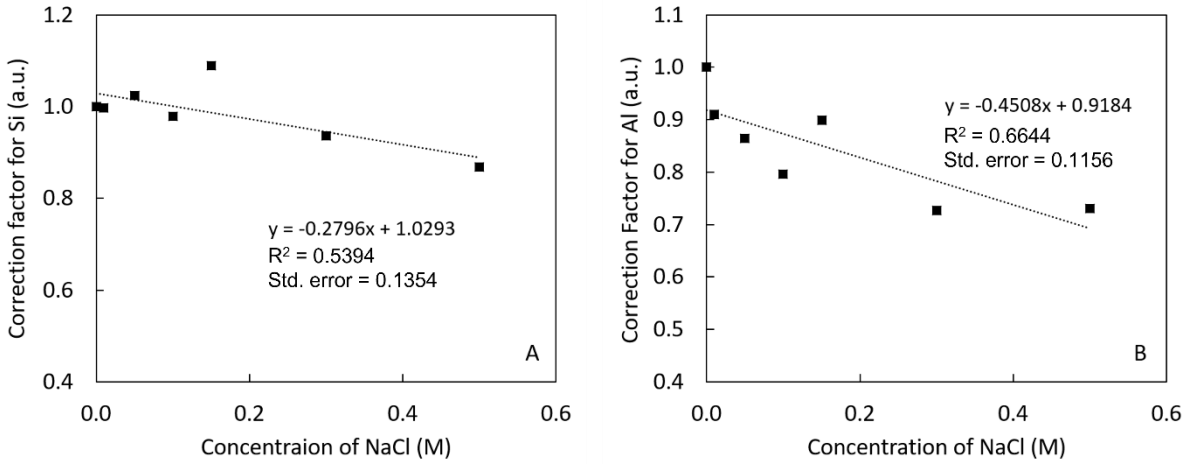


Figure *5.2: Linear fit of the concentration of NaCl against the correction factor for each salinity for A) Si B) Al, which can be applied to the measured concentrations in the experimental fluids to obtain final concentrations of these elements which consider matrix effects of saline fluids on ICP-OES measurements (quantitative data displayed in Table A25 of the Appendix).*

Linear fits were applied to each fluid set (excluding 0 M NaCl) and the gradient value of each equation was in turn plotted against the salinity of that fluid for both Si and Al (Figure 5.2).The pre-gradient factor (one each for Si and Al) for the final linear fit of this resulting set of data is then used as a correction factor, to gain a value for the concentration that accounts for matrix effects of the saline fluids on ICP-OES measurements. The fluids from the batch experiments were measured using the conditions described in the basic fluid preparation at the start of this section, and the appropriate correction factor (for Si or Al) applied to each measurement result. The associated R^2 values and standard errors for the linear fits displayed in Figure 5.2 indicate a reasonable amount of error is present. This error is likely due to a combination of errors incurred through this calibration method, including; equipment error associated with adding specific amounts of silicon to the solutions using an air displacement pipette, equipment error associated with adding specific amounts of NaCl to the solutions using an analytical balance and air displacement pipettes, and the instrument error associated with ICP-OES analysis which is reported as 10%. Although there is a reasonable error in the measurement, the

correction factor still enables estimation of the true concentrations of Si and Al in the fluids to me made, enabling the following analysis and discussion points.

5.3 Results

5.3.1 Characterisation of mineral samples

5.3.1.1 PXRD

PXRD and PDF reference patterns (ICDD, 2018) were used to identify the main mineral phase in each bulk crushed feldspar sample (Figure 5.3). As the mineral samples were described on purchase as albite and anorthite, these particular mineral reference patterns were closely compared to the measured samples patterns. Both samples appear to have some matching peaks for both albite and anorthite. Since plagioclase feldspar forms a solid solution series, it seems likely that both minerals will contain both Ca and Na in their structures, and therefore have PXRD patterns that have some albite and anorthite characteristics. This bulk analysis technique confirms the samples are likely of feldspar composition, with more precise geochemical techniques needed to define their compositions in more detail.

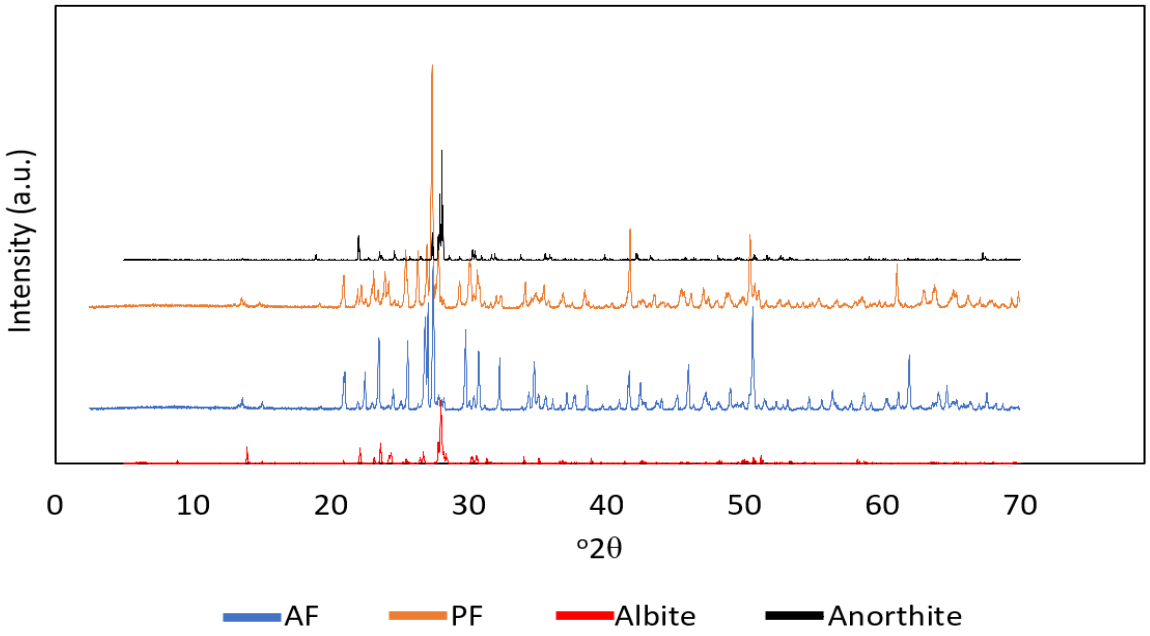


Figure *5.3: PXRD patterns for the mineral samples AF and PF, alongside reference patterns for albite and anorthite pure endmember minerals.*

5.3.1.2 Microscopy

SEM micrographs of the crushed mineral samples were obtained to confirm the surfaces were free of small particulates (Figure 5.4). Little evidence of fine particulates was observed, and the samples appeared to have sharp rough edges in general. The particle size appears to be relatively even across the samples.

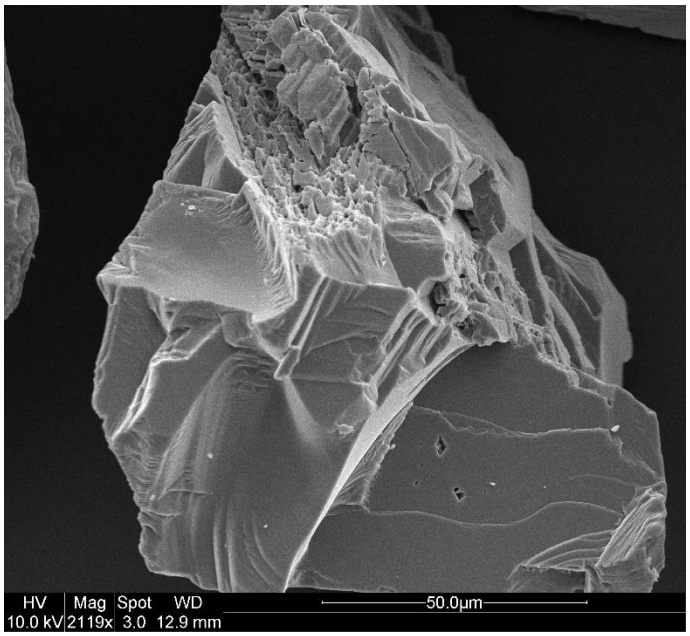


Figure *5.4: SEM micrograph example of sample AF, imaged with a beam voltage of 10 kV and a spot size of 3. Very few fine particulates are observed on the surface.*

5.3.1.3 Geochemical analysis

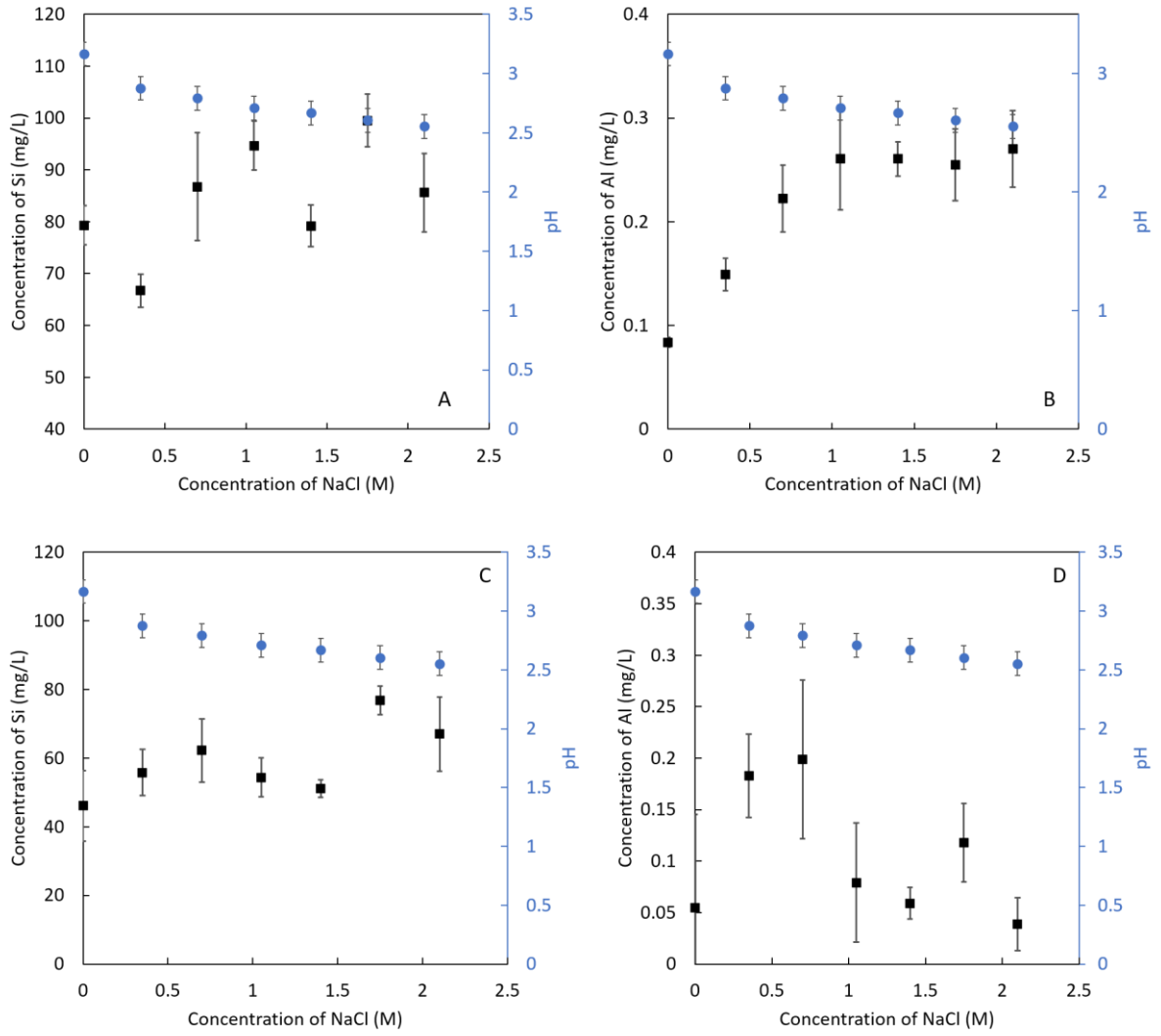
The chemical composition of the mineral samples was determined via EMPA, by taking an average of 20-point analyses from each polished mineral surface. The results are reported in major element oxide percentages (Table 5.1) and allow the calculation of a normalised geochemical mineral formula for each sample. The formula of sample AF ($Na_{0.45}K_{0.55}AlSi_3O_8$) and its relatively high wt.% silica content indicates it is an alkali feldspar, with significant K content as well as Na within its structure and may be referred to as sanidine. The formula for sample PF ($Na_{0.33}K_{0.02}Ca_{0.65}Al_{1.40}Si_{2.60}O_8$) and its lower wt.% silica content indicates it is a plagioclase feldspar with some Na content as well as Ca and may be referred to as labradorite.

Table 5.1: Geochemical composition of mineral sample AF and PF, expressed in terms of wt.% oxides, determined via an average of 20-point analyses with EMPA.

Oxide	AF (wt.%)	PF (wt.%)
Na_2O	4.95	3.99
CaO	0.02	12.12
K_2O	9.26	0.86
SiO_2	66.31	54.37
Al_2O_3	18.82	26.18

5.3.2 Experimental fluid analysis

The experimental fluids were examined using ICP-OES analysis to quantitatively measure any changes in the concentrations of the elements Al and Si, which are key indicators of mineral dissolution of feldspar minerals. The matrix effects correction factors previously discussed (Figure 5.2) are applied to the raw data obtained from the ICP equipment, to yield final values for the measured concentrations of Si and Al in the experimental fluids (Figure 5.5). All experiments had a significant increase in the concentration of Si in the experimental fluids compared to pre-experimental values, up to tens of mg/L. The measured Al concentrations in the fluids are much lower compared to Si concentrations, with a maximum of around 0.28 mg/L. In almost all experiments with the AF sample, there was a higher concentration of Si in the final solutions compared to the equivalent experiment using the PF sample. This trend is broadly similar for the Al release, although larger error in some of the experiments makes it difficult to confidently conclude this. The experimental series using the AF sample indicates an increase of Al concentration with increasing NaCl concentration initially, but a levelling off of this trend at an NaCl concentration of 1.0 M and above. In the experimental series using the PF sample, the Al concentration slightly increases as the NaCl concentration increases from 0 – 1.0 M, but is then lower for all subsequent NaCl concentrations.



5.5: Elemental concentrations measured via ICP-OES in the experimental fluids collected at the end of each experiment for A) Si concentration from AF sample, B) Al concentration from AF sample, C) Si concentration from PF sample and D) Al concentration from PF sample. The associated measured pH values of the fluids at the start of each experiment are also included on each plot. Error bars for the elemental concentrations in the fluids are calculated based on the standard deviation between experimental repeats and the standard 5% error associated with ICP-OES measurements (quantitative data displayed in Table A26 of the Appendix).

The pH of the starting fluids was also measured to confirm a pH close to 3 was achieved with the addition of a small amount of HCl. A fixed aliquot of HCl was added to each starting fluid; however, the measured value of the starting pH is not 3 for all the fluids and the precise value

for each experiment can be seen in Figure 5.5 in the blue (circular data points) trends. A common trend seems to be a decreasing pH with increasing NaCl concentration in the fluids (Figure 5.5). The solution final pH values after the experiments were also measured (Table 5.2). Generally, the solutions in the experimental series containing the PF samples had final pH roughly around 5, whereas the solutions in the experimental series containing the AF sample had final pH values that remained close to 3.

Table 5.2: pH values in the experimental fluids measured before and after the 7-day duration experiments with each of the mineral samples in varying NaCl concentrations.

Sample	NaCl concentration (Molar)	pH before	pH after	Sample	NaCl concentration (Molar)	pH before	pH after
AF	0	3.2	3.5	PF	0	3.2	5.7
AF	0.35	2.9	3.2	PF	0.35	2.9	5.4
AF	0.70	2.8	2.9	PF	0.70	2.8	5.0
AF	1.05	2.7	3.1	PF	1.05	2.7	5.2
AF	1.40	2.7	3.0	PF	1.40	2.7	5.2
AF	1.75	2.6	3.0	PF	1.75	2.6	3.6
AF	2.10	2.6	2.8	PF	2.10	2.6	5.1

5.4 Discussion

5.4.1 The variation of pH in saline solutions

The measured pH of the starting fluids displays a consistent trend of decreasing pH with increasing concentration of NaCl. The phenomena of saline solutions inducing acidic pH readings is not perfectly understood, though there are a variety of partial explanations. In pure water, the CO_2 in the air enters the solution, and the carbonic acid equilibrium can lead to a pH of around 5.65 (Reddi, 2013). Since the fluids were left to equilibrate with the air for a day prior to use, it seems likely that significant carbonic acid will have had to opportunity to form in the solution. The solubility of CO_2 in water depends on the negatively charged electrons on the oxygen attracting the positively charged H^+ ions in the water. However, the presence of electrolytes (e.g. salts) competes for the H^+ which can reduce the stability of the CO_2 in the solution, and so CO_2 concentrations are slightly lower in saline water compared to pure water, which would lead to a less acidic pH measurement. On the other hand, the presence of electrolytes in solution may stabilise the dissociation products of H_2CO_3, increasing the dissociation constant for carbonic acid (Gando *et al*., 2011) and therefore, increasing the acidity. Additionally, charged ions (Na^+, Cl^-, H^+, HCO_3^-) will tend to cluster together in a thermodynamically favourable arrangement, creating a structured charge distribution that affects the properties of the ions (Fowler, 1990). The ions activity is then no longer proportional to their pure concentrations and particularly the H^+ activity is reduced in saline solutions (Grotzinger and Jordan, 2014). In summary, the combined effects of these processes decreases CO_2 solubility, but also increases the dissociation of carbonic acid, which has been observed to lead to a net reduction in pH (Earle, 2015). This provides some explanation for the observed trend of decreasing starting pH with increasing NaCl concentration in the experimental fluids. The pH in the solutions in this study with a higher NaCl concentration may induce a further reduction in the pH (in addition to the impact from HCl) as increased dissociation of carbonic acid increases the H^+ concentration in the solution, thereby lowering the pH beyond the target value of 3.

5.4.2 Mineral dissolution in acidic solutions

The elevated temperatures of 100°C and the significant acidity induced by the addition of HCl (and the smaller impact of carbonic acid due to solutions being in equilibrium with CO_2 from the air) creates conditions expected to cause feldspar mineral dissolution (e.g., Casey *et al*. (1991), Gudbrandsson *et al*. (2014), Oxburgh *et al*. (1994), and Stefánsson (2001)). The pH values measured after the experiments suggest that the solutions are still acidic in nature after the 7-day duration, indicating conditions expected to cause feldspar mineral dissolution persisted until the experiments were stopped. Dissolution of feldspar minerals will release Si and Al into the solutions, which explains the observed increase in both these elemental concentrations in the fluids compared to pre-experimental values (Figure 5.5). The geochemical formula of feldspar minerals suggests that 2-3 times more Si than Al would be released if stoichiometric mineral dissolution is taking place. The relative strength of Si-O compared to Al-O bonds has been reported to cause non-stoichiometric dissolution, as Al is preferentially released during mineral dissolution leaving a Si-rich surface layer (Oelkers *et al*., 1994; Oelkers and Schott, 1995). These assumptions suggest that expected Si concentrations in the fluids collected after experiments with feldspar dissolution taking place would be 2-3 times higher than the measured Al concentrations. However, the Si concentrations measured in the experimental fluids of this study are approximately 2 orders of magnitude higher than the measured Al concentrations. Previous studies have reported on the low solubility of aluminium species, even in acidic solutions (e.g., Balintova and Petrilakova (2011), Barnhisel and Rich (1965), Schoen and Roberson (1970), and Tole *et al*. (1986)), which may explain why such low concentration of Al are measured in these experimental fluids.

A higher magnitude of element concentrations in the fluids after the AF sample experiments (compared to the PF sample experiments) suggests more extensive mineral dissolution has taken place. This appears to contradict previous findings that feldspar minerals with a higher anorthite content have increased dissolution rates, including in increasingly acidic solutions

(Oelkers *et al*., 1994; Oelkers and Schott, 1995). As discussed, feldspar minerals have increased dissolution rates in more acidic solutions. The experimental series with the AF sample maintained pH levels close to 3, whereas the experimental series with the PF has increased pH values close to 5 at the end of most experiments (Table 5.2). This indicates the experiments with the AF sample had more acidic conditions for an increased experimental duration, likely causing more extensive mineral dissolution resulting in higher concentrations of the measured elements in solution as is observed. It is possible that the higher anorthite content of the PF sample (Table 5.1) initially underwent rapid dissolution compared to the AF sample, consuming more of the H^+ ions in the acidic solutions and therefore increasing the pH of the solutions. Feldspar minerals are reported to have pH buffering capacity (e.g., Baines and Worden (2004), Hangx and Spiers (2009), Yu *et al*. (2012), and Zhang *et al*.(2015), supporting the idea that rapid dissolution of minerals with a high anorthite content has increased the experimental pH. Since pH values closer to neutral result in slower feldspar dissolution, possibly the dissolution of the PF sample slowed down after an initial spike. In contrast, experimental fluids in the AF sample series have remained close to pH 3, so mineral dissolution has continued at an appreciable rate, resulting in a higher overall magnitude of mineral dissolution and increased concentrations of Si in the experimental fluids. However, there is no direct evidence to support this idea and an additional set of experiments with fluid sampling at regular intervals throughout the experimental duration would be needed to examine this further. It can simply be concluded that the AF sample is not as effective at buffering the acidic pH of the starting fluids as the PF sample after these 7-day experiments. Since the only significant variable between these two sets of experiments is the geochemical character of the two minerals, it can be concluded that the sample with the higher anorthite content was more effective at buffering the acidic pH under these conditions.

5.4.3 Impacts of salinity of mineral dissolution

An examination of the literature prior to the start of this study led to a variety of predications on the impact of increasingly saline solutions on the dissolution of feldspar minerals. Some

studies reported that feldspar mineral dissolution was inhibited by increasing concentrations of Na^+ in solutions (Min and Jun, 2016), whereas others reported whole rock dissolution rates may increase in the presence of saline fluids (Marieni *et al*., 2020; Wolff-Boenisch, 2011). This present study aimed to examine the impact of increasing concentrations of NaCl in solutions on the dissolution of feldspar minerals with differing compositions, and therefore discuss the impact of dissolving CO_2 in seawater rather than freshwater for injection into volcanic rock reservoirs for carbon sequestration. However, the effect of the increased acidity with increasing concentration of NaCl in the experimental fluids makes it difficult to separate the impacts of increased salinity, from the secondary impacts of increased acidity.

If increasing Na^+ concentration was inhibiting mineral dissolution, an observed decreasing trend in Si and Al release with increasing NaCl concentrations would be expected. In contrast, increasing acidity is expected to cause and increasing trend in element concentrations. The measured Si concentrations in the experiments with both samples show little evidence of a decreasing or increasing trend outside experimental error. The measured Al concentration in the AF experimental series appear to have a slight increasing trend with increasing NaCl concentrations up to 1.0 M NaCl, whereas the experimental series with the PF sample appears to have an increasing trend up to 1.0 M NaCl, followed by a slight decreasing trend in Al concentrations with continued NaCl increase. It is possible that a mixture of the two scenarios is occurring; an increasing concentration of Na^+ is slightly inhibiting mineral dissolution while the increasing acidity (associated with increasing NaCl concentrations) is slightly increasing mineral dissolution. In the case of the AF sample, this has resulted in an initial increase in measured Al concentration with increasing acidity, but then the impact of increasing Na^+ concentration inhibiting mineral dissolution comes into effect around 1.0 M NaCl, which causes an overall levelling off in the measured Al concentrations. In the case of the PF sample, there is also an initial increase in measured Al concentration with increasing acidity, but then around 1.0 M NaCl the impact of increasing Na^+ concentration does cause a decrease in the measured Al concentration. Further experiments need to be conducted to confirm this, with

more control over the starting pH of the fluids so that the impact of NaCl alone can be examined.

5.4.4 Implications for CO_2 sequestration in volcanic rocks using seawater.

Previous studies have reported that seawater may be an effective medium for CO_2 dissolution for injection into volcanic rocks, to alleviate the strains on freshwater needed for the CarbFix carbon sequestration method (Marieni *et al*., 2021; Voigt *et al*., 2021; Wolff-Boenisch and Galeczka, 2018). The carbon sequestration potential of volcanic rocks is evaluated in terms of its ability to release divalent cations into solution via mineral dissolution (Gislason *et al*., 2010; McGrail *et al*., 2003), with increased dissolution rates of minerals containing divalent cations ideal for appreciable carbonation reactions. The mineral samples used in this study were feldspar minerals, as these minerals have been identified as key features that can improve carbon sequestration potential by releasing divalent cations and by buffering the injected acidic solutions to allow carbonation reactions to take place. The results of this study indicate that mineral dissolution is taking place in acidic fluids with elevated concentrations of NaCl, suggesting that using seawater may be an appropriate medium for CO_2 dissolution as it will not significantly hinder feldspar mineral dissolution. The experiments suggest the PF sample with a higher anorthite content was better at buffering the pH of the acidic solutions compared to the AF sample. The PF sample also has a higher content of Ca^{2+} which can be released as it dissolves, therefore targeting formations which contain a higher content of labradorite type feldspars (compared to alkali type feldspars) may increase the efficiency of carbon sequestration. Ideally, further experiments would be conducted with a wider range of mineral compositions, increased experimental timescales and increased sampling frequencies to confirm these ideas more confidently.

5.5 Conclusions

In this study, acidic fluids were used to simulate the pH conditions experienced during CO_2 dissolution for reinjection into the subsurface. Increasing concentrations of NaCl were used to examine the impact of using seawater instead of freshwater on the dissolution of feldspar minerals considered important for successful carbon sequestration via mineralisation on appreciable timescales. ICP-OES analysis of the experimental fluids provided evidence that feldspar mineral dissolution had occurred, with measured Si concentration increases in the fluids between 40 and 100 mg/L after a 7-day experimental duration, with experimental conditions of 100ºC, a pH close to 3 and NaCl concentrations ranging from 0 to 2.1 M. This indicates that using seawater will not completely inhibit mineral dissolution, and it may be an effective medium for CO_2 dissolution and injection into volcanic rock reservoirs. The feldspar mineral sample with a higher anorthite content was found to buffer the pH of the acidic fluids more effectively than the alkali feldspar sample, with pH values close to 5 measured in most of the post-experiment fluids with the PF sample, compared to the AF sample where values remained close to 3.

Some qualitative observations of Al concentrations imply that elevated concentrations of Na^+ in solution may slightly inhibit feldspar dissolution however, more experiments need to be conducted to confirm this. Experiments with more control over the starting pH should be conducted, which can account for the effect of increasing NaCl concentrations decreasing the measured pH.

Overall, it proved challenging to separate the impact of increasing NaCl concentration on mineral dissolution from increasing acidity in this study and designing experiments with more pH control would assist in solving this challenge. Further experiments should also be conducted to examine the heightened ability of the feldspar sample with a higher anorthite content to buffer the acidic pH of the solutions, when compared to the alkali feldspar samples. In this present study, no attempts were made to calculate quantitative values for mineral dissolution, since only one final value could be used for the change in concentration with time

of each element at the end of the 7-day experiments, and there was significant error in the relatively small BET surface area measurements. Future experiments should include sampling intervals to monitor the changing pH and elemental concentrations in the fluids over time, to examine the rate of this buffering more closely. Increased experimental durations could be used to determine whether the alkali feldspar sample would eventually have a buffering effect on the acidic solutions.

5.6 References

Bader, M.S.H., 2007. Sulfate removal technologies for oil fields seawater injection operations. J. Pet. Sci. Eng. 55, 93–110. https://doi.org/10.1016/j.petrol.2006.04.010

Baines, S., Worden, R., 2004. The long-term fate of CO2 in the subsurface: natural analogues for CO2 storage. Geol. Soc. London, Spec. Publ. 233, 59–85. https://doi.org/10.1144/GSL.SP.2004.233.01.06

Balintova, M., Petrilakova, A., 2011. Study of pH Influence on Selective Precipitation of Heavy Metals from Acid Mine Drainage, in: 14th International Conference on Progress Integration, Modelling and Optimisation for Energy. pp. 5–10.

Barnhisel, R.I., Rich, C.I., 1965. Gibbsite, Bayerite, and Nordstrandite Formation as Affected by Anions, pH, and Mineral Surfaces, in: Soil Science Society of America Proceedings. pp. 531–534.

Casey, W.H., Westrich, H.R., Holdren, G.R., 1991. Dissolution rates of plagioclase at pH = 2 and 3. Am. Mineral. 76, 211–217.

Chen, X., 1995. Matrix Effects in Inductively Coupled Plasma Mass Spectrometry. Retrosp. Theses Diss. 10770. Iowa State University. https://doi.org/10.2116/analsci.3.305

Clark, D.E., Oelkers, E.H., Gunnarsson, I., Sigfússon, B., Snæbjörnsdóttir, S., Aradóttir, E.S., Gíslason, S.R., 2020. CarbFix2: CO2 and H2S mineralization during 3.5 years of continuous injection into basaltic rocks at more than 250 °C. Geochim. Cosmochim. Acta 279, 45–66. https://doi.org/10.1016/j.gca.2020.03.039

Dai, Z., Kan, A.T., Shi, W., Zhang, N., Zhang, F., Yan, F., Bhandari, N., Zhang, Z., Liu, Y., Ruan, G., Tomson, M.B., 2017. Solubility Measurements and Predictions of Gypsum, Anhydrite, and Calcite Over Wide Ranges of Temperature, Pressure, and Ionic Strength with Mixed Electrolytes. Rock Mech. Rock Eng. 50, 327–339. https://doi.org/10.1007/s00603-016-1123-9

Earle, S., 2015. Physical geology. Victoria, B.C.: BCcampus. https://doi.org/10.1038/018266a0

Eggleston, C.M., Hochella, M.F., George, P.A., 1989. Sample preparation and aging effects on the dissolution rate and surface composition of diopside. Geochim. Cosmochim. Acta 53, 797–804. https://doi.org/10.1016/0016-7037(89)90026-4

Fowler, C.M.R., 1990. An introduction to global geophysics, The Solid earth. https://doi.org/10.1029/90eo00309

Gando, A., Gando, Y., Ichimura, K., Ikeda, H., Inoue, K., Kibe, Y., Kishimoto, Y., Koga, M., Minekawa, Y., Mitsui, T., Morikawa, T., Nagai, N., Nakajima, K., Nakamura, K., Narita, K., Shimizu, I., Shimizu, Y., Shirai, J., Suekane, F., Suzuki, A., Takahashi, H., Takahashi, N., Takemoto, Y., Tamae, K., Watanabe, H., Xu, B.D., Yabumoto, H., Yoshida, H., Yoshida, S., Enomoto, S., Kozlov, A., Murayama, H., Grant, C., Keefer, G., Piepke, A., Banks, T.I., Bloxham, T., Detwiler, J.A., Freedman, S.J., Fujikawa, B.K., Han, K., Kadel, R., O'Donnell, T., Steiner, H.M., Dwyer, D.A., McKeown, R.D., Zhang, C., Berger, B.E., Lane, C.E., Maricic, J., Miletic, T., Batygov, M., Learned, J.G., Matsuno, S., Sakai, M., Horton-Smith, G.A., Downum, K.E., Gratta, G., Tolich, K., Efremenko, Y., Perevozchikov, O., Karwowski, H.J., Markoff, D.M., Tornow, W., Heeger, K.M., Decowski, M.P., 2011. Partial radiogenic heat model for Earth revealed by geoneutrino measurements. Nat. Geosci. 4, 647–651. https://doi.org/10.1038/ngeo1205

Gerotto, M., Dell' Andrea, E., Bortoli, A., Marchiori, M., Palonta, M., Troncon, A., 1995. Interference effects and their control in ICP-MS analysis of serum and saline solutions. Microchem. J. 51, 73–87.

Gislason, S.R., Wolff-Boenisch, D., Stefansson, A., Oelkers, E.H., Gunnlaugsson, E., Sigurdardóttir, H., Sigfússon, B., Broecker, W.S., Matter, J.M., Stute, M., Axelsson, G., Fridriksson, T., 2010. Mineral sequestration of carbon dioxide in basalt : A pre-injection overview of the CarbFix project. Int. J. Greenh. Gas Control 4, 537–545. https://doi.org/10.1016/j.ijggc.2009.11.013

Global CCS Institute, 2020. Global Status of CCS 2020.

Global CCS Institute, 2018. The global status of CCS: 2018, The Global Status of CCS.

Goldberg, D.S., Takahashi, T., Slagle, A.L., 2008. Carbon dioxide sequestration in deep-sea basalt. Proc. Natl. Acad. Sci. U. S. A. 105, 9920–5. https://doi.org/10.1073/pnas.0804397105

Grotzinger, J.P., Jordan, T.H., 2014. The Hydrologic Cycle and Groundwater, in: Understanding Earth. pp. 466–489.

Gudbrandsson, S., Wolff-Boenisch, D., Gislason, S.R., Oelkers, E.H., 2014. Experimental determination of plagioclase dissolution rates as a function of its composition and pH at 22°C. Geochim. Cosmochim. Acta 139, 154–172. https://doi.org/10.1016/j.gca.2014.04.028

Gunnarsson, I., Aradóttir, E.S., Oelkers, E.H., Clark, D.E., Arnarson, M.Þ., Sigfússon, B., Snæbjörnsdóttir, S., Matter, J.M., Stute, M., Júlíusson, B.M., Gíslason, S.R., 2018. The rapid and cost-effective capture and subsurface mineral storage of carbon and sulfur at the CarbFix2 site. Int. J. Greenh. Gas Control 79, 117–126. https://doi.org/10.1016/j.ijggc.2018.08.014

Hangx, S.J.T., Spiers, C.J., 2009. Reaction of plagioclase feldspars with CO2 under hydrothermal conditions. Chem. Geol. 265, 88–98. https://doi.org/10.1016/j.chemgeo.2008.12.005

ICDD, 2018. PDF-4. International Centre for Diffraction Data.

IPCC, 2018. Summary for Policymakers, in: Masson-Delmotte, V., Zhai, P., Portner, H.-O., Roberts, D., Skea, J., Shukla, P.R., Pirani, A., Moufouma-Okia, W., Pean, C., Pidcock, R., Connors, S., Matthews, J.B.R., Chen, Y., Zhou, X., Gomis, M.I., Lonnoy, E., Maycock, T., Tignor, M., Waterfield, T. (Eds.), Global Warming of 1.5oC. An IPCC Special Report on the Impacts of Global Warming of 1.5oC above Pre-Industrial Levels and Related Global Greenhouse Gas Emission Pathways, in the Context of Strengthening the Global Response to the Threat of Climate Change,. Geneva.

IPCC, 2005. Carbon dioxide capture, IPCC Special Report on Carbon DIoxide Capture and Storage. Prepared by Working Group III of the Intergovernmental Panel on Climate Change. Cambridge University Press. https://doi.org/10.1002/9783527818488.ch15

Luhmann, A.J., Tutolo, B.M., Tan, C., Moskowitz, B.M., Saar, M.O., Seyfried, W.E., 2017. Whole rock basalt alteration from CO2-rich brine during flow-through experiments at 150 °C and 150 bar. Chem. Geol. 453, 92–110. https://doi.org/10.1016/j.chemgeo.2017.02.002

Marieni, C., Matter, J.M., Teagle, D.A.H., 2020. Experimental study on mafic rock dissolution rates within CO2-seawater-rock systems. Geochim. Cosmochim. Acta 272, 259–275. https://doi.org/10.1016/j.gca.2020.01.004

Marieni, C., Přikryl, J., Aradóttir, E.S., Gunnarsson, I., Stefánsson, A., 2018. Towards 'green'

geothermal energy: Co-mineralization of carbon and sulfur in geothermal reservoirs. Int. J. Greenh. Gas Control 77, 96–105. https://doi.org/10.1016/j.ijggc.2018.07.011

Marieni, C., Voigt, M., Clark, D.E., Gíslason, S.R., Oelkers, E.H., 2021. Mineralization potential of water-dissolved CO2 and H2S injected into basalts as function of temperature: Freshwater versus Seawater. Int. J. Greenh. Gas Control 109. https://doi.org/10.1016/j.ijggc.2021.103357

Matter, J.M., Stute, M., Snæbjörnsdóttir, S.Ó., Oelkers, E.H., Gislason, S.R., Aradóttir, E.S., Sigfússon, B., Gunnarsson, I., Sigurdardóttir, H., Gunnlaugsson, E., Axelsson, G., Alfredsson, H.A., Wolff-Boenisch, D., Mesfin, K.G., Dideriksen, K., Broecker, W.S., 2016. Rapid carbon mineralization for permanent disposal of anthropogenic carbon dioxide emissions. Science (80-.). 352, 1312–1314. https://doi.org/10.1126/science.aad8132

McGrail, B.P., Ho, A.M., Reidel, S.P., Schaef, H.T., 2003. Use and Features of Basalt Formations for Geologic Sequestration. Greenh. Gas Control Technol. - 6th Int. Conf. II, 1637–1640. https://doi.org/10.1016/b978-008044276-1/50264-6

McGrail, B.P., Schaef, H.T., Ho, A.M., Chien, Y.-J., Dooley, J.J., Davidson, C.L., 2006. Potential for carbon dioxide sequestration in flood basalts. J. Geophys. Res. Solid Earth 111. https://doi.org/10.1029/2005JB004169

Min, Y., Jun, Y.S., 2016. Anorthite Dissolution under Conditions Relevant to Subsurface CO2 Injection: Effects of Na+, Ca2+, and Al3+. Environ. Sci. Technol. 50, 11377–11385. https://doi.org/10.1021/acs.est.6b02207

Oelkers, E.H., Schott, J., 1995. Experimental study of anorthite dissolution and the relative mechanism of feldspar hydrolysis. Geochim. Cosmochim. Acta 59, 5039–5053. https://doi.org/10.1016/0016-7037(95)00326-6

Oelkers, E.H., Schott, J., Devidal, J.L., 1994. The effect of aluminum, pH, and chemical affinity on the rates of aluminosilicate dissolution reactions. Geochim. Cosmochim. Acta 58, 2011–2024. https://doi.org/10.1016/0016-7037(94)90281-X

Olivares, J.A., Houk, R.S., 1986. Suppression of Analyte Signal by Various Concomitant Salts in Inductively Coupled Plasma Mass Spectrometry. Anal. Chem. 58, 20–25. https://doi.org/10.1021/ac00292a008

Oxburgh, R., Drever, J.I., Sun, Y.T., 1994. Mechanism of plagioclase dissolution in acid solution at 25°C. Geochim. Cosmochim. Acta 58, 661–669. https://doi.org/10.1016/0016-7037(94)90496-0

Reddi, B.A., 2013. Why Is Saline So Acidic (and Does It Really Matter?). Int. J. Med. Sci 10. https://doi.org/10.7150/ijms.5868

Rosenbauer, R.J., Thomas, B., Bischoff, J.L., Palandri, J., 2012. Carbon sequestration via reaction with basaltic rocks: Geochemical modeling and experimental results. Geochim. Cosmochim. Acta 89, 116–133. https://doi.org/10.1016/J.GCA.2012.04.042

Schoen, R., Roberson, C.E., 1970. Structures of Aluminum Hydroxide and Geochemical Implications. Am. Mineral. 55, 43–77.

Shibuya, T., Yoshizaki, M., Masaki, Y., Suzuki, K., Takai, K., Russell, M.J., 2013. Reactions between basalt and CO2-rich seawater at 250 and 350°C, 500bars: Implications for the CO2 sequestration into the modern oceanic crust and the composition of hydrothermal vent fluid in the CO2-rich early ocean. Chem. Geol. 359, 1–9. https://doi.org/10.1016/j.chemgeo.2013.08.044

Snæbjörnsdóttir, S., Gislason, S.R., 2016. CO2 storage potential of basaltic rocks offshore

Iceland. Energy Procedia 86, 371–380. https://doi.org/10.1016/j.egypro.2016.01.038

Snæbjörnsdóttir, S.Ó., Sigfússon, B., Marieni, C., Goldberg, D.S., Oelkers, E.H., 2020. Carbon dioxide storage through mineral carbonation. Nat. Rev. Earth Environ. https://doi.org/10.1038/s43017-019-0011-8

Stefánsson, A., 2001. Dissolution of primary minerals of basalt in natural waters I. Calculation of mineral solubilities from 0°C to 350°C. Chem. Geol. 172, 225–250. https://doi.org/10.1016/S0009-2541(00)00263-1

Takaya, Y., Nakamura, K., Kato, Y., 2015. Dissolution of altered tuffaceous rocks under conditions relevant for CO2 storage. Appl. Geochemistry 58, 78–87. https://doi.org/10.1016/j.apgeochem.2015.03.012

Tan, S.H., Horlick, G., 1987. Matrix-effect observations in inductively coupled plasma mass spectrometry. J. Anal. At. Spectrom. 2, 745–763.

Tole, M.P., Lasaga, A.C., Pantano, C., White, W.B., 1986. The kinetics of dissolution of nepheline (NaAlSiO4). Geochim. Cosmochim. Acta 50, 379–392. https://doi.org/10.1016/0016-7037(86)90191-2

Voigt, M., Marieni, C., Baldermann, A., Galeczka, I.M., Wolff-Boenisch, D., Oelkers, E.H., Gislason, S.R., 2021. An experimental study of basalt–seawater–CO2 interaction at 130 °C. Geochim. Cosmochim. Acta 308, 21–41. https://doi.org/10.1016/j.gca.2021.05.056

Wells, R.K., Xiong, W., Giammar, D., Skemer, P., 2017. Dissolution and surface roughening of Columbia River flood basalt at geologic carbon sequestration conditions. Chem. Geol. 467, 100–109. https://doi.org/10.1016/j.chemgeo.2017.07.028

Wolff-Boenisch, D., 2011. On the buffer capacity of CO2-charged seawater used for carbonation and subsequent mineral sequestration. Energy Procedia 4, 3738–3745. https://doi.org/10.1016/j.egypro.2011.02.307

Wolff-Boenisch, D., Galeczka, I.M., 2018. Flow-through reactor experiments on basalt-(sea)water-CO2 reactions at 90 °C and neutral pH. What happens to the basalt pore space under post-injection conditions? Int. J. Greenh. Gas Control 68, 176–190. https://doi.org/10.1016/j.ijggc.2017.11.013

Yu, Z., Liu, L., Yang, S., Li, S., Yang, Y., 2012. An experimental study of CO 2-brine-rock interaction at in situ pressure-temperature reservoir conditions. Chem. Geol. 326–327, 88–101. https://doi.org/10.1016/j.chemgeo.2012.07.030

Zhang, R., Zhang, X., Hu, S., 2015. Basalt-water interactions at high temperatures: 1. Dissolution kinetic experiments of basalt in water and NaCl-H2O at temperatures up to 400°C, 23MPa and implications. J. Asian Earth Sci. 110, 189–200. https://doi.org/10.1016/j.jseaes.2015.03.042

Chapter 6: The impact of mineralogy on the water adsorption capacity of andesitic geothermal reservoir rocks.

6.1 Introduction

The amount of water adsorbed in a geothermal reservoir can strongly influence the reservoir performance forecasts, hence geothermal energy companies have a great interest in the water adsorption capacity of a system, to assist in reserve estimation and lifetime production performance of the reservoir (Bertani *et al*., 1999; Horne *et al*., 1995; Roman, 1996). It has been reported that the adsorbed liquid represents most of the fluid in a reservoir and is therefore essential for the sustained energy production from that reservoir (Horne *et al*., 1995). While the amount of heat is effectively constant in a geothermal well, the production capacity can decrease over the lifetime of well as water is removed from the system. For example, reservoir vapour pressures have been declining at the Geysers Geothermal Reservoir in California since the 1980's. A report by Gruszkiewicz *et al*. (2001) found that steam is the pressure-controlling fluid in larger fractures at the Geysers and liquid water is stored in the matrix between the fractures, held by adsorption and capillary forces in smaller fractures and pores. As production of the field has continued, the system has become depressurized as the steam is extracted, causing matrix water to be flashed to steam. Due to this discovery, geothermal energy companies now reinject fluids into the reservoir systems to attempt to minimise this depressurization and maximise the energy extraction possible.

Understanding the water adsorption capacity of a reservoir can assist in predicting the power output of time of a reservoir. Bertani and Cappetti (1995) conducted simulations of the injection zone close to the Larderello Geothermal field in Italy, with results indicating that the average electrical power for 20 years roughly increases from 15 MW with a water adsorption value of 0 mg/g, to 35 MW with a water adsorption value of 0.42 and 0.79 mg/g). This again highlights the value in knowing the water adsorption capacity of target reservoir rocks.

Some laboratory based water adsorption experiments on geothermal reservoir rock samples are reported in the literature. Bertani *et al*. (1999) used samples from Monteverdi (the main lithologic formation in the samples is gneiss), southwest of the Larderello geothermal field in Italy to examine water adsorption at 170-200^{o}C. They report the measured surface area of the samples to be on the order of 3 m^2/g with the amount of water adsorbed around 2 mg/g, with no significant differences for the different temperatures. Shang *et al*. (1995) reported results from nitrogen and water adsorption studies using sandstone rock samples. They collected isotherms by measuring pressure and volume changes as steam was incrementally introduced into the experimental equipment. They highlight the importance of maintaining much of the equipment at high temperatures to avoid the formation of condensation. The reported isotherms show significant hysteresis, and the nitrogen and water isotherms for different samples appear visually different, which suggests the adsorption mechanisms for the two gases are different. Chemical interactions in the case of water adsorption are likely and would explain this observed difference. The authors also briefly mention the challenges encountered when attempting to measure the water retention at relative pressures beyond 0.95. Shang *et al*. (1995) found the water adsorption capacity of selected samples to be 2.7 mg/g at 120^{o}C. The BET surface area of these samples was 0.9 m^2/g. They also used samples directly from the Geysers geothermal site in California, and found a water adsorption capacity of 1.2 mg/g and a BET surface area of 0.24 m^2/g. These results give some suggestion that a higher sample surface area will give a higher water adsorption capacity.

Gruszkiewicz *et al*. (2000) reported results from water adsorption experiments using samples from geothermal well cores taken from the Geysers site in the US, and Awibengkok geothermal fields in Indonesia, at temperatures of 150, 200 and 250^{o}C. They found one of the samples from the Indonesian site adsorbed more water than any other geothermal well core sample, with roughly 45 mg/g (the BET surface area was 11.10 m^2/g). The Geysers samples had a water adsorption of close to 8 mg/g and a BET surface area of 1.31 m^2/g. They suggested that the capacity of the rocks for water adsorption depends on both the mineral

compositions and pore system features. The conclusions also suggest the use of nitrogen to gain BET specific surface areas was a poor predictor for the capacity of these geothermal rocks for water adsorption, and postulate this is likely due to the chemical interactions that take place in water adsorption, compared to purely physical interaction in nitrogen adsorption.

Johansen and Dunning (1959) examined water vapor adsorption on selected clay mineral samples, rather than whole rocks. They reported that montmorillonite and kaolinite have distinctive adsorption isotherms, which could be used to distinguish and identify them. The isotherm for illite was at an intermediate level between the other two. Montmorillonite had a maximum water adsorption of around 300 mg/g, with illite and kaolinite around 70 and 50 mg/g respectively. The montmorillonite isotherm displayed strong hysteresis with a distinctive steep section in the middle interpreted to be associated with hydration of the clay platelets and indicates that swelling type clays may be identified in samples by examining their adsorption isotherms. Evidently, clay minerals have a very high water adsorption capacity, with respect to bulk rock types, and so their presence in a rock sample is likely to significantly impact the water adsorption capacity of the measured whole rock.

Despite the interest in the impacts of reinjection on the host rock reservoirs, to the author's knowledge there are no reported studies that specifically examine any changes that might occur in water adsorption capacities of geothermal reservoir samples before and after reaction with representative geothermal fluids. The comparison before and after experiment may be important for determining whether any induced changes in mineralogy has a quantifiable impact on the water adsorption capacity of the samples. If fluids containing dissolved CO_2 are injected at geothermal energy sites, it is likely that this will cause some changes in the mineralogy of the systems, and therefore it is important to investigate whether this will have a potential impact on the long-term adsorbed water at the site. Changes in mineralogy may affect the systems due to different adsorption capacities of different minerals and/or because secondary minerals are precipitating in pore spaces, which could also reduce the permeability of the reservoir (Wolff-Boenisch, 2011; Wolff-Boenisch and Galeczka, 2018). This is a clear

knowledge gap in the literature that this study aims to address. Adsorption and desorption isotherms for water can be measured to examine the magnitude of adsorption, and the presence of any hysteresis gap between adsorption and desorption curves can provide characteristic information on the mineralogy present and the mechanisms of water adsorption within solid samples. For this study, gas adsorption equipment commonly used for nitrogen BET experiments was first optimised to use instead for water adsorption experiments. A number of the geothermal rock samples used in Chapter 3 of this study were used in water adsorption experiments here, to investigate possible differences in the magnitude and shape of adsorption isotherms before and after batch reactor experiments with acidic fluids. The aim is to examine whether dissolution/precipitation reactions that take place as a result of rock-fluid interactions have an impact on the water adsorption capacity of the samples used throughout this project. The results from Chapter 3 indicate that dissolution of aluminosilicate minerals such as plagioclase and precipitation of aluminium hydroxide minerals such as gibbsite had taken place. Since the injection of CO_2 into geothermal reservoirs will induce acidic fluids, the examination of any changes in water adsorption capacity of the samples used in the acidic experiments may indicate if CO_2 injection is likely to have an impact on the adsorbed water in the reservoir systems, with implications for reservoir production capabilities. The results will be compared to previous other studies which have examined water adsorption of geothermal reservoir rocks.

6.2 Theoretical Background

Conducting water adsorption experiments produces adsorption isotherms which describe the equilibrium relationship between the partial pressure of the adsorbate and the amount of water adsorbed at a constant temperature. The shapes of the resulting isotherms depend on the chemical composition and physical structure of the adsorbent. A paper published by Brunauer (1943) divides isotherm shapes into five types, as Shang *et al*. (1995) have summarised and sketched:

- Type *i* isotherms. These are observed for adsorption in microporous solids. Figure 6.1 demonstrates monolayer adsorption, which can be described using the Langmuir adsorption isotherm (*x/m* is the amount of solute adsorbed, *P* is pressure and P_s is the pressure where maximum solute is adsorbed).

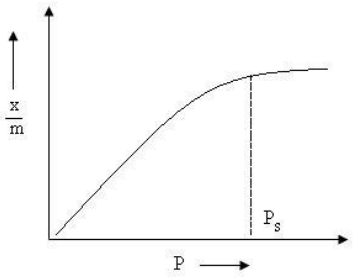


Figure 6.1: Type i isotherm.

- Type *ii* isotherms. This is common for both nonporous and microporous adsorbents. This type is shown by the isotherm in Figure 6.2, which represents unrestricted monolayer-multilayer adsorption. The intermediate flat region corresponds to monolayer formation.

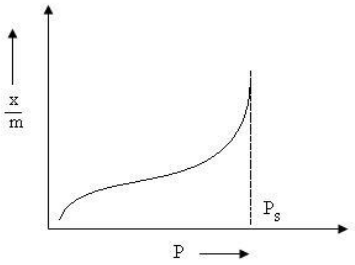


Figure 6.2: Type ii isotherm.

- Type *iii* isotherms. This is not a common form of isotherm, however, it has been observed for water vapour adsorption. This isotherm explains the formation of multilayer adsorption, with the flat middle portion (showing monolayer formation) missing as can be seen in Figure 6.3.

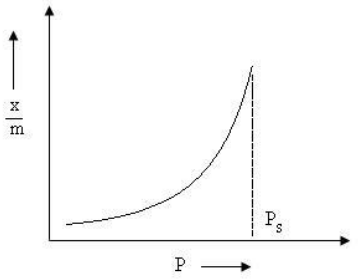


Figure 6.3: Type iii isotherm.

- Type *iv* isotherms. This isotherm is characterised by a hysteresis loop (not shown in Figure 6.4), associated with capillary condensation in mesopores. A hysteresis loop is a gap between the adsorption and desorption isotherms. At lower pressures, the isotherm in Figure 6.4 shows monolayer followed by multilayer formation, similar to type ii.

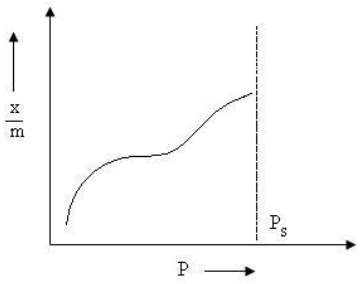


Figure 6.4: Type iv isotherm.

- At the higher pressures, the saturation level is reached at a pressure below the saturation vapour pressure. Gases condensing in the tiny capillary pores of adsorbent at pressures below the saturation pressure of the gas explains this observation.
- Type *v* isotherm. This is also characterised by the presence of a hysteresis loop. It is related to Type iii, again it is not common but has been seen for water vapour adsorption and is shown in Figure 6.5.

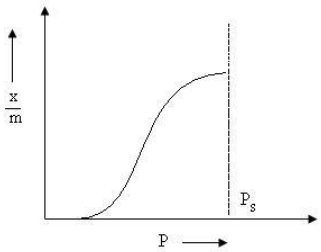


Figure 6.5: Type v isotherm.

Capillary condensation is a phenomenon is represented by the Kelvin equation (von Helmholtz, 1886):

$$RTln\left(\frac{p}{p^0}\right) = -\frac{2\gamma V}{r} \qquad (6.1)$$

The Kelvin equation (Equation 6.1) relates the equilibrium vapour pressure of a liquid to the curvature of the liquid vapour interface. In this equation, *γ* is the interfacial tension between liquid adsorbate and its vapour, *V* is the molar volume of the liquid adsorbate and r is the

effective pore radius. It is generally recognized that the Kelvin equation is valid for pore radii between 1 and 25 nm, which are classed as mesopores. Below 1 nm pore radius, multilayer adsorption develops and the micropores become filled by an adsorbed layer of water on opposing walls meeting in the middle. High uptake of adsorbent at low relative pressure is characteristic of micropore adsorption (Shang *et al*., 1995).

The presence of hysteresis loops in an adsorption/desorption isotherm can partially be explained by capillary condensation effects and the Kelvin equation. On adsorption, the pore will only become filled when the equilibrium vapour pressure is reached that satisfies the largest radius of the pore, but on desorption liquid will remain in the pore until equilibrium vapour pressure that satisfies the smallest radius of the pore is reached. Hence adsorption proceeds differently from desorption. Water molecules have the ability to form hydrogen bonds due to their polar nature. This means chemical interactions with solid surfaces are more likely to occur compared to other less reactive gases such as nitrogen, especially at increased temperatures. Chemical interactions can therefore also contribute to large amounts of hysteresis often seen in water adsorption experiments on geothermal reservoir rocks (Brunauer, 1943; Shang *et al*., 1995).

6.3 Methods

6.3.1 Experimental samples

The samples used in these investigations were taken directly from some of the samples used in the experiments described in Chapter 3 of this report, which examined rock-fluid interactions with andesitic samples under neutral and acidic fluid conditions (Table 3.4). In summary, parallel experiments were run with starting pH values either close to neutral, or close to 3 induced by the addition of a small amount of HCl. The experimental fluids also included 1000 mg/L of Na^+, 150 mg/L of K^+ and 20 mg/L of Ca^{2+} and were heated to a temperature of 100^{o}C for 360 hours. The crushed rock samples used for the rock-fluid experiments were initially prepared in bulk. Therefore, a portion of the bulk prepared crushed sample was used in the water adsorption experiments and is assumed to accurately represent the bulk properties of the whole sample before use in the rock-fluid experiments. The exact solid samples of RDB1 and RDC1 used in the rock-fluid experiments were collected and dried post experiment at 50^{o}C in a temperature-controlled oven for 5 days and then used in these water adsorption experiments.

6.3.2 Water Adsorption Experiments

For the water adsorption experiments, a 3Flex surface characterisation analyser from Micromeritics was used to measure adsorption isotherms using dynamic vapour sorption. This technique measures the changing mass of a sample at a constant temperature as a result of changing humidity. The sample is first degassed overnight under a vacuum at 100^{o}C and the dry weight of the combined sample tube and rock samples is obtained. The sample tube is then fitted to the 3Flex machine and submerged in a temperature-controlled water bath (Figure 6.1).

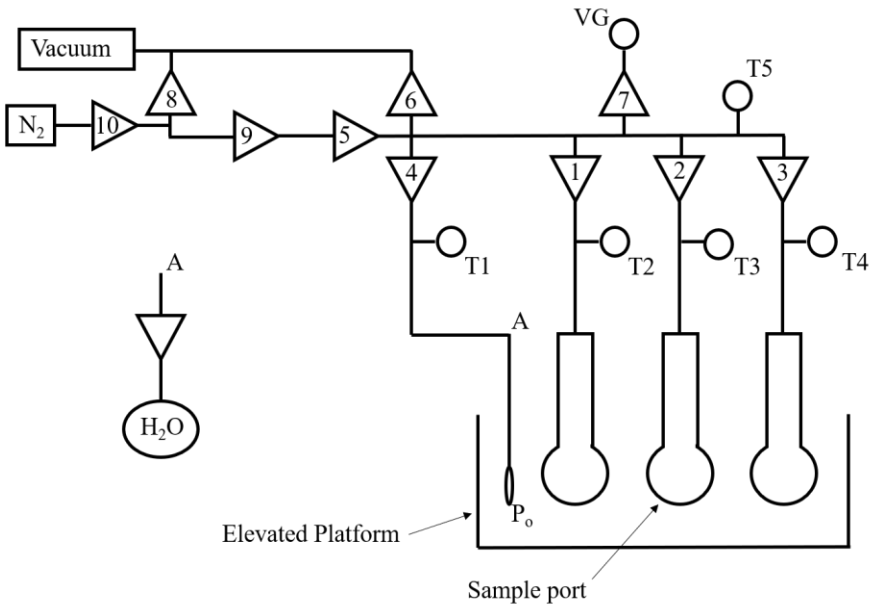


Figure 6.1: Instrument schematic for Micromeritics 3flex Analyzer, including 3 sample ports, p_o, an elevator platform which can house a liquid nitrogen Dewar or controlled temperature water bath, vacuum apparatus and a nitrogen gas source. Numbered features are 1-3) sample port valves, 4) p_o port valve, 5-6, 8-9) gas and vacuum isolation valves, 7) vacuum isolation valve, 10) gas isolation valve, T1) p_o port transducer, T2-T4) sample port transducer, T5) manifold transducer, VG) vacuum gauge. Point 'A' denotes where the p_o port can be switched out for a pure water source vessel, which is illustrated on the left of the diagram and contains an additional water shut-off valve.

The water vapor is sourced from a small vessel attached to the 3flex containing 10 mL of MQ water (Figure 6.1). Before the adsorption experiments can be initiated, the water must first go through a series degassing purification steps. The H_2O vessel (with its isolation valve closed) is submerged in liquid nitrogen to rapidly freeze the water molecules. Once frozen, the isolation valve is opened to introduce the headspace of the water vessel to the vacuum of the equipment, so any volatile impurities left in this space are evacuated to be removed from the system. The isolation valve is then closed, and the water heated back up to 35^{o}C. This process was repeated three times until a pressure reading between 40 and 45 µm Hg for the water at 35^{o}C in the vapour source was achieved, indicating complete degassing. During the

experiments, the 3flex doses precise amounts of water vapour into the tubes, allows equilibrium to be reached and measures the mass. This process is repeated until a relative pressure (p/p_o) of 0.90 is reached. The reverse process is then initiated, and the sample tube is incrementally evacuated to obtain the desorption isotherm.

Some issues initially arose with the equipment, as the water bath does not submerge the entire neck of the sample tube. In the section of the tubes above the water level exposed to the temperature fluctuations of the room, water vapour condensed on the inside. This invalidates the results as the true mass change cannot be measured. Several insulation set-ups and water bath temperatures were trialled over several months in an attempt to solve this. Using a water bath temperature of 20^{o}C worked best, likely due to being closest to room temperature, meaning the sections of the tube above and below the water level are at the same temperature. Another issue included finding a compromise between the equilibrium interval time after each dose which yields more accurate results and the total experimental time. An equilibrium interval of 15 seconds led to a total experiment run time of 50 hours. An equilibrium interval of 20 seconds showed a slight increase in water adsorption of the samples, likely closer to true adsorption, however led to the total experiment time exceeding 70 hours, which was not compatible in the long-term with the operation of the laboratory. This compromise needs to be carefully considered when obtaining water adsorption isotherms. The 3Flex equipment is also limited to a maximum vapour temperature of 35^{o}C, which places a set restriction on the conditions an experiment may be run at.

For all adsorption experiments, the crushed rock samples were added to the sample tube (approx. 1 g of solids), weighed, and then degassed overnight at 100^{o}C. The tubes were then backfilled with nitrogen and re-weighed to obtain the sample dry weight. The sample tube was then fitted to the 3flex adsorption equipment and evacuated as part of the equipment set-up process, before commencing the adsorption experiments.

6.3.3 Nitrogen BET analysis

BET (Brunauer-Emmett-Teller) theory allows calculation of the specific surface area of a sample by calculating the amount of an adsorbed gas corresponding to a monolayer on the surface of a sample. The BET adsorption isotherm equation is as follows (Equation 6.2) (Brunauer, 1943):

$$\frac{1}{\left[V_a\left(\frac{p_0}{p}-1\right)\right]} = \frac{C-1}{V_m C} \times \frac{p}{p_0} + \frac{1}{V_m C} \tag{6.2}$$

Where *P* is the partial pressure of adsorbed gas in equilibrium with the surface at 77 K, P_0 is the saturated vapour pressure of adsorbed gas, V_a is the volume of gas adsorbed at standard temperature and pressure (STP), V_m is the volume of gas adsorbed at STP to produce an apparent monolayer on the sample surface and *C* is a dimensionless constant related to the enthalpy of adsorption of the adsorbate gas on the sample (Brunauer, 1943). The BET equation is plotted as an adsorption isotherm, usually at relative pressure (p/p_0) between 0.05 and 0.35, which should give a straight line. The monolayer capacity (n_m) is found by (Equation 6.3):

$$n_m = \frac{1}{gradient - intercept} \tag{6.3}$$

And the BET constant C is found via Equation 6.4:

$$C = 1 + \frac{gradient}{intercept} \tag{6.4}$$

The surface area (s_{total}) can be calculated using the molecular cross-sectional area, *s* (Equation 6.5):

$$s_{total} = \frac{n_m N s}{V} \tag{6.5}$$

Where *N* is Avogadro's number and *V* is the molar volume of the adsorbed gas (Brunauer, 1943).

Nitrogen adsorption experiments were also run on the 3flex machine, whereby nitrogen gas is dosed into the sample tubes rather than water vapour. Analysis is performed at 77 K, achieved by submerging the tubes in liquid nitrogen for the duration of the experiment. Once the surface area of a sample is measured, it can be compared to water adsorption experiment results, to assess whether there are any links between the calculated BET surface area and the magnitude of water adsorption.

6.4 Results

6.4.1 Nitrogen BET experiments

The surface areas of the powder before and after reaction can be found in Table 6.1. According to nitrogen BET experiments, the C1 sample has a larger surface area than B1. After reaction with neutral geothermal fluids, the BET surface area of the collected B1 remains similar whereas after reaction with acidic fluids, it has noticeably increased by 0.9 m^2/g. After the reaction with neutral geothermal fluids, the collected C1 powder already has a significantly increased surface area by almost 1.5 m^2/g compared to pre-experiment. After reaction with acidic fluids, this value has increased even more, by 3.0 m^2/g.

Table 6.1: Calculated BET surface areas and maximum water adsorption of samples RDB1 and RDC1 in neutral and acidic fluid conditions, taken before and after 360-hour experiments.

Sample, condition	Surface Area (m^2/g) of rock powder: post (pre) experiment	Maximum water adsorption (mg/g) post (pre) experiment
B1, Neutral	1.0 ± 0.1 (1.1 ± 0.1)	5.1 ± 0.1 (5.0 ± 0.1)
B1, Acidic	2.0 ± 0.1 (1.1 ± 0.1)	6.0 ± 0.1 (5.0 ± 0.1)
C1, Neutral	3.2 ± 0.1 (1.7 ± 0.1)	10.9 ± 0.1 (9.2 ± 0.1)
C1, Acidic	4.7 ± 0.1 (1.7 ± 0.1)	12.6 ± 0.1 (9.2 ± 0.1)

6.4.2 Water adsorption isotherms

For all sample water adsorption isotherms, a hysteresis loop is observed with a hysteresis 'gap' between the associated adsorption and desorption isotherms. This is generally characteristic of type *iv* and *v* isotherms (Thommes *et al*., 2015). At lower pressures monolayer formation is observed (indicated by the flatter middle portion), followed by multilayer formation. The presence of the monolayer formation indicates the isotherms can be more narrowly characterised as type *iv* isotherms.

The water adsorption isotherms (Figure 6.6) and maximum adsorption values (Table 6.1) indicate that sample C1 has a higher water adsorption capacity of 9.2 mg/g compared to sample RDB1 with 5.0 mg/g. In a similar trend to the changes in BET surface area, the B1 sample has effectively no change in the maximum water adsorption capacity after the neutral experiment, with an increase of 0.1 mg/g insignificant when accounting for an experimental error of 0.1 mg/g. A more significant change occurs after the acidic experiment, with an increase of 1.0 mg/g. The C1 sample's maximum water adsorption capacity increases by 1.7 mg/g after the neutral experiment, and 3.4 mg/g after the acidic fluids experiment. The C1 sample also displays a larger hysteresis gap between adsorption and desorption isotherms. The hysteresis gap appears to widen in the isotherms for both samples after they have been subjected to the acidic fluid experiments.

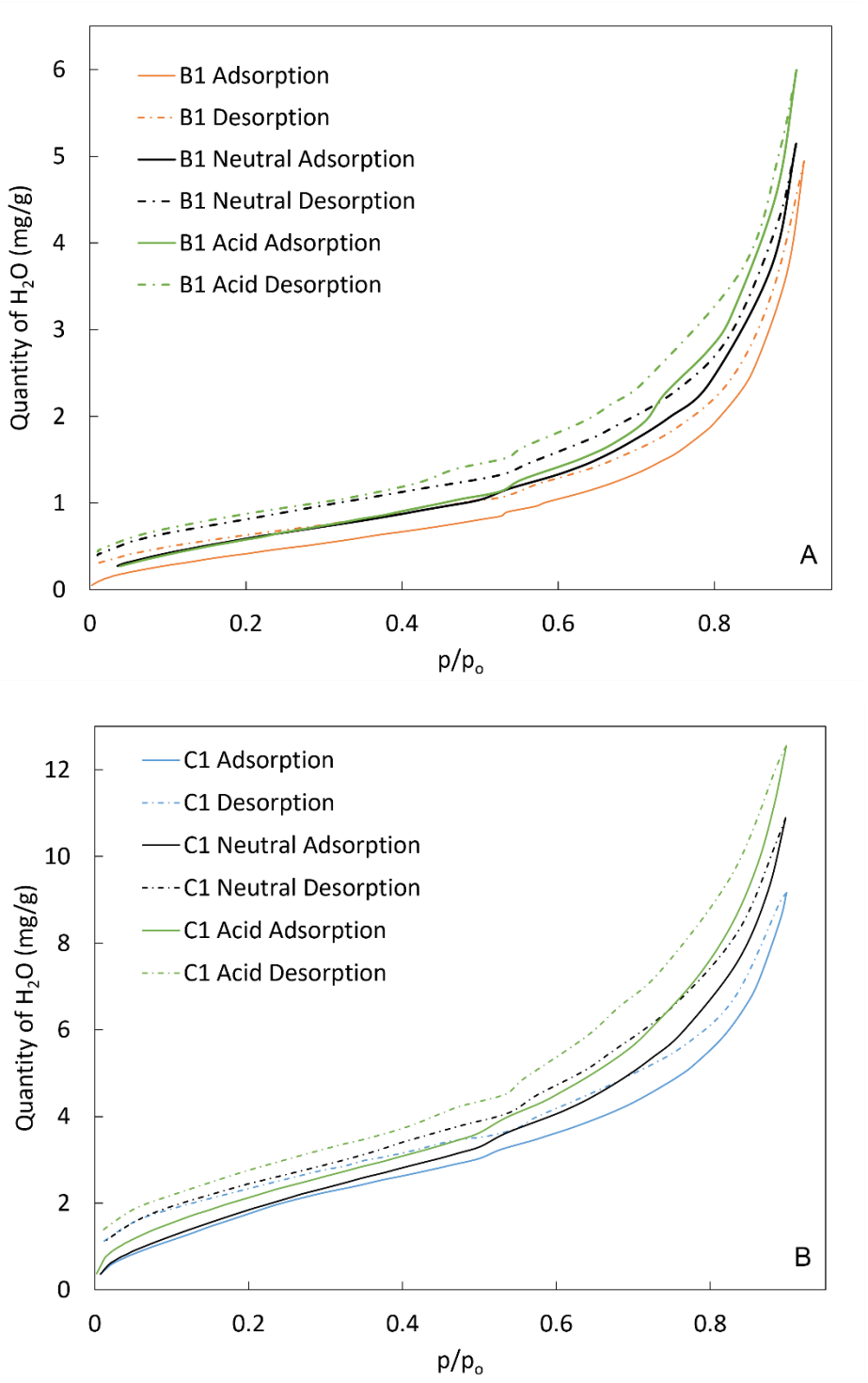


Figure 6.6: Water adsorption isotherms for the crushed rock samples before and after experiments for; A) the B1 sample and B) the C1 sample. The adsorption isotherm is illustrated by a solid line and the desorption isotherm is illustrated by a dotted line for each sample.

6.5 Discussion

6.5.1 Impact of rock-fluid interactions on surface areas

The nitrogen BET experiments indicate the C1 sample has a larger surface are than B1 (Table 6.1). Clay separation experiments (Chapter 3) indicate the crushed B1 sample contains approximately 6% clay components, and the C1 samples contains about 14% clay components, which likely explains the higher surface area of C1, as clay type minerals tend to have a high surface area due to their small particle size and layered structures (Keppert *et al*., 2016). After reaction with neutral fluids, the BET results indicate that the surface area of sample B1 did not change much, whereas the C1 sample's surface area increased by 0.9 m^2/g. The results from fluid and solid analysis in Chapter 3 included evidence to suggest the C1 sample underwent more dissolution than the B1 sample, even in the neutral fluid condition. Any partial dissolution would cause an increase in surface area, as features such as dissolution etch pits and other texture inducing phenomena inevitably lead to a larger overall surface area (Holdren and Speyer, 1987; Wells *et al*., 2017). The surface area of both samples increases more significantly after reaction with the acidic fluids, to be expected as a reduced pH is known to increase dissolution of the types of minerals present in the samples (plagioclases, chlorite etc), so increased dissolution in the acidic conditions has led to an increase in surface areas as textured dissolution features are created (Carroll and Knauss, 2005; Hellmann, 1994; Siegel and Pfannkuch, 1984; Wells *et al*., 2017).

6.5.2 Impact of rock-fluid interactions on water adsorption capacity

The higher water adsorption capacity of the original C1 sample of 9.2 mg/g compared to the B1 sample of 5.0 mg/g is likely due to the higher clay content of 14% compared to 6% for B1 (found from the clay separation analysis in Chapter 3). Clay minerals, and particularly expanding clays, have a large water adsorption capacity and surface area and tend to show larger hysteresis gaps than other minerals (Johansen and Dunning, 1959). For example, quartz and calcite can adsorb around 1 mg of water per g of solid, whereas clay minerals can

have values up to hundreds of mg/g (Keppert *et al*., 2016). Clay minerals have layered silicate structures, some of which can expand through hydration of exchangeable cations between the layers. This hydration ability combined with the small particle size and therefore high surface area is why clays have a relatively high water adsorption capacity (Deer *et al*., 2013; Hatch *et al*., 2012). Hydrophilic sites present on clay minerals provide more opportunities for water cluster formation and growth, hence a higher water adsorption capacity for samples containing such minerals (Chen *et al*., 2021). A generally higher surface area is also likely to increase the water adsorption capacity (even with a lack of clay minerals), so the higher measured BET surface area of the C1 bulk powder compared to the B1 bulk powder may have some influence on the higher water adsorption capacity.

There effectively no change in the water adsorption capacity of the B1 sample after reaction with neutral fluids, and 1.0 mg/g after reactions with acidic fluids. The C1 sample had an increase of 1.7 mg/g in its maximum water adsorption capacity after reaction with neutral fluids, and a 3.4 mg/g increase after reaction with acidic fluids. Mineral dissolution takes place at reactive surfaces, which may not be evenly distributed across the whole surface of the sample. Etch pits and other surface artefacts will be created through dissolution, which increases the overall surface area of the sample (Ali *et al*., 2017; Wells *et al*., 2017). The findings from Chapter 3 indicated the C1 sample underwent more extensive dissolution compared to B1, even in the neutral conditions, reflected in this study with more significant increases in surface areas. Acidic fluids also caused more extensive dissolution for both samples, which in turn has led to increased surface areas of the samples. Shang *et al*. (1994) found the surface area is a crucial factor in determining the amount of water retained in the rock sample. The findings of this present study reflect those of Shang *et al*. (1994), as the increases in water adsorption capacity are all associated with increased in the measured surface area of the samples.

However, the difference between the two samples maximum adsorption capacity pre-experiment is reasonably large (9.2 mg/g for C1 vs. 5.0 mg/g for B1) relative to the less

significant difference between the pre-experimental measured BET surface areas (1.7 m^2/g vs 1.1 m^2/g). This may suggest that it is not only the overall surface area that influences the adsorption capacity. Additionally, the measured surface area of the B1 sample after the acidic experiment (2.0 m^2/g) is higher than the measured BET surface area of the C1 sample prior to experiment (1.7 m^2/g), and yet the B1 sample maximum water adsorption capacity after the acidic experiments is still significantly lower than C1 sample pre-experiment (Table 6.1). This clearly indicates that the mineralogy of the sample has a strong influence on the water adsorption capacity, and not only the bulk measured surface area. Since clays are already known to have a high capacity for water adsorption, and results indicate that the C1 sample has more than double the clay content compared to the B1 sample, it seems reasonable to assume that the clay mineralogy of a sample may be particularly relevant when predicting its water adsorption capacity.

The measured water adsorption capacities for the andesitic samples used in this study (5.0 – 9.2 mg/g) are roughly equivalent to Gruszkiewicz *et al*. (2000) who reported (8 mg/g), or higher than those measured for rock samples taken from other geothermal reservoir locations such as the Geysers sandstone samples (Shang *et al*., 1995) (1.2 – 2.7 mg/g) or the Larderello site in Italy (Bertani *et al*., 1999) (2 mg/g). The study by Gruszkiewicz *et al*. (2000) did report on one sample from a geothermal reservoir in Indonesia that had a particularly high water adsorption capacity, at 45 mg/g. That sample had a high reported composition of illite, a clay mineral which is known to have a reasonably high water adsorption capacity (Johansen and Dunning, 1959). The Geysers, Larderello and the Indonesia sites are all proven to be successful geothermal reservoir sites, with the additional results from this study indicating they all tend to have a water adsorption capacity of about 1 mg/g or higher. Potentially the water adsorption capacity can be used as a diagnostic tool for selecting geothermal sites in the future. Though this would require further research with comparisons to samples from sites deemed unsuitable for geothermal energy extraction, to examine if a lower water adsorption capacity matched this characteristic. Clearly, the presence of alteration clay-type minerals

increases the water adsorption capacity, an investigation into a link between consistent reservoir pressures and high relative clay mineral content of a reservoir should be conducted. The results at least do indicate that the potential formation of alteration minerals as a result of acidic gas injection is unlikely to negatively affect the water adsorption, and therefore production capacity of the reservoir, in terms of mineralogical changes (purely linked to their water adsorption capacity). However, changes in mineralogy may impact porosity and permeability of the reservoir if precipitates occur in flow fractures for example, as discussed further in 6.5.4.

6.5.3 Isotherm hysteresis loops

Physical adsorption processes rely on relatively weak interactions between the adsorbate and adsorbent, such as Van der Waals forces. Here, the adsorbed molecules retain their identities as no bonds are broken (Carroll, 2014). Chemisorption refers to adsorption mechanisms which result in stronger chemical bonds, such as some stronger hydrogen bonds and the formation of new covalent bonds between the adsorbent and the adsorbate. In this case, the bonds of the adsorbed molecules may be broken, and new bonds formed between the adsorbent and the adsorbate (Brown, 1990). If water molecules undergo chemical reactions during the adsorption process, they are unlikely to be fully desorbed during the reverse experiment, which contributes to the existence of hysteresis loops in sorption isotherms.

The presence of hysteresis gaps between the water adsorption and desorption isotherms are more pronounced in the C1 samples compared to the B1 samples. Johansen and Dunning (1959) noted that swelling clays cause significant hysteresis in water adsorption isotherms. As results from Chapter 3 strongly indicate the presence of clays in the samples, it is reasonable to assume the hysteresis in these samples is a result of the presence of clay minerals. The desorption isotherms do not return to their original adsorption values even at the lowest pressures, particularly the C1 sample, which suggests some of the adsorbed water is still retained at the end of the adsorption experiments. This is likely the result of some

chemisorption processes taking place (Brantley *et al*., 2008). This means some stronger electrostatic bonds (such as hydrogen bonds) or even covalent bonding has taken place between the adsorbed water and the rock samples. The layered structure of clays and their hydrophilic nature arising from their ability to sustain charged surfaces means these minerals are highly likely to be susceptible to chemisorption mechanisms (Deer *et al*., 2013; Hatch *et al*., 2012; Lahn *et al*., 2020; Sang *et al*., 2019; Seemann *et al*., 2017; Zolfaghari *et al*., 2017). The dissolution and precipitation reactions that have taken place in the experiments, particularly in the acidic condition, have caused an increase in surface area of the samples, likely in the form of features such as dissolution etch pits. This can lead to the formation of more reactive surfaces, which can then undergo more chemisorption processes with water molecules as they undergo adsorption with the rock sample surfaces. This likely explains why the hysteresis gaps become larger between the isotherms for the samples that have undergone rock-fluid interactions compared to the original rock sample, and why this gap is even more pronounced for the isotherms collected for the rock samples after reaction in the acidic conditions compared to the neutral conditions.

6.5.4 Impact of other alteration minerals

The impact on the water adsorption capacity if aluminium oxide/hydroxide species are formed also needs to be investigated. These minerals can form in layered structures (Huestis *et al*., 2018) and if charged under non-neutral fluid conditions, these structures may have a higher water adsorption capacity than the original mineralogy, which could result in a positive impact in terms of a reservoir's water adsorption capacity. Aluminium hydroxide species are also capable of ion-exchange reactions and may undergo chemisorption processes (Hem and Roberson, 1967), which could impact the water adsorption capacity of the samples. Evidence from the ICP-OES fluid data and chemical modelling calculations (Figure 3.5) indicated that aluminium hydroxide species did form in the batch reactor experiments, though the extent is uncertain. If aluminium hydroxide species do adsorb more water, their formation may have a positive impact on the longevity of a geothermal reservoir system. Further experiments would

need to be conducted to examine this idea, as the aluminium hydroxide species may transform into other mineral phases over time, and those species impact of water adsorption and reservoir longevity would need to be examined.

A variety of other minerals may also form in geothermal reservoir systems which are initially acidic but equilibrate are nearer neutral conditions due to fluid-rock interactions over time. For example, carbonate minerals which were observed in Chapter 4 (Figure 4.4) when reacting the andesitic samples with acidic fluids and have also been observed in a plethora of other studies examining similar systems (McGrail *et al*., 2009; Schaef *et al*., 2013, 2011, 2009; Stockmann *et al*., 2011). Of saline fluids are used, other species such as salts may also precipitate, as was also observed in the experiments reported in Chapter 4 (Figure 4.3). Any mineral precipitation needs to be examined for its effect on porosity and permeability on the whole system, which is of course essential to maintain for reservoir performance.

6.6 Conclusions

Previous research has found that a higher surface area results in a higher water adsorption capacity, which is partially supported in the results of this study, as samples which had increased surface area after dissolution reactions have an increased water adsorption capacity. However, results also indicate that the clay content of a sample has a significant impact on the water adsorption capacity, and observed changed cannot solely be attributed to surface area. The sample with 14% initial clay content has a capacity of 9.2 mg/g, whereas a sample with a 6% clay content has a lower water adsorption capacity of 5.0 mg/g. This finding may be of interest to geothermal energy companies, to use as a positive indicator when selecting a new geothermal energy extraction site. More adsorbed water in the initial system to support the mobile water present is a positive indication for the longevity potential of the reservoir.

By comparing the changes in water adsorption of the samples before and after experiments with representative acidic geothermal fluids, evidence that the adsorption capacity increases after reaction with geothermal fluids is also a positive indication that reinjection of acidic fluids may not negatively affect the productivity of the geothermal reservoir, at least in terms of altering the mineralogy. If injection of CO_2 into the subsurface at geothermal reservoir sites is being considered, this study indicates that the water adsorption capacity of the reservoir may not be negatively impacted by associated changes in mineralogy. Similar water adsorption experiments should be conducted examining the impact of changes in mineralogy after potential carbonate precipitation on the water adsorption capacity of the system.

Contrary to the positive water adsorption impact discussed in this study, formation of secondary minerals may also act the reduce the porosity and permeability of a reservoir, by precipitating in the pore spaces present in the rock (Ahmad *et al*., 2018). Different clay minerals for example have different effects, and the impacts will need to be considered by geothermal energy companies, who may find clay minerals are formed due to feldspar

weathering in fluid reinjection locations. Other alterations minerals such as zeolites, aluminosilicate minerals and carbonates may also form, and their impact on the water adsorption capacity of these andesitic systems should also be investigated. Further research and literature reviews should be conducted and compared with the results of this study, to examine whether the benefits of increased water adsorption due to alterations minerals is outweighed by their permeability reducing properties. This present study in combination with others such as Ahmad *et al*. 2018, highlight the complexity of analysing such systems. Although the results here indicate the formation of alteration minerals in the system may increase water adsorption capacity, other factors such as the impact of flow through fractures have not been examined. Many more experiments would need to be designed to examine these factors in combination, to allow geothermal energy companies to make accurate predictions about the impact of secondary mineral formation on the longevity of the reservoir.

Overall, results from just two samples make it challenging to draw firm conclusions form this study. A more wide-ranging selection of samples should be studied, including individual clay and mineral samples as well as more representative geothermal reservoir samples, to attempt to link more strongly the mineralogical to the bulk rock characteristics of water adsorption. Samples from locations proven to be poor geothermal energy sources could also be investigated, to compare adsorption capacities and enable more conclusive links to be made between the magnitude of the water adsorption capacity of a sample and its suitability as a geothermal reservoir host. Experiments such as these provide useful information for stakeholders in geothermal energy companies who wish to know the potential capacity of a reservoir and/or the impacts of fluid reinjection into these systems. Work such as this should be undertaken using a more dedicated piece of equipment, that can be left for long equilibrium times to ensure true adsorption and desorption isotherms are being collected.

6.7 References

Ahmad, K.M., Kristaly, F., Docs, R., 2018. Effects of clay mineral and physico-chemical variables on sandstone rock permeability. J. Oil, Gas Petrochemical Sci. 1, 18–26. https://doi.org/10.30881/jogps.00006

Ali, A.M., Padmanabhan, E., Baioumy, H., 2017. Characterization of Alkali-Induced Quartz Dissolution Rates and Morphologies. Arab. J. Sci. Eng. https://doi.org/10.1007/s13369-017-2483-5

Bertani, R., Cappetti, G., 1995. Numerical simulation of the monteverdi zone, in: Proceedings of the World Geothermal Congress 1995. Florence, Italy, pp. 1735–1740.

Bertani, R., Parisi, L., Perini, R., Tarquini, B., 1999. High-temperature measurements of water adsorption in geothermal rocks. Geothermics 28, 277–294.

Brantley, S.L., White, A.F., Kubicki, J.D., 2008. Kinetics of water-rock interaction, Kinetics of Water-Rock Interaction. Springer. https://doi.org/10.1007/978-0-387-73563-4

Brown, G.E., 1990. Spectroscopic studies of chemisorption reaction mechanisms at oxide-water interfaces, in: Hochella, M.F., White, A.F. (Eds.), Mineral-Water Interface Geochemistry. De Gruyter, pp. 309–364.

Brunauer, S., 1943. The Adsorption of Gases and Vapors Volume 1. Oxford University Press.

Carroll, S.A., Knauss, K.G., 2005. Dependence of labradorite dissolution kinetics on CO2(aq), Al(aq), and temperature. Chem. Geol. 217, 213–225. https://doi.org/10.1016/j.chemgeo.2004.12.008

Carroll, S.B., 2014. Physical Adsorption of Nitrogen Gas and The Adsorption Isotherm. https://doi.org/10.13140/2.1.3997.6643

Chen, J., Gai, H., Xiao, Q., 2021. Effects of composition and temperature on water sorption in overmature Wufeng-Longmaxi shales. Int. J. Coal Geol. 234, 103673. https://doi.org/10.1016/j.coal.2020.103673

Deer, W.A., Howie, R.A., Zussman, J., 2013. Layered Silicates, in: Am Introduction to the Rock-Forming Minerals. pp. 174–246.

Gruszkiewicz, M., Horita, J., Simonson, J.M., Mesmer, R.E., 2000. High-temperature adsorption on geothermal reservoir rocks, in: World Geothermal Congress. Tohoku, Japan.

Gruszkiewicz, M.S., Horita, J., Simonson, J.M., Mesmer, R.E., Hulen, J.B., 2001. Water adsorption at high temperature on core samples from The Geysers geothermal field, California, USA. Geothermics 30, 269–302. https://doi.org/10.1016/S0375-6505(00)00049-3

Halsey, G.D., 1951. A New Multilayer Isotherm Equation with Reference to Surface Area. J. Am. Chem. Soc. 73, 2693–2696. https://doi.org/10.1021/ja01150a076

Hatch, C.D., Wiese, J.S., Crane, C.C., Harris, K.J., Kloss, H.G., Baltrusaitis, J., 2012. Water Adsorption on Clay Minerals As a Function of Relative Humidity: Application of BET and Freundlich Adsorption Models. Langmuir 28, 1790–1803. https://doi.org/10.1021/la2042873

Hellmann, R., 1994. The albite-water system: Part I. The kinetics of dissolution as a function of pH at 100, 200, and 300°C. Geochim. Cosmochim. Acta 58, 595–611. https://doi.org/10.1016/0016-7037(94)90491-X

Hem, J., Roberson, C.E., 1967. Form and Stability of Aluminum Hydroxide Complexes in Dilute Solution, USGS Water Supply Paper.

Holdren, G.R., Speyer, P.M., 1987. Reaction rate-surface area relationships during the early stages of weathering. II. Data on eight additional feldspars. Geochim. Cosmochim. Acta 51, 2311–2318. https://doi.org/10.1016/0016-7037(87)90284-5

Horne, R.N., Ramey, H.J., Shang, S., Correa, A., Hornbrook, J., Program, S.G., 1995. The Effects of Adsorption and Desorption on Production and Reinjection in Vapor-Dominated Geothermal Fields, in: Stanford Geothermal Programme. U.S. Department of Energy, Stanford University, pp. 1973–1977.

Huestis, P., Pearce, C.I., Zhang, X., N'Diaye, A.T., Rosso, K.M., LaVerne, J.A., 2018. Radiolytic stability of gibbsite and boehmite with adsorbed water. J. Nucl. Mater. 501, 224–233. https://doi.org/10.1016/j.jnucmat.2018.01.043

Johansen, R.T., Dunning, H.N., 1959. Water-Vapor Adsorption on Clays, in: Proceedings of the Sixth National Conference on Clays and Clay Minerals. Berkeley, California, pp. 249–258.

Keppert, M., Žumár, J., Čáchová, M., Koňáková, D., Svora, P., Pavlík, Z., Vejmelková, E., Černý, R., 2016. Water Vapor Diffusion and Adsorption of Sandstones: Influence of Rock Texture and Composition. Adv. Mater. Sci. Eng. 2016, 1–7. https://doi.org/10.1155/2016/8039748

Lahn, L., Bertier, P., Seemann, T., Stanjek, H., 2020. Distribution of sorbed water in the pore network of mudstones assessed from physisorption measurements. Microporous Mesoporous Mater. 295. https://doi.org/10.1016/j.micromeso.2019.109902

McGrail, B.P., Schaef, H.T., Glezakou, V.A., Dang, L.X., Owen, A.T., 2009. Water reactivity in the liquid and supercritical CO2 phase: Has half the story been neglected?, in: Energy Procedia. pp. 3415–3419. https://doi.org/10.1016/j.egypro.2009.02.131

Roman, M.B.S., 1996. Optimization of Injection into Vapour-Dominated Geothermal Reservoirs Considering Adsorption. Stanford University .

Sang, G., Liu, S., Elsworth, D., 2019. Water Vapor Sorption Properties of Illinois Shales Under Dynamic Water Vapor Conditions: Experimentation and Modeling. Water Resour. Res. 55, 7212–7228. https://doi.org/10.1029/2019WR024992

Schaef, H.T., McGrail, B.P., Owen, A.T., 2011. Basalt reactivity variability with reservoir depth in supercritical CO 2 and aqueous phases, in: Energy Procedia. Elsevier Ltd, pp. 4977–4984. https://doi.org/10.1016/j.egypro.2011.02.468

Schaef, H.T., McGrail, B.P., Owen, A.T., 2009. Basalt- CO2-H2O interactions and variability in carbonate mineralization rates. Energy Procedia 1, 4899–4906. https://doi.org/10.1016/j.egypro.2009.02.320

Schaef, H.T., McGrail, B.P., Owen, A.T., Arey, B.W., 2013. Mineralization of basalts in the CO2-H2O-H2S system. Int. J. Greenh. Gas Control 16, 187–196. https://doi.org/10.1016/j.ijggc.2013.03.020

Seemann, T., Bertier, P., Krooss, B.M., Stanjek, H., 2017. Water vapour sorption on mudrocks. Geol. Soc. London, Spec. Publ. 454, 201–233. https://doi.org/10.1144/SP454.8

Shang, S., Home, R.N., Ramey, H.J., 1994. Experimental Study of Water Vapor Adsorption on Geothermal Reservoir Rocks. Stanford, California.

Shang, S., Horne, N.R., Ramey, H.J.J., 1995. Water vapor adsorption on geothermal

reservoir rocks. Geothermics 24, 523–540. https://doi.org/10.1016/0375-6505(95)00008-E

Siegel, D.I., Pfannkuch, H.O., 1984. Silicate mineral dissolution at pH 4 and near standard temperature and pressure. Geochim. Cosmochim. Acta 48, 197–201. https://doi.org/10.1016/0016-7037(84)90362-4

Stockmann, G.J., Wolff-Boenisch, D., Gislason, S.R., Oelkers, E.H., 2011. Do carbonate precipitates affect dissolution kinetics? 1: Basaltic glass. Chem. Geol. 284, 306–316. https://doi.org/10.1016/J.CHEMGEO.2011.03.010

Thommes, M., Kaneko, K., Neimark, A. V., Olivier, J.P., Rodriguez-Reinoso, F., Rouquerol, J., Sing, K.S.W., 2015. Physisorption of gases, with special reference to the evaluation of surface area and pore size distribution (IUPAC Technical Report), Pure and Applied Chemistry. https://doi.org/10.1515/pac-2014-1117

von Helmholtz, R., 1886. Investigations of vapors and mists, especially of such things from solutions. Ann. Phys. 263, 508–543.

Wells, R.K., Xiong, W., Giammar, D., Skemer, P., 2017. Dissolution and surface roughening of Columbia River flood basalt at geologic carbon sequestration conditions. Chem. Geol. 467, 100–109. https://doi.org/10.1016/j.chemgeo.2017.07.028

Wolff-Boenisch, D., 2011. On the buffer capacity of CO2-charged seawater used for carbonation and subsequent mineral sequestration. Energy Procedia 4, 3738–3745. https://doi.org/10.1016/j.egypro.2011.02.307

Wolff-Boenisch, D., Galeczka, I.M., 2018. Flow-through reactor experiments on basalt-(sea)water-CO2 reactions at 90 °C and neutral pH. What happens to the basalt pore space under post-injection conditions? Int. J. Greenh. Gas Control 68, 176–190. https://doi.org/10.1016/j.ijggc.2017.11.013

Zolfaghari, A., Dehghanpour, H., Holyk, J., 2017. Water sorption behaviour of gas shales: I. Role of clays. Int. J. Coal Geol. 179, 130–138. https://doi.org/10.1016/j.coal.2017.05.008

Chapter 7: Concluding Remarks

7.1 Rock sample characterisation

All three rock core samples provided by Supreme Energy PT for this project are volcanic rock samples, mainly composed of varying types of feldspar minerals (approximately 69-75%), quartz (approximately 21-25%) and various alteration minerals (e.g., clay-type minerals) (approximately 1-10%). Further examination using a variety of techniques such as PXRD, XRF, electron microscopy and petrographic analysis found the feldspar minerals in each sample had varying amounts of alkali- and calcic-plagioclase content and alteration minerals such as chamosite, calcite and minor amounts of anhydrite. In general, the rock samples can all be described as andesitic in composition, which made them suitable to use in subsequent experiments, with the aim of comparing the carbon sequestration potential of andesite type rocks to the known potential of basaltic types.

7.2 Mineral dissolution and release of divalent cations from andesitic rock samples

The Paris Climate Agreement and rising global temperatures linked to increasing CO_2 concentrations in the atmosphere has highlighted the urgent need to advance and expand carbon capture and storage technologies (Department of Energy and Climate Change, 2016; Edenhofer *et al*., 2014; IPCC, 2018; McCarthy *et al*., 2001). More common place forms of geological CCS involve injecting supercritical or gaseous CO_2 into porous type reservoirs with an overlying impermeable caprock layer to store the CO_2 via physical and dissolution trapping mechanisms (Gunter *et al*., 1993). Eventually, mineral trapping will occur but this process can take thousands of years to be considered permanent in porous sedimentary systems (Snæbjörnsdóttir *et al*., 2020). Basaltic rock systems have more recently been proven to be highly suitable targets for carbon sequestration via mineral trapping mechanisms due to the high abundance of divalent cations, with field scale studies reporting successful sequestration in just 2 years (Matter *et al*., 2016; McGrail *et al*., 2017). The dissolution rate of the minerals capable of releasing divalent cations in these basaltic systems is considered to be the rate limiting step for this particular sequestration process (Oelkers *et al*., 2008; Wolff-Boenisch *et al*., 2006). A wide range of laboratory scale research was conducted using basaltic samples prior to the implementation of field scale studies, which indicated that basaltic rocks would have appreciable dissolution rates and release significant volumes of divalent cations to make them a promising target for permanent carbon sequestration and the formation of solid calcite minerals was often observed in these studies, including but not limited to: McGrail *et al*. (2009, 2006 and 2003), Schaef *et al*. (2013, 2011 and 2010), Schaef and McGrail (2009), Stockmann *et al*. (2011), Wolff-Boenisch *et al*. (2006 and 2004) and Zhang *et al*. (2015). Significantly fewer studies have been dedicated to examining whether other rock types, such as andesitic, would also make suitable targets (Marieni *et al*., 2018; Takaya *et al*., 2015), with the authors of those studies reporting encouraging results and strongly suggesting more research should be conducted. The ability to expand the technique of permanently sequestrating CO_2 emissions

to an expanded set of locations would greatly assist in the efforts to increase CCS projects and help contribute towards reducing global CO_2 emissions, hence it is clearly an area of research that needs to be more closely examined.

The results from batch reactor experiments described in Chapter 3 indicated a bulk dissolution rate of 10^{-11} mol/m^2/s for andesitic geothermal reservoir rocks. This was calculated from examining the release rate of silicon into acidic fluids, as measured by ICP-OES analysis, from crushed andesitic rock samples. This calculated dissolution rate is slightly slower than reported dissolution rate for basaltic rock samples, which typically are in the range of 10^{-9} to 10^{-10} mol/m^2/s (Gudbrandsson *et al*., 2011). Despite slightly slower dissolution rates compared to basaltic samples, the andesitic samples still released appreciable levels of the divalent cations Ca^{2+} and Mg^{2+}. These batch experiments most closely simulate conditions likely to be experienced by andesitic rocks close to the site of acidic gas injection, with the low pH nature of the fluids initiating mineral dissolution. The release of appreciable divalent cations into the experimental solutions and a dissolution rate approaching that of basaltic samples is a positive indication that further research of andesitic systems is likely to confirm them as suitable targets for carbon sequestration via mineral trapping mechanisms on appreciable timescales.

The ICP-OES analysis of the experimental fluids extracted from batch experiments conducted using resin embedded rock samples and elevated CO_2 pressures also indicated mineral dissolution had taken place and divalent cations were released into solutions. Further evidence of mineral dissolution was found using electron microscopy techniques and MLA of the rock samples surfaces. The I1 sample in particular released the most calcium into the sampled fluids in the experimental condition with increased CO_2 pressures (and no added calcium). Results from the MLA and microprobe characterisation of the specific I1 polished sample surface indicate it has a plagioclase composition with the highest anorthite content, which gives some explanation for the higher calcium release compared to the other samples. That specific I1 sample also had a relatively high content of alteration minerals such as chamosite within its surface.

These promising results add to the limited but growing number of studies investigating the feasibility of permanent carbon sequestration in volcanic rock types other than basaltic. The experiments indicate an appreciable level of divalent cations are likely to be released from andesitic type rocks on contact with acidic fluids associated with injection of CO_2. Formations with a plagioclase feldspar type with a higher anorthite content are likely to be of most interest, and areas with calcium containing alteration minerals.

This is a research area that should be expanded further. Laboratory studies of increased durations should be conducted to examine the maximum extent of divalent cation release over more relevant time periods. Fluid flow modelling experiments will be essential as a way to predict whether the dissolution and possible subsequent precipitation reactions that take place in these andesitic rock systems will have an impact on the permeability of the whole system. There is some suggestion that a slightly slower dissolution rate of andesite rocks will mean a slower rate of neutralisation of the injected acidic fluids, which may actually have a positive impact on permeability concerns, as precipitation is likely to occur further from the injection site. These are the types of questions that modelling experiments will need to consider, which in combination with further laboratory studies could provide the evidence needed to push forward with larger field scale studies in the future.

7.3 Potential for carbonate mineral formation in andesitic rock systems

The results from the acidic fluids dissolution experiments in Chapter 3 indicated that divalent cation release from the andesitic samples would occur, therefore the batch experiments conducted in Chapter 4 included several additional variables, including increased pressures of CO_2 and increased concentrations of calcium. These experiments were designed to simulate conditions both near and far from injection after significant mineral dissolution and release of divalent cations has already occurred, to examine whether any carbonate mineral formation could be observed using these andesitic samples, under conditions relevant to carbon sequestration. The experiments were conducted over short timescales of just 3 days, and evidence of calcite mineral formation was observed, using electron microscopy and energy dispersive x-ray techniques, on the surface of the C1 and I1 samples used in the experimental set-ups that included increased concentrations of CO_2 and calcium in the fluids at the start. The C1 and I1 samples were found to have a plagioclase composition with a higher anorthite content compared to the B1 sample as well as a higher amount of alteration minerals. It is suggested that these samples therefore, had an increased capacity to neutralise the acidic fluids and thereby allow calcite precipitation. The observation of calcite formation only in the experimental conditions with increased calcium and CO_2 concentrations suggests both these components are necessary in sufficient quantities to result in rapid calcite precipitation. It is possible that the presence of certain alteration minerals may increase the carbon sequestration potential of a reservoir and/or systems with high amounts of calcic-type plagioclase minerals would make better targets. Previous laboratory studies conducted with basaltic samples observed calcite formation over timescales of weeks/months/years (McGrail *et al*., 2009; Schaef *et al*., 2013, 2011; Schaef and McGrail, 2009; Stockmann *et al*., 2011), and these positive indications led to upscaled studies within basaltic systems. Therefore, the observation of calcite formation in andesitic rocks used in this study over just 3 days, indicate andesite rocks should be strongly considered as promising targets for carbon sequestration, with confirmation from increased research focus.

However, further experiments are essential to confirm these ideas. Laboratory experiment should be conducted that have the ability to test the pH in situ, to examine whether the neutralisation capacity of more anorthite containing samples does correspond with calcite precipitation. Modelling experiments and longer time laboratory experiments should be conducted to examine the magnitude of this precipitation over increased timescales, to enable predictions regarding both the potential for carbon sequestration in theses andesitic rock systems and also the possible impact on the permeability of the reservoirs. The effect on the permeability of an andesitic system as a result of the formation of alterations minerals such as carbonates and clays should receive particular focus, as the success of injecting CO_2 into geothermal reservoir systems relies on the assumption that it will not negatively affect the injectivity of the whole reservoir. It is important to understand the fate of CO_2 if it is dissolved in fluids to be injected into a reservoir. It is important to ensure the CO_2 does not transition into its gaseous phase within the subsurface, as migration of gaseous CO_2 has been interpreted to cause changes in the fracture systems of volcanic rock systems and therefore hazardous evolution of CO_2 at the surface (Peiffer *et al*., 2018).

7.4 The impact of elevated NaCl concentrations on the magnitude of feldspar dissolution

The CarbFix method for permanent carbon sequestration in basaltic reservoirs has been proven successful in basaltic reservoirs (Matter *et al*., 2016), but it involves using huge volumes of freshwater to dissolve the CO_2 for injection into the subsurface. Therefore, there is an increased interest in examining whether non-freshwater sources, such as seawater, could be used instead, to reduce the challenges associated with using large volumes of freshwater in some regions, making the method more viable for a larger range of locations (Snæbjörnsdóttir *et al*., 2020). As discussed, this thesis has a focus on examining whether andesitic type rock systems could be suitable targets for permanent carbon sequestration, in the same way the CarbFix method has been proven to be in basaltic systems. Feldspar minerals are commonly present in both volcanic rock types, and have been suggested as being key contributors when considering a volcanic rock system's potential for carbonate mineral formation (Marieni and Oelkers, 2018). Therefore, it is important to examine the impact using saline fluids might have on the magnitude of feldspar mineral dissolution, as mineral dissolution is considered to be the key limiting factor in the process of carbon sequestration via mineral trapping.

Experiments conducted using crushed feldspar samples and fluids ranging in NaCl concentration from 0 – 2.1 M, under increased temperature and acidic pH conditions relevant to CO_2 injection into the subsurface indicated that feldspar mineral dissolution had taken place. The ICP-OES results in Chapter 5 indicate than Si was released into the fluids, with a final concentration in the range of 40 – 100 mg/L after a 7-day experimental duration. The feldspar mineral with a higher anorthite content appeared to be more effective at buffering the acidic fluids, with a notable increase in pH by the end of the experimental duration compared to the feldspar mineral with a more alkali-feldspar composition. There was some indication that an increased concentration of NaCl in the fluids slightly inhibits feldspar dissolution, but this effect was minor in this experimental set-up. These results give some indication that using saline

fluids instead of freshwater to dissolve and inject CO_2 into a volcanic reservoir is unlikely to inhibit carbon sequestration potential.

However, further laboratory experiments would be needed to more definitely separate the effects of salinity and pH on the dissolution of feldspar minerals. Other laboratory scale and modelling studies should also be conducted examining the potential impacts of the different alteration mineral that may form in acidic saline systems, as this may have significant implications for the permeability of a system. Experiments using dissolved CO_2 as the acidity source (instead of HCl) should be conducted alongside the use of saline fluids to more closely simulate carbon sequestration conditions.

7.5 The impact of rock sample mineralogy on the water adsorption capacity of andesitic geothermal reservoir rocks

The water adsorption capacity of a geothermal reservoir can be used as an indication of its production potential and estimated lifetime, with a higher capacity one indication of a better geothermal energy production potential. Water adsorption experiments have been conducted using basaltic samples from representative geothermal sites, as well as on individual minerals, but to the authors knowledge no research has been conducted examining the impact of a changing mineralogy on the water adsorption capacity of andesitic-type samples. The experiments reported in Chapter 6 indicate the andesitic samples used have a water adsorption capacity ranging from approximately 5 – 9 mg/g, which is comparable to other studies that used samples from successful geothermal energy reservoir rocks (Gruszkiewicz *et al*., 2000). Comparing the water adsorption isotherms for andesitic samples taken before and after interaction with neutral and acidic fluids indicated an increase in water adsorption capacity of the rock samples. This indicates that reinjection of acidic fluids into an andesitic geothermal reservoir may not negatively impact its water adsorption capacity in terms of changing mineralogy.

More research should be conducted however, to examine the impact of changing porosity and permeability on the water adsorption capacity of rock samples as a result of acidic fluid interaction. The samples used in this study appear to have mainly undergone dissolution reactions, however, rock samples exposed to increased concentrations of CO_2 and calcium may result in carbonate mineral precipitation, and so the impact of these changes on the water adsorption capacity of a system may give an insight into the longevity potential of a reservoir under those conditions. It seems likely that other alteration minerals are likely to form, such as clay minerals. The impact on the water adsorption capacity of a reservoir with changing concentrations of clay minerals remains unclear, as some evidence suggests clays increase the water adsorption capacity of a sample, whilst others suggest that such minerals will precipitate in pore spaces and thus reduce the overall capacity of a geothermal reservoir

system. Clearly more research needs to be conducted to examine these ideas, to gain further understanding on the impact of changing mineralogy on the water adsorption capacity of a reservoir, and enable this to be used as a useful indicator for geothermal energy companies to utilise as a site selection tool.

7.6 References

Department of Energy and Climate Change, 2016. UK Energy Statistics, 2015 and Q4 2015. Stat. Press Release 1–16.

Edenhofer, O., Pichs-Madruga, R., Sokona, Y., Farahani, E., Kadner, S., Seyboth, K., Adler, A., Baum, I., Brunner, S., Eickemeier, P., Kriemann, B., Savolainen, J., Schlömer, S., Stechow, C. v., Zwickel, T., Minx, J.C., 2014. Climate change 2014: Mitigation of Climate Change. Contribution of Working Group III to the Fifth Assessment Report of the Intergovernmental Panel on Climate Change, IPCC. Cambridge University Press, Cambridge, United Kingdom and New York, NY, USA.

Gruszkiewicz, M., Horita, J., Simonson, J.M., Mesmer, R.E., 2000. High-temperature adsorption on geothermal reservoir rocks, in: World Geothermal Congress. Tohoku, Japan.

Gudbrandsson, S., Wolff-Boenisch, D., Gislason, S.R., Oelkers, E.H., 2011. An experimental study of crystalline basalt dissolution from $2 \leqslant pH \leqslant 11$ and temperatures from 5 to 75°C. Geochim. Cosmochim. Acta 75, 5496–5509. https://doi.org/10.1016/j.gca.2011.06.035

Gunter, W.D., Perkins, E.H., McCann, T.J., 1993. Aquifer disposal of CO_2-rich gases: Reaction design for added capacity. Energy Convers. Manag. 34, 941–948. https://doi.org/10.1016/0196-8904(93)90040-H

IPCC, 2018. Summary for Policymakers, in: Masson-Delmotte, V., Zhai, P., Portner, H.-O., Roberts, D., Skea, J., Shukla, P.R., Pirani, A., Moufouma-Okia, W., Pean, C., Pidcock, R., Connors, S., Matthews, J.B.R., Chen, Y., Zhou, X., Gomis, M.I., Lonnoy, E., Maycock, T., Tignor, M., Waterfield, T. (Eds.), Global Warming of 1.5oC. An IPCC Special Report on the Impacts of Global Warming of 1.5^{o}C above Pre-Industrial Levels and Related Global Greenhouse Gas Emission Pathways, in the Context of Strengthening the Global Response to the Threat of Climate Change,. Geneva.

Marieni, C., Oelkers, E., 2018. Carbon sequestration potential of altered mafic reservoirs. Energy Procedia 146, 68–73. https://doi.org/10.1016/j.egypro.2018.07.010

Marieni, C., Přikryl, J., Aradóttir, E.S., Gunnarsson, I., Stefánsson, A., 2018. Towards 'green' geothermal energy: Co-mineralization of carbon and sulfur in geothermal reservoirs. Int. J. Greenh. Gas Control 77, 96–105. https://doi.org/10.1016/j.ijggc.2018.07.011

Matter, J.M., Stute, M., Snæbjörnsdóttir, S.Ó., Oelkers, E.H., Gislason, S.R., Aradóttir, E.S., Sigfússon, B., Gunnarsson, I., Sigurdardóttir, H., Gunnlaugsson, E., Axelsson, G., Alfredsson, H.A., Wolff-Boenisch, D., Mesfin, K.G., Dideriksen, K., Broecker, W.S., 2016. Rapid carbon mineralization for permanent disposal of anthropogenic carbon dioxide emissions. Science 352, 1312–1314. https://doi.org/10.1126/science.aad8132

McCarthy, J.J., Canziani, O.F., Leary, N.A., Dokken, D., White, K.S., 2001. Climate Change 2001: Impacts, Adaptation, and Vulnerability. Cambridge University Press, Cambridge, United Kingdom.

McGrail, B.P., Ho, A.M., Reidel, S.P., Schaef, H.T., 2003. Use and Features of Basalt Formations for Geologic Sequestration. Greenh. Gas Control Technol. - 6th Int. Conf. II, 1637–1640. https://doi.org/10.1016/b978-008044276-1/50264-6

McGrail, B.P., Schaef, H.T., Glezakou, V.A., Dang, L.X., Owen, A.T., 2009. Water reactivity in the liquid and supercritical CO2 phase: Has half the story been neglected?, in: Energy Procedia. pp. 3415–3419. https://doi.org/10.1016/j.egypro.2009.02.131

McGrail, B.P., Schaef, H.T., Ho, A.M., Chien, Y.-J., Dooley, J.J., Davidson, C.L., 2006. Potential for carbon dioxide sequestration in flood basalts. J. Geophys. Res. Solid Earth 111. https://doi.org/10.1029/2005JB004169

McGrail, P., Schaef, H.T., Spane, F.A., Cliff, J.B., Qafoku, O., Horner, J.A., Thompson, C.J., Owen, A.T., Sullivan, C.E., 2017. Field validation of supercritical CO_2 reactivity with basalts. Environ. Sci. Technol. Lett. 4, 6–10. https://doi.org/10.1021/acs.estlett.6b00387

Oelkers, E.H., Gislason, S.R., Matter, J.M., 2008. Mineral Carbonation of CO_2. Elements 4, 333–337. https://doi.org/10.2113/gselements.4.5.333

Peiffer, L., Wanner, C., Lewicki, J.L., 2018. Unraveling the dynamics of magmatic CO_2 degassing at Mammoth Mountain, California. Earth Planet. Sci. Lett. 484, 318–328. https://doi.org/10.1016/j.epsl.2017.12.038

Schaef, H.T., McGrail, B.P., 2009. Dissolution of Columbia River Basalt under mildly acidic conditions as a function of temperature: Experimental results relevant to the geological sequestration of carbon dioxide. Appl. Geochemistry 24, 980–987. https://doi.org/10.1016/j.apgeochem.2009.02.025

Schaef, H.T., McGrail, B.P., Owen, A.T., 2011. Basalt reactivity variability with reservoir depth in supercritical CO_2 and aqueous phases, in: Energy Procedia. Elsevier Ltd, pp. 4977–4984. https://doi.org/10.1016/j.egypro.2011.02.468

Schaef, H.T., McGrail, B.P., Owen, A.T., 2010. Carbonate mineralization of volcanic province basalts. Int. J. Greenh. Gas Control 4, 249–261. https://doi.org/10.1016/j.ijggc.2009.10.009

Schaef, H.T., McGrail, B.P., Owen, A.T., Arey, B.W., 2013. Mineralization of basalts in the CO_2-H_2O-H_2S system. Int. J. Greenh. Gas Control 16, 187–196. https://doi.org/10.1016/j.ijggc.2013.03.020

Snæbjörnsdóttir, S.Ó., Sigfússon, B., Marieni, C., Goldberg, D.S., Oelkers, E.H., 2020. Carbon dioxide storage through mineral carbonation. Nat. Rev. Earth Environ. https://doi.org/10.1038/s43017-019-0011-8

Stockmann, G.J., Wolff-Boenisch, D., Gislason, S.R., Oelkers, E.H., 2011. Do carbonate precipitates affect dissolution kinetics? 1: Basaltic glass. Chem. Geol. 284, 306–316. https://doi.org/10.1016/J.CHEMGEO.2011.03.010

Takaya, Y., Nakamura, K., Kato, Y., 2015. Dissolution of altered tuffaceous rocks under conditions relevant for CO_2 storage. Appl. Geochemistry 58, 78–87. https://doi.org/10.1016/j.apgeochem.2015.03.012

Wolff-Boenisch, D., Gislason, S.R., Oelkers, E.H., 2006. The effect of crystallinity on dissolution rates and CO_2 consumption capacity of silicates. Geochim. Cosmochim. Acta 70, 858–870. https://doi.org/10.1016/j.gca.2005.10.016

Wolff-Boenisch, D., Gislason, S.R., Oelkers, E.H., Putnis, C. V., 2004. The dissolution rates of natural glasses as a function of their composition at pH 4 and 10.6, and temperatures from 25 to 74°C. Geochim. Cosmochim. Acta 68, 4843–4858. https://doi.org/10.1016/j.gca.2004.05.027

Zhang, R., Zhang, X., Hu, S., 2015. Basalt-water interactions at high temperatures: 1. Dissolution kinetic experiments of basalt in water and NaCl-H_2O at temperatures up to 400°C, 23MPa and implications. J. Asian Earth Sci. 110, 189–200. https://doi.org/10.1016/j.jseaes.2015.03.042

Appendix

Table A1: B1_HPnoCa resin sample MLA results pre-experiment.

Mineral	Formula	Weight%	Area microns
Quartz	SiO_2	23.99	26542049.51
Stilbite	$NaCa_4(Al_8Si_{27}O_{72}).nH_2O$	6.03	10482231.97
Plagioclase	$NaAlSi_3O_8$ - $CaAl_2Si_2O_8$	5.72	6185144.27
Pyrite	FeS_2	0	0
Hornblende	$Ca_2(Mg,Fe,Al)_5(Al,Si)_8O_{22}(OH)_2$	0.08	78000.32
Pseudobrookite	Fe_2TiO_5	0.59	390228.24
Andesine	$(Ca/Na)(Al,Si)_4O_8$ $(0.3\text{-}0.5_{an})$	0.03	33436.02
Chamosite	$(Fe^{2+},Mg,Fe^{3+})_5Al(Si_3Al)O_{10}(OH,O)_8$	3.97	3601197.37
Chlorapatite	$Ca_5(PO_4)_3Cl$	0.21	193677.39
Zircon	ZrSiO	0.03	20231.24
Manganoan ilmenite	$(Mn)FeTiO_3$	0.11	69343.36
Calcite	$CaCO_3$	0.63	677157.97
Microcline	$KAlSi_3O_8$	9	10208594.75
Titanite	$CaTiSiO_5$	0.03	22468.59
Anhydrite	$CaSO_4$	0.03	29268.4
Titanite/pseudobrookite	$CaTiSiO_5$	0.53	287967.98
Orthoclase	$KAlSi_3O_8$	12.93	14666574.55
Prehnite	$Ca_2Al(AlSi_3O_{10})(OH)_2$	0.03	27586.73
Pumpellyite-(Fe2)	$Ca_2MgAl_2(SiO_4)(Si_2O_7)(OH)_2.(H_2O)$	0.12	110244.54
Epidote	$Ca_2Al_2(Fe,Al)(SiO_4)(Si_2O_7)O(OH)$	0.41	348106.02
Altered titanite	$CaTiSiO_5$	0.22	164957.56
Albite	$NaAlSi_3O_8$	34.86	38632968.53
Grothite-titanite	$CaTiSiO_5$	0.45	582545.67
Salt	NaCl	0	0

Table A2: B1_HPnoCa resin sample MLA results post-experiment.

Mineral	Formula	Weight%	Area microns
Quartz	SiO_2	23.81	26989539.27
Stilbite	$NaCa_4(Al_8Si_{27}O_{72}).nH_2O$	5.68	10111942.53
Plagioclase	$NaAlSi_3O_8$ - $CaAl_2Si_2O_8$	6.05	6702710.14
Pyrite	FeS_2	0	0
Hornblende	$Ca_2(Mg,Fe,Al)_5(Al,Si)_8O_{22}(OH)_2$	0.08	86214.06
Pseudobrookite	Fe_2TiO_5	0.61	414533.94
Andesine	$(Ca/Na)(Al,Si)_4O_8$ $(0.3\text{-}0.5_{an})$	0.06	67375.82
Chamosite	$(Fe^{2+},Mg,Fe^{3+})_5Al(Si_3Al)O_{10}(OH,O)_8$	3.83	3561168.64
Chlorapatite	$Ca_5(PO_4)_3Cl$	0.18	172282.61
Zircon	ZrSiO	0.03	20954.9
Manganoan ilmenite	$(Mn)FeTiO_3$	0.12	73580.73
Calcite	$CaCO_3$	0.02	16787.73
Microcline	$KAlSi_3O_8$	6.15	7149007.15
Titanite	$CaTiSiO_5$	0.02	17832.83
Anhydrite	$CaSO_4$	0	0
Titanite/pseudobrookite	$CaTiSiO_5$	0.58	325435.93
Orthoclase	$KAlSi_3O_8$	14.82	17220693.52
Prehnite	$Ca_2Al(AlSi_3O_{10})(OH)_2$	0.01	13427.54
Pumpellyite-(Fe2)	$Ca_2MgAl_2(SiO_4)(Si_2O_7)(OH)_2.(H_2O)$	0.07	68579.67
Epidote	$Ca_2Al_2(Fe,Al)(SiO_4)(Si_2O_7)O(OH)$	0.43	367451.56
Altered titanite	$CaTiSiO_5$	0.23	171594.69
Albite	$NaAlSi_3O_8$	36.77	41755387.56
Grothite-titanite	$CaTiSiO_5$	0.39	521028.21
Salt	NaCl	0.05	74651.83

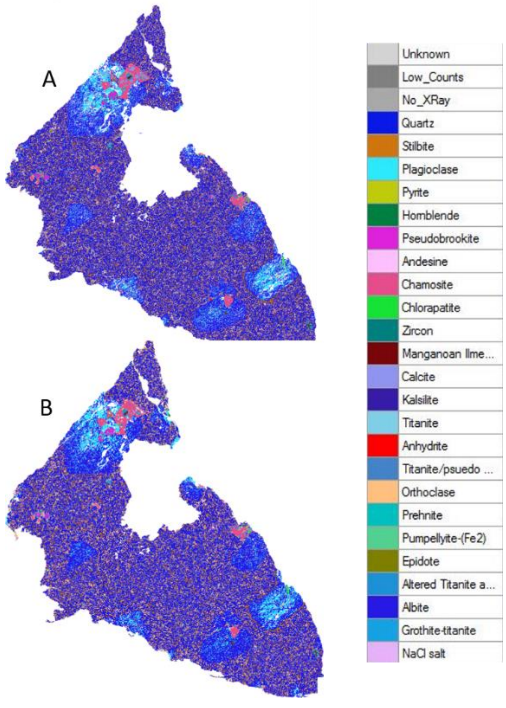


Figure A1: B1_HPnoCa resin sample MLA phase map A) pre-experiment and B) post-experiment.

Table A3: B1_HPCa resin sample MLA results pre-experiment.

Mineral	Formula	Weight%	Area microns
Quartz	SiO_2	29.02	34124421.59
Stilbite	$NaCa_4(Al_8Si_{27}O_{72}).nH_2O$	7.07	13069512.97
Plagioclase	$NaAlSi_3O_8$ - $CaAl_2Si_2O_8$	1.53	1761858.09
Pyrite	FeS_2	0	0
Hornblende	$Ca_2(Mg,Fe,Al)_5(Al,Si)_8O_{22}(OH)_2$	0.07	76750.03
Pseudobrookite	Fe_2TiO_5	0.71	499390.66
Andesine	$(Ca/Na)(Al,Si)_4O_8$ $(0.3\text{-}0.5_{an})$	0.02	18249.79
Chamosite	$(Fe^{2+},Mg,Fe^{3+})_5Al(Si_3Al)O_{10}(OH,O)_8$	3.21	3099832.57
Chlorapatite	$Ca_5(PO_4)_3Cl$	0.07	68458.66
Zircon	ZrSiO	0.03	17547.88
Manganoan ilmenite	$(Mn)FeTiO_3$	0.03	17226.17
Calcite	$CaCO_3$	0.4	460288.14
Microcline	$KAlSi_3O_8$	9.85	11878984.53
Titanite	$CaTiSiO_5$	0.01	12919.62
Anhydrite	$CaSO_4$	0.02	16707.04
Titanite/pseudobrookite	$CaTiSiO_5$	0.57	331720.69
Orthoclase	$KAlSi_3O_8$	16.21	19538494.16
Prehnite	$Ca_2Al(AlSi_3O_{10})(OH)_2$	0.02	19492.77
Pumpellyite-(Fe2)	$Ca_2MgAl_2(SiO_4)(Si_2O_7)(OH)_2.(H_2O)$	0.11	107531.93
Epidote	$Ca_2Al_2(Fe,Al)(SiO_4)(Si_2O_7)O(OH)$	0.33	291872.39
Altered titanite	$CaTiSiO_5$	0.09	68999.72
Albite	$NaAlSi_3O_8$	30.18	35547488.66
Grothite-titanite	$CaTiSiO_5$	0.45	619966.51
Salt	NaCl	0	1389.21

Table A4: B1_HPCa resin sample MLA results post-experiment.

Mineral	Formula	Weight%	Area microns
Quartz	SiO_2	29.58	34529556.33
Stilbite	$NaCa_4(Al_8Si_{27}O_{72}).nH_2O$	6.51	11941998.46
Plagioclase	$NaAlSi_3O_8$ - $CaAl_2Si_2O_8$	1.74	1985371.97
Pyrite	FeS_2	0	0
Hornblende	$Ca_2(Mg,Fe,Al)_5(Al,Si)_8O_{22}(OH)_2$	0.06	67419.79
Pseudobrookite	Fe_2TiO_5	0.67	467840.23
Andesine	$(Ca/Na)(Al,Si)_4O_8$ $(0.3\text{-}0.5_{an})$	0.01	11122.04
Chamosite	$(Fe^{2+},Mg,Fe^{3+})_5Al(Si_3Al)O_{10}(OH,O)_8$	2.48	2378741.72
Chlorapatite	$Ca_5(PO_4)_3Cl$	0.07	63469.78
Zircon	ZrSiO	0.02	14438.43
Manganoan ilmenite	$(Mn)FeTiO_3$	0.03	18819.84
Calcite	$CaCO_3$	0	2952.4
Microcline	$KAlSi_3O_8$	7.41	8863727.54
Titanite	$CaTiSiO_5$	0.01	10717.6
Anhydrite	$CaSO_4$	0	0
Titanite/pseudobrookite	$CaTiSiO_5$	0.93	533143.47
Orthoclase	$KAlSi_3O_8$	18.45	22080756.79
Prehnite	$Ca_2Al(AlSi_3O_{10})(OH)_2$	0.01	10663.68
Pumpellyite-(Fe2)	$Ca_2MgAl_2(SiO_4)(Si_2O_7)(OH)_2.(H_2O)$	0.09	82168.29
Epidote	$Ca_2Al_2(Fe,Al)(SiO_4)(Si_2O_7)O(OH)$	0.33	296709.1
Altered titanite	$CaTiSiO_5$	0.11	86482.3
Albite	$NaAlSi_3O_8$	30.97	36214511.86
Grothite-titanite	$CaTiSiO_5$	0.4	549010.91
Salt	NaCl	0.12	164350.06

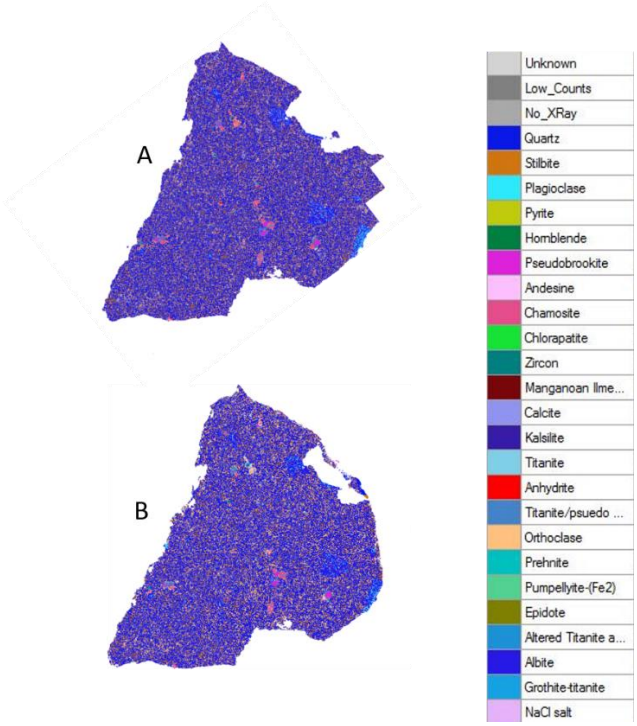


Figure A2: B1_HPCa resin sample MLA phase map A) pre-experiment and B) post-experiment.

Table A5: B1_LPCa resin sample MLA results pre-experiment.

Mineral	Formula	Weight%	Area microns
Quartz	SiO_2	27.74	25919224.15
Stilbite	$NaCa_4(Al_8Si_{27}O_{72}).nH_2O$	6.92	10168519.79
Plagioclase	$NaAlSi_3O_8$ - $CaAl_2Si_2O_8$	2.43	2220727.77
Pyrite	FeS_2	0	0
Hornblende	$Ca_2(Mg,Fe,Al)_5(Al,Si)_8O_{22}(OH)_2$	0.08	70184.2
Pseudobrookite	Fe_2TiO_5	0.59	327231.36
Andesine	$(Ca/Na)(Al,Si)_4O_8$ $(0.3\text{-}0.5_{an})$	0.02	18900.53
Chamosite	$(Fe^{2+},Mg,Fe^{3+})_5Al(Si_3Al)O_{10}(OH,O)_8$	2.98	2286415.33
Chlorapatite	$Ca_5(PO_4)_3Cl$	0.11	85589.77
Zircon	ZrSiO	0.04	19112.56
Manganoan ilmenite	$(Mn)FeTiO_3$	0.01	6192.94
Calcite	$CaCO_3$	0.3	270442.04
Microcline	$KAlSi_3O_8$	10.46	10022090.06
Titanite	$CaTiSiO_5$	0.02	10674.96
Anhydrite	$CaSO_4$	0.03	21094.01
Titanite/pseudobrookite	$CaTiSiO_5$	0.66	303775.7
Orthoclase	$KAlSi_3O_8$	14.39	13787243.1
Prehnite	$Ca_2Al(AlSi_3O_{10})(OH)_2$	0.02	15383.64
Pumpellyite-(Fe2)	$Ca_2MgAl_2(SiO_4)(Si_2O_7)(OH)_2.(H_2O)$	0.11	84083.58
Epidote	$Ca_2Al_2(Fe,Al)(SiO_4)(Si_2O_7)O(OH)$	0.37	262172.6
Altered titanite	$CaTiSiO_5$	0.09	57198.77
Albite	$NaAlSi_3O_8$	32.35	30197930.45
Grothite-titanite	$CaTiSiO_5$	0.38	423093.95
Salt	NaCl	0	0

Table A6: B1_LPCa resin sample MLA results post-experiment.

Mineral	Formula	Weight%	Area microns
Quartz	SiO_2	28.44	26492418.89
Stilbite	$NaCa_4(Al_8Si_{27}O_{72}).nH_2O$	6.18	9047382.77
Plagioclase	$NaAlSi_3O_8$ - $CaAl_2Si_2O_8$	2.88	2626972
Pyrite	FeS_2	0	0
Hornblende	$Ca_2(Mg,Fe,Al)_5(Al,Si)_8O_{22}(OH)_2$	0.06	54275.56
Pseudobrookite	Fe_2TiO_5	0.51	282499.84
Andesine	$(Ca/Na)(Al,Si)_4O_8$ $(0.3\text{-}0.5_{an})$	0.02	16137.07
Chamosite	$(Fe^{2+},Mg,Fe^{3+})_5Al(Si_3Al)O_{10}(OH,O)_8$	2.2	1681666.1
Chlorapatite	$Ca_5(PO_4)_3Cl$	0.1	77503.78
Zircon	ZrSiO	0.04	18765.92
Manganoan ilmenite	$(Mn)FeTiO_3$	0.02	8897.63
Calcite	$CaCO_3$	0	2143.52
Microcline	$KAlSi_3O_8$	6.64	6344928.99
Titanite	$CaTiSiO_5$	0.01	8735.86
Anhydrite	$CaSO_4$	0	0
Titanite/pseudobrookite	$CaTiSiO_5$	0.65	299634.53
Orthoclase	$KAlSi_3O_8$	17.67	16874805.7
Prehnite	$Ca_2Al(AlSi_3O_{10})(OH)_2$	0.01	7252.92
Pumpellyite-(Fe2)	$Ca_2MgAl_2(SiO_4)(Si_2O_7)(OH)_2.(H_2O)$	0.04	34255.89
Epidote	$Ca_2Al_2(Fe,Al)(SiO_4)(Si_2O_7)O(OH)$	0.4	285452.24
Altered titanite	$CaTiSiO_5$	0.09	56769.59
Albite	$NaAlSi_3O_8$	33.33	31101689.33
Grothite-titanite	$CaTiSiO_5$	0.33	366245.44
Salt	NaCl	0.36	401161.91

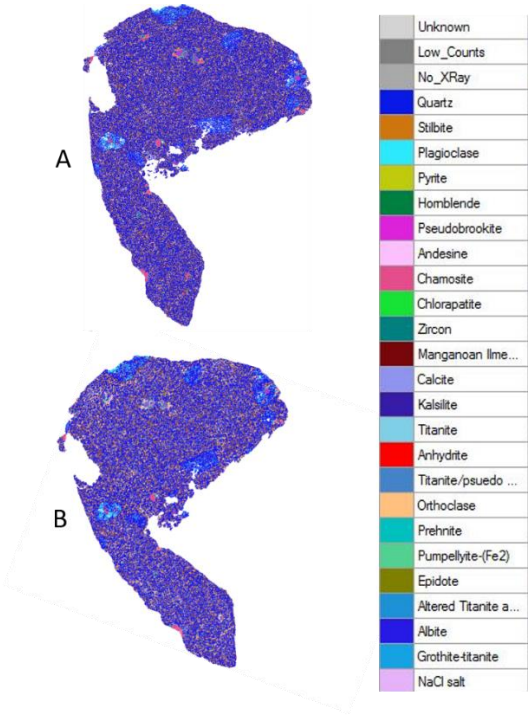


Figure A3: B1_LPCa resin sample MLA phase map A) pre-experiment and B) post-experiment.

Table A7: C1_HPnoCa resin sample MLA results pre-experiment.

Mineral	Formula	Weight%	Area microns
Quartz	SiO_2	13.29	19178828.48
Stilbite	$NaCa_4(Al_8Si_{27}O_{72}).nH_2O$	6.8	15420350.94
Plagioclase	$NaAlSi_3O_8$ - $CaAl_2Si_2O_8$	1.51	2129968.69
Pyrite	FeS_2	0.54	410342.49
Hornblende	$Ca_2(Mg,Fe,Al)_5(Al,Si)_8O_{22}(OH)_2$	1.13	1481589.24
Pseudobrookite	Fe_2TiO_5	0.01	4386.97
Andesine	$(Ca/Na)(Al,Si)_4O_8$ ($0.3\text{-}0.5_{an}$)	0.03	42714.46
Chamosite	$(Fe^{2+},Mg,Fe^{3+})_5Al(Si_3Al)O_{10}(OH,O)_8$	23.58	27903369.98
Chlorapatite	$Ca_5(PO_4)_3Cl$	0.06	64585.79
Zircon	ZrSiO	0	190.1
Manganoan ilmenite	$(Mn)FeTiO_3$	0.02	12700.28
Calcite	$CaCO_3$	0	979.76
Microcline	$KAlSi_3O_8$	2.57	3803188.06
Titanite	$CaTiSiO_5$	0.19	207730.31
Anhydrite	$CaSO_4$	0	701.92
Titanite/pseudobrookite	$CaTiSiO_5$	0.03	18454.52
Orthoclase	$KAlSi_3O_8$	3.21	4741363.4
Prehnite	$Ca_2Al(AlSi_3O_{10})(OH)_2$	2.96	3899752.57
Pumpellyite-(Fe2)	$Ca_2MgAl_2(SiO_4)(Si_2O_7)(OH)_2.(H_2O)$	1.63	1925718.71
Epidote	$Ca_2Al_2(Fe,Al)(SiO_4)(Si_2O_7)O(OH)$	1.25	1376609.06
Altered titanite	$CaTiSiO_5$	0.06	58507.55
Albite	$NaAlSi_3O_8$	39.73	57429545.73
Grothite-titanite	$CaTiSiO_5$	1.4	2369014.65
Salt	NaCl	0	0

Table A8: C1_HPnoCa resin sample MLA results post-experiment.

Mineral	Formula	Weight%	Area microns
Quartz	SiO_2	13.58	19795898.59
Stilbite	$NaCa_4(Al_8Si_{27}O_{72}).nH_2O$	6.29	14419733.08
Plagioclase	$NaAlSi_3O_8$ - $CaAl_2Si_2O_8$	1.09	1549428.4
Pyrite	FeS_2	0.54	412647.95
Hornblende	$Ca_2(Mg,Fe,Al)_5(Al,Si)_8O_{22}(OH)_2$	1.04	1367458.33
Pseudobrookite	Fe_2TiO_5	0.01	8992
Andesine	$(Ca/Na)(Al,Si)_4O_8$ $(0.3\text{-}0.5_{an})$	0.03	48802.17
Chamosite	$(Fe^{2+},Mg,Fe^{3+})_5Al(Si_3Al)O_{10}(OH,O)_8$	22.5	26906320.6
Chlorapatite	$Ca_5(PO_4)_3Cl$	0.06	68296.07
Zircon	ZrSiO	0	943.69
Manganoan ilmenite	$(Mn)FeTiO_3$	0.02	12847.64
Calcite	$CaCO_3$	0	984.13
Microcline	$KAlSi_3O_8$	1.74	2599281.68
Titanite	$CaTiSiO_5$	0.18	197460.04
Anhydrite	$CaSO_4$	0	0
Titanite/pseudobrookite	$CaTiSiO_5$	0.12	87115.91
Orthoclase	$KAlSi_3O_8$	3.97	5933777.46
Prehnite	$Ca_2Al(AlSi_3O_{10})(OH)_2$	2.95	3930691.11
Pumpellyite-(Fe2)	$Ca_2MgAl_2(SiO_4)(Si_2O_7)(OH)_2.(H_2O)$	1.51	1799748.48
Epidote	$Ca_2Al_2(Fe,Al)(SiO_4)(Si_2O_7)O(OH)$	1.28	1421558.63
Altered titanite	$CaTiSiO_5$	0.12	114806.43
Albite	$NaAlSi_3O_8$	41.46	60550211.94
Grothite-titanite	$CaTiSiO_5$	1.08	1844668.04
Salt	NaCl	0.44	777181

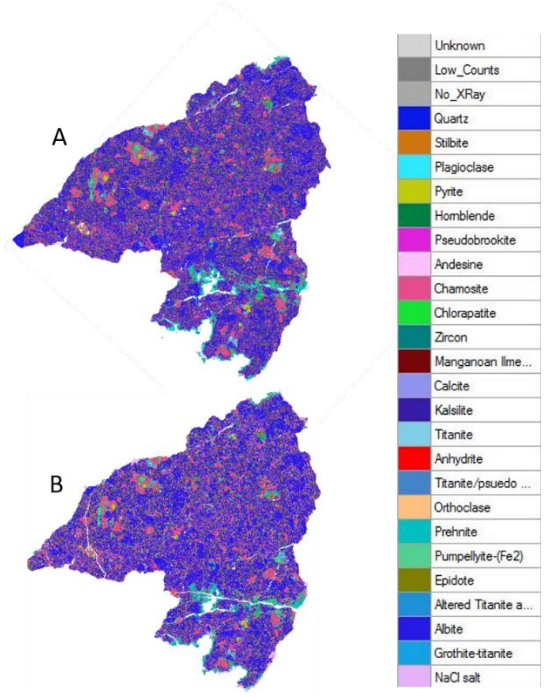


Figure A4: C1_HPnoCa resin sample MLA phase map A) pre-experiment and B) post-experiment.

Table A9: C1_HPCa resin sample MLA results pre-experiment.

Mineral	Formula	Weight%	Area microns
Quartz	SiO_2	11.51	10058399.54
Stilbite	$NaCa_4(Al_8Si_{27}O_{72}).nH_2O$	7.71	10594852.78
Plagioclase	$NaAlSi_3O_8$ - $CaAl_2Si_2O_8$	1.49	1276944.43
Pyrite	FeS_2	0.81	369858.08
Hornblende	$Ca_2(Mg,Fe,Al)_5(Al,Si)_8O_{22}(OH)_2$	0.89	703172.7
Pseudobrookite	Fe_2TiO_5	0	175.48
Andesine	$(Ca/Na)(Al,Si)_4O_8$ $(0.3\text{-}0.5_{an})$	0.02	12919.62
Chamosite	$(Fe^{2+},Mg,Fe^{3+})_5Al(Si_3Al)O_{10}(OH,O)_8$	21.78	15620901.25
Chlorapatite	$Ca_5(PO_4)_3Cl$	0.08	58909.69
Zircon	ZrSiO	0	138.92
Manganoan ilmenite	$(Mn)FeTiO_3$	0.02	11786.32
Calcite	$CaCO_3$	0	0
Microcline	$KAlSi_3O_8$	2.37	2123037.28
Titanite	$CaTiSiO_5$	0.19	125723.23
Anhydrite	$CaSO_4$	0	0
Titanite/pseudobrookite	$CaTiSiO_5$	0.02	6675.51
Orthoclase	$KAlSi_3O_8$	4.13	3705475.63
Prehnite	$Ca_2Al(AlSi_3O_{10})(OH)_2$	1.18	945486.95
Pumpellyite-(Fe2)	$Ca_2MgAl_2(SiO_4)(Si_2O_7)(OH)_2.(H_2O)$	0.59	424651.33
Epidote	$Ca_2Al_2(Fe,Al)(SiO_4)(Si_2O_7)O(OH)$	0.58	385599.99
Altered titanite	$CaTiSiO_5$	0.06	31915.2
Albite	$NaAlSi_3O_8$	45.42	39783794.89
Grothite-titanite	$CaTiSiO_5$	1.14	116775.29
Salt	NaCl	0	0

Table A10: C1_HPCa resin sample MLA results post-experiment.

Mineral	Formula	Weight%	Area microns
Quartz	SiO_2	11.75	10349212.77
Stilbite	$NaCa_4(Al_8Si_{27}O_{72}).nH_2O$	6.56	9082475.43
Plagioclase	$NaAlSi_3O_8$ - $CaAl_2Si_2O_8$	1.19	1026871.48
Pyrite	FeS_2	0.81	375171.73
Hornblende	$Ca_2(Mg,Fe,Al)_5(Al,Si)_8O_{22}(OH)_2$	0.77	615606.71
Pseudobrookite	Fe_2TiO_5	0.01	6855.96
Andesine	$(Ca/Na)(Al,Si)_4O_8$ $(0.3\text{-}0.5_{an})$	0.01	11038.36
Chamosite	$(Fe^{2+},Mg,Fe^{3+})_5Al(Si_3Al)O_{10}(OH,O)_8$	20.66	14928158.25
Chlorapatite	$Ca_5(PO_4)_3Cl$	0.07	49129.95
Zircon	ZrSiO	0	105.88
Manganoan ilmenite	$(Mn)FeTiO_3$	0.02	9794.22
Calcite	$CaCO_3$	0.01	7292.73
Microcline	$KAlSi_3O_8$	1.6	1448592.25
Titanite	$CaTiSiO_5$	0.15	99914.32
Anhydrite	$CaSO_4$	0	0
Titanite/pseudobrookite	$CaTiSiO_5$	0.21	91178.93
Orthoclase	$KAlSi_3O_8$	4.84	4369229.96
Prehnite	$Ca_2Al(AlSi_3O_{10})(OH)_2$	1.26	1011002.19
Pumpellyite-(Fe2)	$Ca_2MgAl_2(SiO_4)(Si_2O_7)(OH)_2.(H_2O)$	0.54	388539.53
Epidote	$Ca_2Al_2(Fe,Al)(SiO_4)(Si_2O_7)O(OH)$	0.62	418253.09
Altered titanite	$CaTiSiO_5$	0.06	34941.56
Albite	$NaAlSi_3O_8$	47.7	42084260.02
Grothite-titanite	$CaTiSiO_5$	1.01	1041880.47
Salt	NaCl	0.14	149864.87

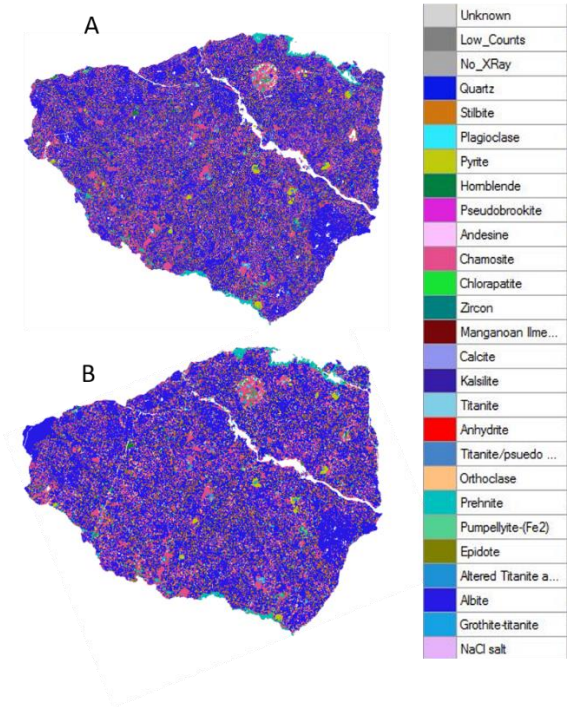


Figure A5: C1_HPCa resin sample MLA phase map A) pre-experiment and B) post-experiment.

Table A11: C1_LPCa resin sample MLA results pre-experiment.

Mineral	Formula	Weight%	Area microns
Quartz	SiO_2	13.55	17248825.16
Stilbite	$NaCa_4(Al_8Si_{27}O_{72}).nH_2O$	4.41	8813377.63
Plagioclase	$NaAlSi_3O_8$ - $CaAl_2Si_2O_8$	1.16	1440454.09
Pyrite	FeS_2	1.25	831674.35
Hornblende	$Ca_2(Mg,Fe,Al)_5(Al,Si)_8O_{22}(OH)_2$	0.65	746559.83
Pseudobrookite	Fe_2TiO_5	0	3290.23
Andesine	$(Ca/Na)(Al,Si)_4O_8$ $(0.3\text{-}0.5_{an})$	0.04	47525.5
Chamosite	$(Fe^{2+},Mg,Fe^{3+})_5Al(Si_3Al)O_{10}(OH,O)_8$	19.14	19982477.4
Chlorapatite	$Ca_5(PO_4)_3Cl$	0.07	74900.19
Zircon	ZrSiO	0	928.58
Manganoan ilmenite	$(Mn)FeTiO_3$	0.18	131133.83
Calcite	$CaCO_3$	0.01	9709.83
Microcline	$KAlSi_3O_8$	1.71	2232484.85
Titanite	$CaTiSiO_5$	0.23	222368.17
Anhydrite	$CaSO_4$	0	3341.41
Titanite/pseudobrookite	$CaTiSiO_5$	0.05	28288.64
Orthoclase	$KAlSi_3O_8$	5.72	7459105.56
Prehnite	$Ca_2Al(AlSi_3O_{10})(OH)_2$	4.06	4715780.06
Pumpellyite-(Fe2)	$Ca_2MgAl_2(SiO_4)(Si_2O_7)(OH)_2.(H_2O)$	1.69	1761090.37
Epidote	$Ca_2Al_2(Fe,Al)(SiO_4)(Si_2O_7)O(OH)$	1.02	989875.77
Altered titanite	$CaTiSiO_5$	0.08	71222.45
Albite	$NaAlSi_3O_8$	43.41	55348681.86
Grothite-titanite	$CaTiSiO_5$	1.56	2340418.92
Salt	NaCl	0	4562.45

Table A12: C1_LPCa resin sample MLA results post-experiment.

Mineral	Formula	Weight%	Area microns
Quartz	SiO_2	13.72	17521007.09
Stilbite	$NaCa_4(Al_8Si_{27}O_{72}).nH_2O$	5.21	10457928.66
Plagioclase	$NaAlSi_3O_8$ - $CaAl_2Si_2O_8$	1.26	1570106.81
Pyrite	FeS_2	1.23	8241977.22
Hornblende	$Ca_2(Mg,Fe,Al)_5(Al,Si)_8O_{22}(OH)_2$	0.62	714621.02
Pseudobrookite	Fe_2TiO_5	0.01	4817.7
Andesine	$(Ca/Na)(Al,Si)_4O_8$ $(0.3\text{-}0.5_{an})$	0.04	52941
Chamosite	$(Fe^{2+},Mg,Fe^{3+})_5Al(Si_3Al)O_{10}(OH,O)_8$	18.59	19480990.21
Chlorapatite	$Ca_5(PO_4)_3Cl$	0.07	76593.48
Zircon	ZrSiO	0	886.77
Manganoan ilmenite	$(Mn)FeTiO_3$	0.16	113838.01
Calcite	$CaCO_3$	0	277.94
Microcline	$KAlSi_3O_8$	1.89	2475847.75
Titanite	$CaTiSiO_5$	0.21	201840.43
Anhydrite	$CaSO_4$	0	0
Titanite/pseudobrookite	$CaTiSiO_5$	0.08	47951.99
Orthoclase	$KAlSi_3O_8$	5.46	7148354.36
Prehnite	$Ca_2Al(AlSi_3O_{10})(OH)_2$	3.95	4610419.35
Pumpellyite-(Fe2)	$Ca_2MgAl_2(SiO_4)(Si_2O_7)(OH)_2.(H_2O)$	1.69	1768003.09
Epidote	$Ca_2Al_2(Fe,Al)(SiO_4)(Si_2O_7)O(OH)$	1.07	1035302.46
Altered titanite	$CaTiSiO_5$	0.09	72834.62
Albite	$NaAlSi_3O_8$	43.05	55096945.93
Grothite-titanite	$CaTiSiO_5$	1.45	2187579.72
Salt	NaCl	0.17	258342.52

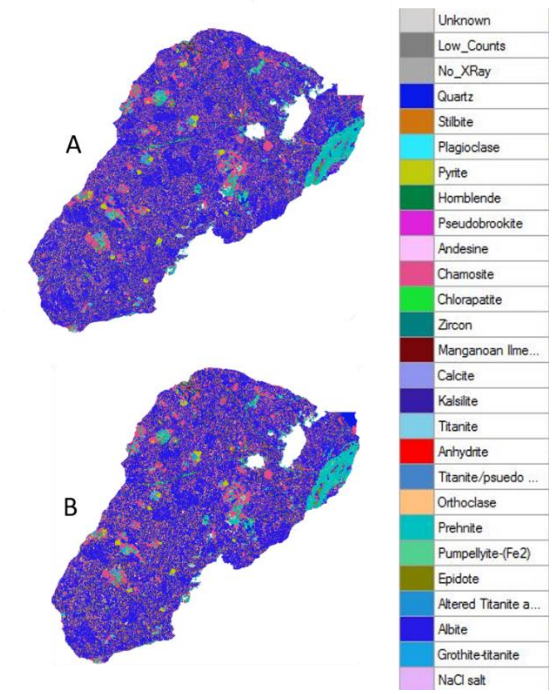


Figure A6: C1_LPCa resin sample MLA phase map A) pre-experiment and B) post-experiment.

Table A13: I1_HPnoCa resin sample MLA results pre-experiment.

Mineral	Formula	Weight%	Area microns
Quartz	SiO_2	15.23	13147425.55
Stilbite	$NaCa_4(Al_8Si_{27}O_{72}).nH_2O$	6.74	9136463.3
Plagioclase	$NaAlSi_3O_8$ - $CaAl_2Si_2O_8$	10.89	9136463.3
Pyrite	FeS_2	0.09	42421.99
Hornblende	$Ca_2(Mg,Fe,Al)_5(Al,Si)_8O_{22}(OH)_2$	0.14	107422.26
Pseudobrookite	Fe_2TiO_5	0.11	56006.98
Andesine	$(Ca/Na)(Al,Si)_4O_8$ $(0.3\text{-}0.5_{an})$	0.64	541988.13
Chamosite	$(Fe^{2+},Mg,Fe^{3+})_5Al(Si_3Al)O_{10}(OH,O)_8$	6.99	4951411.49
Chlorapatite	$Ca_5(PO_4)_3Cl$	0.15	107129.79
Zircon	ZrSiO	0.02	8956.73
Manganoan ilmenite	$(Mn)FeTiO_3$	0.31	151138.41
Calcite	$CaCO_3$	0.02	17357.78
Microcline	$KAlSi_3O_8$	15.89	14058072.65
Titanite	$CaTiSiO_5$	0.04	28215.52
Anhydrite	$CaSO_4$	0	3429.15
Titanite/pseudobrookite	$CaTiSiO_5$	0.31	130505.03
Orthoclase	$KAlSi_3O_8$	13.59	12028726.42
Prehnite	$Ca_2Al(AlSi_3O_{10})(OH)_2$	0.02	17876.9
Pumpellyite-(Fe2)	$Ca_2MgAl_2(SiO_4)(Si_2O_7)(OH)_2.(H_2O)$	0.12	84807.43
Epidote	$Ca_2Al_2(Fe,Al)(SiO_4)(Si_2O_7)O(OH)$	0.5	325454.64
Altered titanite	$CaTiSiO_5$	0.1	55246.57
Albite	$NaAlSi_3O_8$	27.69	23939574.97
Grothite-titanite	$CaTiSiO_5$	0.41	413698.52
Salt	NaCl	0	0

Table A14: I1_HPnoCa resin sample MLA results post-experiment.

Mineral	Formula	Weight%	Area microns
Quartz	SiO_2	14.88	13489161.68
Stilbite	$NaCa_4(Al_8Si_{27}O_{72}).nH_2O$	5.82	8294834.5
Plagioclase	$NaAlSi_3O_8$ - $CaAl_2Si_2O_8$	11.36	10071705.33
Pyrite	FeS_2	0.08	37681.29
Hornblende	$Ca_2(Mg,Fe,Al)_5(Al,Si)_8O_{22}(OH)_2$	0.14	118232.17
Pseudobrookite	Fe_2TiO_5	0.12	63305.1
Andesine	$(Ca/Na)(Al,Si)_4O_8$ $(0.3\text{-}0.5_{an})$	0.59	522508.63
Chamosite	$(Fe^{2+},Mg,Fe^{3+})_5Al(Si_3Al)O_{10}(OH,O)_8$	7.1	5276426.61
Chlorapatite	$Ca_5(PO_4)_3Cl$	0.14	105036.44
Zircon	ZrSiO	0.02	8655.98
Manganoan ilmenite	$(Mn)FeTiO_3$	0.32	161181.17
Calcite	$CaCO_3$	0	0
Microcline	$KAlSi_3O_8$	8.85	8226301.4
Titanite	$CaTiSiO_5$	0.02	15313.4
Anhydrite	$CaSO_4$	0	0
Titanite/pseudobrookite	$CaTiSiO_5$	0.41	183932.89
Orthoclase	$KAlSi_3O_8$	20.23	18805003.43
Prehnite	$Ca_2Al(AlSi_3O_{10})(OH)_2$	0.03	23334.08
Pumpellyite-(Fe2)	$Ca_2MgAl_2(SiO_4)(Si_2O_7)(OH)_2.(H_2O)$	0.14	103474.66
Epidote	$Ca_2Al_2(Fe,Al)(SiO_4)(Si_2O_7)O(OH)$	0.46	314672.55
Altered titanite	$CaTiSiO_5$	0.13	75997.89
Albite	$NaAlSi_3O_8$	28.7	26062483.98
Grothite-titanite	$CaTiSiO_5$	0.37	389651.3
Salt	NaCl	0.11	118960.12

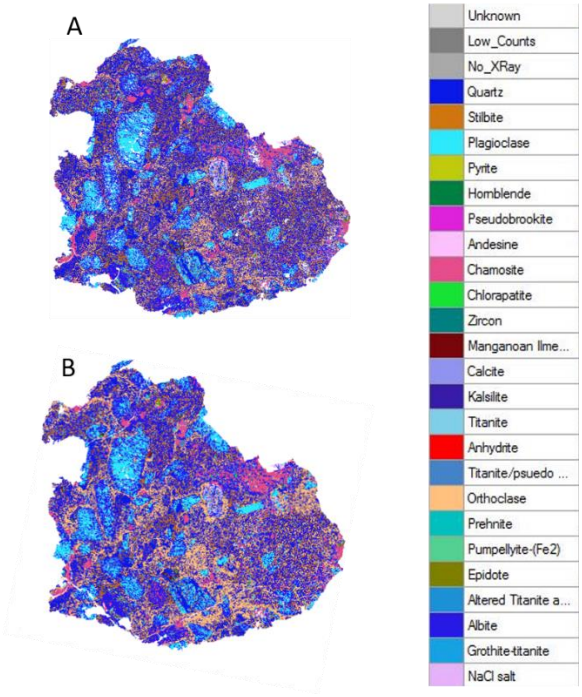


Figure A7: I1_HPnoCa resin sample MLA phase map A) pre-experiment and B) post-experiment.

Table A15: I1_HPCa resin sample MLA results pre-experiment.

Mineral	Formula	Weight%	Area microns
Quartz	SiO_2	16.52	16196734.85
Stilbite	$NaCa_4(Al_8Si_{27}O_{72}).nH_2O$	5.21	8028088.18
Plagioclase	$NaAlSi_3O_8$ - $CaAl_2Si_2O_8$	3.94	3779403.37
Pyrite	FeS_2	0.12	63179.67
Hornblende	$Ca_2(Mg,Fe,Al)_5(Al,Si)_8O_{22}(OH)_2$	0.47	419694.05
Pseudobrookite	Fe_2TiO_5	0.08	47730.23
Andesine	$(Ca/Na)(Al,Si)_4O_8$ $(0.3\text{-}0.5_{an})$	0.54	517048.21
Chamosite	$(Fe^{2+},Mg,Fe^{3+})_5Al(Si_3Al)O_{10}(OH,O)_8$	4.46	3589805.87
Chlorapatite	$Ca_5(PO_4)_3Cl$	0.12	93983.51
Zircon	ZrSiO	0.02	11676.65
Manganoan ilmenite	$(Mn)FeTiO_3$	0.17	93296.22
Calcite	$CaCO_3$	0.01	10228.95
Microcline	$KAlSi_3O_8$	9.68	9730722.18
Titanite	$CaTiSiO_5$	0.07	54149.83
Anhydrite	$CaSO_4$	0.13	109359.84
Titanite/pseudobrookite	$CaTiSiO_5$	0.16	77854
Orthoclase	$KAlSi_3O_8$	9.7	9752386.49
Prehnite	$Ca_2Al(AlSi_3O_{10})(OH)_2$	0.03	30950.07
Pumpellyite-(Fe2)	$Ca_2MgAl_2(SiO_4)(Si_2O_7)(OH)_2.(H_2O)$	0.16	131331.24
Epidote	$Ca_2Al_2(Fe,Al)(SiO_4)(Si_2O_7)O(OH)$	8.13	6062696.33
Altered titanite	$CaTiSiO_5$	0.06	38451.79
Albite	$NaAlSi_3O_8$	39.69	38979239.33
Grothite-titanite	$CaTiSiO_5$	0.52	597154.27
Salt	NaCl	0	0

Table A16: I1_HPCa resin sample MLA results post-experiment.

Mineral	Formula	Weight%	Area microns
Quartz	SiO_2	15.89	17943667.74
Stilbite	$NaCa_4(Al_8Si_{27}O_{72}).nH_2O$	4.21	7478285.57
Plagioclase	$NaAlSi_3O_8$ - $CaAl_2Si_2O_8$	5.88	6489078.13
Pyrite	FeS_2	0.11	67406.84
Hornblende	$Ca_2(Mg,Fe,Al)_5(Al,Si)_8O_{22}(OH)_2$	0.93	952289.69
Pseudobrookite	Fe_2TiO_5	0.07	44355.1
Andesine	$(Ca/Na)(Al,Si)_4O_8$ $(0.3\text{-}0.5_{an})$	0.47	523317.52
Chamosite	$(Fe^{2+},Mg,Fe^{3+})_5Al(Si_3Al)O_{10}(OH,O)_8$	5.92	5487739.62
Chlorapatite	$Ca_5(PO_4)_3Cl$	0.13	119279.98
Zircon	ZrSiO	0.02	10490.29
Manganoan ilmenite	$(Mn)FeTiO_3$	0.13	84648.57
Calcite	$CaCO_3$	0.05	55383.55
Microcline	$KAlSi_3O_8$	7.03	8135475.33
Titanite	$CaTiSiO_5$	0.08	68281.03
Anhydrite	$CaSO_4$	0	2071.16
Titanite/pseudobrookite	$CaTiSiO_5$	0.26	142708.29
Orthoclase	$KAlSi_3O_8$	12.55	14533637.62
Prehnite	$Ca_2Al(AlSi_3O_{10})(OH)_2$	0.13	138229.74
Pumpellyite-(Fe2)	$Ca_2MgAl_2(SiO_4)(Si_2O_7)(OH)_2.(H_2O)$	0.53	487368.11
Epidote	$Ca_2Al_2(Fe,Al)(SiO_4)(Si_2O_7)O(OH)$	7.05	6053381.43
Altered titanite	$CaTiSiO_5$	0.06	45094.8
Albite	$NaAlSi_3O_8$	37.41	42329435.94
Grothite-titanite	$CaTiSiO_5$	0.62	827024.87
Salt	NaCl	0.46	631582.7

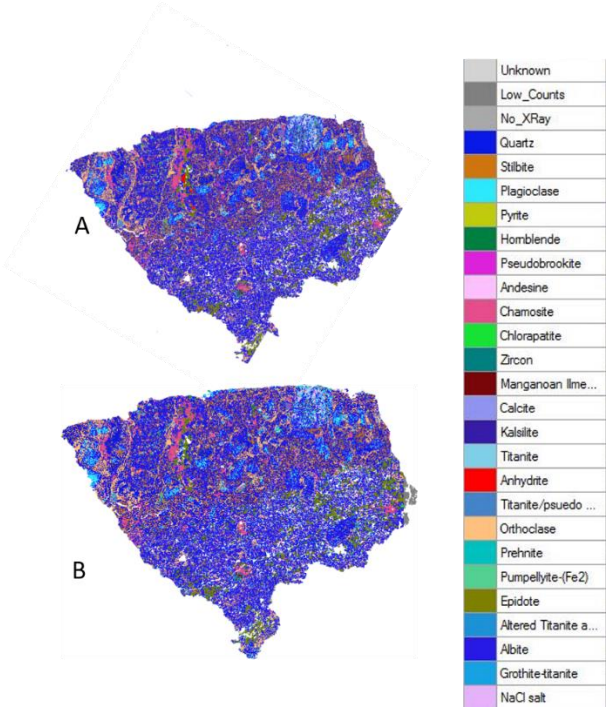


Figure A8: I1_HPCa resin sample MLA phase map A) pre-experiment and B) post-experiment.

Table A17: I1_LPCa resin sample MLA results pre-experiment.

Mineral	Formula	Weight%	Area microns
Quartz	SiO_2	24.32	14813355.24
Stilbite	$NaCa_4(Al_8Si_{27}O_{72}).nH_2O$	7.21	6903166.86
Plagioclase	$NaAlSi_3O_8$ - $CaAl_2Si_2O_8$	9.61	5721200.32
Pyrite	FeS_2	0.07	21715.5
Hornblende	$Ca_2(Mg,Fe,Al)_5(Al,Si)_8O_{22}(OH)_2$	0.17	91716.91
Pseudobrookite	Fe_2TiO_5	0.18	63903.52
Andesine	$(Ca/Na)(Al,Si)_4O_8$ $(0.3\text{-}0.5_{an})$	0.33	198963.68
Chamosite	$(Fe^{2+},Mg,Fe^{3+})_5Al(Si_3Al)O_{10}(OH,O)_8$	4.88	2439769.16
Chlorapatite	$Ca_5(PO_4)_3Cl$	0.07	35015.33
Zircon	ZrSiO	0.01	3568.07
Manganoan ilmenite	$(Mn)FeTiO_3$	0.02	7406.67
Calcite	$CaCO_3$	0.01	3100.13
Microcline	$KAlSi_3O_8$	19.94	12457881.7
Titanite	$CaTiSiO_5$	0.02	10075.41
Anhydrite	$CaSO_4$	0	43.87
Titanite/pseudobrookite	$CaTiSiO_5$	0.39	117680.45
Orthoclase	$KAlSi_3O_8$	10.55	6593190.92
Prehnite	$Ca_2Al(AlSi_3O_{10})(OH)_2$	0.03	14484.31
Pumpellyite-(Fe2)	$Ca_2MgAl_2(SiO_4)(Si_2O_7)(OH)_2.(H_2O)$	0.07	34313.41
Epidote	$Ca_2Al_2(Fe,Al)(SiO_4)(Si_2O_7)O(OH)$	0.71	331333.17
Altered titanite	$CaTiSiO_5$	0.02	8642.33
Albite	$NaAlSi_3O_8$	21.15	12907516.81
Grothite-titanite	$CaTiSiO_5$	0.25	175961.34
Salt	NaCl	0	0

Table A18: I1_LPCa resin sample MLA results post-experiment.

Mineral	Formula	Weight%	Area microns
Quartz	SiO_2	23.51	15479834.87
Stilbite	$NaCa_4(Al_8Si_{27}O_{72}).nH_2O$	6.08	6294994.32
Plagioclase	$NaAlSi_3O_8$ - $CaAl_2Si_2O_8$	10.56	6793888.3
Pyrite	FeS_2	0.06	21303.36
Hornblende	$Ca_2(Mg,Fe,Al)_5(Al,Si)_8O_{22}(OH)_2$	0.19	115218.35
Pseudobrookite	Fe_2TiO_5	0.19	72786.47
Andesine	$(Ca/Na)(Al,Si)_4O_8$ $(0.3\text{-}0.5_{an})$	0.3	193787.93
Chamosite	$(Fe^{2+},Mg,Fe^{3+})_5Al(Si_3Al)O_{10}(OH,O)_8$	6.96	3756438.31
Chlorapatite	$Ca_5(PO_4)_3Cl$	0.06	34954.18
Zircon	ZrSiO	0.01	3039.49
Manganoan ilmenite	$(Mn)FeTiO_3$	0.02	6912.83
Calcite	$CaCO_3$	0	860.74
Microcline	$KAlSi_3O_8$	11.12	7503731.25
Titanite	$CaTiSiO_5$	0.01	5635.17
Anhydrite	$CaSO_4$	0	0
Titanite/pseudobrookite	$CaTiSiO_5$	0.55	177837.31
Orthoclase	$KAlSi_3O_8$	17.23	11634040.81
Prehnite	$Ca_2Al(AlSi_3O_{10})(OH)_2$	0.06	35801.48
Pumpellyite-(Fe2)	$Ca_2MgAl_2(SiO_4)(Si_2O_7)(OH)_2.(H_2O)$	0.11	62000.3
Epidote	$Ca_2Al_2(Fe,Al)(SiO_4)(Si_2O_7)O(OH)$	0.65	324566.88
Altered titanite	$CaTiSiO_5$	0.02	8002.21
Albite	$NaAlSi_3O_8$	21.94	14468786.11
Grothite-titanite	$CaTiSiO_5$	0.26	204735.49
Salt	NaCl	0.11	85388.27

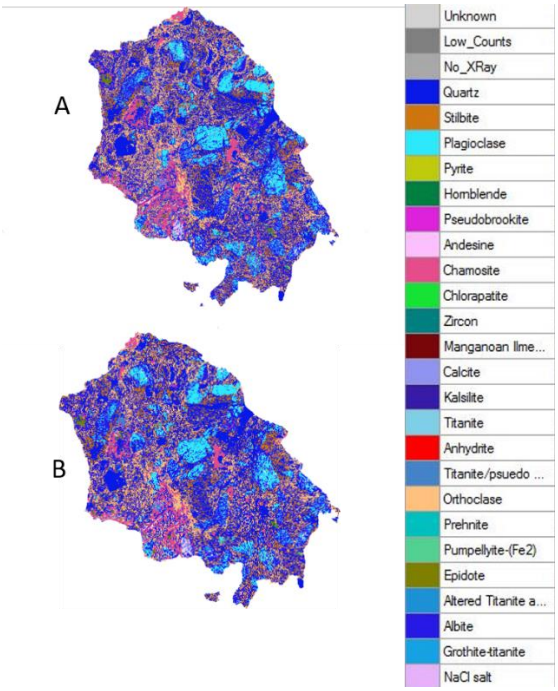


Figure A9: I1_LPCa resin sample MLA phase map A) pre-experiment and B) post-experiment.

Table A19: Average chemical composition of samples B1, C1 and I1.

	B1	C1	I1
Na_2O	8.63	3.67	7.27
SiO_2	65.04	51.21	59.65
K_2O	0.64	0.38	0.14
FeO	0.15	1.58	0.29
Al_2O_3	21.54	28.21	26.36
CaO	3.70	12.79	6.06
SrO	n.d.	n.d.	n.d.
SO_3	n.d.	n.d.	n.d.
TiO_2	n.d.	0.52	<0.02
MgO	n.d.	0.61	n.d.
P_2O_5	<0.02	0.09	<0.02
F	0.067	0.08	<0.02
Cl	n.d.	<0.02	<0.02
Total	99.79	99.15	99.83

n.d. *Not detected*

< Less than detection limit

Stoichiometric calculations (based on 8 oxygens).

	B1	C1	I1
Na	0.369	0.165	0.313
Si	1.436	1.185	1.326
K	0.018	0.011	0.004
Fe	0.003	0.031	0.005
Al	0.562	0.767	0.691
Ca	0.088	0.316	0.144
Sr	-	-	-
S	-	-	-
Ti	-	0.010	-
Mg	-	0.022	-
P	-	0.002	-
F	0.005	0.006	-
Cl	-	-	-
Total	2.481	2.515	2.486

Table A20: Error associated with each of the linear fits described in figure 3.5 B. These errors are relatively small, suggesting a good linear fit with the data. The associated experimental errors in the data (approximately 10% of the measured values) are larger than the statistical errors calculated here and are displayed within Figure 3.5 (Chapter 3).

Experiment name	R^2 value for linear fit	Standard error (mg/L)
B1 Neutral	0.99	0.24
B1 Acidic	0.99	0.03
C1 Neutral	0.98	0.31
C1 Acidic	0.97	0.31
I1 Neutral	0.99	0.10
I1 Acidic	0.95	0.40

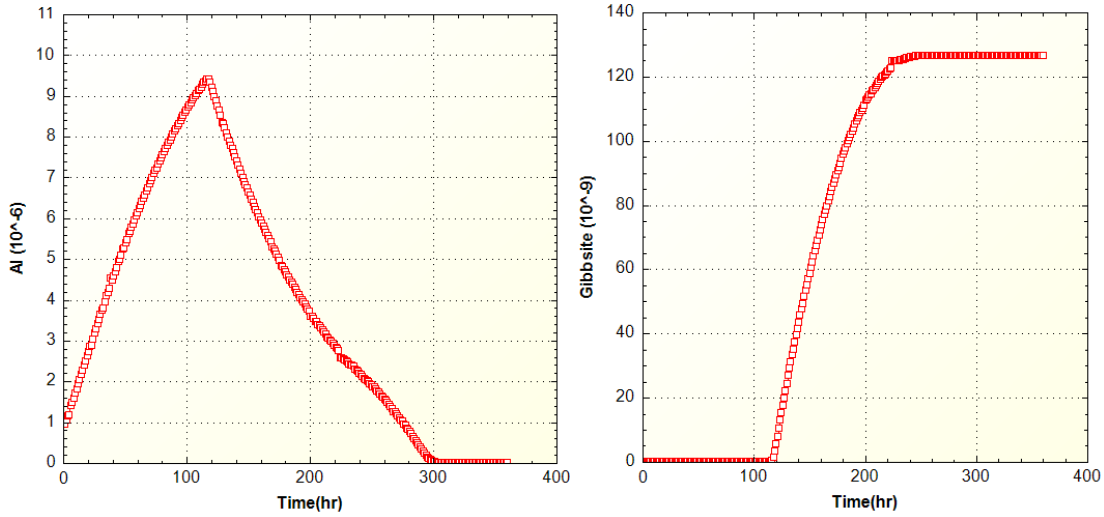


Figure A10: Graphical output from phreeqc calculations (Chapter 3) for concentration of Al in the fluids (left) and concentration of Gibbsite (right) (molL^{-1}).

Table A21: Concentrations (mg/L) of cation species in solutions collected from batch experiments discussed in Chapter 3, Figure 3.5, measured by ICP-OES analysis. A 10% error is associated with each measurement.

RDB1 Neutral																
Hours	0.00	3.00	5.50	22.50	30.50	46.50	53.00	127.5	151.5	174.5	203.0	222.5	293.5	318.5	341.5	363.5
Si	-0.12	2.97	4.79	8.23	9.06	9.45	9.61	10.69	12.56	13.75	11.98	12.40	12.53	13.02	13.09	13.36
Al	0.00	0.64	1.27	2.29	2.45	2.45	2.49	2.40	2.21	2.08	2.18	2.11	1.83	2.00	2.11	1.88
Na	746.71	707.95	704.00	706.49	716.49	711.86	716.06	710.83	736.53	729.77	718.30	718.31	708.48	707.60	721.61	678.70
K	159.12	256.30	279.00	260.82	271.10	281.05	296.88	240.28	261.55	328.23	311.55	270.33	300.57	287.42	300.25	298.07
Ca	19.70	26.26	26.57	28.64	28.56	28.64	28.53	29.20	29.78	30.38	29.89	29.40	29.88	30.39	29.39	30.18
Mg	0.03	0.31	0.28	0.27	0.21	0.23	0.22	0.18	0.21	0.22	0.17	0.19	0.19	0.15	0.14	0.15
RDB1 Acidic																
Hours	0.00	3.00	4.50	21.00	26.00	44.00	51.00	65.50	69.00	141.00	162.50	186.00	208.00	307.00	331.50	353.50
Si	-0.16	2.27	3.56	8.21	8.42	10.02	10.73	11.66	11.76	16.28	14.47	25.66	21.53	18.76	21.41	22.93
Al	0.02	0.02	0.04	0.05	0.04	0.03	0.03	0.02	0.02	0.01	0.01	0.03	0.03	0.02	0.02	0.05
Na	675.60	656.18	667.71	687.16	697.51	690.23	777.22	662.03	671.40	670.70	672.69	693.72	684.45	707.83	668.91	715.83
K	179.11	180.48	179.16	178.95	183.02	180.13	189.46	176.48	180.45	181.92	181.76	184.40	184.41	441.44	274.38	331.34
Ca	19.98	22.33	23.03	24.84	24.50	25.00	25.46	24.59	24.69	27.36	25.52	36.30	33.82	29.47	30.69	27.42
Mg	0.03	2.22	2.36	3.05	2.89	3.07	3.36	3.44	3.35	4.14	3.64	4.67	4.50	4.27	4.34	3.87
RDC1 Neutral																
Hours	0.00	4.50	6.00	23.50	29.50	46.00	69.00	76.50	94.50	165.50	214.00	214.00	243.00	262.50	340.00	357.50
Si	-0.11	3.31	3.74	6.96	6.59	8.44	10.41	11.21	11.82	15.00	17.48	17.48	15.92	17.21	19.42	19.11
Al	0.02	0.02	0.04	0.05	0.04	0.03	0.03	0.02	0.02	0.01	0.01	0.03	0.03	0.02	0.02	0.05
Na	667.28	677.82	678.34	689.96	685.63	682.66	671.49	702.59	694.33	664.84	694.01	720.16	659.15	678.96	664.64	644.12
K	176.20	169.61	174.96	166.43	169.78	176.17	174.67	172.50	176.82	178.06	179.56	179.56	177.70	175.58	181.24	175.61
Ca	16.88	18.92	19.46	19.46	19.36	20.91	21.41	22.04	22.44	22.53	23.61	23.61	23.29	24.25	26.77	24.34
Mg	0.03	1.71	1.75	2.19	1.48	2.17	2.50	2.53	2.50	3.28	3.45	3.45	3.49	3.55	3.78	3.57
RDC1 Acidic																
Hours	0.00	3.00	5.00	24.00	28.00	44.50	52.50	74.00	143.00	169.00	189.50	217.00	238.00	309.25	337.00	358.00
Si	-0.13	3.06	4.15	9.09	11.18	14.89	15.40	15.52	26.16	26.73	27.80	25.16	25.19	30.65	32.08	28.32
Al	0.01	0.02	0.02	0.03	0.07	0.04	0.05	0.04	0.15	0.15	0.15	0.08	0.09	0.11	0.12	0.07
Na	695.29	704.12	659.94	673.24	651.01	653.40	671.97	637.89	641.83	682.84	657.90	653.90	634.61	644.18	644.76	
K	151.08	182.81	213.74	225.05	181.85	260.75	202.42	174.54	222.02	155.25	159.04	178.25	158.24	158.78	157.18	172.07
Ca	19.96	25.07	26.12	28.14	30.64	32.78	35.04	34.56	48.91	50.13	49.69	46.32	47.26	53.16	56.10	53.36
Mg	0.03	3.85	4.12	5.21	5.38	5.71	5.73	5.46	6.21	6.13	6.22	6.05	6.03	6.28	6.24	5.98
RDI1 Neutral																
Hours	0.00	3.00	5.00	24.00	30.50	54.50	130.00	150.00	172.50	197.50	222.50	294.50	318.50	342.50	360.00	360.00
Si	0.22	3.21	5.00	9.46	11.09	18.40	16.54	21.81	19.50	19.59	21.34	22.56	25.01	23.22	26.84	26.84
Al	0.00	0.00	0.00	1.32	0.00	0.00	1.26	0.77	1.01	1.68	0.00	1.33	0.00	0.00	1.03	1.03
Na	976.23	889.72	914.95	912.87	974.60	830.30	848.79	839.64	823.67	816.93	775.22	831.89	824.15	824.16	848.50	848.50
K	152.91	140.56	147.38	159.12	163.67	159.07	154.46	152.01	147.24	163.26	162.68	159.54	155.96	163.25	159.05	159.05
Ca	24.31	58.91	52.78	48.82	53.40	58.93	52.81	54.62	53.75	48.67	59.71	51.92	51.55	57.30	54.14	54.14
Mg	0.01	1.01	1.20	0.77	1.06	1.62	0.57	1.16	0.80	0.37	1.35	0.53	0.69	0.78	0.65	0.65

RDI1 Acidic																
	Z	A	B	C	D	E	F	G	H	I	J	K	L	M	N	O
Si	0.10	1.33	4.05	8.53	9.70	11.43	11.84	13.79	15.15	16.51	16.69	17.41	19.41	18.82	19.06	19.43
Al	0.13	0.22	0.28	0.41	0.30	2.02	1.70	1.46	2.09	0.82	1.61	1.54	1.54	1.35	0.92	1.64
Na	802.80	797.20	807.43	784.68	807.75	807.17	800.66	797.07	771.41	787.81	764.75	770.48	772.51	769.81	759.66	785.28
K	158.37	155.85	159.43	158.86	158.82	156.99	159.08	158.59	159.95	158.54	159.24	158.07	156.08	159.09	161.74	159.50
Ca	23.79	49.29	53.68	56.32	57.59	59.94	59.80	61.00	60.93	66.21	63.38	64.71	65.51	63.37	63.62	61.44
Mg	-0.24	0.59	0.94	1.04	1.02	1.03	1.09	1.01	0.89	1.02	0.73	1.01	0.92	0.87	0.92	0.56

Table A22: Variation in pH (±0.1) of solutions collected from batch experiments discussed in Chapter 3, Figure 3.6.

Time (hrs)	B1 Neutral	Time (hrs)	B1 Acid	Time (hrs)	C1 Neutral	Time (hrs)	C1 Acid	Time (hrs)	I1 Neutral	Time (hrs)	I1 Acid
0.0	7.3	0.0	3.2	0.0	7.0	0.0	3.4	0.0	6.5	0.0	3.0
3.0	8.1	3.0	6.2	4.5	7.0	3.0	5.3	3.0	6.3	2.0	5.9
5.5	8.4	4.5	6.5	6.0	7.1	5.0	5.2	5.0	6.6	5.0	6.3
22.5	8.5	21.0	6.3	23.5	6.6	24.0	6.0	24.0	6.8	23.0	6.6
30.5	8.4	26.0	6.5	29.5	6.8	28.0	5.0	30.5	7.4	29.0	6.7
46.5	8.4	44.0	6.4	46.0	6.8	44.5	4.8	54.5	6.2	47.0	6.0
53.0	8.4	51.0	6.6	69.0	6.2	52.5	4.7	130.0	7.8	52.0	6.4
127.5	8.4	65.5	6.3	76.5	6.1	74.0	4.9	150.0	7.2	72.0	6.3
151.5	7.9	69.0	6.2	94.5	6.1	143.0	4.1	172.5	7.4	96.0	6.3
174.5	7.8	141.0	6.3	165.5	5.9	169.0	4.4	197.5	7.9	168.0	6.3
203.0	8.0	162.5	6.4	190.0	5.7	189.5	4.4	222.5	7.0	191.5	6.1
222.5	8.0	186.0	5.8	214.0	5.8	217.0	4.5	294.5	7.5	216.5	6.5
293.5	7.7	208.0	5.8	243.0	5.7	238.0	4.6	318.5	7.3	240.0	6.7
318.5	7.9	307.0	6.6	262.5	5.7	309.3	4.4	342.5	7.2	264.0	6.9
341.5	7.9	331.5	6.3	340.0	5.5	337.0	4.4	360.0	7.2	336.0	6.1
363.5	8.0	353.5	6.6	357.5	5.7	358.0	4.6			360.0	6.5

Table A23: Concentrations (mg/L) of cation species in solutions collected from batch experiments discussed in Chapter 4, measured by ICP-OES analysis. A 10% error is associated with each measurement.

C1_HpnoCa							
Time (hrs)	0	1	7	24	31.5	48	49
Si	0	0	0	0.221188	0.302126	0.329683	0.232908
Al	0.00824	0.271555	0.422868	0.439314	0.406814	0.355806	0.29766
Ca	0	71.17496	16.05551	13.14062	17.69219	15.10108	13.80194
Mg	0.009486	0.142932	0.05272	0.077034	0.085652	0.087426	0.106625
C1_HPCa							
Time (hrs)	0	0.5	17	23.5	42	47	48
Si	0	0	0.118258	0.17004	0.310609	0.34445	0.291243
Al	0.145932	0.401651	0.676323	0.647737	0.590489	0.582911	0.452849
C1_LPCa							
Time (hrs)	0	0.5	5.5	23	29.5	47	49
Si	0	0	0	0.069029	0.124071	0.244597	0.104546
Al	0.142201	0.215347	0.272614	0.264437	0.264973	0.23585	0.239677
B1_HpnoCa							
Time (hrs)	0	0.5	7	24	31	48	49
Si	0	0	0	0.080708	0.149142	0.35295	0.281041
Al	0.009394	0.424977	0.828895	0.782868	0.762002	0.621417	0.68284
Ca	0	52.19578	24.5093	1.04404	8.908669	12.31616	8.479484
Mg	0.004235	0.743403	0.211611	0.22627	0.272747	0.36073	0.362003
B1_HPCa							
Time (hrs)	0	1	16.5	25.5	42	48	49
Si	0	0	0.022534	0.007092	0.186364	0.187781	0.11385
Al	0.145736	0.663006	1.337673	1.144806	0.896009	0.897836	0.795848
B1_LPCa							
time	0	1	7	24.5	32	48	49
Si	0	0	0	0.000496	0	0.071515	0
Al	0.141008	0.261764	0.319123	0.318271	0.323177	0.293787	0.167709
I1_HPnoCa							
Time (hrs)	0	1	17.5	26.5	41.5	47.5	49
Si	0	0.022181	0.311107	0.388392	0.459479	0.482383	0.433229
Al	0	1.023056	0.891263	0.822184	0.689614	0.676226	0.614998
Ca	0	148.3526	119.7232	116.9788	112.3487	110.5848	114.4095
Mg	0.042401	0.376767	0.317162	0.337029	0.312493	0.329106	0.32769
I1_HPCa							
Time (hrs)	0	0.5	6.5	23.5	30	47	48
Si	0	0	0.044778	0.213767	0.264949	0.390699	0.301939
Al	0.129892	0.538965	1.035939	1.024584	0.975872	0.906769	0.790428
I1_LPCa							
Time (hrs)	0	1	17.5	26	42.5	47.5	49
Si	0	0	0.209116	0.288258	0.419681	0.324713	0.234704
Al	0.125975	0.427964	0.46059	0.445708	0.364198	0.359692	0.357244

Table A24: Concentrations for Si and Al (mg/L) measured using ICP-OES when known concentrations of each species was added to the solutions alongside varying concentrations of NaCl (M), displayed in Figure 5.1 of Chapter 5.

Si

	0 mg/L	0.1 m/L	1 mg/L	3 mg/L	5 mg/L	7 mg/L	10 mg/L
0 M	-0.03	0.10	1.32	3.07	4.67	6.80	9.91
0.01 M	-0.02	0.07	1.06	3.29	5.14	7.07	9.98
0.05 M	0.01	0.08	1.30	3.05	5.01	7.17	9.69
0.1 M	0.01	0.10	1.27	3.26	5.21	7.22	10.28
0.15 M	0.09	0.16	1.43	3.12	5.03	6.57	9.34
0.3 M	-0.01	0.12	1.28	3.28	5.50	7.70	10.62
0.5 M	0.12	0.10	1.27	3.79	5.88	8.35	11.48

Al

	0 mg/L	0.1 m/L	1 mg/L	3 mg/L	5 mg/L	7 mg/L	10 mg/L
0 M	0.00	0.08	0.94	2.72	4.38	6.69	9.77
0.01 M	0.00	0.11	1.03	3.37	5.39	7.57	11.03
0.05 M	0.00	0.12	1.41	3.59	5.88	8.30	11.56
0.1 M	0.00	0.14	1.44	3.85	6.27	8.78	12.65
0.15 M	0.00	0.13	1.31	3.33	5.36	7.47	11.39
0.3 M	0.00	0.16	1.44	4.18	6.90	9.43	13.89
0.5 M	0.00	0.14	1.40	4.19	6.75	9.80	13.60

Table A25: Concentrations of NaCl (M) and the associated correction factor discussed in Chapter 5, Figure 5.2, used to estimate true silicon and aluminium concentrations in the experimental fluids discussed in Chapter 5.

Si

[NaCl] M	Correction factor
0	1
0.01	0.9974
0.05	1.0237
0.1	0.9792
0.15	1.0898
0.3	0.9367
0.5	0.8683

Al

[NaCl] M	Correction factor
0	1
0.01	0.9107
0.05	0.8643
0.1	0.7967
0.15	0.8989
0.3	0.727
0.5	0.7308

Table A26: Concentrations for Si and Al (mg/L) measured using ICP-OES with varying concentrations of NaCl (M) added to the solutions, displayed in Figure 5.5 of Chapter 5.

AF sample			
starting pH	NaCl (M)	Si (mg/L)	Al (mg/L)
3.17	0.00	78.12	0.09
2.88	0.35	65.90	0.15
2.79	0.70	85.93	0.23
2.71	1.05	94.07	0.27
2.67	1.40	78.88	0.27
2.61	1.75	99.33	0.26
2.55	2.10	85.61	0.28

PF Sample			
starting pH	NaCl (M)	Si (mg/L)	Al (mg/L)
3.17	0.00	46.10	0.05
2.88	0.35	55.11	0.19
2.79	0.70	61.68	0.20
2.71	1.05	54.01	0.08
2.67	1.40	50.88	0.06
2.61	1.75	76.64	0.12
2.55	2.10	67.01	0.04